

NORTHWESTERN UNIVERSITY

Paving a Path towards Rational Design of Semiconductor Materials: Exploratory and *In Situ*

Synthesis of Chalcogenides

A DISSERTATION

SUBMITTED TO THE GRADUATE SCHOOL

IN PARTIAL FULFILLMENT OF THE REQUIREMENTS

for the degree

DOCTOR OF PHILOSOPHY

Field of Chemistry

By

Rebecca McClain

EVANSTON, ILLINOIS

March 2022

© Copyright by Rebecca McClain 2021

All Rights Reserved

Abstract

Paving a Path towards Rational Design of Semiconductor Materials: Exploratory and *In Situ* Synthesis of Chalcogenides

Rebecca McClain

As the interest in rational synthesis for solid-state materials accelerates, there is an urgent need to understand the design principles concealed within these reactions. *In situ* material synthesis provides such an avenue to not only uncover these assembling rules, but also for finding new materials even in seemingly familiar phase spaces. Historically, this technique was largely employed for crystallization observations. However, as described in this dissertation, the increased accessibility of in-house diffractometer setups – and consequent decreased requirement for synchrotron or spallation sources – enabled the application of this powerful technique to the chalcogenide and heteroanionic systems. As detailed in the first chapters, all *in situ* material synthesis measurements yield novel information that build toward an overall understanding of the driving force for reaction progressions and assembly rules. The *in situ* investigations of the KBiQ_2 (Q = S, Se) and BiOCuSe reactions highlight the power of panoramic synthesis to uncover new phases in a well-known system, while tuning precursor ratios, and to unveil a structural intermediate that underlies the formation of the compounds in the A-Pn-Q (A = alkali metal; Pn = Sb, Bi) compositional space. The study of the $\text{Bi}_2\text{O}_2\text{Se} + \text{Cu}_2\text{Se}$ versus $\text{Bi}_2\text{O}_3 + \text{Bi} + 3 \text{Cu} + 3 \text{Se}$ reaction pathways to form BiOCuSe underscores the influence the selection of precursors has on the reaction progression and establishes an understanding of the effects of the chosen precursors. As heteroanionic materials are further investigated, six new materials are discovered. The four

novel heteroanionic materials, $\text{In}_8\text{S}_{3-x}\text{Te}_{6+x}(\text{Te}_2)_3$ ($x = 0.18$), $\text{Ba}_2\text{SnS}_{1.2}\text{Te}_{2.8}$, $\text{Ba}_3\text{SnS}_4\text{Te}$, and $\text{Ba}_3\text{SnS}_{5.62}\text{Te}_{0.13}$ are comprised of S^{2-} , Te^{2-} , S_2^{2-} and/or Te_2^{2-} with their crystallographically distinct sites. Two solid solutions $\text{Ba}_7\text{Sn}_5\text{S}_{15-x}\text{Te}_x$ and $\text{Ba}_8\text{Sn}_4\text{S}_{15-y}\text{Te}_y$ ($x = 0.7$, $y = 0.76$) are also discovered in these investigations. The advances in *in situ* PXRD as well as interrogations into novel compositional spaces, point the way towards more wide-ranging studies to fully flesh out the design principles that can be applied to larger families of materials, as well as combinatorial studies with complementary probes or calculations that can guide or confirm these design principles to enable rational design of complex solid-state materials.

Acknowledgements

I have had the great privilege over the past several years to meet and form relationships with many incredible people. They have each contributed in unique ways to the successful completion of my doctoral studies as well as my professional development. I would like to thank my advisor, Mercouri Kanatzidis, for taking me into his lab and guiding me into the world of solid-state synthesis. I also want to thank my committee members, Danna Freedman, James Rondinelli, and Kenneth Poeppelmeier for their helpful suggestions and insights into my projects.

I thank my mentors without whom my PhD and future career path would have been untenable. Words can hardly describe the appreciation and gratitude I feel towards Christos Malliakas for allowing endless questions and sparing no effort in helping me become the solid-state chemist I am today. I also want to thank Fred Northrup for taking me under his wing and providing me the guidance as well as the freedom to explore my identity as an educator. I would also like to thank Haijie Chen for encouraging me and eagerly discussing my science conundrums.

My groupmates have also been invaluable on my journey for both helping me to succeed in my projects and bringing levity to what can be a difficult time. I have been so fortunate to stumble into a group of labmates that so easily create a collaborative and enjoyable work environment. I would like to thank the “downstairs crew” for innumerable brainstorming sessions and needed science breaks. So, in no particular order, I would like to thank Daniel Chica, Mike Quintero, Craig Liang, Abishek Iyer, Ben Oxley, and Eric Quan as well as honorary labmate Allison Wustrow. I would like to thank my other labmates (and friends) for their support, help, and friendship, including Justin Hoffman, Shelby Cuthriell, Shobhana Panuganti, Eugenia Vasileiadou, Xioatong Li, and Songting Cai.

My appreciation also goes to the excellent researchers with whom I have had the fortune to collaborate, in particular the APS staff scientists Saul Lapidus (11-BM-B), Andrey Yakovenko (17-BM-B), and Wenqian Xu (17-BM-B).

As a counter-balance to the weight of graduate school, my friends have brought me so much happiness, elicited so many laughs, and created such beautiful memories. Thank you all for rallying around me. I am so grateful for our unique combination of science and worldly chats, Janet McMillan. Thank you to Michelle Szemanski, Kerri Killeen, and Tonya Lucas for making sure I remember to go out and enjoy our wonderful city (as well as a cocktail or two). Thank you, Sam Harvey, for taking endless laps with me around Tech as we ponder our most recent concerns and celebrate our victories; quite frankly, you're probably the primary reason I could reach 10,000 steps! Thank you, Alex Tamerius, for being such a positive influence and, without fail, making sure we leave our conversations with a smile. Thank you, Elamar Hakim Mouly, for your infectious joy, so much coffee, and being such a brilliant, effervescent person.

There are three friends without whom I would not have made it through graduate school. You three have cheered my successes, cherished me in the depths of grief, and been present in whatever way I need you. Thank you, Monish Shah, for an outside perspective and grounding me repeatedly. Our weekend visits were such a safe haven when I needed to reset. Words can hardly express my love and gratitude for Maureen Murray. We have been there for each other since high school and continue to help each stay accountable as well as mindful of our personal needs. Thank you for sitting with me on the phone for the endless hours of evening glovebox time. Kyle McCall has been a guiding light, role model, and dearest partner. Thank you for reminding me that I am a worthy, brilliant scientist when I doubt myself. Thank you for building me up. Thank you for being

a sounding board. Your patience and kindness are saint-like. I am inspired by your drive and passion.

I would also like to thank my family. We have been through a tumultuous couple of years and each had many crises of our own. Despite that, thank you so much for listening to my science-babble, being excited when I am excited, and also giving me a loving place to turn. I wish Mom and Brandon could celebrate with us as I graduate and take my next step. I know they would be proud.

Acknowledgement of Support

This work was supported by the National Science Foundation through the MRSEC program (NSF-DMR 1720139) at the Materials Research Center. Use was made of the IMSERC Facility at Northwestern University, which has received support from the Soft and Hybrid Nanotechnology Experimental (SHyNE) Resource (NSF ECCS-1542205), the State of Illinois, and International Institute for Nanotechnology (IIN). Use of the Advanced Photon Source (11-BM-B, 11-ID-B, and 17-BM-B beamlines) at Argonne National Laboratory was supported by the U. S. Department of Energy, Office of Science, Office of Basic Energy Sciences, under Contract No. DE-AC02-06CH11357.

\

List of Abbreviations

DFT	Density Functional Theory
DTA	Differential Thermal Analysis
EDS	Energy Dispersive X-ray Spectroscopy
HSAB	Hard-Soft Acid-Base Theory
PDF	Pair Distribution Function
PXRD	Powder X-Ray Diffraction
SEM	Scanning Electron Microscopy
UV-Vis	Ultraviolet-Visible
VBM	Valence Band Maximum
VT	Variable Temperature
XRD	X-Ray Diffraction
o.d.	Outer Diameter
0D	Zero-Dimensional
1D	One-Dimensional
2D	Two-Dimensional
3D	Three-Dimensional

Table of Contents

Abstract.....	3
Acknowledgements	5
Acknowledgement of Support.....	8
List of Abbreviations	9
Table of Contents	10
List of Figures.....	14
List of Tables	21
Chapter 1. Introduction to in situ synthesis	22
1.1. Experimental Approaches.....	25
Chapter 2. Experimental Methods for In Situ Syntheses in Capillaries.....	31
2.1. Preface.....	31
2.2. Determine Radiation, Capillary Diameter, and Dilution (if applicable) to Use	31
2.3. How to Carbon Coat a Capillary.....	35
2.4. How to Sieve and Pack a Capillary.....	37
2.5. How to Evacuate and Seal a Capillary.....	39
2.6. How to Prepare the Capillary for PXRD Measurements.....	40
Chapter 3. Mechanistic Insight of KBiQ₂ (Q = S, Se) using Panoramic Synthesis towards Synthesis-by-Design	42
3.1. Abstract.....	42

	11
3.2. Introduction.....	43
3.3. Experimental details.....	46
Synthesis.....	46
Physical Measurements.....	48
Computational Methods.....	50
3.4. Results and Discussion	51
3.5. Conclusion	72
Chapter 4. In Situ Mechanistic Studies of Two Divergent Synthesis Routes forming the Heteroanionic BiOCuSe	74
4.1. Abstract	74
4.2. Introduction.....	75
4.3. Experimental details.....	78
Synthesis	78
Starting Material Preparation for In Situ Synchrotron Powder Diffraction (PXRD)	78
Physical Measurements.....	79
Computational Methods.....	80
4.4. Results and Discussion	81
4.5. Conclusion	96
Chapter 5. Synthesis, Structure, and Electronic and Physical Properties of the Mixed Anion Semiconductor $\text{In}_8\text{S}_{3-x}\text{Te}_{6+x}(\text{Te}_2)_3$ ($x = 0.18$)	98
5.1. Abstract	98
5.2. Introduction.....	98

	12
5.3. Experimental Methods	101
Synthesis	101
Physical Measurements.....	102
Computational Methods.....	104
5.4. Results and Discussion	104
5.5. Conclusion	109
Chapter 6. Harnessing HSAB Theory to Create Novel Heteroanionic Materials in the Ba-Sn-	
Q (Q = S, Te) Phase Space.....	111
6.1. Abstract	111
6.2. Introduction.....	111
6.3. Experimental Methods	113
Synthesis	113
Physical Measurements.....	114
Computational Methods.....	116
6.4. Results and Discussion	116
6.5. Conclusion	127
Concluding Remarks and Outlook.....	128
Appendix A: Tips and Procedures for PXRD work at the Advanced Photon Source at	
Argonne National Laboratory	131
General APS Tips	131
Tips for 17-BM-B	131
Tips for 11-BM-B	131

	13
Walk through guide to 17-BM-B	132
General need to know	132
Moving the detector	132
Setting up the scan	132
How to make the calibration file.....	135
Types of scans.....	135
A more direct way to move the detector and sample.....	136
Appendix B: Supplementary Information for Chapter 3.	137
Appendix C: Supplementary Information for Chapter 4.	157
Appendix D: Supplementary Information for Chapter 5.	165
Appendix E: Supplementary Information for Chapter 6	171
References	269
Curriculum Vitae	286

List of Figures

- Figure 1: In situ panoramic synthesis: a route to rational synthesis of inorganic extended solids.
 24
- Figure 2: Left: cross-sectional view of the imaging-plate holder and vacuum chamber. The main components of the experimental station are: (1) thermal barrier; (2) hot zone; (3) cold zone; (4) heating element; (5) sample alignment stage; (6) gas-flow system; (7) the detector system which consists of a translating curved holder that supports the imaging plate; (8) thermocouple. Right: cross-sectional view of the open chamber.⁴² 27
- Figure 3: (a) An ‘exploded’ representation of the flow-cell/furnace components, indicating how they fit together; (b) the fully assembled flow-cell/furnace; (c) an expanded view of the sample region, indicating the relative position of the sample and thermocouple tip within the furnace hot zone; (d) a top view of the flow-cell/furnace, with a corresponding cross section through the sample plane showing the gas/fluid path; (e) a photograph of the flow-cell/furnace mounted in a goniometer head. Heat shields have been omitted for clarity.⁴¹
 27
- Figure 4: a) First published in situ capillary setup by Norby et al.⁵³ Capillary mounted on goniometer. A: Capillary, measuring 0.5–1 mm. B: Goniometer head. C: Swagelok T-piece. D: Pressure tube. b) In situ capillary setup by Becker et al.⁵⁴ capable of reaching supercritical conditions for H₂O and other solvents.¹⁰ 28
- Figure 5: Schematic of pressure cell developed for hydrothermal in situ reactions.³⁷ 28
- Figure 6: Screenshots of the user interface for x-ray absorption computations. The boxes indicate the default settings of the interface that it is recommended the user modify for this

calculation.....	32
Figure 7: Graph of the calculated x-ray absorption that has a black vertical line indicating the provided radiation wavelength and two horizontal lines indicating a μ_r value (i.e. x-ray absorption) of 5 (red line) or 1 (blue line).	33
Figure 8: Comparing μ_r values for KBiSe_2 using copper, molybdenum, and silver radiation.	34
Figure 9: Pictorial guide on how to carbon coat a capillary. (1) Gather open-ended quartz capillaries of desired size. (2) Run acetone through capillaries. (3) Carbon coat with gentle flame and using small torch tip or a lighter. (4) Seal tip of capillary using torch. (5) Soak capillary in centrifuge tube with acetone soaked kim-wipe. (6) Carbon coat tip with gentle flame.	36
Figure 10: Pictorial guide on how to prepare your samples. (1) Calculate appropriate ratios (also dilution, if applicable). (2) Sieve material or precursors. [Skip (3) if not running a reaction.] (3) Mix the precursors together thoroughly. [Skip (4-5) if not diluting the material or mixture.] (4) Add appropriate amount of glassy carbon or sieved fused silica. (5) Combine dilutant with sample thoroughly.	37
Figure 11: Three ways to pack your capillary using (1) a 20 mL scintillation vial, (2) tweezers, or (3) 13-15 mm o.d. glass or quartz tube.	38
Figure 12: Picture of the (A) Ultra-Torr adapter from Swagelok for connecting the capillary to a sealing line and (B) the recommended flame intensity and position for sealing the capillary.	40
Figure 13: Image of a sealed capillary placed within an outer, larger capillary and secured with silica wool (left) as well as of a cutting stone (right).	41

- Figure 14: (a) Heat map of $1.5 \text{ K}_2\text{S} + 1 \text{ Bi}_2\text{S}_3$. Asterisks indicate observed peaks from cristobalite formation. (b) Reaction map of $1.5 \text{ K}_2\text{S} + 1 \text{ Bi}_2\text{S}_3$. relative compositions are shown; dashed lines represent an amorphous phase..... 53
- Figure 15: (a) Ball and stick representation of K_3BiS_3 (left) and an illustration of the three different octahedra of KS_6 and all BiS_3 units (right). (b) Isolated representations of the KS_6 distorted octahedra. 54
- Figure 16: Reaction progression of the starting materials, K_2S and Bi_2S_3 , to KBiS_2 through the intermediate phase K_3BiS_3 . Unique cation coordination environment is shown for each structure. A bismuth atom in K_3BiS_3 is shown within the cavity formed by the KS_6 distorted octahedra. 56
- Figure 17: (a) Overlaid diffraction patterns of $1 \text{ K}_2\text{S} + 1 \text{ Bi}_2\text{S}_3$. (b) Reaction map of $1 \text{ K}_2\text{S} + 1 \text{ Bi}_2\text{S}_3$. Nominal compositions are shown; dashed lines represent a noncrystalline phase. (c) Structure solution for $\beta\text{-KBiS}_2$ (d) Structural representation of the ordered rocksalt, $\beta\text{-KBiS}_2$ 57
- Figure 18: (a) Overlaid diffraction pattern for $\text{K}_2\text{Se} + \text{Bi}_2\text{Se}_3$ Panoramic synthesis. Asterisks indicate cristobalite (SiO_2) crystallization (b) Reaction map of $1 \text{ K}_2\text{Se} + 1 \text{ Bi}_2\text{Se}_3$. Nominal compositions are shown; dashed lines represent an amorphous phase. 60
- Figure 19: PDF fits for $\alpha\text{-KBiS}_2$ using a (a) $\text{Fm}\bar{3}\text{m}$ model and (b) $\text{P}2_1\bar{3}$ model. These models are zoomed in to the short range ($r < 8 \text{ \AA}$), highlighted in grey, for the $\text{Fm}\bar{3}\text{m}$ model (c) and for the $\text{P}2_1\bar{3}$ model (d). In the PDF fits, red is the calculated PDF pattern, blue is the experimental data, and green is the difference pattern. PDF fits for $\alpha\text{-KBiSe}_2$ using a (e) $\text{Fm}\bar{3}\text{m}$ model and (f) $\text{P}2_1\bar{3}$ mode; zoomed in region shown for the $\text{Fm}\bar{3}\text{m}$ model (g) and

for the $P2_13$ model (h). (i) Shows a $2 \times 2 \times 2$ unit cell representation of KBiQ_2 and (j) highlights the off-centering of bismuth in the $[\text{BiS}_6]^{3-}$ and $[\text{BiSe}_6]^{3-}$ octahedra. 62

Figure 20: (a) Experimental band gaps for the known $\alpha\text{-KBiQ}_2$ ($\text{Fm}\mathbf{3m}$) and discovered $\beta\text{-KBiQ}_2$ phases ($\text{R}\mathbf{3m}$). (b) Illustration of dimension reduction from the 3D covalent framework in the high temperature (HT) phase, $\alpha\text{-KBiQ}_2$, to the layered 2D covalent framework in the low temperature (LT) phase, $\beta\text{-KBiQ}_2$. For both structures, only covalent bonds (e.g. Bi-Q bonds) are shown. The site occupancy of bismuth and potassium in $\alpha\text{-KBiQ}_2$ was randomized, while constrained to maintain equivalent amounts of the cations. The inset for $\alpha\text{-KBiQ}_2$ tilts the indicated portion of the structure to highlight the 3D connectivity through the plane. (c) Depiction of valence band maxima, conduction band minima, and band gap energies for $\alpha\text{-KBiQ}_2$, $\beta\text{-KBiQ}_2$, $\text{Si}^{138-139}$, CdTe^{140} , MAPbI_3^{141} , and TiO_2 (anatase)¹⁴²⁻¹⁴³. 64

Figure 21: Phase diagram of (a) K-Bi-S and (b) K-Bi-Se phase space. The band structure and partial density of states (PDOS) of (c) $\beta\text{-KBiS}_2$ ($\text{R}\mathbf{3m}$) and (d) $\beta\text{-KBiSe}_2$ ($\text{R}\mathbf{3m}$)..... 66

Figure 22: (a) The DFT-calculated change in band gap as bismuth is increasingly off-centered in the K-Bi-K direction from its ideal position. The bandgaps are calculated with the ordered $\text{R}\mathbf{3m}$ rocksalt structures for $\alpha\text{-KBiS}_2$ and $\alpha\text{-KBiSe}_2$. The unfolded band structure of (b) $\alpha\text{-KBiS}_2$ and (c) $\alpha\text{-KBiSe}_2$, which is unfolded to the Brillouin zone of $\text{R}\mathbf{3m}$ structures. The color bar indicates the band intensity..... 68

Figure 23: Representative illustrations of ABiQ_2 ($A = \text{alkali metal, Q = S, Se, Te}$) structures that crystallize in the (a) rocksalt structure type ($\text{Fm}\mathbf{3m}$) (b) $\alpha\text{-NaFeO}_2$ structure type ($\text{R}\mathbf{3m}$) and (c) CsSbS_2 structure type ($\text{P}2_1/\text{c}$). Monovalent cation shown in blue, trivalent cation in

black, and chalcogenide in yellow. (d) Chart of ABiQ_2 reported in literature and in this paper..... 69

Figure 24: (a) In situ VT-PXRD for the reaction of $\text{Bi}_2\text{O}_2\text{Se} + \text{Cu}_2\text{Se}$. Below is the DTA of the heating portion of the reaction, which is intentionally aligned with the heat map and reaction map to show the corresponding temperatures in the reaction. (b) Reaction map of $\text{Bi}_2\text{O}_2\text{Se} + \text{Cu}_2\text{Se}$, comparing the relative moles of each material over the duration of the reaction. A combination of $\alpha\text{-Cu}_2\text{Se}$ and $\beta\text{-Cu}_2\text{Se}$ are present at the start of the reaction and, as temperature increases the $\alpha\text{-Cu}_2\text{Se}$ fully converts to the high temperature $\beta\text{-Cu}_2\text{Se}$ polymorph. Upon further heating, $\text{Bi}_2\text{O}_2\text{Se}$ and $\beta\text{-Cu}_2\text{Se}$ react to form the target quaternary, BiOCuSe 83

Figure 25: Reaction pathway of $\beta\text{-Cu}_2\text{Se} + \text{Bi}_2\text{O}_2\text{Se}$ into BiOCuSe 84

Figure 26: (a) In situ VT-PXRD for the reaction of $\text{Bi}_2\text{O}_3 + \text{Bi} + 3\text{Cu} + 3\text{Se}$. Below is the DTA of the heating portion of the reaction, which is intentionally aligned with the heat map and reaction map to show the corresponding temperatures in the reaction. The thermal signals have been highlighted in the DTA graph for clarity. (b) Reaction map of $\text{Bi}_2\text{O}_3 + \text{Bi} + 3\text{Cu} + 3\text{Se}$, comparing the moles of each material over the course of the reaction. 86

Figure 27: Schematic pathway of $\text{Cu} + \text{Se} \rightarrow \text{CuSe}$ 87

Figure 28: (a) Reaction pathway of $\text{Bi} + \text{Se} \rightarrow \text{Bi}_3\text{Se}_4$. (b) Gibbs reaction energy of $4\text{Bi}_2\text{Se}_3 + \text{Bi} \rightarrow 3\text{Bi}_3\text{Se}_4$ calculated at increasing temperatures to determine the stability of Bi_3Se_4 . Positive Gibbs reaction energy values indicate the reverse reaction (i.e. the decomposition of Bi_3Se_4) is spontaneous, while negative values indicate the spontaneous formation of Bi_3Se_4 89

- Figure 29: Lattice parameter and volume changes in Bi_3Se_4 as the reaction progresses. By symmetry, the a and b axes are equivalent. 91
- Figure 30: (a) Structure of Bi_2O_3 , represented as ball-and-stick and polyhedra. The ball-and-stick representation is viewed down the b-axis and highlights the alternating sheets of bismuth and oxygen in the material. The polyhedra, viewed down the c-axis, highlights the bismuth lone pair expression into the material's columns running parallel to the c-axis. (b) Coordination spheres for the reaction of Bi_2O_3 , Bi_2Se_3 , Bi_3Se_4 , and Cu_2Se to form BiOCuSe 93
- Figure 31: Summary of product formation temperatures and reaction pathway for $\text{Bi}_2\text{O}_3 + \text{Bi} + 3\text{Cu} + 3\text{Se}$ upon heating from room temperature (RT) to maximum temperature (500°C). 95
- Figure 32: Crystal structure of $\text{In}_8\text{S}_{2.82}\text{Te}_{12.18}$ viewed down the c-axis. Purple spheres are indium, yellow sulfur, and brown tellurium..... 106
- Figure 33: (a) The band structure and partial density of states (PDOS) of $\text{In}_8\text{S}_{2.82}\text{Te}_{12.18}$. (b) Experimental band gap of $\text{In}_8\text{S}_{2.82}\text{Te}_{12.18}$ 108
- Figure 34: The electrical transport properties of $\text{In}_8\text{S}_3\text{Te}_{12}$ including (a) Seebeck coefficient (b) electrical conductivity and (c) power factor calculated at 300K with relaxation time fixed at 10 fs. Blue lines and red lines are holes and electrons, respectively. 109
- Figure 35: Compositional map of A-M-Q, where A is an alkaline earth metal, M is Ge, Sn, or Pb, and Q is S, Se, or Te. The shaded pentagonal arrows are to indicate that these relationships are identical and were not connected for clarity of reading the scheme. 112
- Figure 36: Illustration of (A) the four-coordinate, distorted SnSTe_2Q (Q: S = 0.2, Te = 0.8;

SnS_{1.2}Te_{2.8}) tetrahedra, (B) the eight-coordinate BaS₂Te₄Q₂ (BaS_{2.4}Te_{5.6}) polyhedra for Ba1 and (C) the seven-coordinate BaSTe₄Q₂ (BaS_{1.4}Te_{5.6}) polyhedra for Ba2. 120

Figure 37: (A) Illustration of the more closely packed Ba₂SnS_{1.2}Te_{2.8} by viewing down the [4 0 3] vector, where the distorted SnQ₄ tetrahedra are stacked parallel to the viewing vector. (B) A view of Ba₂SnS_{1.2}Te_{2.8} down the a-axis highlights the polarity of the SnQ₄ units, indicating potential as a non-linear optical material. (C) A view of Ba₂SnSe₄ c-axis to contrast the packing of the Se-analogue and heteranionic analogues. The barium sites are colored light and dark green for clarity for Ba1 and Ba2, respectively. 121

Figure 38: Crystal structure of Ba₃SnS₄Te. SnS₄ tetrahedra shown (A) without differentiating Ba and S sites and (B) with differentiating between Ba1 (light green), Ba2 (dark green), S1 (yellow) and S2 (orange) sites. The polyhedra of (C) SnS₄, (D) BaS₆Te₂ for Ba1 and (E) BaS₆Te₂ for Ba2 are shown, with S1 and S2 sites labeled accordingly. 123

Figure 39: Structure of (A) Ba₃SnS₄Te with the distorted TeBa₆ octahedra indicated, (B) Ba₃SnS₄Te with the distorted TeBa₆ octahedra highlighted and all M-S bonds removed, and (C) the TeBa₆ distorted octahedra with bond lengths shown. 124

Figure 40: Crystal structure of (A) Ba₃GeS₅ with the GeS₄ tetrahedra shown in pink and of (B) Ba₃SnS_{5.62}Te_{0.13} with the SnS₄ tetrahedra shown in purple. (C) The heteronionic unit comprised of S²⁻, Te²⁻, and S₂²⁻ is highlighted (left) and the occupancy distribution (right) is shown. 126

Figure 41: Crystal structure of (A) Ba₇Sn₅S_{14.3}Te_{0.7} and (B) Ba₈Sn₄S_{14.24}Te_{0.76} shown with 2x2x2 unit cells. 127

List of Tables

Table 1: Crystal data and structure refinement for $\text{In}_8\text{S}_{2.82}\text{Te}_{12.18}$ at 100 K.....	105
Table 2: Crystal data and structure refinements for $\text{Ba}_2\text{SnS}_{1.20}\text{Te}_{2.80}$, $\text{Ba}_3\text{SnS}_4\text{Te}$, and $\text{Ba}_3\text{SnS}_{5.62}\text{Te}_{0.13}$	119
Table 3: Bond lengths for Ba-Q in $\text{Ba}_2\text{SnS}_{1.2}\text{Te}_{2.8}$	120

Chapter 1. Introduction to in situ synthesis

The current technological revolution demands new materials with higher efficiencies and new capabilities. To that point, there have been many research thrusts centered on material design correlated with targeted properties,¹⁻⁴ and recently there has been a push to utilize machine learning to design materials *ab initio*.⁵⁻⁷ However, the synthetic insight needed to realize these compounds does not yet exist for most systems. This is due to the historically *ex situ* nature of traditional solid-state synthesis, in which only indirect information about the reaction pathways is obtainable. *In situ* techniques can address this dearth of insight as they are powerful tools for the direct observation of changes in long- or short-range order over the course of a reaction. Depending on the technique(s) employed, information gleaned may include crystallization kinetics and/or processes (e.g. such as those effecting particle size or morphology), nucleation kinetics and/or processes, changes in coordination environments, or observation of transient phases, including competitive product or polymorph formation.⁸⁻¹³ With the ability to uncover transient phases, *in situ* approaches neatly address both the themes of materials discovery and synthetic insight towards the rational design of materials.

Traditionally, syntheses of inorganic materials have been determined through heuristic means, with knowledge of only the inputs (starting materials) and outputs (final products). Using this approach, the observer does not gain intuition for the reaction progression leading to products. The observer is not privy to information on when the product(s) begin to grow or, moreover, if transient phases form that do not remain on completion of the reaction. Previously, product crystal growth was monitored by quenching mid-reaction. These *ex situ* studies can be conducted in laboratory conditions and may also reveal previously unknown transient phases, such as

polymorphs or intermediate phases. However, these studies are performed under the assumption that quenching does not alter the reaction or crystal growth process. In contrast, *in situ* studies enable continuous monitoring of the reactions with minimal or no alteration to reaction conditions.

Using *in situ* powder X-ray diffraction, all crystalline phases, even transient ones, may be observed in snapshots from simultaneously collected diffraction data. This “panoramic” view of phase evolution not only illuminates the reaction progression, but also unveils possible metastable phases. The realization of metastable phases has been sought through methods such as *chimie douce*,¹⁴ “turning down the heat,”¹⁵ flux syntheses,¹⁶⁻²⁰ and metathesis reactions,²¹⁻²² as they widen the accessible compositional space. As more panoramic syntheses are conducted in increasingly broader compositional space, reaction progressions can be systematically cataloged to build understanding of syntheses. Comparisons can be drawn within similar reaction types to determine patterns in ordering principles and those ordering principles will then subsequently be tested, as illustrated in Figure 1. Ultimately, these ordering principles combine to formulate synthetic design principles akin to retrosynthesis used by organic chemists. The experimental synthesis design strategies compliment of this the ongoing *in silico* materials design efforts however a lot of new information will need to be generate and added before theory and experiment can converge to a single coherent synthesis science.²³

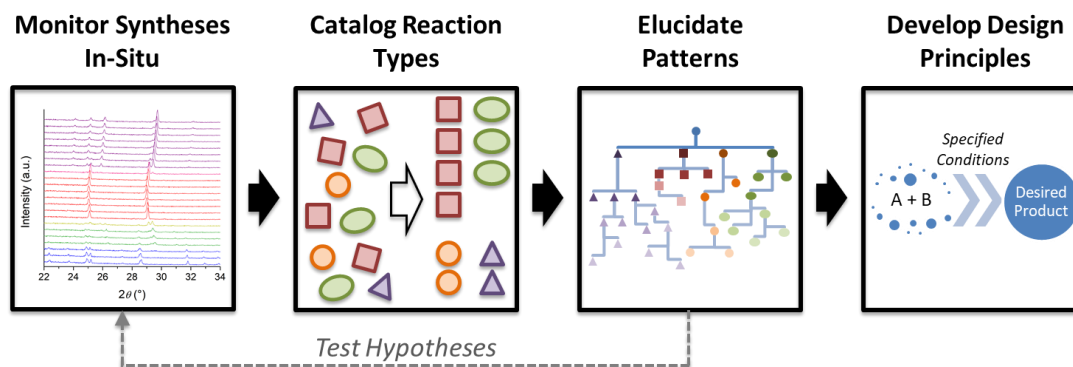


Figure 1: In situ panoramic synthesis: a route to rational synthesis of inorganic extended solids.

This chapter will focus on *in situ* X-ray or neutron diffraction, as other panoramic methods have been summarized elsewhere.^{8, 24-25} Historically, this panoramic technique was primarily used for hydrothermal syntheses of molecular sieves, such as zeolites. Early studies sought to exploit control of product particle size, crystal growth rate, structural transformations, porosity, and/or morphology.²⁶⁻²⁷ Later studies shifted to enlightening the pathways to these materials.^{13, 26, 28} As studies of panoramic syntheses continue to proliferate, systematic alterations to the synthetic conditions should be applied for optimal comparison across similar reaction types. Known syntheses can then be probed by altering parameters to evaluate the phase and energetic landscape. Such parameterization can include the effects of (1) starting materials, whether that be their ratio²⁹ or composition³⁰, (2) heating conditions, or (3) use of non-reactive fluxes³¹.

In the following sections, we explore and summarize the panoramic syntheses that have been reported to date. The experimental and analytical requirements are detailed, followed by a discussion of the *in situ* diffraction studies reported for oxides, chalcogenides, heteroanions as well as intermetallics and pnictogens, which have been grouped according to these chemical classes. These works highlight the utility of panoramic synthesis to derive the chemistry that drives

compound formation in these diverse systems, showcasing this technique as a pathway towards materials by design.

1.1. Experimental Approaches

Pivotal to the success of this technique is the spatial and temporal resolution of the instrument's detector and optics. The spatial resolution of the detector is crucial for distinguishing Bragg peaks, particularly when using high energy X-ray sources. The spatial resolution of the optics is also important: the radiation source should be focused on a small area of the sample, particularly when working with reaction vessels such as capillaries. High temporal resolution data collection is desired to accurately capture phase evolution and glean insight into the kinetics of a reaction. Overall, the data collection rate for two-dimensional detectors, such as image plates, pixel array detectors, and charge-coupled devices (CCDs), are higher than that of strip or point detectors. Near-simultaneous data collection³²⁻³³ is coming to fruition with the continually improved detector technologies.

Panoramic syntheses can be conducted using in-house radiation sources as well as synchrotron or spallation sources.³⁴ In-house *in situ* experiments have been conducted using both angular^{10, 29-30, 35} and energy dispersive^{10, 36-37} X-ray diffractometers coupled with a furnace attachment. Angular dispersive X-ray diffraction (ADXRD) is the most common detection method for in-house X-ray diffractometers. In ADXRD, a monochromatic energy beam irradiates the sample and a diffractogram is measured at multiple scattering angles. Energy dispersive XRD (EDXRD), on the other hand, uses a fixed scattering angle and irradiates the sample using a broad energy range. The fixed scattering angle enables a faster acquisition time relative to ADXRD. When working with highly attenuating samples, such as heavy metals, or when thick sample

vessels must be penetrated such as with hydrothermal reactions, the in-house radiation source needs to be of sufficiently high energy to penetrate the sample. Commonly, molybdenum and silver radiation are used in place of copper radiation. In cases where the samples are too attenuating for these sources, radiation from particle accelerators can be employed. Neutrons, from reactors or spallation sources, are usually intrinsically more penetrating than X-rays, due to their weak interaction with matter, and synchrotrons can provide high fluxes of X-rays at energies greater than those readily available from laboratory tube sources, providing greater penetrating power.³⁴

While powder diffraction data for materials under non-ambient conditions have been recorded since the earliest days of X-ray and neutron diffraction, panoramic synthesis requires more specialized equipment.³⁸⁻³⁹ Depending on the reaction type, a specific, specialized reaction cell is required. To date, hydrothermal, bulk solid-state, gas-flow, flux, and self-propagating high-temperature syntheses have been conducted *in situ*. Capillary reactors have been coupled with X-ray sources for hydrothermal, solid-state, flux, and gas-flow syntheses.⁴⁰⁻⁴¹ The capillary reactors use a furnace, resistive coil heater, or hot air blower. Designs for X-ray furnaces are widely available in the literature (Figure 2);⁴²⁻⁴³ in addition, furnaces are commercially available as attachments for in-house diffractometers. Resistive coil heaters, such as those designed by Chupas and coworkers, can be used with flow cells or furnaces, depending on if the starting materials are placed in the cell's capillary or sealed in an inner capillary (Figure 3 and Figure 4).⁴¹ Other X-ray diffraction panoramic syntheses were conducted, on flat sample holders or on layers mounted on a resistive strip heater, to monitor gas-flow or self-propagating high-temperature syntheses.⁴⁴⁻⁴⁸ Hydrothermal reaction cells have been developed as pressure cells or flow cells, as shown in a representative schematic in Figure 5.^{13, 24, 28, 34, 37, 49-52} **Error! Reference source not found.**

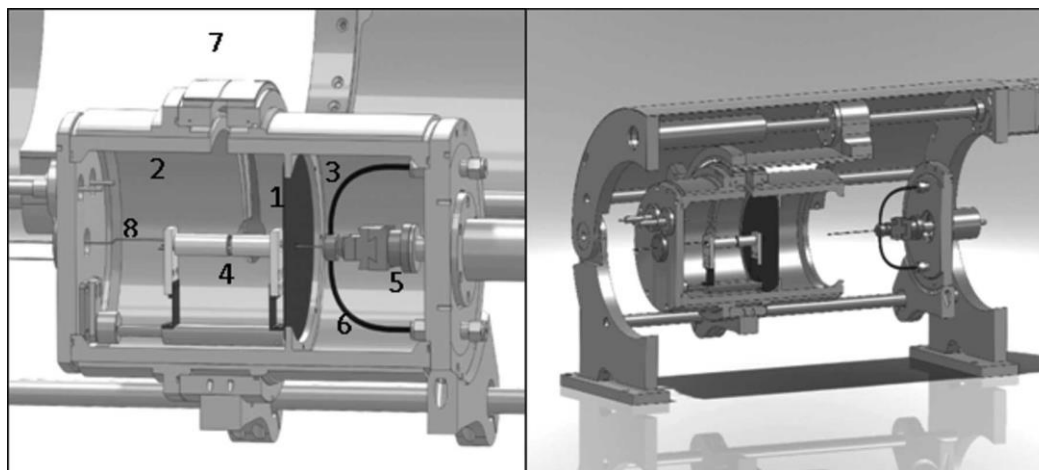


Figure 2: Left: cross-sectional view of the imaging-plate holder and vacuum chamber. The main components of the experimental station are: (1) thermal barrier; (2) hot zone; (3) cold zone; (4) heating element; (5) sample alignment stage; (6) gas-flow system; (7) the detector system which consists of a translating curved holder that supports the imaging plate; (8) thermocouple. Right: cross-sectional view of the open chamber.⁴²

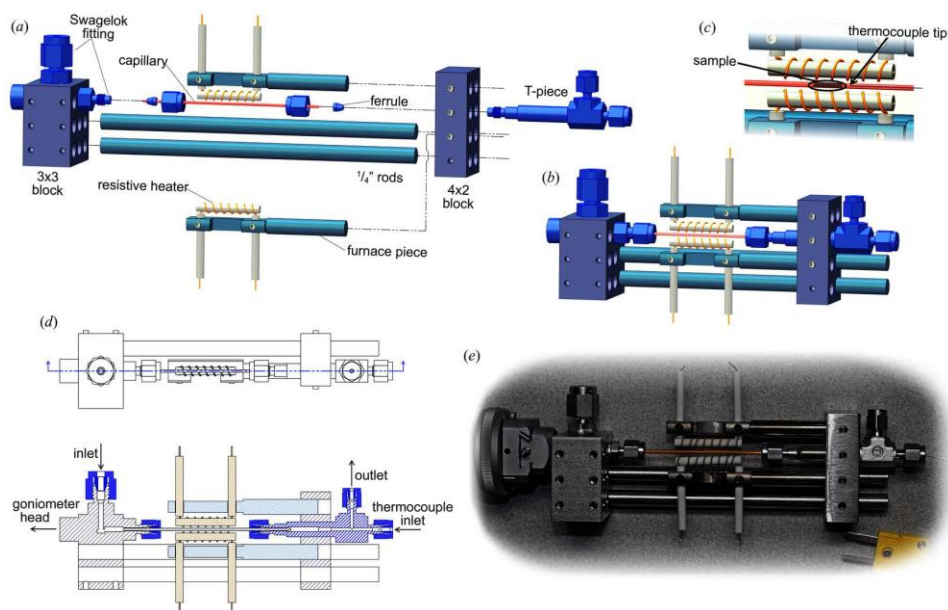


Figure 3: (a) An ‘exploded’ representation of the flow-cell/furnace components, indicating how they fit together; (b) the fully assembled flow-cell/furnace; (c) an expanded view of the sample region, indicating the relative position of the sample and thermocouple tip within the furnace hot zone; (d) a top view of the flow-cell/furnace, with a corresponding cross section through the sample plane showing the gas/fluid path; (e) a photograph of the flow-cell/furnace mounted in a goniometer head. Heat shields have been omitted for clarity.⁴¹

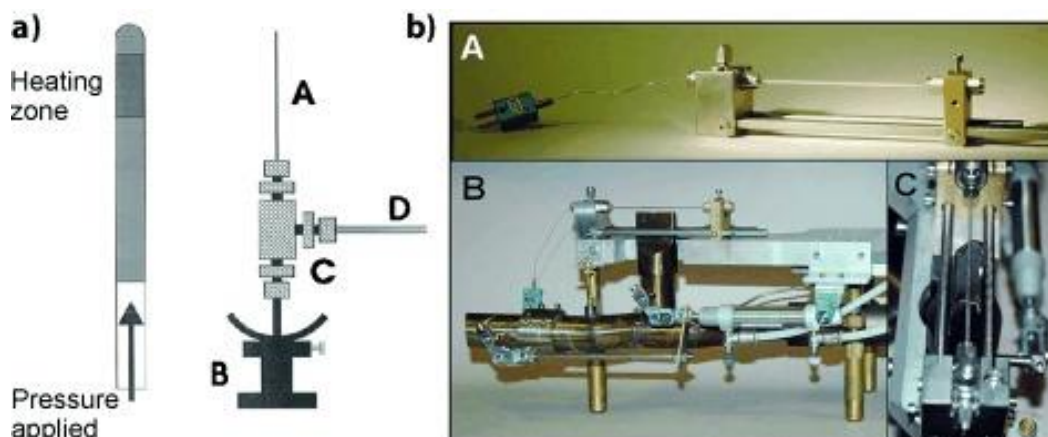


Figure 4: a) First published in situ capillary setup by Norby et al.⁵³ Capillary mounted on goniometer. A: Capillary, measuring 0.5–1 mm. B: Goniometer head. C: Swagelok T-piece. D: Pressure tube. b) In situ capillary setup by Becker et al.⁵⁴ capable of reaching supercritical conditions for H₂O and other solvents.¹⁰

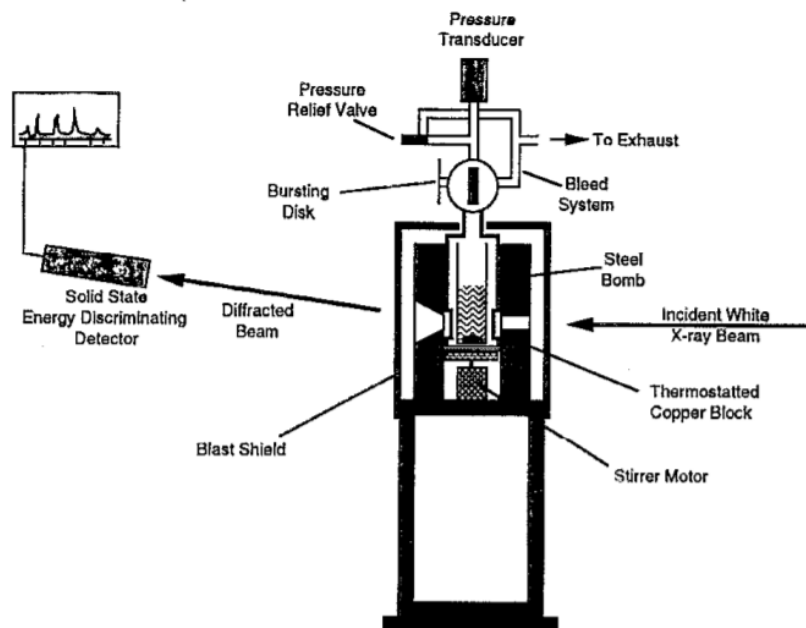


Figure 5: Schematic of pressure cell developed for hydrothermal in situ reactions.³⁷

While *in situ* diffraction techniques detect the phase evolution of crystalline materials,

changes in local order or the growth and identity of amorphous phases are inaccessible with these techniques. Therefore, complementary *in situ* probes are crucial when evaluating local order and the amorphous phases that may also inform the guiding synthetic principles of a reaction.^{10, 23, 34} Spectroscopic techniques, like Raman or infrared spectroscopy, can indicate functional groups or bonding schemes present in a reaction. Simultaneous scattering techniques, such as small-angle X-ray scattering, can distinguish between amorphous and crystalline nanostructure. Absorption techniques, such as X-ray absorption spectroscopy, can determine the local coordination or electronic structure. Simultaneous collection of these complementary *in situ* probes is optimal as it guarantees the reaction conditions are exactly matched.

Beyond these, other experimental approaches deserve mention due to their value when preparing for, or trying to understand, an *in situ* study. They include co-refinements using *in situ* neutron and X-ray diffraction data, where the different dependence of scattering power on atomic number for these two techniques can enable the distribution of elements over the available crystallographic sites to be determined even in complex materials. X-ray scattering techniques, such as Pair Distribution Function, can also be paired with diffraction techniques to elucidate changes in local structure. Thermal analyses such as differential thermal analyses (DTA) and differential scanning calorimetry (DSC) indicate when an exothermic or endothermic event occurs. These events may indicate phase formation, phase transition, or melting/crystallization. DSC also enables the calculation of reaction enthalpies for these events, which provides insight into the driving energetics of the reaction. Knowledge of the temperatures for the events also proves advantageous, as it indicates noteworthy temperature points for further study. This is particularly useful for *in situ* diffraction setups that do not have continuous collection, but stepwise collection.

Conducting successful panoramic syntheses involves surmounting many challenges including sample size effects, adverse reactions (such as reactions with the container and incongruent evaporation), poor signal-to-noise ratio, and sample movement. For X-ray diffraction, very small samples are investigated. Therefore, obtaining data from a representative portion of the reaction mixture may be difficult and the results may be difficult to reproduce. In contrast, neutron diffraction is not similarly limited. This is because neutron sources produce large, relatively weak neutron beams, so the sample volume required for neutron diffraction is inherently large and better reflects the behavior of a bulk reaction mixture. The selection of the sample vessel must also be thoughtfully considered, as reactions between the reaction mixture and vessel are possible. For example, the attack of glass capillaries by alkali binaries⁵⁵ has been observed, and the attack of silica-containing capillaries by some oxides would be expected. Carbon coating the capillary can mitigate these problems. Care must be taken not only when preparing the vessel, but also the reaction mixture. When using fluxes or highly attenuating samples, signal-to-noise ratios may suffer,⁵⁶ and dilution should be considered. Glassy carbon and ground fused silica are amorphous and have been used as diluents. Test runs should be done *ex situ* prior to the *in situ* experiment to ensure that there is no reaction between the reaction materials and the diluent. Finally, when measuring highly mobile samples such as reactions using fluxes or those going to the melt, one must be careful to ensure the reaction mixture does not move outside the beam during data collection.⁵⁷ When possible, the sample vessel should be oriented vertically or the sample should be rastered for full data collection. To jump start future investigators, guidance and tips are detailed in the next chapter.

Chapter 2. Experimental Methods for In Situ Syntheses in Capillaries

2.1. Preface

In order to facilitate future investigators, I detail here the tricks of the trade, so to speak. The following chapter details how to determine sample preparation requirements, carbon coat a capillary, prepare and pack a sample, and seal the capillary. The trickiest part of the process involves torch-handling and thus, where possible, I have created figures that indicate the suggested heat of the flame as well as where to place the capillary. These guidelines are applicable for measurements loading just one phase (e.g. variable temperature powder x-ray diffraction (VT-PXRD)) or a mixture of phases or precursors (e.g. *in situ* PXRD). As detailed in Chapter 1, VT-PXRD provides information on phase changes and thermal expansion or compression, while *in situ* PXRD gives insight to reaction pathways, presence of intermediate or transient phases, and/or reaction or crystallization rates.

2.2. Determine Radiation, Capillary Diameter, and Dilution (if applicable) to Use

Once a reaction or sample is selected, the radiation required should first be determined. In the IMSERC and Cohen facilities at Northwestern University, Cu, Mo, and Ag radiations are possible. The first step is to calculate the attenuation of your sample. As of 2021, the attenuation can be calculated at 11-BM website¹. If the constituents of the synthesis are light elements, they will be lowly attenuating and Cu radiation can be first used. If the constituents are heavier elements, they will be more highly attenuating, and Mo or Ag radiation should be selected. Enter

¹ <https://11bm.xray.aps.anl.gov/absorb/absorb.php>

the wavelength or energy of the chosen radiation in the first box shown in Figure 6, then enter the chemical formula of your sample or reaction mixture (e.g. 1 K₂S : 1 Bi₂Se₃ becomes K₂Bi₂S₄ or KBiS₂). The capillary diameters most often used in this work are 0.3, 0.5, and 0.7 mm from Charles Supper. If the precursor materials are highly attenuating, you should input 0.15 mm radius. (Please note the website asks for the radius, while the commercial capillaries are labeled with the diameters.) If you are unsure, use 0.25 mm as a placeholder. Unless you know the density of your final product and can put in the density, leave the packing fraction as is. Once you hit calculate, a new page will open.

The figure displays two side-by-side screenshots of the 'Compute X-ray Absorption' web utility interface. The left screenshot shows the default settings: Wavelength (Å) set to 0.41, Chemical Formula empty, Sample Radius set to 0.40, and Packed Fraction set to 0.5. The right screenshot shows the same interface with several modifications: the Wavelength (Å) field is empty, the Sample Radius field is empty, and a text box next to it says 'If suspect it is high absorbing, start with 0.3 mm o.d. capillary'. Purple arrows point from the left screenshot to the right one, highlighting the changes in the Wavelength, Chemical Formula, Sample Radius, and Compute buttons.

Figure 6: Screenshots of the user interface for x-ray absorption computations. The boxes indicate the default settings of the interface that it is recommended the user modify for this calculation.

In the new window demonstrated in Figure 7, a graph with the calculated x-ray absorption for your sample appears. In the upper left of the graph, you can find the legend that shows the contribution for each of the elemental constituents as well as the line that shows the total. On the graph, there is also a vertical line indicating the wavelength input as well as two horizontal lines

that highlight when the μR (i.e. x-ray absorption) is 5 or 1. The intersection of the vertical and horizontal lines show you where your μR value lies. If your μR value is much greater than 1, you must decrease the capillary size, consider dilution, and/or change your radiation source. (These are given in an order of increasing difficulty to implement.) If your μR value is much lower than 1, you must either increase the capillary size to increase the volume of material interacting with the beam or change your radiation source. For reference, a μR value of 1 corresponds to ~10% transmission of x-rays, which is the lower bound of transmission for acceptable signal-to-noise (S/N).

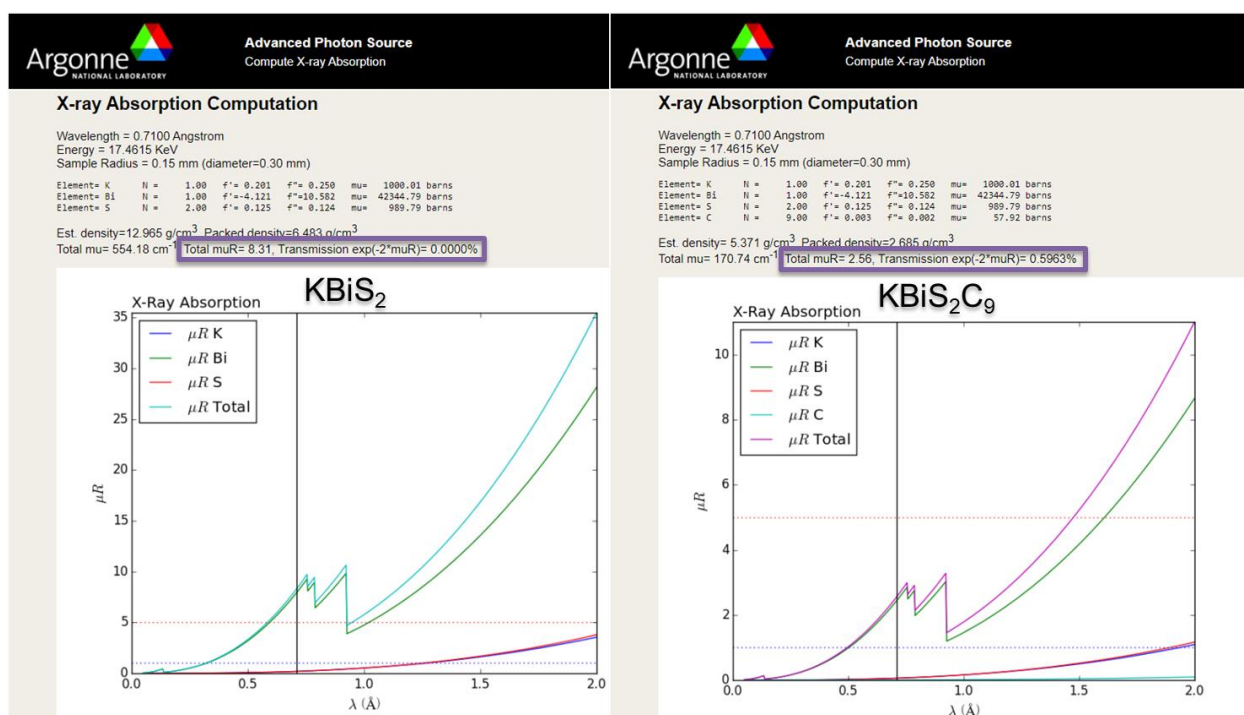


Figure 7: Graph of the calculated x-ray absorption that has a black vertical line indicating the provided radiation wavelength and two horizontal lines indicating a μR value (i.e. x-ray absorption) of 5 (red line) or 1 (blue line).

If you care considering diluting your sample, consider what dilutant makes sense with your material or reaction. Common options are glassy carbon, boron, and fused silica as they are amorphous (i.e. they will minimally impact your diffractograms) and are low Z (i.e. they will likely

have less attenuation than your material). However, these materials are known to react with certain classes of materials. For example, glassy carbon reacts with oxides and elemental transition metals, while boron reacts with oxides. Fused silica has been shown to crystallize during *in situ* reactions.⁵⁸

Once the dilutant is selected, the material can be incorporated into the chemical formula and the μ_r recalculated. For convenience of the future weight percent calculations, I recommend using a convenient ratio (e.g. 1:9 so weight percents can be calculated using 1/10 and 9/10 fractions). For example, to generate calculation in Figure 7 for a dilution of 9 mol C : 1 mol KBiS_2 , “ KBiS_2C_9 ” was entered.

If your μ_r value is greater than 1 and you decide to change your radiation source, please note that a decrease in radiation wavelength may not be suitable depending on your sample. I give the example in Figure 8 of KBiSe_2 where I test the composition at copper, molybdenum, and silver wavelengths. Copper radiation does not penetrate the sample sufficiently; however, when the radiation is exchanged for molybdenum, we do not see the expected penetration gains. This is a result of the proximity of the molybdenum radiation to the band edge of selenium. Be sure to be mindful of this when selecting the x-ray source to use.

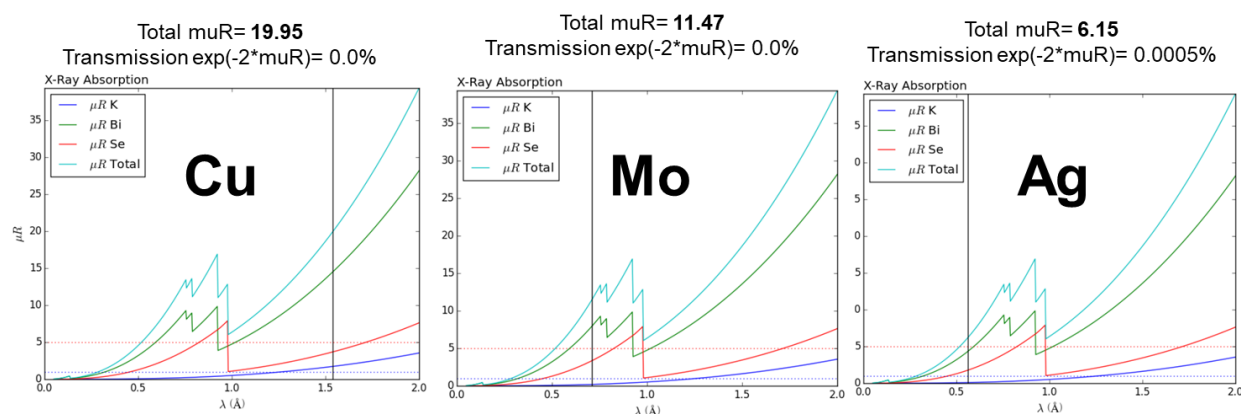


Figure 8: Comparing μ_r values for KBiSe_2 using copper, molybdenum, and silver radiation.

Before moving on to preparing your sample, it is important to determine the composition of the capillary that will be used. The composition is largely dictated by the maximum temperature of the reaction. If the capillary is subjected to temperatures higher than its softening temperature, the structural integrity of the capillary will be compromised. The softening temperatures of special glass, borosilicate, and quartz are 715°C, 820°C, and 1730°C. The price of the capillary from our vendor (Charles Supper) typically increases in correspondence with the increase in softening temperature. If the constituents of the synthesis may react with the capillary, the capillary can be carbon coated as described in the following section.

2.3. How to Carbon Coat a Capillary

Once you have determined the composition and size of your capillary, gather the open ended, funneled capillary, acetone, and gentle wipes, such as Kim-Wipes (Figure 9-1). First you will gently spray acetone into the capillary using its funneled neck (Figure 9-2). Through capillary action, the acetone will travel through the capillary and bead at the bottom. To expedite the process, you may use a Kim-Wipe to gently dab the tip of the capillary to remove the solution. Once complete, you will attach the small torch tip and ignite the methane torch flame or retrieve a lighter. If using the torch, have a moderate flame similar to the one shown in Figure 9-3. You will hold the capillary such that the length of it is perpendicular to the flame, then gently and briefly pass it through the very top of the cone, as shown in Figure 9-3. The capillary should begin to turn a soft grey wherever it has touched the flame. You will only need to carbon coat the bottom two-thirds to three-fourths of the capillary. Pass the capillary through the flame as needed until you start to

see a carbon coat. You may also need to repeat step 2.

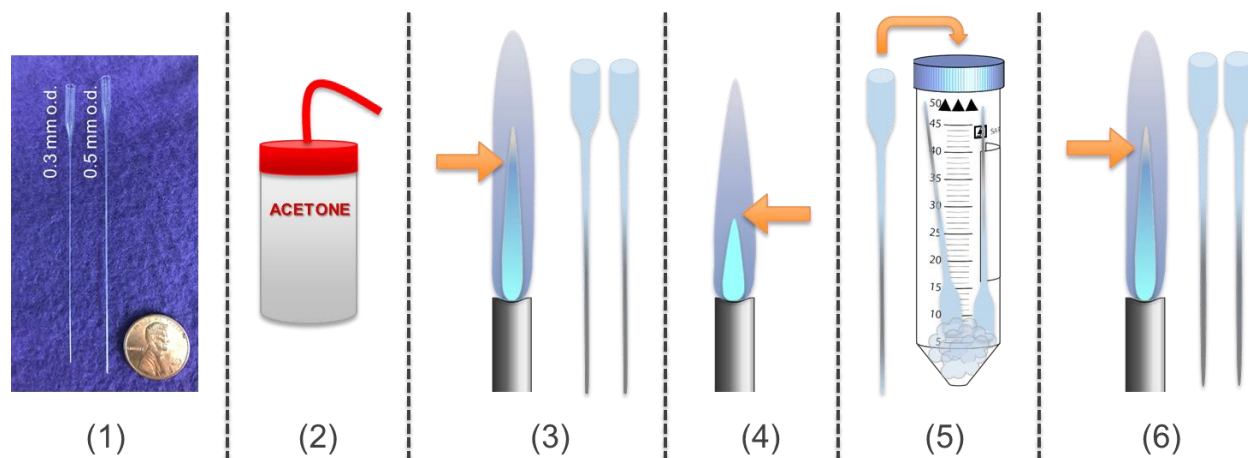


Figure 9: Pictorial guide on how to carbon coat a capillary. (1) Gather open-ended quartz capillaries of desired size. (2) Run acetone through capillaries. (3) Carbon coat with gentle flame and using small torch tip or a lighter. (4) Seal tip of capillary using torch. (5) Soak capillary in centrifuge tube with acetone soaked kim-wipe. (6) Carbon coat tip with gentle flame.

Once the bottom two-thirds to three-fourths of the capillary are carbon coated, you will then seal the tip of the capillary followed by a second carbon coating. First, increase the intensity of the flame (as shown in Figure 9-4) and seal the top of capillary. Be sure to rotate as you do so in order to avoid having the glass asymmetrically seal, such that one side of the tip has more of the glass and then it will not fit into the capillary holder described in Section 2.6. Likely the tip of the capillary no longer has a carbon coat. (If it conserves its carbon coat, move onto the next section.) In order to reapply the carbon coat, the capillary will be placed in acetone atmosphere and reheated. Place acetone-soaked wipes into a centrifuge tube that is longer than the capillary (e.g. a 50 mL centrifuge tube). Then place the capillaries inside with the funnel-end directly above or on the soaked wipes (Figure 9-5). After at least 15 minutes, the tip can again be placed into a gentle flame to carbon coat it. Repeat steps 5-6 as needed to carbon coat the tip.

2.4. How to Sieve and Pack a Capillary

To properly pack the capillary, the material or reaction constituents must be sieved to a size smaller than the diameter of your capillary. (I often use sieves in the 32 – 76 μm range for the 0.3 – 0.7 mm o.d. capillaries.) If you are running a reaction or diluting, I recommend first calculating the appropriate ratios for the precursors and/or dilutant. Once calculated, sieve your materials with the selected sieve (Figure 10-2). If you are running a reaction, mix the precursors thoroughly using a mortar and pestle (Figure 10-3) – even past when they visually appear to be mixed. Next add the appropriate amount of your dilutant to your material or reaction and thoroughly combine the mixture.

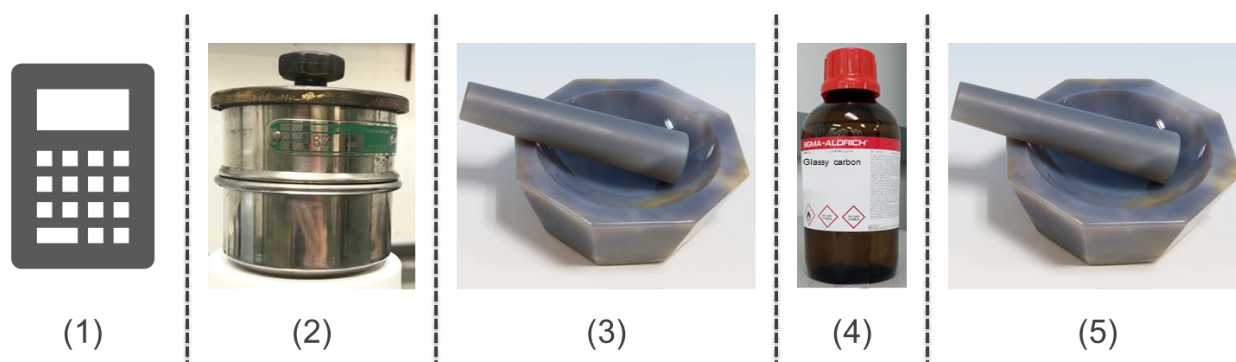


Figure 10: Pictorial guide on how to prepare your samples. (1) Calculate appropriate ratios (also dilution, if applicable). (2) Sieve material or precursors. [Skip (3) if not running a reaction.] (3) Mix the precursors together thoroughly. [Skip (4-5) if not diluting the material or mixture.] (4) Add appropriate amount of glassy carbon or sieved fused silica. (5) Combine dilutant with sample thoroughly.

Once your material is prepared, you can use the funnel of the capillary to transfer the sample to the capillary and take one (or a combination) of the below approaches to pack the capillaries. First option is to place the capillary in a 20 mL scintillation vial (Figure 11-1) and tap the edge of the vial on counter. I recommend you keep your fingers close to either side of the capillary to prevent the capillary from flying out. The second option is to hold the capillary by the

neck and gently slide it across the ridges of a pair of tweezers (Figure 11-2). Likely this will make a “zipper” sound. Be careful not to hold the neck of the capillary too tightly or it will break. The final option is to place an open 13-15 o.d. glass or quartz tube perpendicular to a benchtop, such that its bottom opening is on the bench, and drop the capillary through the tube. The capillary will then bounce with the tube. Each method can be repeated or combined with other methods until the material is fully packed. If the capillary is carbon coated, I found bringing it up to the light will help you to better see where the sample is in the capillary.

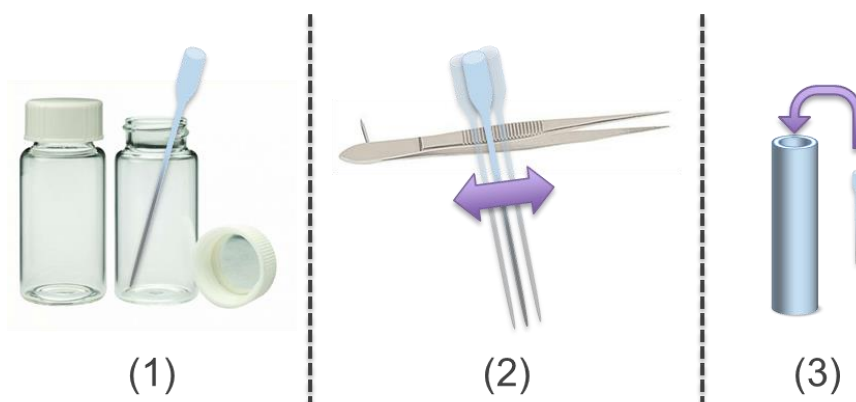


Figure 11: Three ways to pack your capillary using (1) a 20 mL scintillation vial, (2) tweezers, or (3) 13-15 mm o.d. glass or quartz tube.

When working in the glovebox with the capillaries, extra care should be taken. For example, when cycling-in capillaries, you should have them contained within foil or similar material, so they will not get lost and the foil is flexible enough to not break the capillaries. Also, if the glovebox gloves are too large for your hands, be careful with the tips of the fingers. They may get in the way of mixing or packing the materials. You can fold them protruding tips sideways between your fingers, so your two fingers can fix the excess glove away from your capillary or material as its mixed. Finally, when you are covering the capillary after you prepared and packed

it, stretch out the parafilm before wrapping it onto the capillary. If you try to stretch it using the capillary, the capillary neck will likely break off.

2.5. How to Evacuate and Seal a Capillary

When evacuating the capillary in preparation for sealing it, it is vital that you proceed slowly so that you do not have to reprepare or repack your materials. This is particularly crucial if the sample is air or moisture sensitive. Before you attach the capillary to the sealing line, evaluate to where the material fills in the capillary. If the capillary is carbon coated, this can be done by lifting it to the light. Come time, you will seal the capillary just about this line of sample.

Once the level of material fill is noted, carefully remove the parafilm, if applicable, and attach the capillary to an Ultra-Torr adaptor as shown in Figure 12a. The most ideal situation would be to have a glass adapter with a stopcock so that the evacuating pressure can be fine-tuned. However, in the absence of such an adapter, very slowly evacuate the capillary using the main stopcock on the sealing line. Evacuation should be done extremely slowly and methodically to start. When you first open the line to the capillary, stop when the pressure is in the high $\times 10^{-3}$ or low $\times 10^{-2}$ mbar. If you evacuate too quickly, your material will separate (i.e. unpack) and you will need to repack your sample. Continue to slowly evacuate, and only allow the pressure values to increase by $5\text{--}10 \times 10^{-2}$ mbar; any faster and the material will likely unpack. As of 2021, you can

fully open the stopcock when the vacuum settles at $2-5 \times 10^{-3}$ mbar.

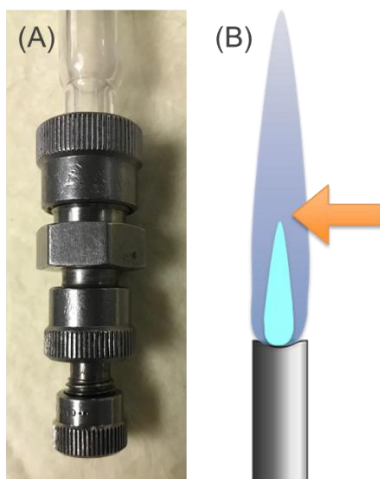


Figure 12: Picture of the (A) Ultra-Torr adapter from Swagelok for connecting the capillary to a sealing line and (B) the recommended flame intensity and position for sealing the capillary.

When preparing to seal the capillary, use the small torch tip and adjust the flame such that it is similar to the flame illustrated in Figure 12b. Sealing will be easier with a strong flame, as the flame will be steady and the cone is smaller. Take a deep, steadying breath – your hands need to be as steady as possible. Then hover the flame just to the side and just above the sample height. When you are ready, move the flame onto the capillary. Once the capillary irradiates, begin to pull down on the capillary. If you are using a 0.5 or 0.7 o.d. quartz capillary, slightly twist as you pull down do avoid creating a hook at the end of the sealed portion of the capillary.

2.6. How to Prepare the Capillary for PXRD Measurements

Once finished at the sealing line, confirm your capillary is sealed and does not have a hooked end using a microscope. If a hook is present, remove only as much as necessary using a capillary cutting stone (Figure 13, top right). Too much and you may break your capillary and need to start over. Depending on the instrumentation set up, you may need to place your capillary inside

an outer capillary (e.g. at IMSERC or Cohen facilities at Northwestern University) or tube (e.g. gas-flow set-up at 17-BM-B at the Advanced Photon Source at Argonne National Laboratories). If applicable, place or test that your capillary fits in the appropriately sized outer vessel (Figure 13, left). If using the in-house facilities at Northwestern, use a 0.7 mm o.d. capillary for 0.3 and 0.5 mm o.d sealed capillaries. If using the in-house facilities, be sure to secure your sample inside the larger capillary using silica wool as pictured in Figure 13. An unused 0.5 mm capillary can facilitate moving the wool into the capillary. If using the facilities at the Advanced Photon Source, please see Appendix A for suggestions and guidelines.

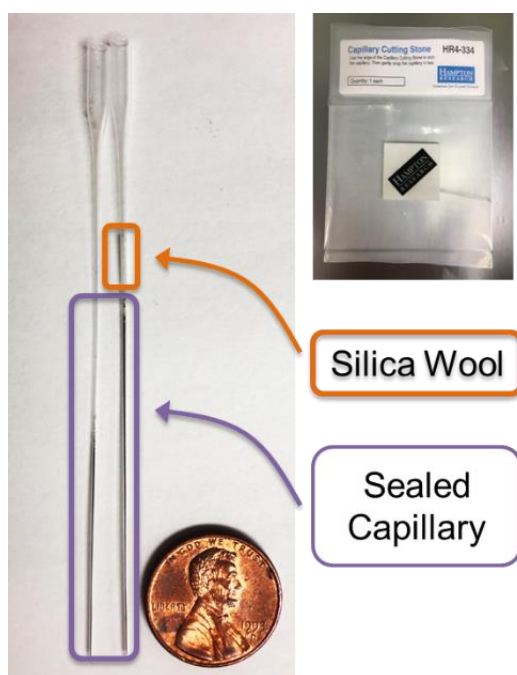


Figure 13: Image of a sealed capillary placed within an outer, larger capillary and secured with silica wool (left) as well as of a cutting stone (right).

Chapter 3. Mechanistic Insight of KBiQ₂ (Q = S, Se) using Panoramic

Synthesis towards Synthesis-by-Design

Reprinted with permission from ‘Rebecca McClain, Christos D. Malliakas, Jiahong Shen, Jiangang He, Chris Wolverton, Gabriela B. González, and Mercouri G. ‘Mechanistic insight of KBiQ₂ (Q= S, Se) using panoramic synthesis towards synthesis-by-design.’ *Chemical Science*, **2021**, 12, 4, 1378-1391.’

Copyright © 2021, The Royal Society of Chemistry

3.1. Abstract

Solid-state synthesis has historically focused on reactants and end products; however, knowledge of reaction pathways, intermediate phases and their formation may provide mechanistic insight of solid-state reactions. With an increased understanding of reaction progressions, design principles can be deduced, affording more predictive power in materials synthesis. In pursuit of this goal, *in-situ* powder X-ray diffraction is employed to observe crystalline phase evolution over the course of the reaction, thereby constructing a “panoramic” view of the reaction from beginning to end. We conducted *in situ* diffraction studies in the K-Bi-Q (Q = S, Se) system to understand the formation of phases occurring in this system in the course of their reactions. Powder mixtures of K₂Q to Bi₂Q₃ in 1:1 and 1.5:1 ratios were heated to 800°C or 650°C, while simultaneously collecting diffraction data. Three new phases, K₃BiS₃, β-KBiS₂, and β-KBiSe₂, were discovered. Panoramic synthesis showed that K₃BiQ₃ serves an important mechanistic role as a structural intermediate in both chalcogen systems (Q = S, Se) in the path to form the KBiQ₂ structure. Thermal analysis and calculations at the Density Functional level (DFT) show that the cation-ordered β-KBiQ₂ polymorphs are the thermodynamically stable phase in this compositional space, while Pair Distribution Function (PDF) analysis shows that all α-KBiQ₂ and β-KBiQ₂ structures

have local disorder due to stereochemically active lone pair expression of the bismuth atoms. The formation of the β -KBiQ₂ structures, both of which crystallize in the α -NaFeO₂ structure type, show a boundary where the structure can be disordered or ordered with regards to the alkali metal and bismuth. A cation radius tolerance for six-coordinate cation site sharing of $\left(\frac{r^+}{r^{3+}}\right) \sim 1.3$ is proposed. The mechanistic insight the panoramic synthesis technique provides in the K-Bi-Q system is progress towards the overarching goal of synthesis-by-design.

3.2. Introduction

The discovery of new materials has led to revolutions in many scientific and technological fields, such as magnetism⁵⁹, radiation detection⁶⁰, optics⁶¹⁻⁶⁴, superconductivity⁶⁵⁻⁶⁶, lithium-ion batteries⁶⁷⁻⁶⁸, thermoelectrics⁶⁹, and phase-change memory⁷⁰. Traditionally, materials discovery of inorganic structures involves exploratory synthesis to identify compounds using heuristically determined reaction conditions, where the compounds are isolated and identified upon completion of the reaction. Within this paradigm, it is unclear whether the desired products form upon heating, cooling, or while dwelling at maximum temperature, or if metastable, short-lived products appear and re-dissolve during the reaction. *In-situ* diffraction techniques are a powerful tool that enable the observation of transient phases during the reaction in efforts towards materials discovery. Moreover, observing these transient phases leads to mechanistic understanding of the reaction; thereby advancing efforts to more rationally design or discover solid-state materials.^{8, 71-73} In particular, rational design is crucial to the pursuit of structural complexity for many fields, such as in thermoelectrics to achieve materials with lower thermal conductivity⁷⁴ and in nonlinear optics for large second harmonic generation.⁶³ To fully realize the potential for rational synthetic design,

a comprehensive long-term approach to analyze solid-state reactions at all stages of the reaction is required.

A powerful tool that provides full awareness of phase identity and phase evolution during a reaction is *in-situ* powder X-ray diffraction. This technique enables the direct observation of all crystalline phases, including intermediate ones, during a solid-state synthesis.^{32, 75} This “panoramic” view of the phase space explored during the reaction enables an understanding of the reaction pathway required to form the final products. To this end, *in-situ* powder X-ray diffraction promotes the discovery of new materials and increased mechanistic understanding of solid-state chemistry.

However, simply conducting *in-situ* powder X-ray diffraction on systems in isolation is not sufficient to achieve the generalized understanding of solid-state reaction dynamics necessary to maximize the potential for discovery. Comprehensive studies of multiple closely related compositions and systems are needed to paint a full picture of reactions that can then be extended to new systems. Therefore, the aggregation of mechanistic data describing material formation and progression of intermediate phases is the first step to determining reaction pathways for rational synthesis.^{8, 18, 22, 71, 76-78} This technique must therefore be applied to a broad, diverse set of systems and phases spaces. Once these reaction pathways of these systems are cataloged and codified, they can be data mined for design principles among similar reaction types.⁷¹ With reaction types and assembly rules, predictive power of material synthesis can be achieved, leading to intentional synthesis of targeted materials with chosen, desired properties.³⁴

In-situ powder X-ray diffraction has been utilized for various interests such as materials discovery^{32, 35, 75} and mechanism elucidation^{30, 34, 45, 57, 79-82}, as well as the investigation of

metathesis reactions^{79, 83}, self-propagating high temperature syntheses^{8, 34, 80}, phase change^{8, 84}, decomposition⁸⁵, and crystallization^{8, 34, 80}. This approach has shown success in discovering new materials, even in systems that were previously investigated.^{32, 75} Furthermore, it has been shown that, by mechanistic insight from *in-situ* studies, the reaction pathway can be influenced.³⁰ Studies focused on building a database of reaction formation and mechanistic understanding for a specific reaction type can be combined in aggregate towards the goal of rational synthesis.

A promising phase space to study is in the A-Pn-Q systems, where A is an alkali metal, Pn is a pnictogen such as bismuth or antimony, and Q is a chalcogenide,⁸⁶⁻⁸⁷ as many are reported structures and have been of interest for their thermoelectric⁸⁸⁻⁹⁴ and optical^{63, 84, 95-96} properties. Moreover, a number of the known compounds are isostructural disordered analogues, such as KBiS₂, NaBiS₂, NaBiSe₂, KBiSe₂, and NaSbS₂, while ordered phases contain similar structural motifs.⁹⁷⁻⁹⁹ Investigation of this family of structures expands the library of known materials, reaction pathways, and understanding of structure-property relationships. Reaction pathways can then be compared within this phase space to understand their design principles. The combination of experimental observation and computational data-mining can accelerate materials discovery and expedite the development of the mechanistic understanding required to achieve rational synthesis of materials.^{78, 100}

Herein, we have applied this *in-situ* diffraction technique using both in-house and synchrotron to the K-Bi-S and K-Bi-Se system, by monitoring the reaction between the respective binaries, K₂Q and Bi₂Q₃ (Q = S, Se). Powder mixtures were heated to 800°C or 650°C, while diffraction data was simultaneously collected. From this investigation, we found that the two systems share an isostructural intermediate phase, K₃BiQ₃. The presence of this intermediate phase

in both reactions suggests K_3BiQ_3 is mechanistically important for KBiQ_2 formation from the binary starting materials. Two additional compounds were discovered: $\beta\text{-KBiS}_2$ and $\beta\text{-KBiSe}_2$. These compounds crystallize in the $\alpha\text{-NaFeO}_2$ structure type and are cation-ordered polymorphs of the known rocksalt ternaries. The ability of KBiQ_2 to form both a disordered and ordered phase, while NaBiQ_2 and RbBiQ_2 crystallize in the rocksalt and $\alpha\text{-NaFeO}_2$ type structures, respectively, suggests that there is a cation radius tolerance $\left(\frac{r^+}{r^{3+}}\right)$ of 1.33 or greater for high symmetry rocksalt formation. This work is one of the pioneer studies in proposing a tolerance factor for a chalcogenide system.¹⁰¹⁻¹⁰³ We have also performed density functional theory (DFT) calculations to show that the cation-ordered $\beta\text{-KBiQ}_2$ polymorphs are thermodynamically stable and demonstrated that DFT can be used as a complimentary tool in the panoramic studies to determine the phase stabilities.

3.3. Experimental details

Reagents. Chemicals in this work were used as-obtained: bismuth metal (99.99%, American Elements), sulfur, (sublimed, 99.99%, Spectrum), selenium pellets (99.99%, American Elements), potassium metal (99.5%, Aldrich), glassy carbon (99.9%, Aldrich). K_2S and K_2Se were synthesized using stoichiometric amounts of the elements in liquid ammonia as described elsewhere.⁹⁶

Synthesis.

Bismuth Sulfide, Bi_2S_3 . A 1.1226-g amount (0.035 mol) of elemental sulfur was combined with 4.8774 g (0.023 mol) of bismuth shots in a 9 mm (O.D.) fused silica tube. The tube was flame sealed under vacuum (10^{-3} mbar). The sample was heated to 500°C in 24 hours and soaked for 24

hours before furnace cooling.

Bismuth Selenide, Bi₂Se₃. A 2.7104-g amount (0.028 mol) of elemental selenium was combined with 3.8296 g (0.018 mol) of bismuth shots in a 9 mm (O.D.) fused silica tube. The tube was flame sealed under vacuum (10^{-3} mbar). The sample was heated to 850°C in 8.5 hours and soaked for 12 hours, then cooled to 450°C in 8 hrs. The sample was annealed at this temperature for 48 hours to minimize selenium vacancies. The sample was then furnace cooled. Sample was ball milled in a Retsch Mixer Mill MM 200 at 20 rps with 20 balls for an accumulative 2.5 hours.

β -KBiS₂. K₂S (0.071 g, 0.64 mmol) and Bi₂S₃ (0.329 g, 0.64 mmol) were mixed in a mortar and pestle and transferred in a N₂ glovebox to a carbon coated 9 mm (O.D.) fused silica tube, which was flame sealed under vacuum (10^{-3} mbar). The sample was heated to 875°C in 12 hrs and soaked for 3 hrs, then cooled to 775°C in 16 hours before furnace cooling. Powder X-ray diffraction (PXRD) shows that the sample is bulk phase pure.

K₃BiS₃. K₂S (0.157 g, 1.4 mmol) and Bi₂S₃ (0.243 g, 0.47 mmol) were mixed in a mortar and pestle in a N₂ glovebox. The mixture was transferred to a carbon coated 9 mm (O.D.) fused silica tube and flame sealed under vacuum (10^{-3} mbar). The sample was heated to 450°C in 6 hrs and soaked for 192 hrs before furnace cooling. The sample was rehomogenized using a mortar and pestle in an N₂ glovebox, then subsequently annealed at 450°C for 48 hours; Rietveld refinement of the sample reveals a 7.7(2) wt% impurity of α -KBiS₂.

β -KBiSe₂. K₂Se (0.077 g, 0.49 mmol) and Bi₂Se₃ (0.0323 g, 0.49 mmol) were added to a carbon coated 9 mm fused silica tube, which was flame sealed under vacuum (10^{-3} mbar). The sample was heated to 800°C in 9 hrs and soaked for 30 minutes before cooling to 575°C in 72 hrs. The sample was then cooled to 475°C in 96 hrs before furnace cooling. Phase purity confirmed

using PXRD.

Physical Measurements.

In-Situ Powder X-ray Diffraction. A STOE STADI MP high-resolution diffractometer with an oven attachment (STOE HT) were used to collect temperature-dependent data. The diffractometer was equipped with an asymmetric curved Germanium monochromator and one-dimensional silicon strip detector (MYTHEN2 1K from DECTRIS). The starting materials were sieved (<45 μm), mixed, and diluted using glassy carbon. Dilutions were required to mitigate sample attenuation of the X-ray beam and, therefore, optimize the signal-to-noise ratio of the diffraction measurement. Samples were then packed into 0.3 mm diameter quartz capillaries, which were flame sealed under vacuum (ca. 3.0×10^{-3} mbar). All capillaries were carbon coated to prevent glass attack. Ground fused silica was used as a spacer at the tip of the capillary, where the capillary was re-sealed and bare of carbon coating. Diffraction data was collected every 15°C using pure-CuK α 1 radiation (1.54056 Å) operated at 40 kV and 40 mA for the sulfide system and pure-MoK α 1 radiation (0.70930 Å) operated at 50 kV and 40 mA for the selenide system. Samples were heated to 800°C or 650°C with a heating rate of 4°C/min and a dwell time at max temperature of 90 minutes. Temperature stability is typically 0.1°C. Samples were spun during collection. The instrument was calibrated against a NIST Silicon standard (640d) prior the measurement.

Ex-Situ Powder X-ray Diffraction. X-ray powder diffraction patterns were collected on a Rigaku Miniflex600 diffractometer with Cu K α radiation (1.5406 Å) operating at 40 kV and 15 mA with a high-speed silicon strip detector. A zero-background silicon sample holder with 0.2 mm x 4 mm well was used. Visualization of the crystal structures was done with Vesta software.¹⁰⁴

PXRD data used for K₃BiS₃ Rietveld refinement was collected at room temperature on a

STOE-STADI-P powder diffractometer equipped with an asymmetric curved Germanium monochromator (pure-CuK α 1 radiation, $\lambda = 1.54056 \text{ \AA}$) and one-dimensional silicon strip detector (MYTHEN2 1K from DECTRIS). The line focused Cu X-ray tube was operated at 40 kV and 40 mA. Powder was packed in a 3 mm metallic mask and sandwiched between two polyimide layers of tape. Intensity data from 3 to 124 degrees two theta were collected over a period of 45 mins. Instrument was calibrated against a NIST Silicon standard (640d) prior to the measurement.

High resolution synchrotron powder diffraction data were collected using beamline 11-BM at the Advanced Photon Source (APS), Argonne National Laboratory using an average wavelength of 0.4577 \AA . Discrete detectors covering an angular range from 2 to 24 $^\circ 2\theta$ are scanned over a 6 $^\circ 2\theta$ range, with data points collected every 0.001 $^\circ 2\theta$ and scan speed of 0.01 $^\circ/\text{s}$.

Pair Distribution Function Measurements and Analysis. Kapton capillaries (0.8 mm diameter) were filled with sieved powder samples (<45 μm) inside a glovebox. X-ray scattering data for alpha- and beta-KBiS₂ and alpha-KBiSe₂ samples were collected at Sector 11-ID-B of the Advanced Photon Source at Argonne National Laboratory using an incident wavelength of 0.143 \AA , up to a Q_{max} of 36.4 \AA^{-1} . The sample-to-detector distance was approximately 175 mm. The sample-to-detector distance was approximately 250 mm resulting in a Q_{max} of 29.1 \AA^{-1} .

GSAS-II was used to calibrate the sample-to-detector distance, detector alignment, and instrumental resolution parameters using a NIST CeO₂ standard and to integrate the data.¹⁰⁵ The empty Kapton capillary signal was subtracted from each scattering data pattern using PDFgetX3¹⁰⁶ prior to obtaining the Pair Distribution Functions (PDFs). PDFgui¹⁰⁷ was used to fit PDFs in the range 2 $\text{\AA} < r < 30 \text{ \AA}$. Subgroups were generated using the Bilbao Crystallographic Server;¹⁰⁸⁻¹¹⁰ space groups investigated included $R\bar{3}m$, $Pm\bar{3}m$, $C2/m$, $P\bar{3}m1$, $I4/mmm$, $Pn\bar{3}m$, $P3_22_1$.

Optical Measurements. Optical diffuse reflectance measurements were made at room temperature with a Shimadzu UV-3600 PC double-beam, double-monochromator spectrophotometer. The measurement of diffuse reflectivity can be used to obtain values for the band gap from a powder sample at room temperature. BaSO₄ powder was used as a reference. The reflectance data was converted to absorbance using the Kubelka-Munk equation: $\alpha/S = (1 - R)^2/2R$. R is the reflectance at a given wavelength, α is the absorption coefficient, and S is the scattering coefficient. Valence band maximum energy (VBM) was measured by photoemission spectroscopy in air on a Riken-Keiki PESA AC-2. Samples are scanned under ambient conditions using UV light (4.20-6.20 eV). The number of photoelectrons generated at each excitation energy is measured and the VBM is the onset of the PESA spectra, as photoelectrons are only generated when the photon energy is higher than the VBM energy. Conduction band minimum energies are found by subtracting the optical band gap from the VBM energy.

Differential Thermal Analysis. Differential thermal analysis (DTA) was performed using a Netzsch STA 449 F3 Jupiter simultaneous thermal analysis (STA) instrument. Samples were loaded into carbon-coated fused silica tube and flame-sealed under vacuum (ca. 3×10^{-3} mbar). Samples were heated to 900°C, cooled to 200°C, then heated once more to 900°C, before cooling to room temperature. The rate for cooling and heating was set to 7.5°C/ min.

Computational Methods.

All density functional theory (DFT) calculations are performed using the projector augmented wave (PAW) method,¹¹¹⁻¹¹² as implemented in the Vienna *Ab initio* Simulation Package (VASP)¹¹³⁻¹¹⁴. The Perdew–Burke–Ernzerhof (PBE) exchange-correlation functional¹¹⁵ and a plane wave basis set with a cutoff energy of 520 eV were used. A Γ -centered k-mesh with ≈ 8000

k-points per reciprocal atom (KPPRA) was used to sample the Brillouin zone. The Open Quantum Material Database (OQMD)^{100, 116} was used for convex hull construction. To calculate the formation energy of the cation-disordered KBiQ_2 $Fm\bar{3}m$ structures, a 32-atom special quasi-random structure (SQS)¹¹⁷ was generated by using the Monte Carlo algorithm (mcsqs) as implemented in the Alloy Theoretic Automated Toolkit (ATAT).^{118,119} The cluster correlations used to define the SQS were specified using a distance-based cutoff of all 2-, 3-, and 4-body clusters with a maximum distance of 5-6 Å. To calculate the effective band structure of the K/Bi disordered cubic phase ($Fm\bar{3}m$), a $2 \times 2 \times 2$ supercell was generated based on the perfect rocksalt structure with bismuth and potassium alternatively stacking along [111] direction. The potassium and bismuth atoms are randomly distributed in the supercells to simulate the cation-disordered KBiQ_2 $Fm\bar{3}m$ structures. Effective band structures were recovered from the supercell calculations using the band unfolding technique proposed by Medeiros et al.¹²⁰⁻¹²¹

3.4. Results and Discussion

Panoramic Synthesis KBiS_2 . The synthesis of KBiS_2 has been previously reported using potassium carbonate, elemental bismuth, and elemental sulfur.^{97, 122} KBiS_2 crystallizes in the simple rocksalt structure,^{97, 122} where potassium and bismuth have equivalent occupancy in the sodium site and sulfur is in the chloride site. Moreover, the K-Bi-S phase space is of interest for thermoelectric materials¹²³ and photovoltaics,¹²⁴ in efforts towards rational design within this phase space, we began with this simple structure.

To monitor the reaction progression in the K-Bi-S system, panoramic syntheses were conducted using a commercial STOE high-temperature furnace (HT) attachment for a STOE STADI-MP powder X-ray diffractometer. In previously reported syntheses, an excess of potassium

starting material was used to form KBiS_2 , therefore a ratio of 1.5 K_2S : 1 Bi_2S_3 is used.¹²² The reaction has a maximum temperature of 800°C . The overlaid diffraction patterns from the panoramic synthesis are shown in Figure 14a. Phases are identified primarily through pattern matching. Different colors are used to highlight different phases that form during the reaction, beginning with the starting materials in blue. A schematic of the reaction pathway with relative mole fractions of the phases is shown in Figure 14b. The relative mole fraction of the starting material amorphous K_2S was determined according to the experimental loading of the material. It is useful to regard the reaction between K_2S and Bi_2S_3 as a Lewis acid-base reaction in which K_2S is the base and Bi_2S_3 is the acid. In this context, basic activity increases with the K_2S fraction and acidic activity increases with the Bi_2S_3 . The end crystalline products shown in brown are KBiS_2 and cristobalite, a high temperature polymorph of SiO_2 . The ground amorphous silica, which was used as a spacer to protect the glass tip of the capillary, crystallized after reaching temperatures above 700°C . To avoid this, all subsequent panoramic syntheses in this system have a maximum temperature of 650°C . An intermediate phase is observed during the reaction, appearing at 270°C and disappearing at 510°C as the product, KBiS_2 , emerges (in red). The intermediate phase was isolated *ex-situ* as described in the Experimental section and determined to be K_3BiS_3 via Rietveld refinement (Figure S1, Table S1-4).

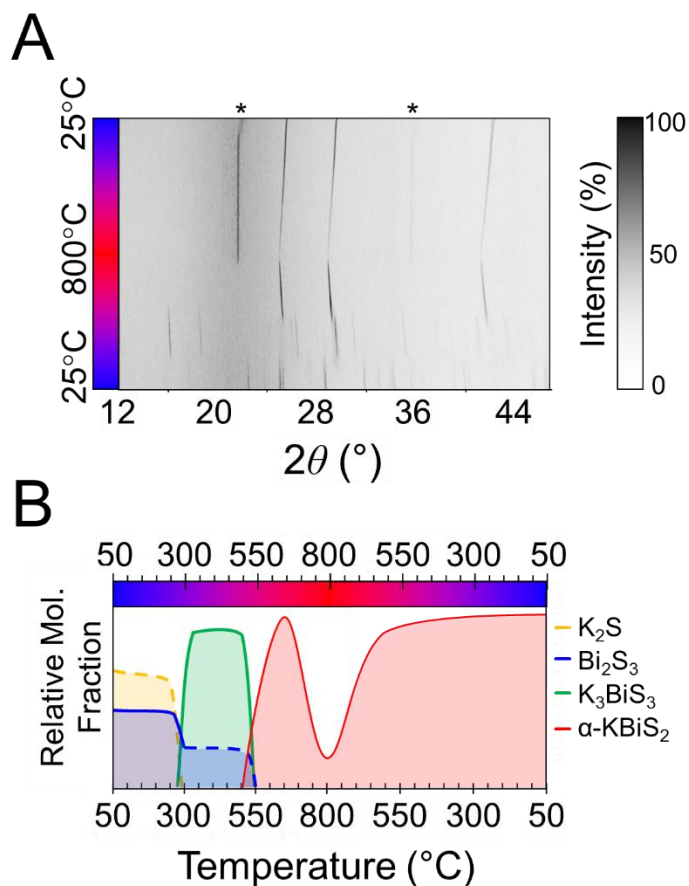


Figure 14: (a) Heat map of $1.5 K_2S + 1 Bi_2S_3$. Asterisks indicate observed peaks from cristobalite formation. (b) Reaction map of $1.5 K_2S + 1 Bi_2S_3$. relative compositions are shown; dashed lines represent an amorphous phase.

The intermediate phase, K_3BiS_3 , shown in Figure 15, crystallizes in the cubic Na_3AsS_3 structure type (space group $P2_13$; $a = b = c = 9.4425(1) \text{ \AA}$) and is isostructural to K_3SbS_3 and Na_3SbS_3 .¹²⁵ The formation of an intermediate phase of this composition is surprising because it implies a reaction of K_2S and Bi_2S_3 in a 3:1 ratio, which is a more basic condition than what is being used in this reaction, where the ratio is 3:2. This suggests that K_3BiS_3 is a kinetic product.

K_3BiS_3 has two structural motifs: trigonal-pyramidal BiS_3 units and distorted octahedral KS_6 units. The isolated pyramidal molecule of $[BiS_3]^{3-}$ makes the structure of K_3BiS_3 essentially

molecular. We synthesized this intermediate *ex-situ* using the conditions identified by the panoramic synthesis experiments and refined its structure using Rietveld refinement (Figure S1). The trigonal-pyramidal units of BiS_3 have bond lengths and bond angles of $2.593(7)$ Å and $99.2(3)^\circ$, respectively. The distorted KS_6 octahedra exhibit three different coordination environments, shown in different colors in Figure 15b. The distortion of octahedra give rise to a range of bond lengths between $3.11(2)$ and $3.53(1)$ Å. The distorted octahedra of K1, shown in blue, is capped by a bismuth and shares a corner with the three other BiS_3 units in the structure. K2, in turquoise, is edge-sharing with three BiS_3 units, while K3, shown in purple, is exclusively corner-sharing with the BiS_3 polyhedra.

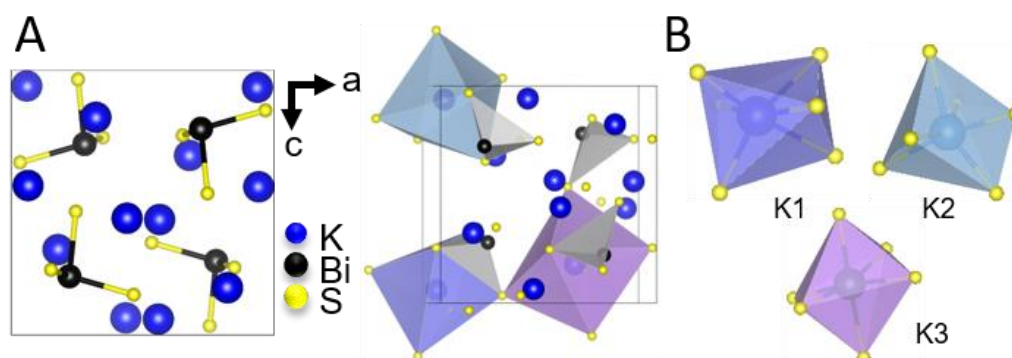


Figure 15: (a) Ball and stick representation of K_3BiS_3 (left) and an illustration of the three different octahedra of KS_6 and all BiS_3 units (right). (b) Isolated representations of the KS_6 distorted octahedra.

By comparing the structures in the $1.5 \text{K}_2\text{S} + \text{Bi}_2\text{S}_3$ reaction, shown in Figure 16, the role of K_3BiS_3 as an intermediate phase in the formation of KBiS_2 is examined. The coordination environment of potassium can be described as a gradual progression from tetrahedral to octahedral. In the starting material, the potassium cation begins in the K_2S anti-fluorite structure consisting of KS_4 tetrahedra with bond lengths of 3.191 Å,¹²⁶ and over the course of the reaction expands to the distorted KS_6 octahedra in K_3BiS_3 . By the final product, potassium forms ideal KS_6 octahedra in

KBiS₂. Of note, the K-S bond lengthens in K₃BiS₃, before shortening to 3.02 Å in the final *Fm* $\bar{3}$ *m* structure.¹²⁷ In contrast, the bismuth coordination sphere does not undergo a gradual progression. In fact, bismuth undergoes an unexpected decrease in coordination number from square pyramidal and distorted octahedral to trigonal-prismatic, before transitioning to octahedral in KBiS₂. In K₃BiS₃, bismuth stereochemically expresses its lone pair into a void created by the potassium cations, then no longer expresses its lone pair in the final product, KBiS₂. The bismuth precursor, Bi₂S₃, contains square-pyramidal BiS₅ units and distorted BiS₆ octahedra, as illustrated in Figure 16. Three different Bi-S bond lengths are present in the BiS₅ units. The bond lengths in the basal plane are divided equally between 2.74(1) and 2.96(1) Å, while the apical Bi-S in BiS₅ is the shortest bond length in the structure at 2.56(1) Å.¹²⁶ The BiS₆ octahedra has two bond lengths at 2.67(1) Å, another two at 2.96(1) Å, as well as one at 3.05(1) and 2.69(1) Å. The Bi-S bond length shortens to 2.62(1) Å in K₃BiS₃, before increasing to 3.02 Å in KBiS₂. A concurrent shortening of the Bi-S bonds and lengthening of the K-S bonds in K₃BiS₃ is likely a result of the concomitant separation of the Bi₂S₃ chains and incorporation of the KS₄ units. Owing to its utility as a structural transition framework, K₃BiS₃ therefore can be considered a structural intermediate for the formation of KBiS₂.

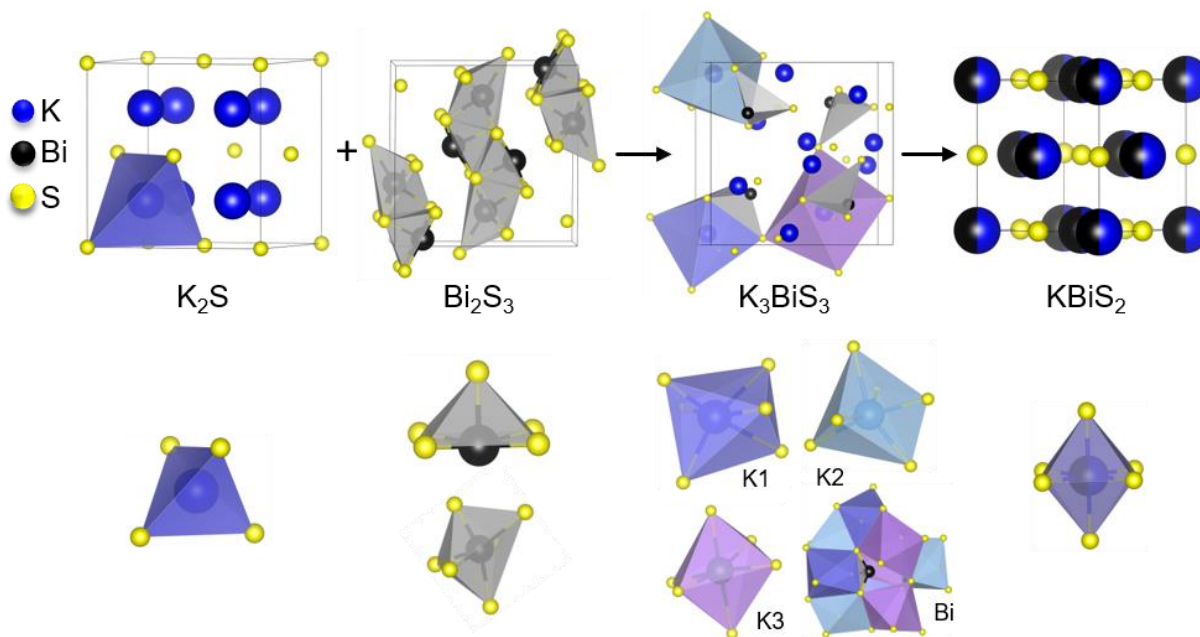


Figure 16: Reaction progression of the starting materials, K_2S and Bi_2S_3 , to $KBiS_2$ through the intermediate phase K_3BiS_3 . Unique cation coordination environment is shown for each structure. A bismuth atom in K_3BiS_3 is shown within the cavity formed by the KS_6 distorted octahedra.

To explore if the formation of rocksalt $KBiS_2$ persists, an increase in amount of Bi_2S_3 relative to K_2S was investigated. The overlaid diffraction patterns and reaction map of the 1 K_2S : 1 Bi_2S_3 panoramic synthesis are shown in Figure 17a and b, respectively. As before, K_3BiS_3 forms first and appears between 240-250°C, which is similar to the formation temperature of 270°C in the K_2S -rich reactions featuring a ratio of 1.5:1. The continued formation of K_3BiS_3 before the crystallization of $KBiS_2$, despite a different final product, corroborates that this kinetic intermediate is mechanistically important for the formation of the rocksalt structure. The $KBiS_2$ rocksalt structure emerges at ca. 435°C (red). The rocksalt phase persists through the maximum temperature and, on cooling, a third phase is observed between 465-480°C (purple). $KBiS_2$ persists until approximately 300°C on cooling, where the third phase is the sole final product.

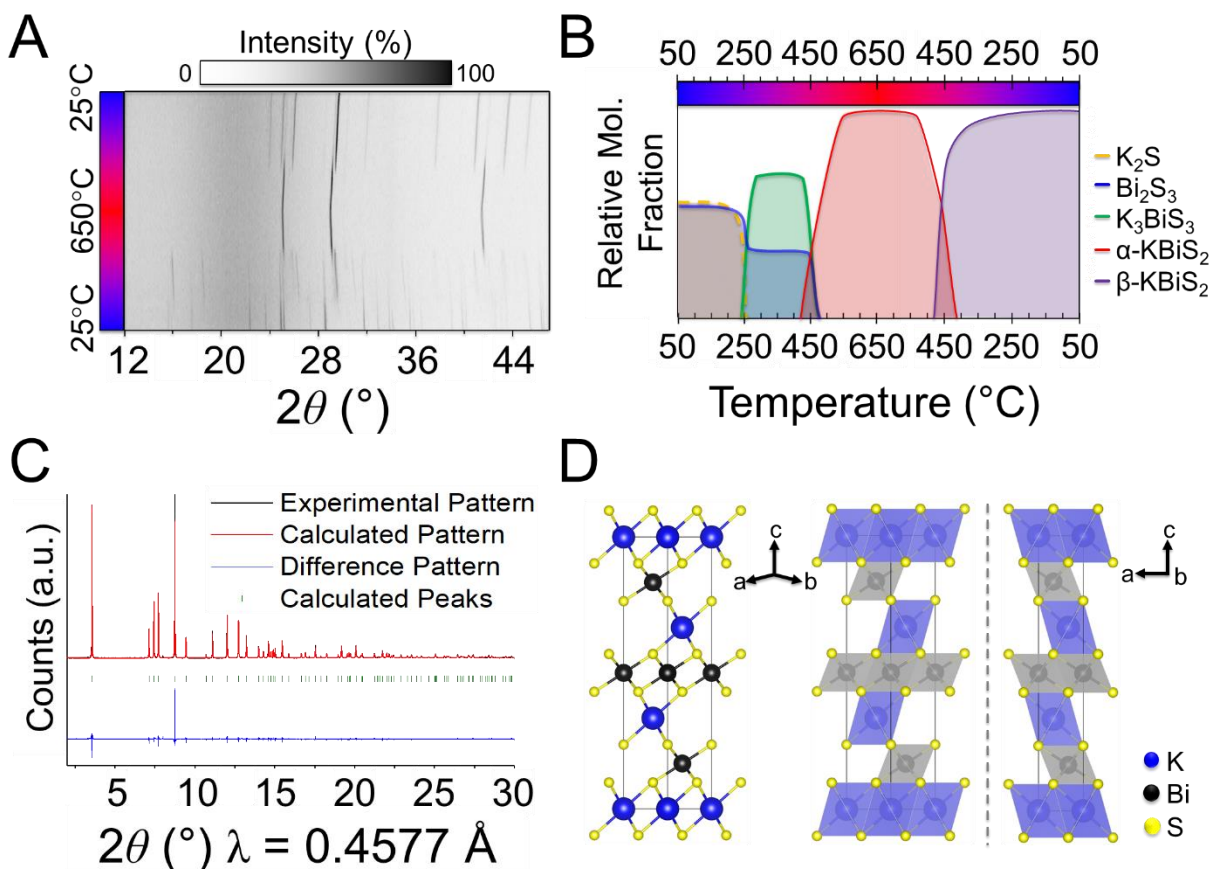


Figure 17: (a) Overlaid diffraction patterns of 1 K_2S + 1 Bi_2S_3 . (b) Reaction map of 1 K_2S + 1 Bi_2S_3 . Nominal compositions are shown; dashed lines represent a noncrystalline phase. (c) Structure solution for β - KBiS_2 (d) Structural representation of the ordered rocksalt, β - KBiS_2 .

The third and final phase in this reaction is a cation-ordered polymorph of KBiS_2 in the rhombohedral α - NaFeO_2 structure type ($R\bar{3}m$, $a = b = 4.12983(3) \text{ \AA}$, $c = 22.09484(17) \text{ \AA}$). The structure of the KBiS_2 polymorph, hereafter named β - KBiS_2 , was determined using Rietveld refinement on synchrotron PXRD data (Figure 17c). β - KBiS_2 is an ordered rocksalt that is isostructural to RbBiS_2 .¹²⁸ In this structure type, cation trigonal anti-prisms are connected through edge-sharing as in the disordered rocksalt structure (Figure 17d).¹²⁹ The layers alternate between CdCl_2 -type $[\text{BiS}_2]^-$ layers and potassium cations. It is notable that the ordered $R\bar{3}m$ forms only

when stoichiometric amounts of bismuth and potassium precursors are used; an excess of just 5% of K_2S yields the rocksalt structure (Figure S4). The original synthesis for the cation-disordered $Fm\bar{3}m$ KBiS_2 (now called α - KBiS_2) also uses an excess of the potassium precursor, K_2CO_3 .¹²² This suggests that an excess of potassium may have a role in destabilizing the lower symmetry structure.

Thermal analysis data of β - KBiS_2 shown in Figure S6 and Density Functional Theory (DFT) calculations, described further below, corroborate the experimental evidence that cation-ordered β - KBiS_2 is the thermodynamically stable phase. The endothermic peak at ca. 480°C upon heating and broad exothermic peak at ca. 405°C upon cooling in the thermal analysis data indicate β - KBiS_2 undergoes a phase transition. The temperature of these peaks corresponds to the transition temperature for the α - KBiS_2 to β - KBiS_2 transition in Figure 17a. This, in conjunction with the identity of the post-thermal analysis product as β - KBiS_2 , confirms these signals result from phase transitions from a low to high temperature phase. Moreover, DFT calculations show that cation-ordered β - KBiS_2 sits on the convex hull and, thus, is the thermodynamically stable phase, while cation-disordered α - KBiS_2 sits at 75 meV/atom above the convex hull (i.e. above β - KBiS_2).

Panoramic Synthesis of KBiSe_2 . KBiSe_2 is reported to crystallize in the rocksalt structure and was hypothesized to proceed through a similar mechanism to α - KBiS_2 owing to their isostructural nature. The panoramic synthesis on 1 K_2Se + 1 Bi_2Se_3 was conducted and is illustrated in Figure 5. At 195°C, again the analogous material, K_3BiSe_3 , forms (Figure S7; $P2_13$; $a = b = c = 9.773(2)$ Å).⁹⁸ The appearance of K_3BiSe_3 as an intermediate phase also in the selenide analogue reaction supports that this molecular salt phase may be important mechanistically to the reaction path.

The reaction selectivity of K_3BiQ_3 ($Q = \text{S}, \text{Se}$) directly preceding the formation of the

KBiQ₂ ternary is postulated to be structural in origin as opposed to energetic. *In-situ* studies observing the phase formation found the composition of the first transient phase to be that which yielded the largest energy release¹³⁰ or the fastest energy release³⁰. The former does not apply for these chalcogenide systems as the formation of K₃BiQ₃ is less energetically favorable than the β -KBiQ₂ phases. Specifically, the formation energies of K₃BiS₃ and K₃BiSe₃ are calculated to be -48 meV/atom and -28 meV/atom below the convex hull, respectively, while those of β -KBiQ₂ are -68 meV/atom and -60 meV/atom below the hull for the sulfide and selenide, respectively. The alpha phases have positive formation energies relative to the convex hull according to DFT calculations and are, therefore, considered unstable. K₃BiQ₃ also does not provide the fastest energy release as diffusion must occur for this phase to form as compared to KBiQ₂. The precursor loading in this work are 3 K₂S : 2 Bi₂S₃ (e.g. 1.5:1) and 1 K₂Q : 1 Bi₂Q₃ (Q= S, Se). The precursors were sieved and thoroughly mixed, such that the average contact between particles are expected to mirror that of the loading ratio. Correspondingly, no notably K₂Q-rich or poor areas are expected. The fastest energy release would therefore be the formation of KBiQ₂, however, K₃BiQ₃ reproducibly forms first in both chalcogenide system regardless of loading ratio. The formation of the K₃BiQ₃ structural intermediate therefore cannot be easily rationalized by current thermodynamic or kinetic theories. However, the formation of the potassium-rich intermediate, persistent even in relatively potassium-poor reactant loading, underscores that this compound is necessary for the formation of the KBiQ₂ ternary in these conditions.

The structural intermediate, K₃BiSe₃, shown in green in Figure 5, persists until a new phase emerges at 285°C, shown in purple. This new phase disappears at 555°C before reappearing at 525°C on cooling as the final product. This phase is isostructural to β -KBiS₂ and hereafter called

β -KBiSe₂ ($R\bar{3}m$, $a = b = 4.26442(1) \text{ \AA}$, $c = 23.0290(1) \text{ \AA}$). When β -KBiSe₂ disappears, the known rocksalt structure-type α -KBiSe₂ begins to emerge. Upon cooling, β -KBiSe₂ reappears by 500°C. In order to isolate α -KBiSe₂, the product was quenched at 650°C and annealed. Attempts to synthesize α -KBiSe₂ using the binaries without quenching, even with an excess of K₂Se, were unsuccessful.

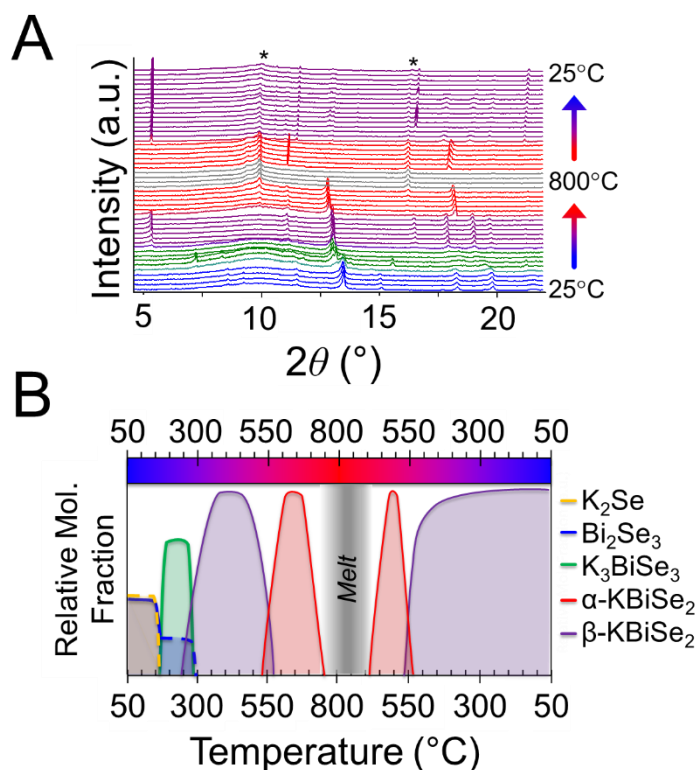


Figure 18: (a) Overlaid diffraction pattern for K₂Se + Bi₂Se₃ Panoramic synthesis. Asterisks indicate cristobalite (SiO₂) crystallization (b) Reaction map of 1 K₂Se + 1 Bi₂Se₃. Nominal compositions are shown; dashed lines represent an amorphous phase.

The overall reaction pathway in the selenide and sulfide systems is similar. Both systems proceed through a K₃BiQ₃ (Q = S, Se) intermediate. The coordination sphere of potassium increases from an anti-fluorite tetrahedron to a distorted octahedron in K₃BiSe₃, as it does in the sulfide system. The coordination sphere of bismuth in the selenide system, however, decreases

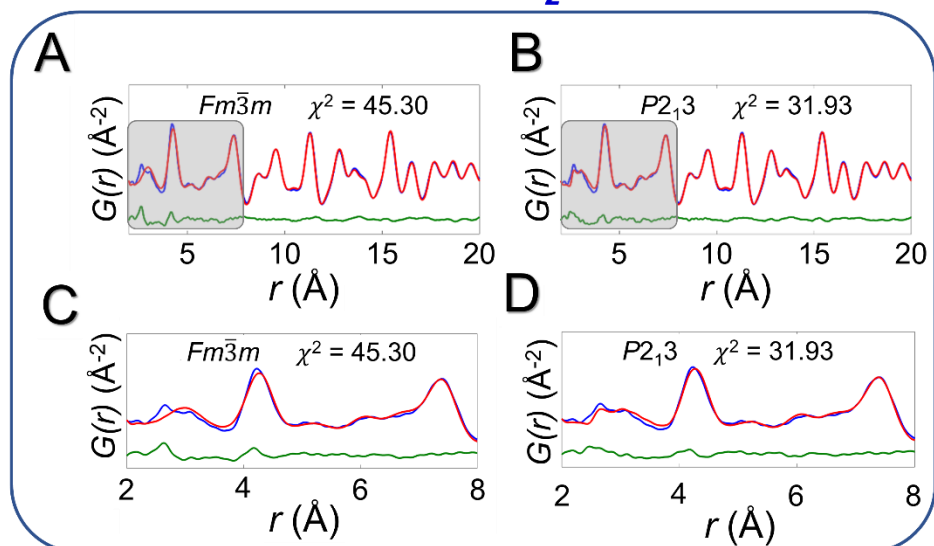
during the intermediate phase from an octahedron in Bi_2Se_3 , shown in Figure S8, to trigonal pyramidal in the discrete ions in K_3BiSe_3 , before returning to an octahedron in the highly dense ordered and disordered rocksalt type KBiSe_2 . The formation temperature of the selenide ternaries is observed lower than that of the sulfide likely as a result of the lower melting points of the selenide binaries, the higher basicity of K_2Se than K_2S , and the more polarizable anionic framework of the selenium ternary, which facilitates ion mobility.¹³¹ Similar to the KBiS_2 system, thermal analysis (Figure S9) and DFT calculations show that the ordered, α - NaFeO_2 type polymorph of KBiSe_2 is the thermodynamically stable phase. Comparable to its sulfur analogue, cation-disordered α - KBiSe_2 sits 76 meV/atom above the ordered, stable β - KBiS_2 phase.

Investigation of Local Structure. Local off-centering from ns^2 lone pairs has been demonstrated previously for materials containing heavy main-group elements as for example the emphanis effects in PbQ .¹³²⁻¹³⁷ The structure of the titular KBiQ_2 compounds is therefore expected to be locally distorted as a result of stereochemical activity of the Bi^{3+} lone pair, while the global structure remains in the rocksalt or α - NaFeO_2 structure type for the alpha and beta phases, respectively. Pair distribution function (PDF) analysis confirms that the data are well fit using $Fm\bar{3}m$ for α - KBiS_2 and α - KBiSe_2 at long r ranges (**Error! Reference source not found.**a and e). However, the split of the first PDF peak is not well fit, as shown in Figure 6c and 6g. The Bilbao Crystallographic Server¹⁰⁸⁻¹¹⁰ was used to generate possible subgroups of space group $Fm\bar{3}m$ assuming the Wyckoff positions 4a and 8c. Those subgroups were used to fit the PDF data. The short range ($r < 6 \text{ \AA}$) were better fit using the lower symmetry space group $P2_13$ with partial site occupations in a cubic lattice cell as shown in **Error! Reference source not found.****Error! Reference source not found.**b, d, f, and h. The split in the first coordination shell was better

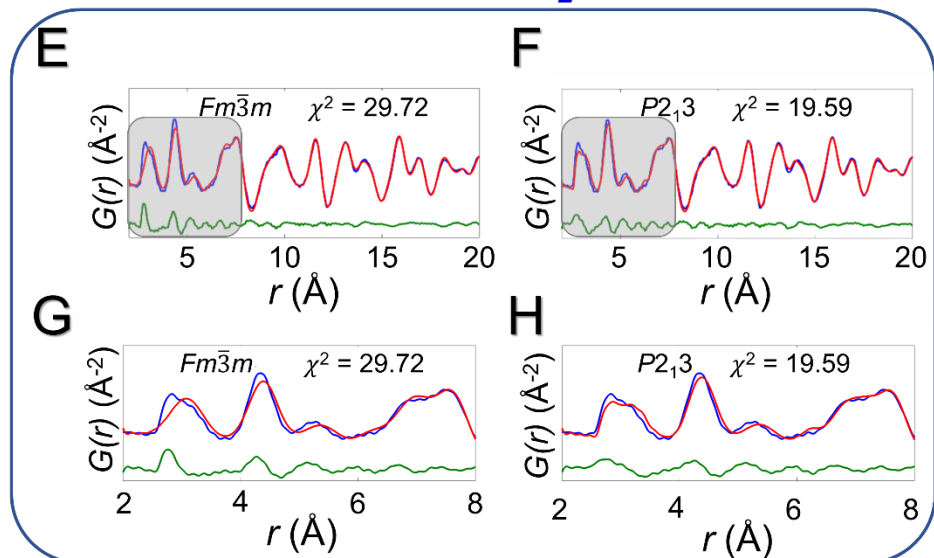
modeled by off-centering the atoms from the ideal rocksalt positions as illustrated in **Error!**

Reference source not found.**Error!** Reference source not found.i and j.

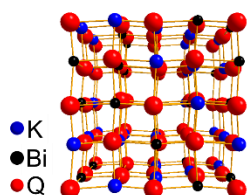
α -KBiS₂



α -KBiSe₂



I



J

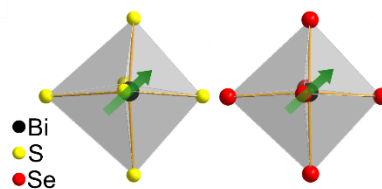


Figure 19: PDF fits for α -KBiS₂ using a (a) Fm $\bar{3}$ m model and (b) P2₁3 model. These models are zoomed in to the short range ($r < 8 \text{ \AA}$), highlighted in grey, for the Fm $\bar{3}$ m model (c) and for the P2₁3 model (d). In the PDF fits, red is the calculated PDF pattern, blue is the experimental data, and green is the difference pattern. PDF fits for α -KBiSe₂ using a (e) Fm $\bar{3}$ m model and (f) P2₁3 mode; zoomed in region shown for the Fm $\bar{3}$ m model (g) and for the P2₁3 model (h). (i) Shows a 2x2x2 unit cell representation of KBiQ₂ and (j) highlights the off-centering of bismuth in the [BiS₆]³⁻ and [BiSe₆]³⁻ octahedra.

Optical Properties of α - and β -KBiQ₂. As the ratio of K₂Q to Bi₂Q₃ becomes stoichiometric in the syntheses, the final product transitions from α -KBiQ₂ to β -KBiQ₂ with band gap energies of 0.84(2) eV and 1.09(2) eV, respectively, for the selenides (red, Figure 20a) and 1.23(2) eV and 1.55(2) eV for the sulfides (blue, Figure 20a). As the compounds undergo a decrease in symmetry moving from the disordered α -KBiQ₂ to the ordered β -KBiQ₂, we observe a subsequent increase in band gap. The dimensional reduction from the ordering of β -KBiQ₂ into layers of [BiQ₂]⁻ and K⁺ (Figure 20b) yields a blue shift in the experimental band gap, as similarly observed for other semiconductors.^{133, 138} Figure 20c shows the energies of the valence band maxima for α -KBiQ₂ and β -KBiQ₂ measured using a Kelvin Probe (see experimental section) as well as for four well-known semiconductors (Si, CdTe, methylammonium lead iodide (MAPbI₃), and TiO₂) for reference. The energies of the conduction band minima are included and were extrapolated using the valence band maxima energies and experimental or known band gaps.

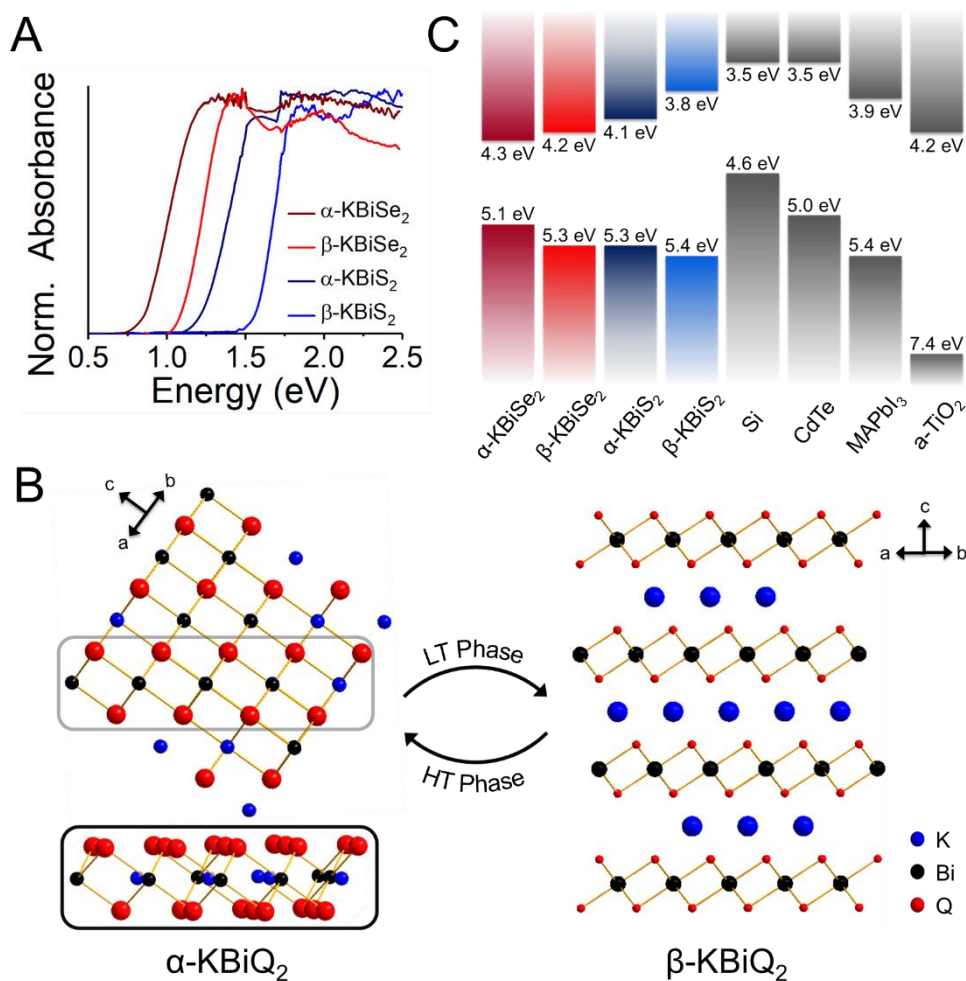


Figure 20: (a) Experimental band gaps for the known α -KBiQ₂ ($Fm\bar{3}m$) and discovered β -KBiQ₂ ($R\bar{3}m$) phases. (b) Illustration of dimension reduction from the 3D covalent framework in the high temperature (HT) phase, α -KBiQ₂, to the layered 2D covalent framework in the low temperature (LT) phase, β -KBiQ₂. For both structures, only covalent bonds (e.g. Bi-Q bonds) are shown. The site occupancy of bismuth and potassium in α -KBiQ₂ was randomized, while constrained to maintain equivalent amounts of the cations. The inset for α -KBiQ₂ tilts the indicated portion of the structure to highlight the 3D connectivity through the plane. (c) Depiction of valence band maxima, conduction band minima, and band gap energies for α -KBiQ₂, β -KBiQ₂, Si¹³⁹⁻¹⁴⁰, CdTe¹⁴¹, MAPbI₃¹⁴², and TiO₂ (anatase)¹⁴³⁻¹⁴⁴.

Calculation of Thermodynamic Stability and Electronic Band Structure. DFT

calculations were performed to determine the thermodynamic stabilities and electronic structures of the α -KBiQ₂ and β -KBiQ₂ materials. When compiling the phase diagram for the K-Bi-S and K-

Bi-Se phase spaces in Figures 8a and b, all compounds stored in the Open Quantum Materials Database¹⁰⁰ are considered and the grand canonical linear programming (GCLP) is used to construct the thermodynamic stability convex hull. The energy calculation for the structure of $\text{KBi}_{6.33}\text{S}_{10}$ and its partial occupancies⁸⁸ is computationally intensive; thus, the compound is included in the phase diagram assuming it has $T = 0\text{K}$ stability. Notably, all ternary phases discovered to date in these phase diagrams lay along the $\text{K}_2\text{Q-Bi}_2\text{S}_3$ composition line, including the titular compounds. The intermediate phases, K_3BiS_3 and K_3BiSe_3 , are also on the convex hull, and hence are considered thermodynamically stable ground state phases at $T = 0\text{K}$. Our calculations show that the ordered phases, $\beta\text{-KBiS}_2$ and $\beta\text{-KBiSe}_2$, are on the convex hull, while the disordered $\alpha\text{-KBiS}_2$ and $\alpha\text{-KBiSe}_2$ structures are 75 and 76 meV/atom above the hull, respectively. This indicates the beta phases are the thermodynamically stable polymorphs, while the alpha phases are metastable. This agrees with the experimental observations as the beta phases are stable at room temperature and the alpha phases are formed at high temperature.

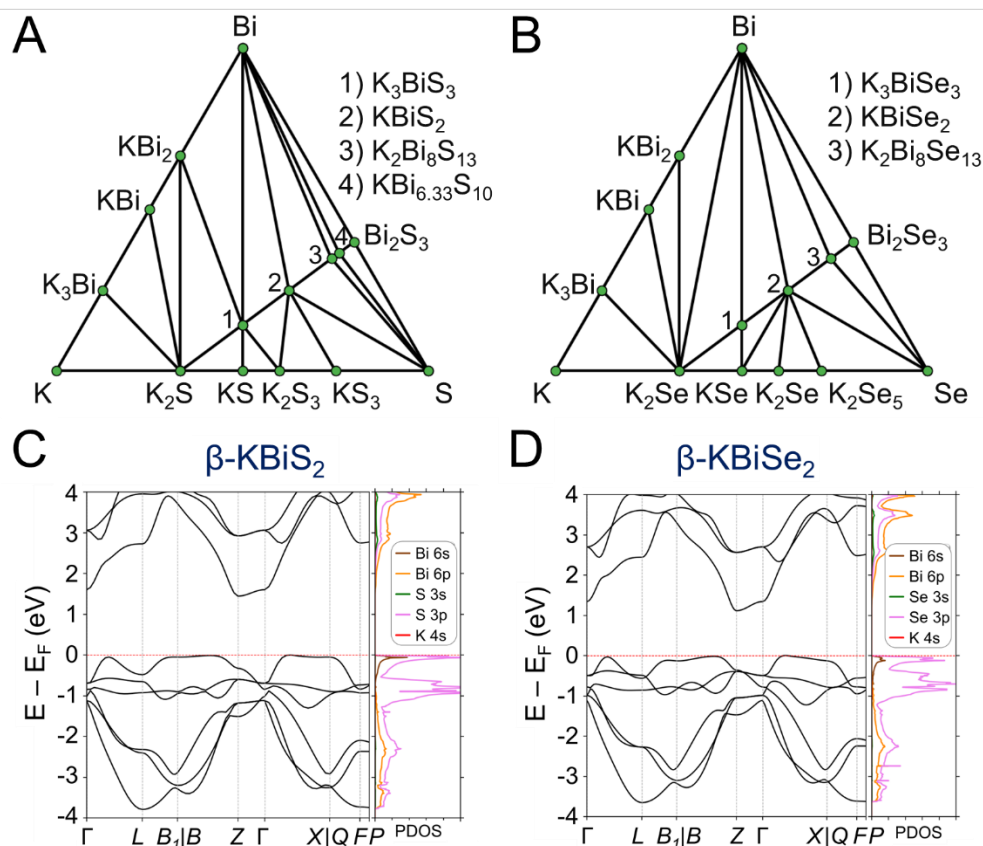


Figure 21: Phase diagram of (a) K-Bi-S and (b) K-Bi-Se phase space. The band structure and partial density of states (PDOS) of (c) β - $KBiS_2$ ($R\bar{3}m$) and (d) β - $KBiSe_2$ ($R\bar{3}m$).

The band structures of β - $KBiS_2$ and β - $KBiSe_2$ are shown in Figures 8c and d, respectively. These two materials are indirect band gap semiconductors with calculated band gaps of 1.45 and 1.12 eV for β - $KBiS_2$ and β - $KBiSe_2$, respectively, using PBE functional method. These are consistent with the experimental band gaps of 1.55(2) eV and 1.09(2) eV as well as the expectation of the more electronegative sulfur analogue having a wider band gap than the selenium. For both β - $KBiQ_2$ phases, the conduction band minimum is at the Z point of the Brillouin zone, while the valence band maxima are in the region along $\Gamma - L$, $Z - B$ and $\Gamma - X$ directions. The conduction band maximum is primarily comprised of the bismuth $6p_z$ orbital with contribution from the sulfur 3s orbital (Figure S11). The bismuth 6s and sulfur 3p orbitals form the valence band maxima

regions (Figure S11). The $\Gamma - L$ and $\Gamma - X$ direction have more contribution from the sulfur $3p_x$ orbital and the bismuth $6s$, sulfur $3p_x$ and $3p_y$ orbitals, respectively. Overall, the conduction band is far more dispersive than the top of the valence band as shown in Figures 8c and d, indicating that, in the beta phase, the charge transport of electrons would be far more efficient than that of holes. The partial density of states (PDOS) shows that the relatively flat valence band maxima is a consequence of the localized S/Se p orbitals that make up this band.

In order to understand the electronic structures of the alpha phases, the effects of bismuth off-centering and K/Bi disorder must be separated. The band gaps of the rocksalt-ordered KBiQ_2 as a function of coherent bismuth off-centering are shown in Figure 9a. As the off-centering of bismuth from its ideal positions increases, the band gaps of $\alpha\text{-KBiS}_2$ and $\alpha\text{-KBiSe}_2$ are calculated to increase. The disordering of $\alpha\text{-KBiQ}_2$ is simulated by randomly arranging potassium and bismuth atoms in supercells and the calculated band gaps using the same PBE functional method are 0.77 and 0.58 eV for $\alpha\text{-KBiS}_2$ and $\alpha\text{-KBiSe}_2$, respectively. The band structures of the alpha phases are shown in Figures 9b and c. Both dimensional reduction,¹³⁸ manifesting as cation ordering (Figure 20b), and stereochemical lone pair expression,¹³³ presenting as the off-centering of the bismuth atom, increase the band gap. Therefore, the band gaps of these compounds observed at finite temperature is a combination of these two effects (i.e. increasing the temperature yields a reduction in cation ordering and, on the other hand, an increase in off-centering). The comparative lower value for the experimental band gaps of disordered $\alpha\text{-KBiQ}_2$ than those of the ordered $\beta\text{-KBiQ}_2$ materials indicates the influence of ordering has a larger effect than that of off-centering on the band gap, which is consistent with our calculations.

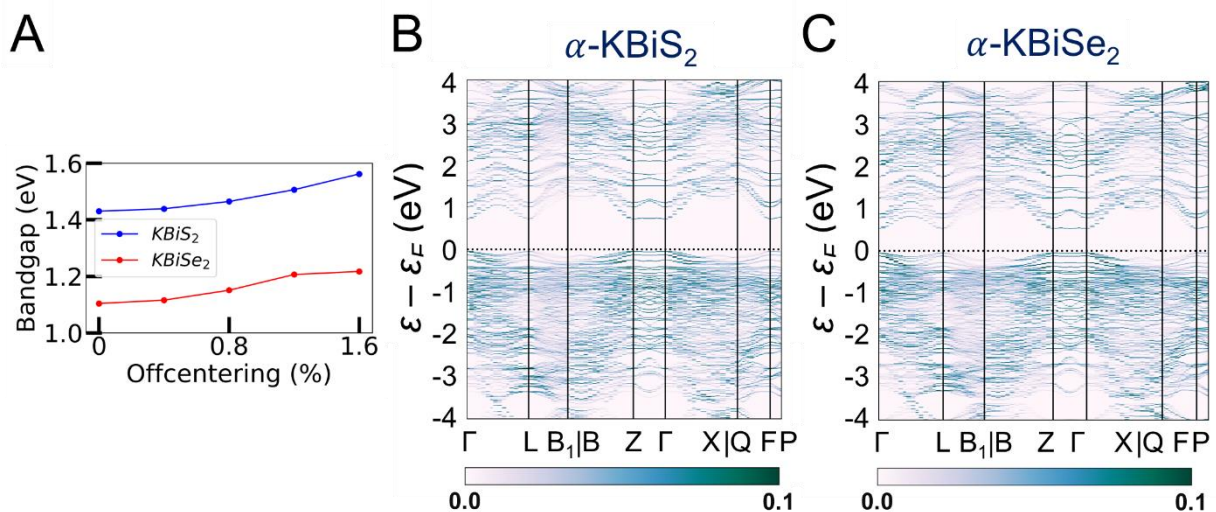


Figure 22: (a) The DFT-calculated change in band gap as bismuth is increasingly off-centered in the K-Bi-K direction from its ideal position. The bandgaps are calculated with the ordered $\text{R}\bar{3}\text{m}$ rocksalt structures for α - KBiS_2 and α - KBiSe_2 . The unfolded band structure of (b) α - KBiS_2 and (c) α - KBiSe_2 , which is unfolded to the Brillouin zone of $\text{R}\bar{3}\text{m}$ structures. The color bar indicates the band intensity.

Comparison of A-Bi-Q. When looking at ABiQ_2 (A = alkali metal, Q = S, Se, Te) compounds, simultaneous trends of decreasing symmetry and dimensionality are observed as the size of the alkali metal increases relative to bismuth (Figure 23). As we move across the sulfides in Figure 23d, the $[\text{BiQ}_2]^{1-}$ framework is progressively broken up by the increasingly larger alkali metal illustrated in Figure 23a-c. This is consistent with the so-called “counterion effect,” where, given an anionic framework, a counteraction can induce a specific structural change as result of steric effects as a function of its size.¹⁴⁵⁻¹⁴⁸ Previous work^{63, 146} has shown that the smaller the counteraction, the higher the dimensionality and the higher coordination numbers of the metal in the covalent framework.

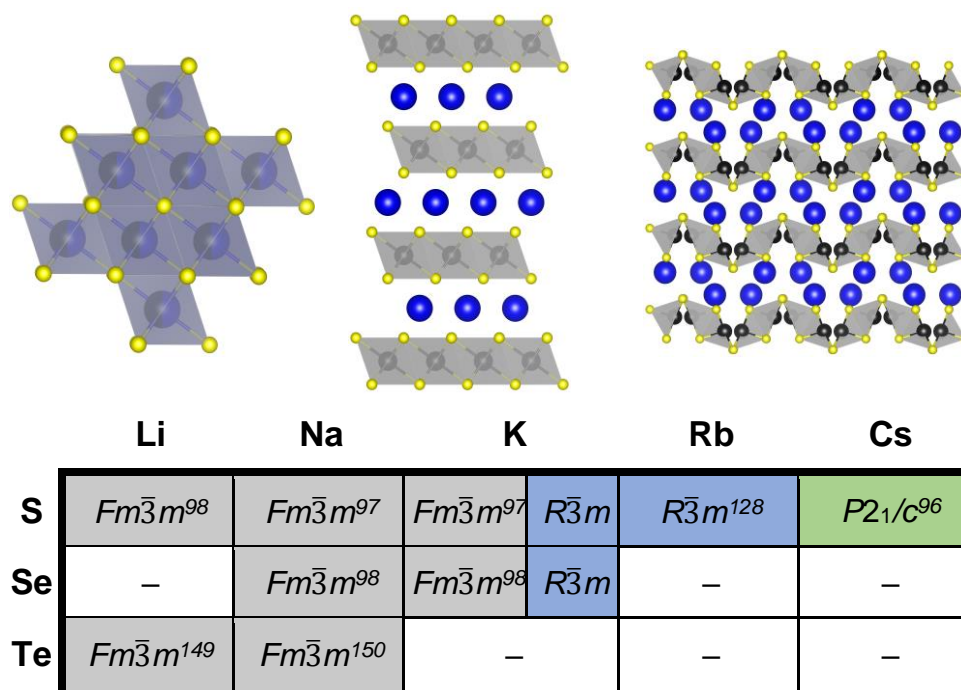


Figure 23: Representative illustrations of $ABiQ_2$ ($A = \text{alkali metal}$, $Q = \text{S, Se, Te}$) structures that crystallize in the (a) rocksalt structure type ($Fm\bar{3}m$) (b) $\alpha\text{-NaFeO}_2$ structure type ($R\bar{3}m$) and (c) CsSbS_2 structure type ($P2_1/c$). Monovalent cation shown in blue, trivalent cation in black, and chalcogenide in yellow. (d) Chart of $ABiQ_2$ reported in literature and in this paper.

As the alkali metal increases in size, there is a decrease in dimensionality in agreement with the counterion effect that results from the end of site-sharing for the alkali metal and pnictogen.¹⁴⁵⁻¹⁴⁶ The previously reported lithium, sodium, and potassium $ABiQ_2$ compounds crystallize in the rocksalt structure with the alkali metal and bismuth sharing the same octahedral cation site, shown in Figure 10a. As observed in this work, KBiS_2 and KBiSe_2 can be directed to crystallize in the β -phase (Figure 23b), which is in the $\alpha\text{-NaFeO}_2$ structure type. DFT mixing entropy calculations, shown in Figure S13, corroborate these experimental results and underscore that the rocksalt structure cannot be stabilized by finite temperature compared to the $\alpha\text{-NaFeO}_2$ structure type. This structure consists of $[\text{BiS}_2]^-$ layers stacked perpendicular to the c -axis and

separated by K^+ cations (Figure 23b). The potassium ternary marks an inflection point of site-sharing of bismuth and the alkali metal, as the rubidium and cesium ternaries also do not exhibit site-sharing of the two cations. The framework here transitions from a three dimensional covalent framework to a two dimensional layered framework, as highlighted previously in Figure 7b. $RbBiS_2$ crystallizes in the α - $NaFeO_2$ structure type, similar to β - $KBiS_2$ and β - $KBiSe_2$, where bismuth and potassium separately occupy sites in alternate layers. $RbBiSe_2$ was synthesized using a 1.5 Rb_2Se : 1 Bi_2Se_3 ratio and is indexed to be in the $R\bar{3}m$ space group. $CsBiS_2$ crystallizes in the $CsSbS_2$ structure type ($P2_1/c$), shown in Figure 23c. This structure exemplifies the transition from a 2D covalent framework to a 1D framework as it comprises extended, corrugated $[BiS_2]^-$ chains separated by Cs^+ atoms.

With potassium acting as an inflection point in the $ABiQ_2$ system, there is a region of stability for six-coordinate site-sharing of bismuth and alkali metal corresponding to a cation radii ratio $\left(\frac{r^+}{r^{3+}}\right)$ of 1.33 or less, using Shannon ionic radii.¹⁵¹ For ratios higher than 1.33, the cation-ordered structure forms (e.g. $RbBiS_2$, $RbBiSe_2$, and $CsBiS_2$). A similar cation radii tolerance is found in the $ALnS_2$ ¹⁰³ and AA_nQ_6 ¹⁵² structures (A = alkali metal or Tl, Ln = lanthanide, An = Th, U, Np), thus supporting the plausibility of this proposed site-sharing tolerance. Inspection of antimony analogues corroborates the cation radii tolerance for metal site sharing. $NaSbS_2$ forms in both the rocksalt structure⁹⁹ and in the $KSbS_2$ structure type.¹⁵³ The $\frac{Na^+}{Sb^{3+}}$ ratio is 1.3, which within approximation agrees with the previous trend for bismuth. $KSbS_2$ crystallizes only in a cation-ordered structure and is not observed in a disordered rocksalt phase; the radius ratio for potassium and antimony $\left(\frac{r^+}{r^{3+}}\right)$ in $KSbS_2$ is 1.8, thereby following the proposed cation radii

tolerance.¹⁵⁴

To demonstrate the robustness of the tolerance factor, the total energies of the three prototypes (Figure 10a-c) were calculated for all reported structures in Figure 10d and their accuracy were subsequently compared to the room-temperature structures. The DFT-calculated predictions found that at $T = 0$ K all structures are most stable in the ordered α -NaFeO₂ structure type. Notably, the energy difference for CsBiS₂ between the rhombohedral and monoclinic structures, as shown in Table S13, is quite small (≤ 10 meV/atom) at 0 K and, thus, the monoclinic CsSbS₂ ($P2_1/c$) structure type is very likely stabilized by temperature. The transition temperature between the rocksalt and α -NaFeO₂ structure types, and therefore their temperature dependence, were investigated by introducing ideal mixing entropy (i.e. the configurational entropy) to the $T = 0$ K energies and fitting the transition temperatures using the experimental transition temperature of KBiS₂. As shown in Table S14, the calculated transition temperatures follow the disorder-to-order trend predicted by the tolerance factor. The lithium ternaries have a transition temperature below room temperature, indicating that the rocksalt phase would be present at room temperature. The sodium ternaries have similarly low transition temperatures, while the potassium, rubidium, and cesium ternaries have a transition temperature of over ~ 700 K, thus confirming the robustness of the proposed tolerance factor.

Understanding and employing this proposed cation radii tolerance profitably impacts the numerous fields using ternary chalcogenide semiconductors. More specifically, alkali metal pnictogen chalcogenide ternaries are of interest for thermoelectrics and non-linear optics. In the field of thermoelectrics, binary chalcogenide semiconductors (i.e. GeQ, SnQ, PbQ) that crystallize in the rocksalt structure type have historically been of great interest. Current studies now capitalize

on structure-property relationships to optimize properties by exploring solid solutions of rocksalt materials.⁹³⁻⁹⁴ These solid solutions of rocksalt structures reduce the lattice thermal conductivity in the thermoelectric material through phonon scattering as well as exploit band gap engineering. The proposed cation radii ratio $\left(\frac{r^+}{r^{3+}}\right)$, therefore, provides guidance for the compositional requirements to form a cation-disordered APnQ₂ ternary (A = alkali metal, Pn = Sb, Bi, Q = S, Se) that may then be mixed with another rocksalt structure. For non-linear optical materials, noncentrosymmetry is a structural requirement. The probability of achieving a noncentrosymmetric space group greatly increases with cation ordering as well as expression of the pnictogen ns² lone pair. Therefore, the proposed cation radii ratio can similarly be used to guide cation selection criterion for non-linear optical materials.

3.5. Conclusion

In this work, panoramic synthesis is shown to be a valuable tool for materials discovery and mechanistic insight into structure formation of KBiS₂ and KBiSe₂. Three new compounds were identified, K₃BiS₃, β-KBiS₂, and β-KBiSe₂. The KBiQ₂ however do not form directly. The appearance of K₃BiQ₃ (Q = S, Se) preceding the formation of KBiQ₂ suggests that this compound is mechanistically important as an intermediate in the reaction pathway. K₃BiQ₃ serves as a transition point for the potassium coordination environment and for cation intermixing. The observation of the KBiQ₂ as both a rocksalt and α-NaFeO₂ type structure, while NaBiQ₂ and RbBiQ₂ crystallize in the *Fm* $\bar{3}$ *m* and *R* $\bar{3}$ *m* space groups, respectively, suggests that there is a cation radius tolerance $\left(\frac{r^+}{r^{3+}}\right)$ of 1.33 or greater for high symmetry rocksalt formation. Thermal analysis data and DFT calculations show that the cation-ordered polymorphs are the thermodynamically

stable phases, while PDF analysis shows that the structures have local off-centering from stereochemically active $6s^2$ lone pair expression on the bismuth. DFT calculations also corroborate the increase in band gap from α -KBiQ₂ to β -KBiQ₂ as a result of dimensional reduction. By continuing to develop and catalog reactions using *in-situ* diffraction techniques, we can work to expand our mechanistic understanding and predictive power towards the ultimate goal of synthesis-by-design.

Chapter 4. In Situ Mechanistic Studies of Two Divergent Synthesis

Routes forming the Heteroanionic BiOCuSe

Reprinted with permission from ‘Rebecca McClain, Christos D. Malliakas, Jiahong Shen, Jiangang He, Christopher Wolverton, and Mercouri G. Kanatzidis. ‘*In Situ* Mechanistic Studies of Two Divergent Synthesis Routes forming the Heteroanionic BiOCuSe.’ *Journal of the American Chemical Society*, **2021**, 143, 31, 12090-12099.’

Copyright © 2021, American Chemical Society

4.1. Abstract

Heteroanionic materials are a burgeoning class of compounds that offer new properties via the targeted selection of anions. However, understanding the design principles and achieving successful syntheses of new materials in this class is in its infancy. To obtain mechanistic insight and a panoramic view of the reaction progression from beginning to end of the formation of a heteroanionic material, we selected BiOCuSe, a well-known thermoelectric compound, and utilized *in situ* synchrotron powder diffraction as a function of temperature and time. BiOCuSe is a layered material, which crystallizes in a common mixed anion structure type: ZrSiAsFe. Two reactions of starting materials ($\text{Bi}_2\text{O}_2\text{Se} + \text{Cu}_2\text{Se}$ and $\text{Bi}_2\text{O}_3 + \text{Bi} + 3\text{Cu} + 3\text{Se}$) were studied to determine the effect of precursors on the reaction pathway. Our *in situ* investigation shows that the ternary-binary $\text{Bi}_2\text{O}_2\text{Se} + \text{Cu}_2\text{Se}$ reaction proceeds without intermediates to directly form BiOCuSe, while the binary-elemental $\text{Bi}_2\text{O}_3 + \text{Bi} + 3\text{Cu} + 3\text{Se}$ reaction generates many intermediates before the final product forms. These intermediates include CuSe, Bi_3Se_4 , Bi_2Se_3 , and Cu_2Se . While the stoichiometric loading of the precursors necessarily dictates the identity of the first intermediates, kinetics also plays a contributing role in stabilizing unexpected

intermediates such as CuSe and Bi₃Se₄. This *in situ* study also observed that BiOCuSe formation occurs as low as 430°C. Understanding and establishing a link between the selection of precursors and the reaction pathways improves the potential for rational synthesis of heteroanionic materials and solid-state reactions in general.

4.2. Introduction

Technological advances are often driven by the discovery and development of functional solid-state materials. Many of these discoveries are predicated on substituting metal cations in the material or introducing co-occupancy in a material's anionic or cationic sites.¹⁵⁵ To date, there has been limited exploration of materials with heteroanionic compositions;¹⁵⁵ that is, materials with more than one anion, which each have crystallographically distinct sites. The heteroanionic approach not only widens the possible combination of elements, but also introduces an additional dimension of tunability through the choice and ordering of each anion. This presents the opportunity for anionic contrasts in electronegativity, charge, ionic radii, and polarizability, providing knobs with the potential to combine desired properties of individual anionic species or even realize emergent potential inaccessible to their single-anion components.¹⁵⁵⁻¹⁵⁷ The rational selection of anions enables the control of the electronic and atomic structure as observed, for example, in valence band engineering.^{156, 158} This approach has yielded many technologically important materials; however, historically, members of this material class have been discovered accidentally during efforts to prepare other targets. To access the broad structural diversity expected in this special class of materials, specific synthetic methodologies need to be invented that currently are not available. Currently, we have a limited understanding of what synthetic routes stabilize these compounds or how they form during the reaction progression, thus

motivating this study.

The structural scaffold of heteroanionic materials consists of either homoleptic polyhedra, where each cation is coordinated by a single type of anion, or heteroleptic polyhedra, where the cations are bonded to more than one type of anion. The former can be explained using hard-soft acid-base (HSAB) theory, where the anions segregate and preferentially bond with their coordinating hard or soft pair.¹⁵⁹⁻¹⁶⁰ The latter occurs when the metal cation are borderline soft or hard Lewis acids and anions are of similar size (e.g. N^{3-} , O^{2-} , S^{2-} , F^-) and are small enough to coordinate about the same metal cation. Homoleptic polyhedra produce long range ordering, whereas heteroleptic polyhedra may in addition to long range ordering have short range order.¹⁶¹ If the anions are similar in size and have similar bonding requirements, they are able to occupy similar crystallographic sites such as in oxynitrides and oxyfluorides.¹⁶⁰

Many mixed-anion materials adopt the $ZrCuSiAs$ structure-type, such as the homoleptic $LnOFeAs$, $LnOCuQ$, $BiOCuQ$ families (Ln = lanthanide, Q = S, Se, Te), which have attracted great interest for their optoelectronic, photocatalytic, thermoelectric, and superconducting properties.¹⁶²⁻¹⁶⁷ $BiOCuSe$, in particular, has been of great interest specifically for thermoelectric applications.^{164, 167-172} $BiOCuSe$ has alternating conductive $[Cu_2Se_2]^{2-}$ and insulating $[Bi_2O_2]^{2-}$ layers, which are stacked along the c -axis, and stabilize the structure by electron transfer between the layers.¹⁶⁵⁻¹⁶⁶ Often synthetic attempts for this class of materials yield a mixture of homoanionic products that are phase segregated according to HSAB theory instead of integrating into a single heteroanionic compound. Successful reactions leading to heteroanionic formation should then be examined to mechanistically inform its full reaction path and provide generalizable insight.

Using *in situ* diffraction techniques, the reaction progression of successful syntheses may

be panoramically observed and studied.^{22, 173} The mechanistic understanding achieved by monitoring such synthetic routes will ultimately enable the better rationalization of synthesis design.^{32, 58, 75} By monitoring the synthesis of heteroanionic materials, an understanding of the synthetic guiding principles can be identified and, in turn, applied to future heteroanionic reactions. Initial efforts have been made in this direction by investigating crystallographic ordering principles for oxyfluorides^{161, 174} and oxynitrides,^{156, 175} but oxychalcogenides have not yet been explored in this manner. Studies have also begun investigating the effects of precursors in solid-state reactions.^{30, 176} Additionally, text-mining efforts have been put forth to investigate the interchangeability of precursors¹⁷⁷ and to catalog both successful and unsuccessful inorganic material syntheses.^{78, 178}

This work investigates the formation of a prototypical oxychalcocogenide in the ZrCuSiAs family, BiOCuSe, employing *in situ* variable temperature X-ray diffraction (VT-PXRD) to elucidate the formation mechanism of this material and using different starting materials to explore precursor effects on product formation. Herein, we describe the reaction progression for a ternary-binary loading of Bi₂O₂Se + Cu₂Se and an elemental-binary loading of Bi₂O₃ + Bi + 3Cu + 3Se. The former proceeds without intermediates, while the latter progresses through a number of intermediates. Initial intermediate formation is determined according to stoichiometric considerations. For the bismuth intermediate, we describe the surprising formation of Se-poor Bi₃Se₄ before Bi₂Se₃ in the elemental reaction, attributed to the preference of Se to coordinate with Cu according to HSAB theory. In the same vein, we observe the formation of a Se-rich binary, CuSe. Both of these intermediates contain the incorrect oxidation states for Cu, Bi and Se. with respect to the oxidation states exhibited by the target compound. Remarkably in the stages before

the formation of BiOCuSe there is a reversal to the correct oxidation states in these elements.

4.3. Experimental details

Reagents. Chemicals in this work were used as-obtained: bismuth oxide (99.999%, Aldrich), bismuth metal (99.5%, 325 mesh, Alfa Aesar), selenium pellets (99.99%, American Elements), and copper metal (99.999%, 100 mesh, Alfa Aesar).

Synthesis

Bi₂O₂Se. A molar ratio of 2:2:3 of Bi₂O₃:Bi:Se were combined and homogenized before loading into an alumina crucible. The crucible was placed in a 15 mm (O.D.) fused silica tube, which was flame sealed under vacuum (ca. 3.0×10^{-3} mbar). The sample was heated to 300°C in four hours and soaked for six hours, then ramped to 500°C in four hours and soaked for 12 hours before furnace cooling. The sample was then re-homogenized and annealed at 500°C for eight hours. Powder X-ray diffraction (PXRD) shows that the sample is bulk phase pure.

Cu₂Se. A molar ratio of 2:1 of Cu:Se were combined and homogenized before loading into a 9 mm (O.D.) fused silica tube, which was flame sealed under vacuum (ca. 3.0×10^{-3} mbar). The sample was heated to 900°C in 12 hours and soaked for 48 hours before furnace cooling to room temperature. No unreacted copper or selenium is present in the final product. The Cu₂Se starting material was confirmed as a 60:40 molar ratio of α - and β -Cu₂Se, respectively.

Starting Material Preparation for In Situ Synchrotron Powder Diffraction (PXRD)

The starting materials were ground, sieved (<45 μ m), and subsequently thoroughly mixed. The Bi₂O₂Se : Cu₂Se were combined in a 1:1 molar ratio, while Bi₂O₃ : Bi : Cu : Se were in a 1:1:3:3 molar ratio. Mixtures were then packed into 0.5 mm diameter fused silica capillaries, which

were flame sealed under vacuum (ca. 3.0×10^{-3} mbar). All capillaries were carbon coated to prevent glass attack.

Physical Measurements

High-Resolution In Situ PXRD with Synchrotron Radiation. *In situ* synchrotron powder diffraction data was collected using beamline 17-BM-B at the Advanced Photon Source (APS), Argonne National Laboratory using an average wavelength of 0.24125 Å. An electrical resistance furnace⁴¹ was used to heat the capillaries to 500°C with a heating rate of 100°C/hr and a soaked at max temperature for three hours. Data was collected every minute using a PerkinElmer a-Si C-window detector at a distance of 700 mm. LaB₆ was used as a standard to refine the sample-to-detector distance and imaging plate tilt relative to the beam. Each PXRD pattern is a sum of twenty 0.5-second exposure frames, with a dark frame collected between each PXRD pattern. Samples were rastered during collection to increase measured sample size and decrease effects of preferred orientation. All raw images were processed in GSAS II.¹⁰⁵ Sequential multi-phase Rietveld refinements were performed up to 250°C on heating and after 400°C on heating. Between 250°C and 400°C, the refinements were unstable due to the number of phases present; consequently, only Le Bail method was used in this temperature range.

Differential Thermal Analysis. Differential thermal analysis (DTA) was performed using a Netzsch STA 449 F3 Jupiter simultaneous thermal analysis (STA) instrument. Samples were loaded into carbon-coated fused silica tube and flame-sealed under vacuum (ca. 3×10^{-3} mbar). Samples were heated to 650°C before cooling to room temperature. The rate for cooling and heating was set to 100°C/hr to mirror the synthetic conditions.

In-Situ Powder X-ray Diffraction. A STOE STADI MP high-resolution diffractometer with

an oven attachment (STOE HT) was used to collect temperature-dependent data. The diffractometer was equipped with an asymmetric curved Germanium monochromator and one-dimensional silicon strip detector (MYTHEN2 1K from DECTRIS). Elemental copper, selenium, and bismuth were sieved ($<65\ \mu\text{m}$) and mixed in proportions of $2\text{Cu} + \text{Se}$ and $2\text{Bi} + 3\text{Se}$. As a result of attenuation and to maximize signal-to-noise ratios, the Bi-Se mixture was diluted to 75 wt% using glassy carbon. The Cu-Se mixture was packed into a 0.5 mm diameter quartz capillary, while the Bi-Se diluted mixture was packed into a 0.3 mm diameter quartz capillary. Both capillaries were flame sealed under vacuum (ca. 3.0×10^{-3} mbar). Diffraction data was collected every 25°C up to 580°C for the Cu-Se system and every 20°C up to 640°C for the Bi-Se system using pure- $\text{AgK}\alpha_1$ radiation ($0.55941\ \text{\AA}$) operated at 50 kV and 50 mA. Samples were heated at a rate of $4^\circ\text{C}/\text{min}$ and a dwell time at max temperature of less than 30 minutes. Temperature stability is typically 0.1°C . Samples were spun during collection. The instrument was calibrated against a NIST Silicon standard (640d) prior the measurement.

Computational Methods

The Vienna *Ab initio* Simulation Package (VASP)¹¹³⁻¹¹⁴ was used to perform density functional theory (DFT) calculations in this work. The projector augmented wave (PAW) method¹¹¹⁻¹¹² and the Perdew–Burke–Ernzerhof (PBE) exchange-correlation functional¹¹⁵ were applied and 520 eV were chosen as the cutoff energy for the plane wave basis set. The Brillouin zone was sampled using a Γ -centered k-mesh with ≈ 8000 k-points per reciprocal atom (KPPRA). The Open Quantum Material Database (OQMD)^{100, 116} was used for convex hull construction¹⁷⁹⁻¹⁸⁰. The structures were fully relaxed until the total energy was converged to 10^{-8} eV and the force on each atom was less than $0.001\ \text{eV}/\text{\AA}$. Phonon calculations were performed with the $2\times 2\times 2$

supercell for Bi_3Se_4 and Bi_2Se_3 and $3\times 3\times 3$ supercell for Bi using the PHONOPY package¹⁸¹.

4.4. Results and Discussion

To understand the step-by-step reaction pathway to BiOCuSe , panoramic syntheses experiments were conducted using *in situ* synchrotron PXRD. This highly attenuating material necessitated synchrotron radiation in order to have optimal radiation penetration; moreover, the capabilities at Argonne National Laboratory's 17-BM-B at the Advanced Photon Source enabled simultaneous heating and fast diffraction collection. Two synthetic routes are commonly employed to synthesize BiOCuSe : the reaction of elementary precursors $\text{Bi}_2\text{O}_3 : \text{Bi} : 3\text{Cu} : 3\text{Se}$ and that of complex precursors $\text{Bi}_2\text{O}_2\text{Se} : \text{Cu}_2\text{Se}$ (referred to here as the ternary-binary reaction). The elementary precursor route is most frequently selected; this route is paired with a wide range of synthetic conditions, including maximum temperatures ranging from $300 - 750^\circ\text{C}$ and soaking times of 6 to 48 hours.^{165, 167, 182-183} Often, the products are subsequently annealed or sintered at high temperatures ($>600^\circ\text{C}$). Time-saving methods for this route have been explored by exchanging the typical solid-state reaction with self-propagating high-temperature synthesis (SHS).¹⁸⁴⁻¹⁸⁵ This method uses an ignition source (e.g. ignition flame or current) and yields the final product in minutes. Yang, et al. observed $\text{Bi}_2\text{O}_2\text{Se}$ as an intermediate in the SHS reaction, which then reacted with Cu_2Se to form BiOCuSe . This ternary-binary reaction of complex precursors ($\text{Bi}_2\text{O}_2\text{Se} + \text{Cu}_2\text{Se}$) has also been conducted via typical solid-state reaction at a maximum temperature of 500°C and soaking time of 24 hrs.¹⁸⁶ To monitor the two synthetic routes, both the ternary-binary reaction and elementary precursor routes for BiOCuSe are investigated and compared.

The Ternary-Binary Reaction to BiOCuSe

The reaction $\text{Bi}_2\text{O}_2\text{Se} + \text{Cu}_2\text{Se}$ commences with the conversion of $\alpha\text{-Cu}_2\text{Se}$ into high-temperature $\beta\text{-Cu}_2\text{Se}$. The Cu_2Se precursor began as a 60:40 molar ratio of $\alpha\text{-}$ and $\beta\text{-Cu}_2\text{Se}$, respectively, until the binary fully converts by 145°C . Figure 24a displays the VT-PXRD heat map of the reaction as well as the thermal data from Differential Thermal Analysis (DTA), while Figure 24b highlights the phase evolution in relative moles of $\alpha\text{-Cu}_2\text{Se}$ to $\beta\text{-Cu}_2\text{Se}$. In this phase change, the monoclinic $\alpha\text{-Cu}_2\text{Se}$ becomes super-ionic as it evolves into the cubic $\beta\text{-Cu}_2\text{Se}$.¹⁸⁷⁻¹⁸⁹ The copper cations disorder and increase in mobility, an advantageous feature for the formation of the target quaternary. This gradual phase transformation is not detected by DTA (heating rate of 100°C/hr) as indicated by the absence of a thermal peak near 145°C , indicating that the transformation is not appreciably exothermic.

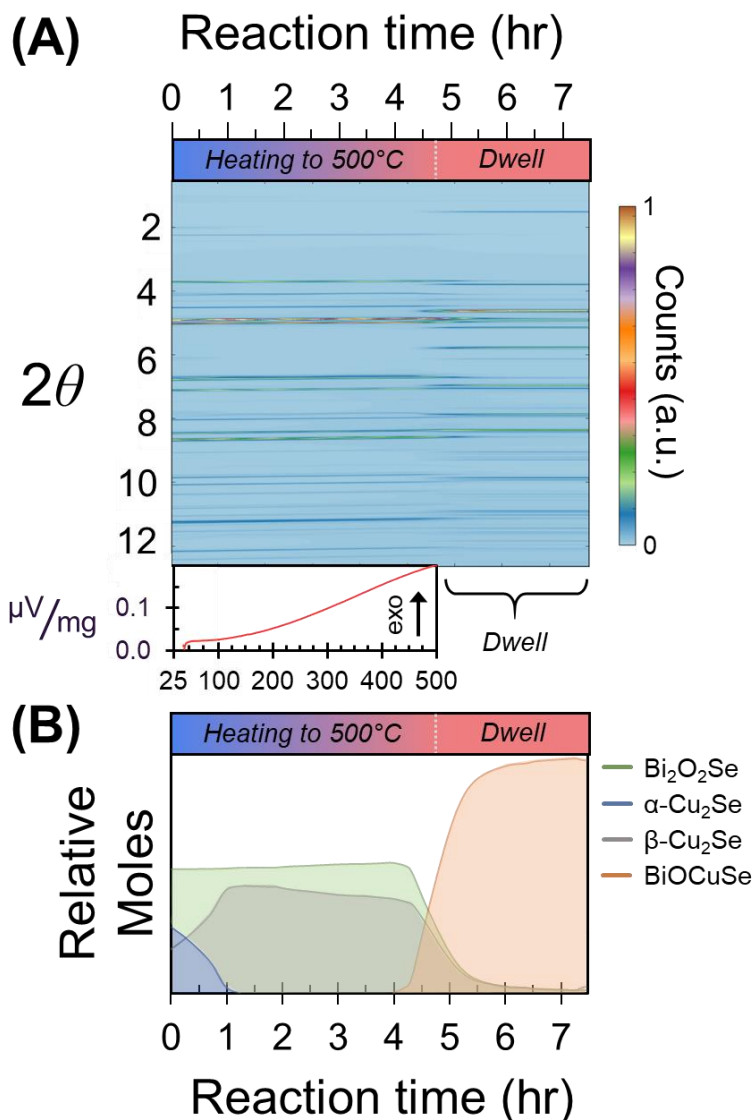


Figure 24: (a) In situ VT-PXRD for the reaction of $\text{Bi}_2\text{O}_2\text{Se} + \text{Cu}_2\text{Se}$. Below is the DTA of the heating portion of the reaction, which is intentionally aligned with the heat map and reaction map to show the corresponding temperatures in the reaction. (b) Reaction map of $\text{Bi}_2\text{O}_2\text{Se} + \text{Cu}_2\text{Se}$, comparing the relative moles of each material over the duration of the reaction. A combination of $\alpha\text{-Cu}_2\text{Se}$ and $\beta\text{-Cu}_2\text{Se}$ are present at the start of the reaction and, as temperature increases the $\alpha\text{-Cu}_2\text{Se}$ fully converts to the high temperature $\beta\text{-Cu}_2\text{Se}$ polymorph. Upon further heating, $\text{Bi}_2\text{O}_2\text{Se}$ and $\beta\text{-Cu}_2\text{Se}$ react to form the target quaternary, BiOCuSe .

The reaction proceeds with no intermediates to bulk phase pure (>90%) BiOCuSe from $\text{Bi}_2\text{O}_2\text{Se} + \beta\text{-Cu}_2\text{Se}$ at 440°C after dwelling for 50 minutes at 500°C (Figure 24). The DTA reveals

there is no detectable enthalpic event for the formation of BiOCuSe. The cubic β -Cu₂Se is an anti-fluorite structure with disordered Cu⁺ in the tetrahedral holes (**Figure 25**). The Cu-Se bond length at 390°C before BiOCuSe formation is 2.411(5) Å with a Se-Cu-Se bond angle of 118.22(17)°. The Bi₂O₂Se structure, on the other hand, comprises of [Bi₂O₂]²⁺ layers between planar square arrays of Se²⁻ (**Figure 25**). Already within this heteroanionic ternary compound, the segregated layers expected based on HSAB theory are present. In Bi₂O₂Se at 390°C, the distorted OBi₄ tetrahedra have Bi-O bond lengths of 2.3302(4) Å and O-Bi-O bond angles of 72.750(13)°. The reaction of Bi₂O₂Se + β -Cu₂Se to form BiOCuSe can be considered a melding of the precursor structures. The tetrahedral Cu⁺ ions combine with the selenium arrays in Bi₂O₂Se to form a [Cu₂Se₂]²⁺ covalent layer, while the insulating [Bi₂O₂]²⁻ layer is largely retained in the final structure. These structural similarities are reflected in the bond lengths and angles of BiOCuSe compared to the precursors, as the quaternary oxide layer has Bi-O lengths of 2.379(9) Å and O-Bi-O bond angles of 72.2(4)° at 445°C, while the chalcogenide layer has Cu-Se bond lengths of 2.532(17) Å and Se-Cu-Se bond angles of approximately 113°. The formal oxidation states of copper, bismuth and selenium in the precursor compounds are the same as the ones in the target compound (Cu⁺, Bi³⁺, Se²⁻), and as expected nowhere in the reaction path is there a change in oxidation state. The oxidation states situation, however, is different in the following reaction type.

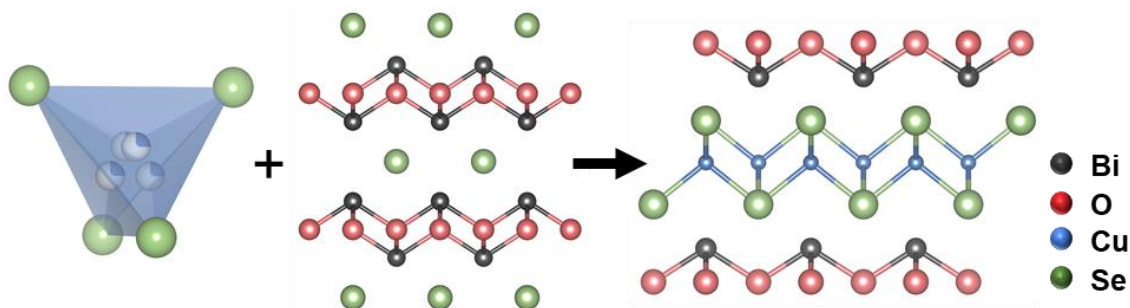


Figure 25: Reaction pathway of β -Cu₂Se + Bi₂O₂Se into BiOCuSe.

BiOCuSe Synthesis through Elementary Precursors

The reaction with elemental precursors, $\text{Bi}_2\text{O}_3 + \text{Bi} + 3 \text{Cu} + 3 \text{Se}$, is significantly more complex than the above reaction type and harbored several surprises. It begins with the crystallization of the originally amorphous selenium, followed by the formation of a particular copper selenide, CuSe, as shown in the heat map of the VT-PXRD (Figure 26). Multiphase, sequential Rietveld refinements show that selenium begins to crystallize at ca. 90°C. The amount of amorphous selenium is deduced by subtracting the current moles of crystalline selenium from the maximum moles that is present in the reaction. This gradual crystallization event is reflected in the DTA as a broad peak and a 93.8(1)°C onset (Figure 26). It should be noted that shortly thereafter a sudden change in relative moles appears between 100 – 120°C and is likely a result of powder drift within the capillary. Following this, the CuSe binary (space group $P6_3/mmc$) forms, but does not appear in the DTA and thus is not appreciably exothermic. This hexagonal structure appears starting at 145°C alongside the consumption of elemental copper and selenium. As shown in Figure 28, the atoms in face-centered packed Cu^0 react with the helical, polymeric chains of Se^0 to form the binary CuSe comprised of trigonal planar CuSe and tetrahedral Cu_2Se_2 layers, Se^{2-} and Se_2^{2-} species and formally mixed valent $\text{Cu}^{+/2+}$ centers.¹⁹⁰ Remnants of the polymeric nature of selenium can be seen in the Se_2^{2-} anions attached to the tetrahedral copper atoms in CuSe. The structure connects the alternating layers by a shared selenium. As the melting point of selenium approaches (~220°C), the disappearance of elemental copper and selenium into CuSe accelerates.

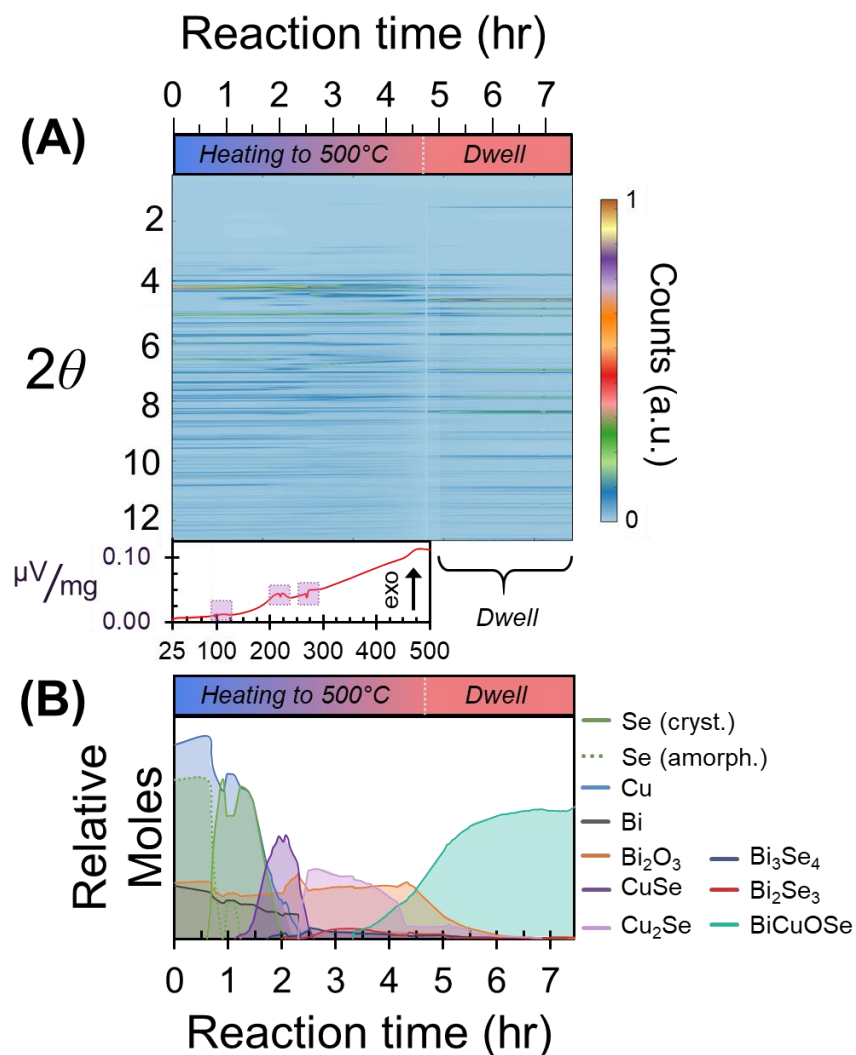


Figure 26: (a) In situ VT-PXRD for the reaction of $\text{Bi}_2\text{O}_3 + \text{Bi} + 3\text{Cu} + 3\text{Se}$. Below is the DTA of the heating portion of the reaction, which is intentionally aligned with the heat map and reaction map to show the corresponding temperatures in the reaction. The thermal signals have been highlighted in the DTA graph for clarity. (b) Reaction map of $\text{Bi}_2\text{O}_3 + \text{Bi} + 3\text{Cu} + 3\text{Se}$, comparing the moles of each material over the course of the reaction.

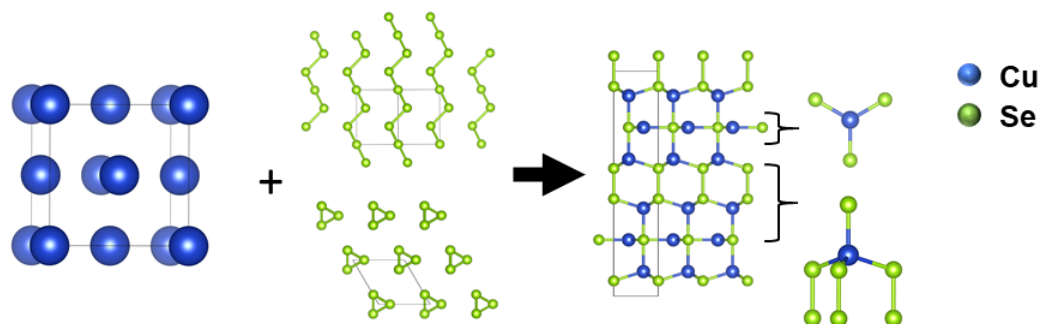


Figure 27: Schematic pathway of $\text{Cu} + \text{Se} \rightarrow \text{CuSe}$.

The formation of higher-valent CuSe, instead of monovalent Cu_2Se , is a surprising occurrence. It can be rationalized, however, using stability and stoichiometric considerations. The thermodynamic stability of all potential copper selenide binaries can be assessed theoretically using DFT calculations, couple with an energy convex hull construction.¹⁷⁹⁻¹⁸⁰ This calculation determined that only three binaries lie on the convex hull: CuSe_2 , CuSe , Cu_3Se_2 . All polymorphs of Cu_2Se lie above the convex hull. The Cu_2Se polymorph with the lowest formation energy is the hypothetical $P2_1$ structure, which lies 30 meV/atom above the hull; thus, the three aforementioned binaries are more probable to form than Cu_2Se . The formation of CuSe over CuSe_2 and Cu_3Se_2 , is rationalized by the 1:1 stoichiometric loading of copper and selenium.

To investigate further the formation of CuSe as the first copper-selenium binary, we performed DFT calculations of the (A) $\text{Cu} + \text{Se} \rightarrow$ and (B) $2\text{Cu} + \text{Se} \rightarrow \text{Cu}_2\text{Se}$ reactions. The respective reaction energies are -26.80 kJ/mol CuSe and -28.21 kJ/mol Cu_2Se . As the values are still relatively close, we conducted panoramic synthesis on $2\text{Cu} + \text{Se}$ to monitor the reaction progression, which yielded the heat map shown in Figure S14. Despite the low signal-to-noise, a similarly progression is observed as in the quaternary reaction. Selenium begins to crystallize at ca. 90°C (Figure S16). Copper and selenium persist as the only two reactants present until two phases concurrently grow starting at ca. 180°C. These phases are the comparatively copper-poor

CuSe₂ and CuSe (Figure S17).

Here, the identity of the binary formed is not dictated by stoichiometry; rather, the selenium appears able to solubilize copper thus producing selenium-rich phase compared to Cu₂Se. Notably, both CuSe and CuSe₂ both maintain remnants of the selenium polymeric chains by way of selenium dimers within the structures. At ca. 250°C, CuSe₂ begins to disappear alongside the disappearance of elemental copper still present in the reaction and the appearance of Cu_{2-x}Se (Figure S18). This can be rationalized as two concurrent reactions of (A) CuSe₂ + Cu → CuSe and (B) CuSe + Cu → Cu_{2-x}Se until 400°C when only Cu_{2-x}Se is present in the reaction. This control experiment shows us that not only CuSe, but also CuSe₂ are inherent part of Cu₂Se formation from the elements.

As the reaction proceeds and the melting point of selenium is progressively approached, selenium and bismuth begin to react to form Bi₃Se₄ between 175 and 190°C (Figure 26). The Bi⁰ atoms combine with the polymeric chains of Se⁰ into covalently bonded layers comprised of planar septuple sheets (e.g. Se-Bi-Se-Bi-Se-Bi-Se), as illustrated in Figure 28a. The structure of Bi₃Se₄ is closely related to that of Bi₂Se₃ but features septuple instead of quintuple sheets.

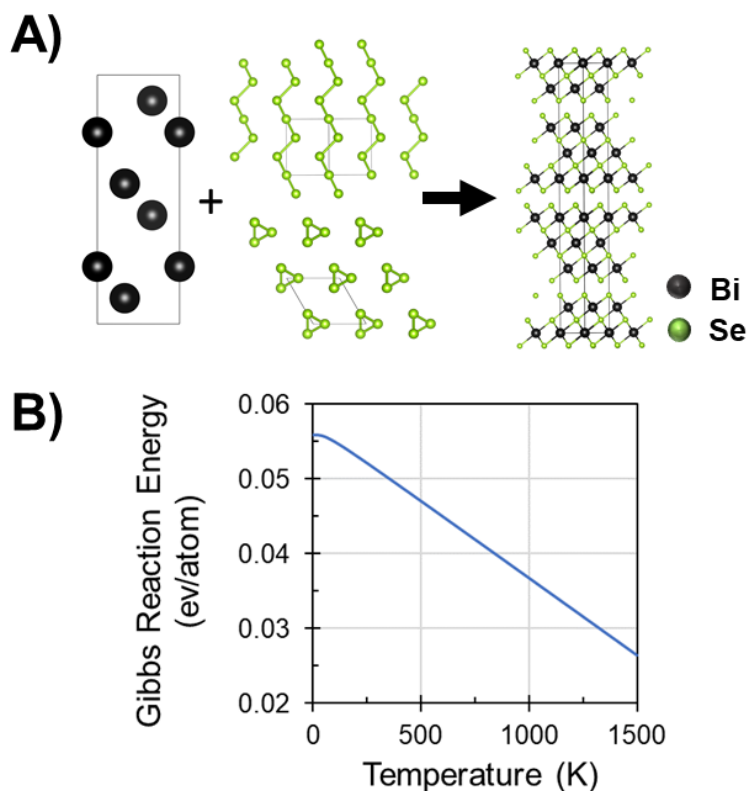


Figure 28: (a) Reaction pathway of $\text{Bi} + \text{Se} \rightarrow \text{Bi}_3\text{Se}_4$. (b) Gibbs reaction energy of $4\text{Bi}_2\text{Se}_3 + \text{Bi} \rightarrow 3\text{Bi}_3\text{Se}_4$ calculated at increasing temperatures to determine the stability of Bi_3Se_4 . Positive Gibbs reaction energy values indicate the reverse reaction (i.e. the decomposition of Bi_3Se_4) is spontaneous, while negative values indicate the spontaneous formation of Bi_3Se_4 .

The formation of low-valent Bi_3Se_4 instead of trivalent Bi_2Se_3 is also a surprising occurrence. The DFT energetics of these compounds provide some insight. The formation energies of Bi_3Se_4 and Bi_2Se_3 are -0.32 eV/atom and -0.39 eV/atom, respectively. According to the Open Quantum Materials Database (OQMD)¹⁰⁰, Bi_2Se_3 is on the convex hull (i.e. stable), while Bi_3Se_4 is 60 meV/atom above the convex hull at $T = 0$ K. Hence, the Bi-rich binary is energetically unstable with respect to decomposition into Bi_2Se_3 and Bi metal ($3\text{Bi}_3\text{Se}_4 \rightarrow \text{Bi} + 4\text{Bi}_2\text{Se}_3$). To investigate if this thermodynamic preference for Bi_2Se_3 persists at higher temperatures, we must compute the entropic contributions to the free energy. One such contribution is the vibrational

entropy, which can be obtained from a calculation of the harmonic phonon density of states (we use the PHONOPY package¹⁸¹). Including these entropic contributions, the free energy of the reaction, $4\text{Bi}_2\text{Se}_3 + \text{Bi} \rightarrow 3\text{Bi}_3\text{Se}_4$, remains positive through the entire temperature range of 0 K to 1500 K, as shown in Figure 28Figure **28b**. Hence, the Bi_3Se_4 intermediate phase formed is thermodynamically unstable with respect to Bi_2Se_3 for all temperatures considered. The presence of this intermediate phase in the experimental synthesis indicates it is metastable.

The formation of Bi_3Se_4 preceding that of Bi_2Se_3 can be thus considered a result of kinetically-controlled competing reactions for selenium-uptake. The reaction loading ratio of Bi : Se : Cu is 1:3:3; where the Cu and Bi are in competition for selenium. Not only are the two cations in competition for selenium, but selenium also preferentially and rapidly bonds with copper over bismuth according to HSAB theory. Therefore, the copper depletes the reaction medium of selenium when forming CuSe , leaving it selenium-poor. As Bi_3Se_4 sequesters less selenium per bismuth atom than Bi_2Se_3 , it is consequently advantageous to form the relatively selenium-poor bismuth binary over Bi_2Se_3 .

Notably, when tracking the evolution of Bi_3Se_4 and the associated structural changes, anisotropic negative thermal expansion is observed within a relatively narrow range of ca. 270°C to ca. 375°C in the a- and b-directions, as shown in Figure **30**. The maximal coefficient of negative thermal expansion along these two axes can be calculated using $\frac{l_{T_2} - l_{T_1}}{l_{T_2}(T_2 - T_1)}$, where l is the cell edge at T_1 or T_2 , and is found to be $\alpha_a = -3.6 \times 10^{-5} \text{ K}^{-1}$. (The full description of the calculation using the a-axis as the cell edge and a table of values are presented in Table S1.) Negative thermal expansion has been observed in oxides,¹⁹¹⁻¹⁹² zeolites,¹⁹³⁻¹⁹⁴ nitrides,¹⁹⁵ and other two dimensional materials, such as Ruddlesden-Popper layered perovskites¹⁹⁶, graphene,¹⁹⁷ and silicene¹⁹⁷⁻¹⁹⁸. Other

chalcogenides, such as ZnCr_2Se_4 , CdCr_2S_4 , and $\text{Sm}_{0.67}\text{Y}_{0.33}\text{S}$, have also demonstrated negative thermal expansion; however, these materials present lower thermal expansion coefficients and at lower temperatures (ZnCr_2Se_4 : $-0.36 \times 10^{-5} \text{ K}^{-1}$ between 21–40 K;¹⁹⁹ CdCr_2S_4 : $-0.18 \times 10^{-5} \text{ K}^{-1}$ between 4.2–120 K;²⁰⁰ and $\text{Sm}_{0.67}\text{Y}_{0.33}\text{S}$: $-3.0 \times 10^{-5} \text{ K}^{-1}$ between 10–255 K). The origins of negative thermal expansion are often an interplay between lattice, electrons, and phonons²⁰¹ and the precise origins for this material are beyond the purview of this study, though show potential for future investigations.

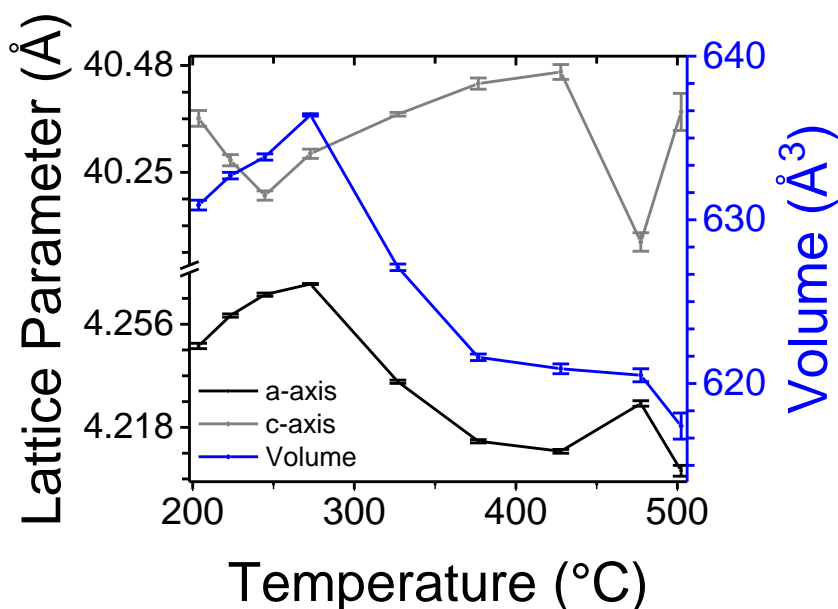


Figure 29: Lattice parameter and volume changes in Bi_3Se_4 as the reaction progresses. By symmetry, the a and b axes are equivalent.

Concurrent with selenium's melting temperature, Bi_2Se_3 begins to appear. The DTA shows a sharp endothermic peak at $219.5(1)^\circ\text{C}$ with an onset at $214.9(1)^\circ\text{C}$; the endothermic nature of the peak indicates that the melting of selenium is the origin of this peak as opposed to the near simultaneous formation of Bi_2Se_3 at 220°C . As the accessibility and mobility increase upon melting, the "selenium-rich" Bi_2Se_3 is able to form. Notably, the bismuth-rich binary, Bi_3Se_4 , does

not decompose for Bi_2Se_3 to appear in the reaction. In fact, the amount of Bi_3Se_4 increases parallel to that of Bi_2Se_3 . A similar control *in situ* experiment was attempted to determine if Bi_3Se_4 is a natural intermediate phase to Bi_2Se_3 (Figure S20). However, as the ordering reflections are the primary difference in the diffractograms of the Bi-Se binaries (Figure S21), the experiment was unable to conclusively determine the presence of intermediate phases. The heat map of the reaction (Figure S20) does indicate one of the phases undergoes negative thermal expansion, which suggests that one of the bismuth-rich binaries may be an intermediate phase.

Between 235°C and 245°C , CuSe and Cu begin to disappear and, by 275°C , are no longer present in the reaction. Cu_2Se rapidly forms starting at ca. 260°C as CuSe and Cu correspondingly disappear. The melting of bismuth is abrupt as seen in the heat map (Figure 26) and as an endothermic peak in the DTA at $269.0(1)^\circ\text{C}$ with an onset at $268.0(1)^\circ\text{C}$. Interestingly, the formation of Bi_3Se_4 and Bi_2Se_3 do not notably accelerate upon the melting of bismuth. Overall, the phase largely plateau until BiOCuSe consumes them for its formation.

The target material, BiOCuSe , begins to form at 430°C and is a gradual process as seen by the broad thermal event in the DTA with an onset at $455.9(1)^\circ\text{C}$. Four binaries are still present as BiOCuSe forms: Bi_2O_3 , Bi_3Se_4 , Bi_2Se_3 , Cu_2Se . By the end of the reaction, these intermediates are consumed and there is 98.9% conversion to BiOCuSe . Notably, this experiment reveals the absence of $\text{Bi}_2\text{O}_2\text{Se}$ as an intermediate phase, although this compound can serve as a precursor to the synthesis of BiOCuSe as described above. Similar to the ternary-binary reaction, the oxide present in this reaction, Bi_2O_3 , can be considered the scaffold in the oxide layer in BiOCuSe .

Bi_2O_3 , when viewed along the $[010]$ as shown in Figure 30a, comprises of alternating sheets of bismuth and oxygen parallel to the c -axis,²⁰² with five-coordinate bismuth in a pseudo-

square pyramidal geometry. These polyhedra are then connected into a three-dimensional framework via corner and edge sharing. The expressed $6s^2$ bismuth lone pair points into the open columns that are parallel to the c-axis in Bi_2O_3 (Figure 30a) and, in BiOCuSe , the lone pairs will be directed between the oxide and chalcogenide layers, nestled between the selenium atoms. To transform the polyhedra in Bi_2O_3 into the required coordination in the $[\text{Bi}_2\text{O}_2]^{2+}$, the apical oxygen must be relinquished and imparted to the chalcogenide bound bismuth in Bi_2Se_3 and Bi_3Se_4 as illustrated in Figure 30b. The distorted BiSe_6 octahedra will have the largest transformation from complete coordination sphere of selenide bonding to oxide. The copper selenide, as in the $\text{Bi}_2\text{O}_2\text{Se} + \text{Cu}_2\text{Se}$ reaction above, is well situated to be incorporated into the target quaternary as the copper is already present in the final tetrahedral coordination in this high temperature cubic phase.

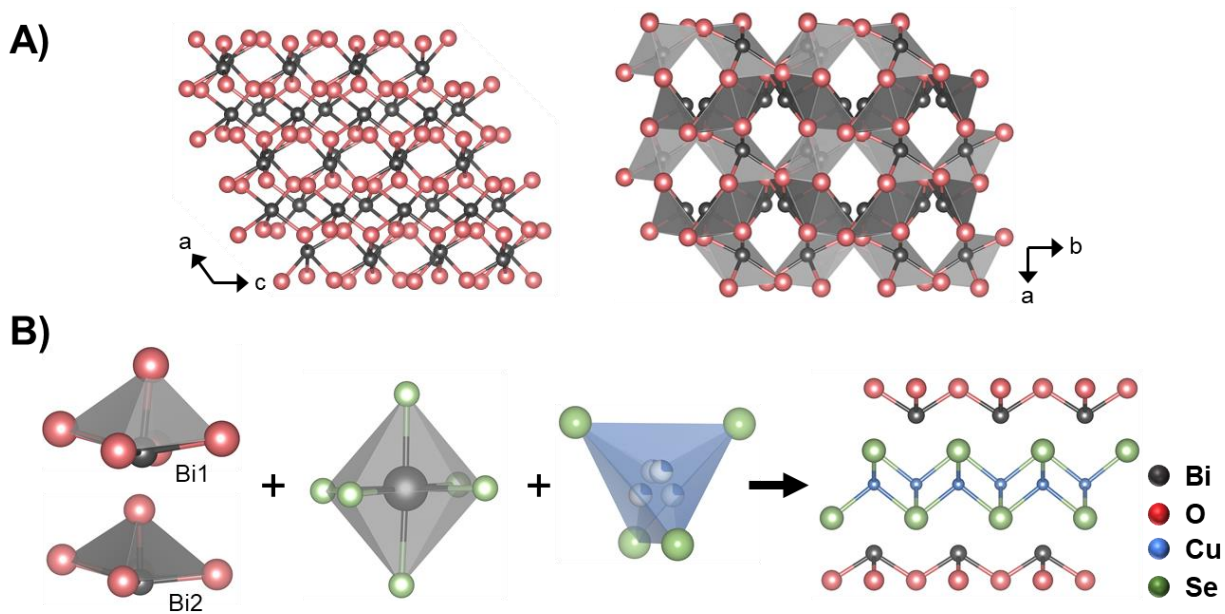


Figure 30: (a) Structure of Bi_2O_3 , represented as ball-and-stick and polyhedra. The ball-and-stick representation is viewed down the b-axis and highlights the alternating sheets of bismuth and oxygen in the material. The polyhedra, viewed down the c-axis, highlights the bismuth lone pair expression into the material's columns running parallel to the c-axis. (b) Coordination spheres for the reaction of Bi_2O_3 , Bi_2Se_3 , Bi_3Se_4 , and Cu_2Se to form BiOCuSe .

Reaction Comparison

The two reaction types can be viewed as being different in the following manner: the first reaction uses more complex but fewer precursors, whereas the second one uses more but simpler precursors. Overall, both reaction types arrive at the same product (98.9% for the elemental precursors and 96.3% for the ternary-binary loading) while proceeding through divergent pathways. The ternary-binary $\text{Bi}_2\text{O}_2\text{Se} + \text{Cu}_2\text{Se}$ reaction involved a simple phase transformation followed by direct BiOCuSe formation. The atom coordination spheres in the target phase are already inherently scaffolded in the complex precursor materials and thus have a straightforward pathway to product formation. Contrastingly, the elemental-binary reaction progressed through multiple binary intermediates, remarkably $\text{Bi}_2\text{O}_2\text{Se}$ not being one of them, as summarized in Figure 31. The occurrence of the intermediates, CuSe and Bi_3Se_4 , is surprising because the elements in their structure are in incorrect oxidation states with respect to those present in BiOCuSe . Specifically, a portion of the selenium in CuSe is in the -1 oxidation state from the Se_2^{2-} dimers and Cu is formally mixed valent $1+/2+$, whereas the bismuth in Bi_3Se_4 is in a reduced oxidation state of +2.67. Ultimately, when the reaction progression is in its latter stages, the Bi_3Se_4 and CuSe react to adjust the incorrect oxidation states to those needed for the formation of BiOCuSe . This finding is entirely unanticipated. Two examples of this unexpected redox activity during a panoramic synthesis is in a double replacement metathesis reaction.^{79, 203} It is as if this elemental-binary reaction pathway takes a counterintuitive, circuitous route, but eventually finds its way to the final product. The authors would have liked to conduct additional studies to explore alternative binary combinations (e.g. $2\text{Bi}_2\text{O}_3 + \text{Bi}_2\text{Se}_3 + 3\text{Cu}_2\text{Se}$) or cation-anion pairs contrary to those found in the final product (e.g. $\text{Bi}_2\text{Se}_3 + \text{Bi} + 3\text{CuO}$) to determine if precursors lead to similarly

unexpected pathways, however the current COVID situation places these studies as potential future studies.

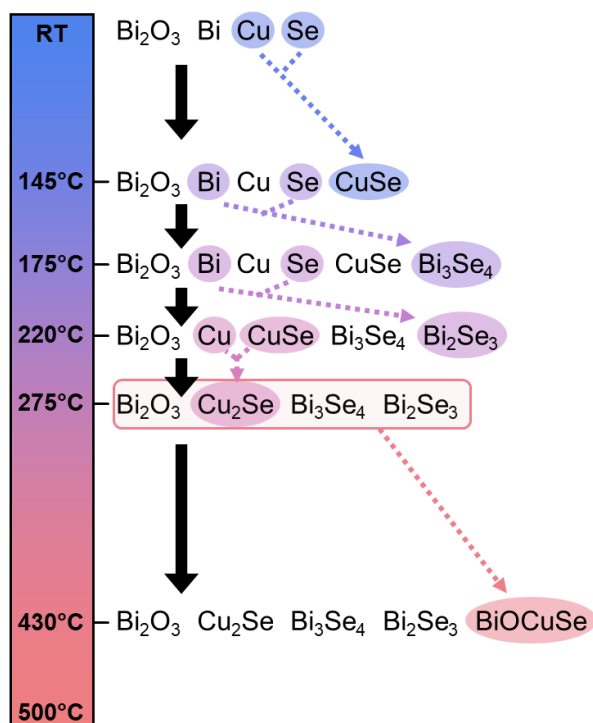


Figure 31: Summary of product formation temperatures and reaction pathway for Bi₂O₃ + Bi + 3Cu + 3Se upon heating from room temperature (RT) to maximum temperature (500°C).

Even with the structural motifs inherently present in Bi₂O₂Se and Cu₂Se, the elemental precursors formed BiOCuSe at a lower temperature and with a higher overall conversion than the complex precursors. The elemental-binary reaction forms the quaternary first at 430°C, while the ternary-binary reaction does not form the target until 440°C. Notably, the formation temperature of BiOCuSe required for both pathways is lower than that previously determined heuristically, as also observed in other *in situ* studies.³⁰

DFT corroborates the favorable formation of BiOCuSe relative to both the elemental and complex pathways. The reaction energy between BiOCuSe and the precursors is ten-fold more negative for

the elemental precursor pathway compared to that of the complex precursors (-58.6 kJ/mol BiOCuSe and -5.8 kJ/mol, respectively). The slighter lower temperature of formation via the elemental pathway may be because the complex precursors must unzip and meld their structures, whereas the elemental precursors begin with bond formation. Additionally, thermal events are observed in the DTA of the binary-elemental reaction (Figure 26a) and not in the ternary-binary synthesis (Figure 24a). These thermal events may provide additional heat to the reaction that can spur the synthesis forward, despite the greater structural reformations and diffusion requirements necessary to generate the final product from elementary precursors.

4.5. Conclusion

In situ variable temperature PXRD provides an exclusive view of reaction types and paths and can be utilized to ultimately develop strong synthetic rationales for new materials. Our panoramic synthesis results show that the ternary-binary reaction proceeded without intermediates to direct BiOCuSe formation, while the binary-elemental reaction formed many intermediates before the final product forms. These intermediates include CuSe, Cu₂Se, Bi₃Se₄, and Bi₂Se₃. Surprisingly, “selenium-rich” CuSe and “selenium-poor” Bi₃Se₄ form first, despite their incorrect oxidation states relative to their later forming counterparts (Cu₂Se and Bi₂Se₃) and the final product. While CuSe forms as a result of high stability and stoichiometric considerations, Bi₃Se₄ formation can be attributed to competition for selenium with copper in accordance with HSAB theory. This study links the selection of precursors to the reaction progression in order to establish an understanding of the effects of precursors and, ultimately, to work towards rational synthetic design for heteroanionic materials and solid-state reactions at large. The panoramic synthesis approach to unraveling the reaction paths of inorganic solids is a powerful tool in further

developing synthesis science and future rational synthetic methodologies.

**Chapter 5. Synthesis, Structure, and Electronic and Physical
Properties of the Mixed Anion Semiconductor $\text{In}_8\text{S}_{3-x}\text{Te}_{6+x}(\text{Te}_2)_3$ ($x =$
 0.18)**

5.1. Abstract

A new heteroanionic ternary, $\text{In}_8\text{S}_{3-x}\text{Te}_{6+x}(\text{Te}_2)_3$ ($x = 0.18$), was synthesized using traditional solid-state reaction methods. The compound crystallizes in the monoclinic space group $C2/c$, with lattice parameters $a = 14.2940(6)$ Å, $b = 14.3092(4)$ Å, $c = 14.1552(6)$ Å, and $\beta = 90.845(3)^\circ$. The 3D framework of $\text{In}_8\text{S}_{3-x}\text{Te}_{6+x}(\text{Te}_2)_3$ is composed of a complex 3D network of corner-connected InQ_4 tetrahedra with 3 Te_2^{2-} dumbbell dimers per formula unit. The optical band gap is 1.12(2) eV. First principles electronic structure calculations using density functional theory (DFT) indicate this material has potential as a p-type thermoelectric material as it is a narrow band gap semiconductor, incorporates several heavy elements, and has multiple overlapping bands near the valence band maximum.

5.2. Introduction

The frontiers of modern chemistry and physics is driven by the discovery and development of functional solid-state materials. Historically, many of these have had multiple cations and single cation which serve to create and control a variety of useful properties. In contrast, heteroanionic materials are underexplored due to their relative complexity and constitute the next chemical horizon to pursue in search of new materials.^{155, 161} Heteroanionic materials are those that have multiple anions, each with their own crystallographically distinct site. The anionic diversity

introduced to the material adds new dimensions of control and functionality, resulting from the different characteristics of the anions, such as charge, radii, electronegativity, and polarizability.^{155,}

¹⁶¹ The introduction of these additional anions, as well as potential structural transformations that result, offer the opportunity to capitalize on structure-property relationships. This class of materials provides the potential to combine desired properties of the individual anionic species or even yield advantageous properties inaccessible to their single-anion predecessors.^{155-157, 204}

The difference in chemical nature of the anions in heteroanionic materials often leads to ordering or layering according to hard-soft acid-base (HSAB) theory, where the anions segregate and preferentially bond with their coordinating hard or soft pair.¹⁵⁹⁻¹⁶⁰ Heteroanionic materials often consist of homoleptic polyhedra, where each cation is coordinated by a single type of anion, or heteroleptic polyhedra, where the cations are bonded to more than one type of anion. Heteroleptic bonding can occur when the metal cations are borderline soft or hard Lewis acids and the anions are of similar size (e.g. N^{3-} , O^{2-} , S^{2-} , F^-) as well as small enough to coordinate about the same metal cation. This in turn may generate irregularities in bonding, such as the lengths of metal-anion bonds, which influence local polarizations and crystal fields.^{155, 205} On the whole, the long range ordering of either of these bonding types yield global changes in the material properties.^{161,}

²⁰⁵

A particularly rich system for such exploration is that of the chalcogenides, which are well known due to the impressive structural and bonding diversity inherent to this materials class.^{18, 206-}
²⁰⁹ Heteroanionic exploration of chalcogenides can harness these features, including the tendency for sulfur, selenium, and tellurium to catenate, so beyond introducing two different anions (such as S^{2-} and Se^{2-}), oligomerized anionic units can also be introduced.²⁰⁷ The plethora of

polychalcogenide anions is vast and can introduce interesting physical properties to these materials alongside the already present new structure types. In addition to discrete anions, chalcogenides have also presented as dumbbells²¹⁰⁻²¹⁶, chains^{18, 208, 217-220}, rings^{214, 221}, nets or sheets^{209, 214, 222-223}, and cross-shaped units²²¹. The versatility of individual chalcogenides coupled with the introduction of an additional chalcogenide leads to great possibilities in what can be achieved in terms of a material's bonding and structure.

Though limited to date, the synthesis of mixed chalcogenides has been demonstrated with the heteroanionic compounds crystallizing in either the same structure type as the parent compound or in a new structure type.^{205, 224} The differences in electronegativity and size is sufficient to produce compounds with anions on distinct crystallographic sites (as opposed to solid solutions, where the anions are positionally disordered).²²⁵⁻²²⁶ In fact, it has been observed that a 10% difference in anionic size stabilizes an ordered structure as opposed to resulting in a solid solution.^{205, 227} It has also been suggested the closer the Q:Q' ratio is to unity, the higher the dimensionality of the structure; for example, a 1:1 ratio often yields a 3D lattice, 2:1 a 2D lattice, and 6:1 a 0D lattice.²⁰⁵ When the anions order, they may remain in the parent structure type or crystallize in a different structure type. Ibers and coworkers exchanged one sulfur for a tellurium in LnCuS_2 ($\text{Ln} = \text{La, Sm}$).²¹⁸ The two sulfurs in the parent structure were on independent crystallographic sites. When Te was introduced, it fully substituted for S in both compounds and preferentially bonded to Cu in accordance with HSAB theory. The resulting compound, LaCuSTe , crystallized in the same parent structure type, but SmCuSTe crystallized in a different structure type. Crystallizing in the parent structure type is also seen when substituting in the compounds $\beta\text{-US}_2$ and $\beta\text{-USe}_2$.²²⁸ More frequently a new structure type forms.^{205, 224, 229-230} There has been

limited exploration into main group elements, particularly for heteroanionic ternaries.

Herein, we describe the synthesis, structure, and properties on the indium heteroanion, $\text{In}_8\text{S}_{3-x}\text{Te}_{6+x}(\text{Te}_2)_3$, which contains the three anions S^{2-} , Te^{2-} , and Te_2^{2-} . In pursuit of a heteroanionic ternary, indium was used as it is amphoteric and therefore willing to bond with both S and Te according to HSAB theories. Additionally, as a narrow band gap semiconductor (1.12(2) eV) and incorporation of heavy elements, this compound shows promise as a thermoelectric material. Its complex structure is expected to scatter phonons and minimize lattice thermal conductivity, while its ordered, crystalline framework would maintain a high carrier mobility.

5.3. Experimental Methods

Reagents. Chemicals in this work were used as-obtained: indium metal (99.99%, American Elements), sulfur (sublimed, 99.99%, Spectrum), tellurium (99.99%, American Elements), and glassy carbon (99.9%, Aldrich).

Synthesis

Indium sulfide, InS. A 1.9542-g amount (17.02 mmol) of indium was combined with 0.5458 g (17.02 mmol) of elemental sulfur in a 9 mm (O.D.) fused silica tube. The tube was flame sealed under vacuum (10^{-3} mbar). The sample was heated to 800°C in 24 hours, soaked for 24 hours, and air quenched.

$\text{In}_8\text{S}_{2.82}\text{Te}_{6.18}(\text{Te}_2)_3$. A 0.3174-g amount (2.16 mmol) of synthesized InS was combined with 0.4826 g (3.78 mmol) of elemental tellurium in a 9 mm (O.D.) fused silica tube. The tube was flame sealed under vacuum (10^{-3} mbar). The sample was heated to 500°C in 6 hours and soaked for 24 hours before furnace cooling for batch synthesis. Single crystals were prepared using the

above procedure, but with a maximum temperature of 650°C and slow cooling at a rate of 2.75°C/min to 450°C before furnace cooling to room temperature.

Physical Measurements

Powder X-ray Diffraction. X-ray powder diffraction patterns were collected on a Rigaku Miniflex600 diffractometer with Ni-filtered Cu K α radiation (1.5406 Å) operating at 40 kV and 15 mA with a high-speed silicon strip detector. The diffraction pattern used a scan width of 0.02° and a scan rate of 10°/min. Visualization of the crystal structures was done with Vesta software.¹⁰⁴

Single Crystal X-ray Diffraction. Intensity data of a black rectangular single crystal of In₈S_{2.82}Te_{6.18}(Te₂)₃ was collected at 100(2) K. A suitable single crystal mounted on a glass fiber | with glue on a STOE StadiVari diffractometer equipped with an AXO Ag K α micro-focus sealed Xray A-MiXS source ($\lambda = 0.560834$ Å), running at 65 kV and 0.68 mA, and a Dectris Pilatus3 R CdTe 300K Hybrid Photon Counting detector. Temperature of the crystal was controlled with an Oxford Cryosystems low-temperature device. Data reduction was performed with the X-Area software package using a numerical absorption correction. The structure was solved with the ShelXT structure solution program using direct methods solution method and by using Olex2 as the graphical interface. The model was refined with ShelXL using least squares minimization.

In-Situ Powder X-ray Diffraction. A STOE STADI MP high-resolution diffractometer with an oven attachment (STOE HT) were used to collect temperature-dependent data. The diffractometer was equipped with an asymmetric curved Germanium monochromator AgK α 1 radiation ($\lambda = 0.559407$ Å) and one-dimensional silicon strip detector (MYTHEN2 1K from DECTRIS). The line focused Ag X-ray tube was operated at 40 kV and 40 mA. The starting materials were sieved (<45 μ m), mixed, and diluted using glassy carbon. Dilutions were required

to mitigate sample attenuation of the X-ray beam and, therefore, optimize the signal-to-noise ratio of the diffraction measurement. Samples were then packed into 0.3 mm diameter quartz capillaries, which were flame sealed under vacuum (ca. 3.0×10^{-3} mbar). Diffraction data was collected at 25, 100, 150, 200, 250, 300, 350, 375, 400, 425, 450, 500, and 550°C upon heating and the reverse upon cooling, with temperature stability typically at 0.1°C. The heating rate was 10.0°C/min and collection range was 2 to 22° 2 θ . Samples were spun during collection. The instrument was calibrated against a NIST Silicon standard (640d) prior to the measurement.

Optical Measurements. Optical diffuse reflectance measurements were made at room temperature with a Shimadzu UV-3600 PC double-beam, double-monochromator spectrophotometer. The measurement of diffuse reflectivity can be used to obtain values for the band gap from a powder sample at room temperature. BaSO₄ powder was used as a reference. The reflectance data was converted to absorbance using the Kubelka-Munk equation: $\alpha/S = (1 - R)^2/2R$. R is the reflectance at a given wavelength, α is the absorption coefficient, and S is the scattering coefficient. Valence band maximum energy (VBM) was measured by photoemission spectroscopy in air on a Riken-Keiki PESA AC-2. Samples are scanned under ambient conditions using UV light (4.20-6.20 eV). The number of photoelectrons generated at each excitation energy is measured and the VBM is the onset of the PESA spectra, as photoelectrons are only generated when the photon energy is higher than the VBM energy. Conduction band minimum energies are found by subtracting the optical band gap from the VBM energy.

Differential Thermal Analysis. Differential thermal analysis (DTA) was performed using a Netzsch STA 449 F3 Jupiter simultaneous thermal analysis (STA) instrument. Samples were loaded into a fused silica tube and flame-sealed under vacuum (ca. 3×10^{-3} mbar). Samples were

heated to 750°C and cooled to room temperature. The rate for cooling and heating was set to 10°C/min.

Computational Methods

All density functional theory (DFT) calculations are performed using the Vienna ab initio simulation package (VASP)¹¹³⁻¹¹⁴ along with the projector augmented wave (PAW)¹¹¹⁻¹¹² method to performed the density functional theory (DFT)^{[4][5]} calculations. The Perdew-Burke-Ernzerhof (PBE)¹¹⁵ generalized gradient approximation (GGA) was used as the exchange-correlation functional. The $x=0$ structure $\text{In}_8\text{S}_3\text{Te}_{12}$ structure was constructed by letting the S/Te mixing sites fully occupied by S atoms, resulting in an ordered 46-atom unit cell. The plane wave cutoff energy was set as 520 eV and the structure was fully relaxed until the total energy converged to within 10^{-8} eV and the force on each atom was less than 10^{-3} eV/Å. We sampled the Brillouin zone using gamma-centered k-point meshes of $6 \times 6 \times 5$ for the unit cell $\text{In}_8\text{S}_3\text{Te}_{12}$. Phonon calculations were performed with the $1 \times 1 \times 1$ unit cell using the PHONOPY package¹⁸¹. The transport properties were calculated using the semiclassical Boltzmann transport theory implemented in the BoltzTraP²³¹ package.

5.4. Results and Discussion

$\text{In}_8\text{S}_{2.82}\text{Te}_{12.18}$ was discovered in search of the In-analogue to the mixed chalcogenide, $\text{Ga}_2\text{S}_2\text{Te}$. Our synthesis approach for $\text{Ga}_2\text{S}_2\text{Te}$ used GaS and Te as starting materials. Therefore, the analogous binary InS was used targeting $\text{In}_2\text{S}_2\text{Te}$. By systematically increasing the amount of tellurium present in the reaction, $\text{In}_8\text{S}_{2.82}\text{Te}_{12.18}$ was discovered. Single crystals were grown after making a bulk phase pure batch and running thermal analysis (Figure S22), which in turn allowed

for an optimal heating profile to be used.

Single-crystal X-ray diffraction reveals that $\text{In}_8\text{S}_{2.82}\text{Te}_{12.18}$ crystallizes in the monoclinic space group $C2/c$, with lattice parameters $a = 14.2940(6)$ Å, $b = 14.3092(4)$ Å, $c = 14.1552(6)$ Å, and $\beta = 90.845(3)^\circ$ at room temperature (Table 1, Table S17-

Table S20). The structure of $\text{In}_8\text{S}_{2.82}\text{Te}_{12.18}$ is comprised of a complex 3D network of corner-connected InQ_4 tetrahedra with 3 Te_2^{2-} dumbbell dimers per formula unit, as shown in Figure 32. There are 4 distinct tetrahedral sites, each of which has 3 Te vertices and 1 S vertex, and these tetrahedra are corner-connected to neighboring tetrahedra as well as bridged by Te_2^{2-} .

Table 1: Crystal data and structure refinement for $\text{In}_8\text{S}_{2.82}\text{Te}_{12.18}$ at 100 K.

Empirical formula	$\text{In}_8 \text{S}_{2.82} \text{Te}_{12.18}$
Formula weight	2563.38
Temperature	100 K
Wavelength	0.56083 Å
Crystal system	Monoclinic
Space group	$C2/c$
Unit cell dimensions	$a = 14.2940(6)$ Å, $\alpha = 90^\circ$ $b = 14.3092(4)$ Å, $\beta = 90.845(3)^\circ$ $c = 14.1552(6)$ Å, $\gamma = 90^\circ$
Volume	2894.93(19) Å ³
Z	4
Density (calculated)	5.881 g/cm ³
Absorption coefficient	9.750 mm ⁻¹
F(000)	4282
θ range for data collection	2.246 to 27.863°
Index ranges	$-23 \leq h \leq 23$, $-23 \leq k \leq 23$, $-23 \leq l \leq 23$
Reflections collected	94832
Independent reflections	7021 [$R_{\text{int}} = 0.0937$]
Completeness to $\theta = 19.664^\circ$	99.9%
Refinement method	Full-matrix least-squares on F^2
Data / restraints / parameters	7021 / 0 / 106
Goodness-of-fit	1.031
Final R indices [$I > 2\sigma(I)$]	$R_{\text{obs}} = 0.0433$, $wR_{\text{obs}} = 0.1108$
R indices [all data]	$R_{\text{all}} = 0.0520$, $wR_{\text{all}} = 0.1166$
Largest diff. peak and hole	3.305 and -4.804 e ⁻ ·Å ⁻³

$R = \frac{\sum ||F_o| - |F_c||}{\sum |F_o|}$, $wR = \left\{ \frac{\sum [w(|F_o|^2 - |F_c|^2)^2]}{\sum [w(|F_o|^4)]} \right\}^{1/2}$ and $w = 1/[\sigma^2(F_o^2) + (0.0786P)^2]$ where $P = (F_o^2 + 2F_c^2)/3$

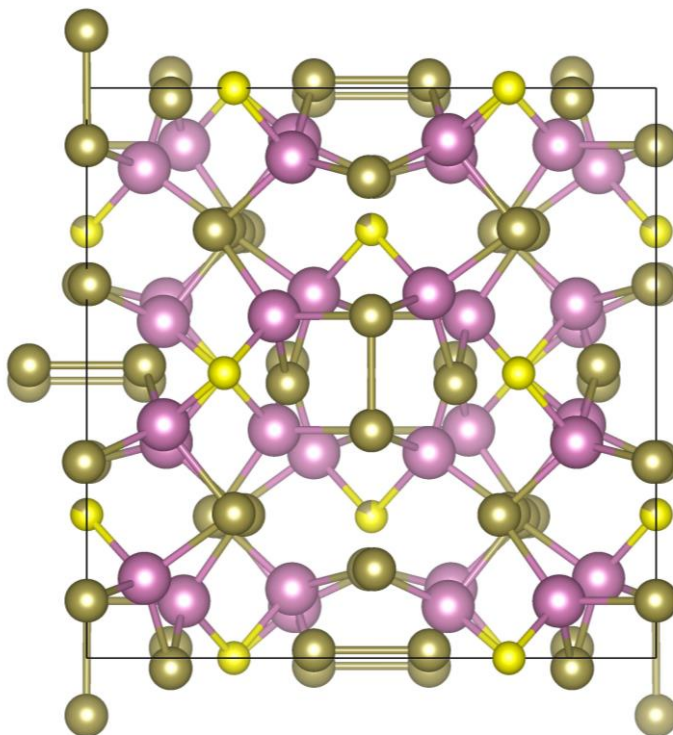


Figure 32: Crystal structure of $\text{In}_8\text{S}_{2.82}\text{Te}_{12.18}$ viewed down the c -axis. Purple spheres are indium, yellow sulfur, and brown tellurium.

The Te-Te bond lengths for the 3 distinct sites Te02, Te04, and Te07 are 2.9246(9) Å, 2.8917(9) Å, and 2.9030(6) Å, respectively; these lengths are similar to those of previous examples of compounds with only Te-Te dimers (2.70 – 2.86 Å)^{208, 214} as well as with a mixture of individual tellurium anions and chains (2.74 – 2.82 Å)²¹⁵⁻²¹⁶. The vertices of these Te_2^{2-} dimers are three-coordinate, sharing corners with two tetrahedra each, while non-dimer Te^{2-} atoms are two-coordinate and bridge neighboring tetrahedra. S02 links the three tetrahedra In01, In02, and In03 for 3-fold coordination, while S01 is two-coordinate and bridges two neighboring In04 tetrahedra.

As viewed down the c -axis, In01 and In03 tetrahedra form infinite chains down the c -axis surrounding the Te04 dimer and are tilted in-phase with each other in mirror-like symmetry. In contrast, the In02 and In04 tetrahedra form similar chains corner-connected to the Te07 dimer,

however the In04 tetrahedra tilt out-of-phase with In02 and the other two tetrahedra, forcing the bridging S01 site out of the a-b plane of the S02 atoms shared by In01, In02, and In03.

The electronic band structure of $\text{In}_8\text{S}_{2.82}\text{Te}_{12.18}$ is shown in Figure 33a. This heteroanionic material is an indirect band gap semiconductor with a calculated band gap of 0.99 eV using the PBE functional method. This is consistent with the experimental band gap of 1.12(2) eV (Figure 33b). The conduction band minimum (CBM) is at the Γ point of the Brillouin zone, while the valence band maxima (VBM) can be found along the $A - I_2$ direction. The conduction bands near the Fermi level are mainly contributed by Te 5p and In 5s orbits while the valence bands near the Fermi level are mainly contributed by Te 5p and S 3p orbits. In $\text{In}_8\text{S}_{2.82}\text{Te}_{12.18}$, sulfur acts as a structural templating agent, but does not significantly affect the electronic behavior, as the S states lie nearly 1 eV below the VBM. Overall, the top of the valence band is more dispersive than the bottom of the conduction band, which is due to the dominated contribution of localized Te 5p orbitals at the top of the valence band as shown in Figure 33. Thus, the charge transport of electrons would be more efficient than that of holes. This is supported by the electron effective mass calculations of 0.627 and 0.571 (in m_0) for the directions $A \rightarrow I_2$ and $\Gamma - Y$, respectively; meanwhile the hole effective mass is calculated to be 4.353 and 0.672 for the directions $A \rightarrow I_2$ and $\Gamma - Y$, respectively.

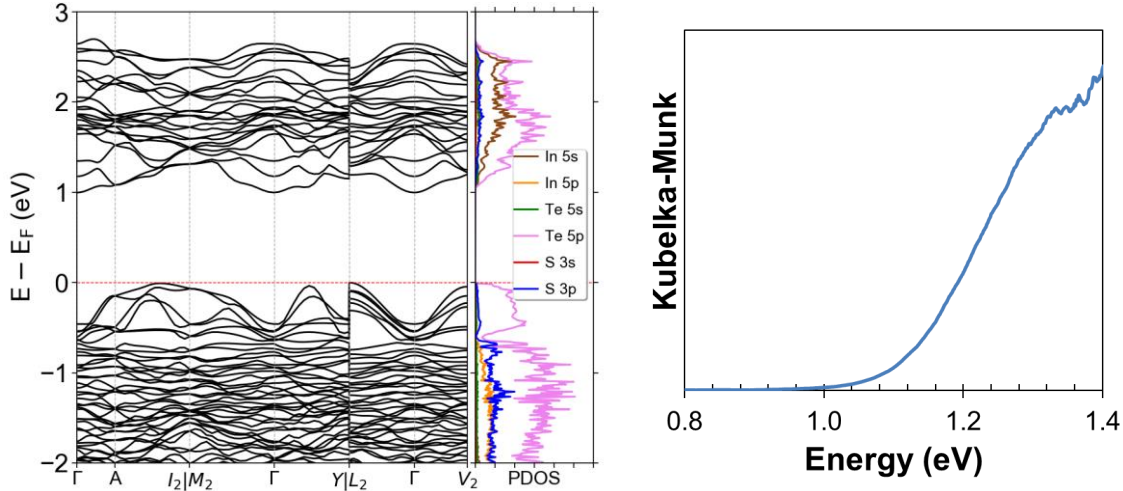


Figure 33: (a) The band structure and partial density of states (PDOS) of $\text{In}_8\text{S}_{2.82}\text{Te}_{12.18}$. (b) Experimental band gap of $\text{In}_8\text{S}_{2.82}\text{Te}_{12.18}$.

As this material is a relatively narrow band gap semiconductor, incorporates several heavy elements, and has multiple overlapping bands near the VBM, it shows potential as a thermoelectric material. Moreover, the complicated structure of this material is expected to scatter phonons and minimize lattice thermal conductivity, while the material's ordered, crystalline framework would maintain a high electric conductivity. Therefore, Seebeck (S), electrical conductivity (σ), and power factor ($S^2\sigma$) calculations were conducted as shown in Figure 34. (The thermal conductivity could not be calculated as the ordered structure used for this calculation has imaginary phonon modes as shown in Figure S24.) The calculated electrical conductivity (as shown in Figure 34) aligns with the argument that the electrical conductivity is higher for holes and electrons. By fixing the relaxation time to 10 fs, our predictions showed that the power factor along yy direction at holes can be over $3 \text{ mWm}^{-1}\text{K}^{-2}$ at 300K. $\text{In}_8\text{S}_{2.82}\text{Te}_{12.18}$ shows promise as a p-type thermoelectric, with a potential power factor similar to that of bulk n-type Bi_2Te_3 at 300K.²³²

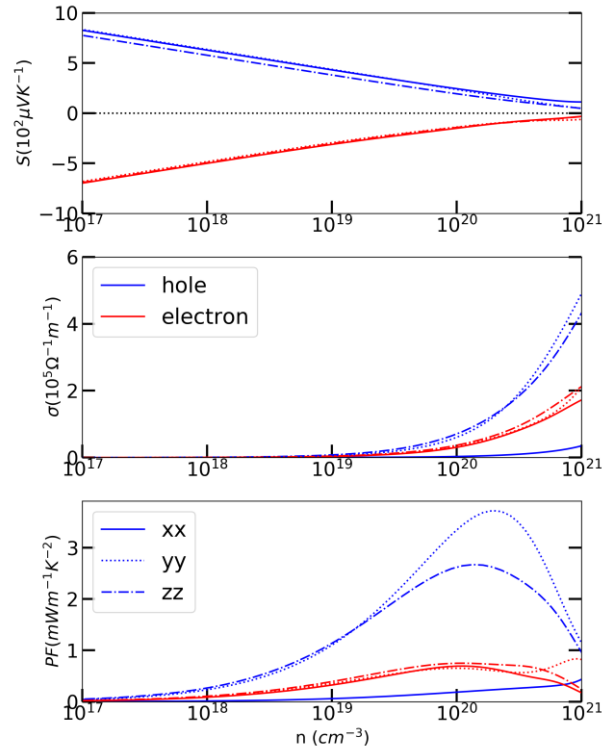


Figure 34: The electrical transport properties of $\text{In}_8\text{S}_3\text{Te}_{12}$ including (a) Seebeck coefficient (b) electrical conductivity and (c) power factor calculated at 300K with relaxation time fixed at 10 fs. Blue lines and red lines are holes and electrons, respectively.

5.5. Conclusion

This new heteroanionic ternary, $\text{In}_8\text{S}_{3-x}\text{Te}_{6+x}(\text{Te}_2)_3$ ($x = 0.18$) features a novel structure in that it comprises three heteroanions: S^{2-} , Te^{2-} , and Te_2^{2-} . While the initial target, $\text{In}_2\text{S}_2\text{Te}$, was never discovered, a novel structure was uncovered during the investigative work. The 3D framework of $\text{In}_8\text{S}_{3-x}\text{Te}_{6+x}(\text{Te}_2)_3$ ($x = 0.18$) is complex and consists of corner-sharing InQ_4 tetrahedra with 3 Te_2^{2-} dumbbell dimers per formula unit. This material's complicated structure in conjunction with its physical and electric properties of the material, that is its narrow band gap, heavy element constituents, and overlapping bands in the valence band maximum, indicate promise as a p-type

thermoelectric material.

Chapter 6. Harnessing HSAB Theory to Create Novel Heteroanionic Materials in the Ba-Sn-Q (Q = S, Te) Phase Space

6.1. Abstract

Five new quaternaries are discovered, with three being heteroanionic, $\text{Ba}_2\text{SnS}_{1.2}\text{Te}_{2.8}$, $\text{Ba}_3\text{SnS}_4\text{Te}$, and $\text{Ba}_3\text{SnS}_{5.62}\text{Te}_{0.13}$, and two as solid solutions of $\text{Ba}_7\text{Sn}_5\text{S}_{15-x}\text{Te}_x$ and $\text{Ba}_8\text{Sn}_4\text{S}_{15-y}\text{Te}_y$ ($x = 0.7$, $y = 0.76$). A new structure type is also introduced with $\text{Ba}_3\text{SnS}_4\text{Te}$. All materials were synthesized using traditional solid-state reaction methods. The heteroanionic materials are composed of the S^{2-} and Te^{2-} anionic units as well as, in the case of $\text{Ba}_3\text{SnS}_{5.62}\text{Te}_{0.13}$, S_2^{2-} dumbbells. All five materials conserve the hallmark QM_4 units indicative of this A-M-Q phase space.

6.2. Introduction

As discussed in previous chapters, heteroanionic materials offer a phase space that has great potential for novel structures and advantageous properties.^{155-157, 161, 204} The A-M-Q phase space, where A is an alkaline earth metal, B is Ge, Sn, or Pb, and Q is S, Se or Te, already presents extraordinary structural diversity.²³³⁻²³⁹ Within this class of material, compounds with discrete tetrahedral MQ_4 anions form a large subsection owing to the flexibility and distortion of these tetrahedral units.²³³ Figure 35 shows how the structures build on each other with the simple addition of AQ, MQ, or Q_2 units. It also highlights the relationship between structures that include polymeric anionic units (e.g. Q_2^{2-} , Q_3^{2-}). For streamlining the interpretation, Ba and Sn are used as A and M, respectively.

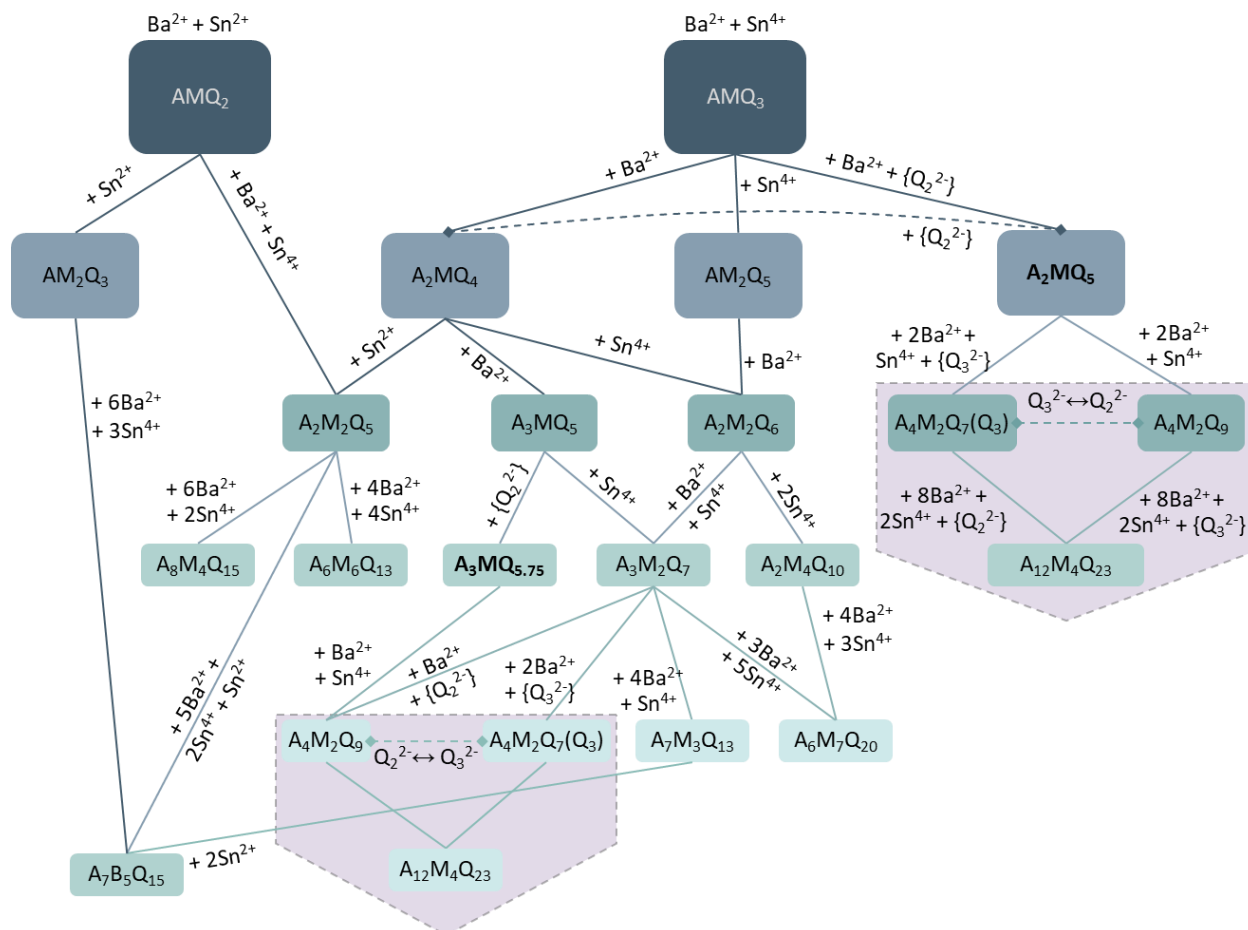


Figure 35: Compositional map of A-M-Q, where A is an alkaline earth metal, M is Ge, Sn, or Pb, and Q is S, Se, or Te. The shaded pentagonal arrows are to indicate that these relationships are identical and were not connected for clarity of reading the scheme.

To being the exploration, the composition A_2MQ_4 is selected as the Ba^{2+} and Sn^{4+} will promote selective bonding with the introduced chalcogens S and Te according to Hard/Soft Acid/Base (HSAB) theory. This approach has yielded five discovered compounds. More specifically, three mixed anion phases $Ba_2SnS_{1.20}Te_{2.80}$, Ba_3SnS_4Te , and $Ba_3SnS_{5.62}Te_{0.13}$ with anions of S^{2-} , Te^{2-} and, in the case, of the latter S_2^{2-} as well as the solid solutions of $Ba_7Sn_5S_{15-x}Te_x$ and $Ba_8Sn_4S_{15-y}Te_y$ ($x = 0.7$, $y = 0.76$).

6.3. Experimental Methods

Reagents. Chemicals in this work were used as-obtained: barium sulfide (99.9%, American Elements), tin (powder, 97%, Aldrich), sulfur (sublimed, 99.99%, Spectrum), tellurium (99.99%, American Elements).

Synthesis

Ba₂SnS_{1.2}Te_{2.8}. Compound was discovered in the reaction of 0.147 g (0.868 mmol) BaS, 0.082 g (0.69 mmol) elemental tin, and 0.118 g (0.925 mmol) elemental tellurium, which were combined in a carbon coated 9 mm (O.D.) fused silica tube. The tube was flame sealed under vacuum (10^{-3} mbar). The sample was heated to 900°C in 12 hours and soaked for 6 hours before cooling to 700°C in 24 hours then furnace cooling to room temperature. Efforts towards bulk phase pure have not yet been successful, however a reaction of 1 BaS : 1 BaTe : 1 Sn : 1 Te reacted to 900°C in 12 hrs, dwelled for 6 hrs, and furnace cooled have been most successful with BaTe and BaS impurities.

β-Ba₂SnS₄. A 0.778-g amount of (4.60 mmol) BaS, 0.272 g (2.30 mmol) powder tin, and 0.148 g (4.60 mmol) elemental sulfur were combined in a carbon coated 9 mm (O.D.) fused silica tube. The tube was flame sealed under vacuum (10^{-3} mbar). The sample was heated to 900°C in 12 hours and soaked for 6 hours before cooling to 700°C in 24 hours then furnace cooling to room temperature. The reaction yielded a pure material.

Ba₃SnS₄Te. Compound was discovered in the reaction of 0.237 g (0.90 mmol) BaTe, 0.080 g (0.67 mmol) elemental tin, and 0.225 g (0.67 mmol) elemental sulfur, which were combined in a carbon coated 9 mm (O.D.) fused silica tube. The tube was flame sealed under vacuum (10^{-3} mbar). The sample was heated to 900°C in 12 hours and soaked for 6 hours before cooling to

700°C in 24 hours then furnace cooling to room temperature. Bulk phase pure material was achieved by combining stoichiometric amounts of β -Ba₂SnS₄ and BaTe then reacting them to 700°C in 7 hours, soaking for 6 hours, and then furnace cooling. The reaction had 71.3 mol% Ba₃SnS₄Te with SnO and BaTe₃ impurities.

Ba₃SnS_{5.62}Te_{0.13}. Compound was discovered in the reaction of 0.147 g (0.868 mmol) BaS, 0.082 g (0.69 mmol) elemental tin, and 0.118 g (0.925 mmol) elemental tellurium, which were combined in a carbon coated 9 mm (O.D.) fused silica tube. The tube was flame sealed under vacuum (10⁻³ mbar). The sample was heated to 900°C in 12 hours and soaked for 6 hours before cooling to 700°C in 24 hours then furnace cooling to room temperature. The reaction led to a bulk phase pure material with SnTe impurities.

Ba₇Sn₅S_{14.3}Te_{0.7} and *Ba₈Sn₄S_{14.24}Te_{0.76}*. Compound was discovered in the reaction of 1 BaS : 1 Sn : 1 Te, which were combined in a carbon coated 9 mm (O.D.) fused silica tube and subsequently flame sealed under vacuum (10⁻³ mbar). The sample was heated to 900°C in 12 hours and soaked for 6 hours before cooling to 700°C in 24 hours then furnace cooling to room temperature. As these compounds yielded solid solutions, not new phases, bulk phase pure syntheses were not pursued.

Physical Measurements

Powder X-ray Diffraction. X-ray powder diffraction patterns were collected on a Rigaku Miniflex600 diffractometer with Ni-filtered Cu K α radiation (1.5406 Å) operating at 40 kV and 15 mA with a high-speed silicon strip detector. The diffraction pattern used a scan width of 0.02° and a scan rate of 10°/min. Visualization of the crystal structures was done with Vesta software.¹⁰⁴

Single Crystal X-ray Diffraction. Suitable single crystals were mounted on a glass fiber

with glue on a STOE StadiVari diffractometer equipped with a micro-focus sealed X-ray tube PhotonJet (Mo) X-ray source and a Hybrid Pixel Array Detector (HyPix) detector. When applicable, temperature of the crystal was controlled with an Oxford Cryosystems low-temperature device. Data reduction was performed with the X-Area software package using a numerical absorption correction. The structure was solved with the ShelXT structure solution program using direct methods solution method and by using Olex2 as the graphical interface. The model was refined with ShelXL using least squares minimization.

Optical Measurements. Optical diffuse reflectance measurements were made at room temperature with a Shimadzu UV-3600 PC double-beam, double-monochromator spectrophotometer. The measurement of diffuse reflectivity can be used to obtain values for the band gap from a powder sample at room temperature. BaSO₄ powder was used as a reference. The reflectance data was converted to absorbance using the Kubelka-Munk equation: $\alpha/S = (1 - R)^2/2R$. R is the reflectance at a given wavelength, α is the absorption coefficient, and S is the scattering coefficient. Valence band maximum energy (VBM) was measured by photoemission spectroscopy in air on a Riken-Keiki PESA AC-2. Samples are scanned under ambient conditions using UV light (4.20-6.20 eV). The number of photoelectrons generated at each excitation energy is measured and the VBM is the onset of the PESA spectra, as photoelectrons are only generated when the photon energy is higher than the VBM energy. Conduction band minimum energies are found by subtracting the optical band gap from the VBM energy.

Second Harmonic Generation Measurements. Currently pending.

Scanning Electron Microscopy. A Hitachi 3400 scanning electron microscope was used to image the microstructure. The accelerating voltage and probe current were set to 20 keV and 70 –

90 mA, respectively. Energy-dispersive X-ray spectroscopy (EDS) was performed using a PGT energy-dispersive X-ray analyzer. Aztec software from Oxford Instruments was used to analyse the EDS data.

Computational Methods

All density functional theory (DFT) calculations are performed using the Vienna ab initio simulation package (VASP)¹¹³⁻¹¹⁴ along with the projector augmented wave (PAW)¹¹¹⁻¹¹² method to performed the density functional theory (DFT) calculations. The Perdew-Burke-Ernzerhof (PBE)¹¹⁵ generalized gradient approximation (GGA) was used as the exchange-correlation functional. The plane wave cutoff energy was set as 520 eV and the structure was fully relaxed until the total energy converged to within 10^{-8} eV and the force on each atom was less than 10^{-3} eV/Å. Phonon calculations were performed with the $1 \times 1 \times 1$ unit cell using the PHONOPY package¹⁸¹. The transport properties were calculated using the semiclassical Boltzmann transport theory implemented in the BoltzTraP²³¹ package.

6.4. Results and Discussion

When investigating this family of A_2MQ_4 compounds (A = alkaline earth, M = Group IV, Q = S, Se, Te), a computational study found that the ionic radius ratio ($r_A/(r_M+r_Q)$) versus force constant of the cations could be used to predict these ternaries' crystal structures.²⁴⁰ The computations indicated that compositions containing large A cations favor the β - K_2SO_4 structure, while compositions with small A cations primarily crystallize in the olivine structure type. Further inspection of these predictions more specifically showed that the β - K_2SO_4 type is favored when the M cation is highly electronegative and has a small ionic radius, while the alkaline earth cation

has a large ionic radii and small electronegativity value.²⁴¹

When applying this study to the Ba-Sn-Q phase space, the predictions align with the experimental results, showing that the structures crystallize in β -K₂SO₄ type as they consist of MQ₄ isolated units linked together and charge balanced by barium cations.²⁴²⁻²⁴³ Previous studies of the sulfide ternaries show that the high and low temperature polymorphs of Ba₂SnS₄ form in a modified β -K₂SO₄ structure type, with the low temperature being closer to the true β -K₂SO₄ structure type.²⁴² The sulfide polymorphs both conserve their discrete, distorted SnS₄ tetrahedra that are connected by edge-sharing with the Ba-S polyhedra.²⁴¹⁻²⁴² The coordination number (CN) of Ba at low temperature (α -phase) is seven and eight, while it is six, seven, and eight in the high temperature phase. The selenium analogue is isostructural to the low temperature phase, α -Ba₂SnS₄.²⁴³

When exchanging tellurium for sulfur in Ba₂SnS₄, the heteroanion Ba₂SnS_{1.2}Te_{2.8} was discovered and crystallizes in the non-centrosymmetric *Ama2* space group with lattice parameters $a = 11.0905(5)$ Å, $b = 11.5151(4)$ Å, $c = 8.0728(3)$ Å, $\alpha = \beta = \gamma = 90^\circ$ (

Table 2, Table S#). As in the Ba_2SnQ_4 structures ($\text{Q} = \text{S}, \text{Se}$), $\text{Ba}_2\text{SnS}_{1.2}\text{Te}_{2.8}$ consists of isolated, distorted MQ_4 units connected into a three-dimensional network by its alkaline earth cation, Ba^{2+} . The distorted tetrahedral units are of the composition $\text{SnS}_{1.2}\text{Te}_{2.8}$ and have bond lengths of 2.421(3) Å, 2.6815(11) Å, and 2.7225(7) Å for Sn-S, Sn-Te/S, and Sn-Te, respectively (Figure 36a). The $\text{Sn}^{4+}\text{-S}^{2-}$ bond lengths are consistent with the Sn-S bond lengths in the isostructural Sr_2SnS_4 (2.372(3) – 2.409(3) Å)²⁴⁴ and those in the parent structure Ba_2SnS_4 (low temperature polymorph, 2.353(3) – 2.427(2) Å).²⁴² The $\text{Sn}^{4+}\text{-Te}^{2-}$ bond lengths are in line with those found in tetrahedral SnTe_4 in $\text{K}_2\text{BaSnTe}_4$ (2.7600(7) Å).²⁴⁵ As expected, the bond length of Sn and the disordered chalcogenide site falls between those of the Sn-S and Sn-Te bond lengths and has more Sn-Te character according to its higher occupancy of Te on the crystallographic site.

Table 2: Crystal data and structure refinements for Ba₂SnS_{1.20}Te_{2.80}, Ba₃SnS₄Te, and Ba₃SnS_{5.62}Te_{0.13}.

Empirical formula	Ba ₂ SnS _{1.2} Te _{2.8}	Ba ₃ SnS ₄ Te	Ba ₃ SnS _{5.62} Te _{0.13}
Formula weight	789.12	786.55	727.48
Temperature	273.15 K	100.01(10) K	100.01(10) K
Wavelength		0.71073 Å	
Crystal system	Orthorhombic	Orthorhombic	Orthorhombic
Space group	<i>Ama2</i>	<i>Cmcm</i>	<i>Pnma</i>
a	11.0905(5) Å	6.95190(10) Å	9.0694(3) Å
b	11.5151(4) Å	16.4208(3) Å	9.7874(3) Å
c	8.0728(3) Å	9.7624(2) Å	12.2373(4) Å
α, β, γ		α = β = γ = 90°	
Volume	1030.96(7) Å ³	1114.43(3) Å ³	1086.25(6) Å ³
Z	4	4	4
Density (calculated)	5.084 g/cm ³	4.688 g/cm ³	4.448 g/cm ³
Absorption coefficient	17.885 mm ⁻¹	15.918 mm ⁻¹	14.354 mm ⁻¹
F(000)	1307	1336	1259
Crystal size	0.04 x 0.03 x 0.02 mm ³	0.151 x 0.091 x 0.032 mm ³	0.146 x 0.085 x 0.041 mm ³
θ range for data collection	3.082 to 30.721°	2.481 to 33.773°	2.665 to 33.881°
Index ranges	-11 ≤ h ≤ 13, -16 ≤ k ≤ 13, -9 ≤ l ≤ 10	-10 ≤ h ≤ 10, -23 ≤ k ≤ 25, -14 ≤ l ≤ 15	-13 ≤ h ≤ 9, -14 ≤ k ≤ 13, -18 ≤ l ≤ 15
Reflections collected	3340	20225	8179
Independent reflections	1183 [R _{int} = 0.0224]	1193 [R _{int} = 0.0341]	1967 [R _{int} = 0.0314]
Completeness to θ = 25.242°	100%	100%	100%
Refinement method		Full-matrix least-squares on F ²	
Data / restraints / parameters	1183 / 1 / 40	1193 / 0 / 31	1967 / 0 / 64
Goodness-of-fit	1.064	1.187	1.113
Final R indices [I > 2σ(I)]	R _{obs} = 0.0162, wR _{obs} = 0.0356	R _{obs} = 0.0114, wR _{obs} = 0.0254	R _{obs} = 0.0224, wR _{obs} = 0.0450
R indices [all data]	R _{all} = 0.0168, wR _{all} = 0.0357	R _{all} = 0.0120, wR _{all} = 0.0256	R _{all} = 0.0271, wR _{all} = 0.0462
Largest diff. peak and hole	1.579 and -1.180 e·Å ⁻³	0.599 and -1.069 e·Å ⁻³	1.212 and -1.730 e·Å ⁻³

$$R = \frac{\sum ||F_o| - |F_c||}{\sum |F_o|}, wR = \left\{ \frac{\sum [w(|F_o|^2 - |F_c|^2)^2]}{\sum [w(|F_o|^4)]} \right\}^{1/2} \text{ and}$$

$$w=1/[\sigma^2(\text{Fo}^2)+(0.0126\text{P})^2+2.3411\text{P}] \text{ where } \text{P}=(\text{Fo}^2+2\text{Fc}^2)/3$$

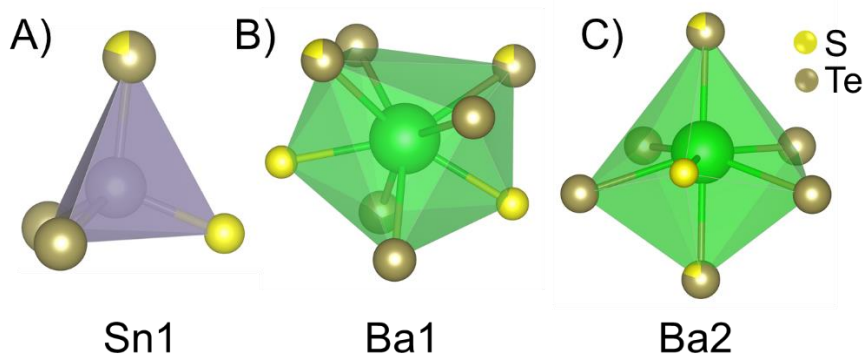


Figure 36: Illustration of (A) the four-coordinate, distorted SnSTe₂Q (Q: S = 0.2, Te = 0.8; SnS_{1.2}Te_{2.8}) tetrahedra, (B) the eight-coordinate BaS₂Te₄Q₂ (BaS_{2.4}Te_{5.6}) polyhedra for Ba1 and (C) the seven-coordinate BaSTe₄Q₂ (BaS_{1.4}Te_{5.6}) polyhedra for Ba2.

Ba-S polyhedra connect the SnQ₄ units together via corner- and edge-sharing, while the Ba polyhedra are connected via edge- and face-sharing. With two barium positions shown in Figure 36b-c, the Ba1 coordination sphere has a composition of BaS_{2.4}Te_{5.6} and forms a highly distorted tetragonal antiprism (CN = 8), while the Ba2 polyhedra has a composition of BaS_{1.4}Te_{5.6} and forms a distorted pentagonal dipyramid (CN = 7). The bond lengths range from 3.064(3) to 3.6301(6) Å, which are detailed in Table 3, and are consistent with the Ba-S values in α -Ba₂SnS₄ that range from 3.091(3) to 3.416(3) Å as well as the Ba-Te values in Ba₂GeSe₂Te₂ ranging 3.445(2) – 3.7606(6) Å.^{242, 246}

Table 3: Bond lengths for Ba-Q in Ba₂SnS_{1.2}Te_{2.8}.

Bond	Length (in Å)	Bond	Length (in Å)
Ba1-S	3.165(1)	Ba2-S	3.064(3)
Ba1-Te	3.6102(7) 3.6301(6)	Ba2-Te	3.5842(8) 3.6975(6)
Ba1-Te/S	3.4838(7)	Ba2-Te/S	3.433(1) 3.601(1)

The computation studies of the A_2MQ_4 compounds (A = alkaline earth, M = Group IV, Q = S, Se, Te) indicate $Ba_2SnS_{1.2}Te_{2.8}$ should be in the same space group as Ba_2SnS_4 and Ba_2SnSe_4 , however the introduction of tellurium undermines this prediction.²⁴⁰⁻²⁴³ The isovalent Te-analogue align with the parent structures in so much as it consists of MQ_4 isolated units linked together and charge balanced by barium cations. Studies into Ba_2GeQ_4 and Ba_2SiQ_4 (Q = S, Se) also observed that, while the A and M radii largely dictate the structure, the chalcogen identity cannot be ignored in structure predictions. Moreover, when comparing the structures of $Ba_2SnS_{1.2}Te_{2.8}$ and its parent composition, Ba_2SnQ_4 (Q = S, Se), the heteroanionic compound is more densely packed than Ba_2SnQ_4 . Figure 37a and c compare the packing of both compounds when oriented such that the distorted SnQ_4 tetrahedra on stacked parallel to the viewing vector. Ba_2SnSe_4 is used as its tetrahedral distortions resulting from Se is more correspondent with the Te-containing Ba_2SnQ_4 . When viewed down the $[4\ 0\ 3]$ vector (Figure 37a) can see the close packing as compared to down $[0\ 0\ 1]$ in Ba_2SnS_4 (Figure 37c).

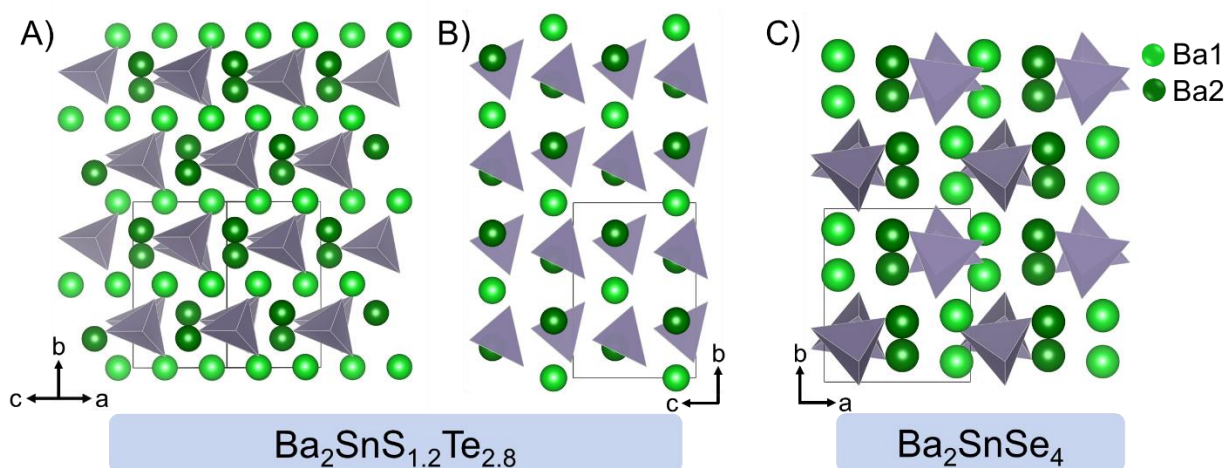


Figure 37: (A) Illustration of the more closely packed $Ba_2SnS_{1.2}Te_{2.8}$ by viewing down the $[4\ 0\ 3]$ vector, where the distorted SnQ_4 tetrahedra are stacked parallel to the viewing vector. (B) A view of $Ba_2SnS_{1.2}Te_{2.8}$ down the a -axis highlights the polarity of the SnQ_4 units, indicating potential as a non-linear optical material. (C) A view of Ba_2SnSe_4 c -axis to contrast the packing of the Se-

analogue and heteranionic analogues. The barium sites are colored light and dark green for clarity for Ba1 and Ba2, respectively.

The polarity of the SnQ_4 polyhedra observed in Figure 37a and c as well as the absence of an inversion center in the structure indicates this material may be a promising non-linear optical (NLO) material.⁶³⁻⁶⁴ Second harmonic generation measurements are currently ongoing to investigate this material's potential as a NLO material. To further investigate potential applications, attempts were made to synthesize this material without disorder, e.g. $\text{Ba}_2\text{SnSTe}_3$. However, these attempts were not fruitful and likely indicate that this structure requires sulfur-tellurium disorder to form.

As we increase the complexity of the structure by adding another BaQ (Q = S, Te) unit, the ternaries $\text{Ba}_3\text{SnS}_4\text{Te}$ and $\text{Ba}_3\text{SnS}_{5.62}\text{Te}_{0.13}$ were discovered. $\text{Ba}_3\text{SnS}_4\text{Te}$ crystallizes in *Cmcm* with lattice parameters $a = 6.95190(10)$, $b = 16.4208(3)$, $c = 9.7624(2)$, $\alpha = \beta = \gamma = 90^\circ$ (

Table 2, Table S#), while $\text{Ba}_3\text{SnS}_{5.62}\text{Te}_{0.13}$ crystallizes in *Pnma* with lattice parameters $a = 9.0694(3)$, $b = 9.7874(3)$, $c = 12.2373(4)$, $\alpha = \beta = \gamma = 90^\circ$ (

Table 2, Table S#). Even with the addition of BaTe, $\text{Ba}_3\text{SnS}_4\text{Te}$ conserves the isolated, distorted SnS_4 units found in the parent composition, Ba_2SnQ_4 ($\text{Q} = \text{S}, \text{Se}$) as seen in Figure 38. Moreover, it is also connected into a three-dimensional network by its alkaline earth cation, Ba^{2+} . The SnS_4 tetrahedra shown in Figure 38c, have Sn-S1 bond lengths of 2.3553(6) and Sn-S2 bond lengths of 2.3421(6) Å. These $\text{Sn}^{4+}\text{-S}^{2-}$ bond lengths are consistent with those in the low temperature Ba_2SnS_4 parent composition 2.353(3) – 2.427(2) Å²⁴² and are ca. 3.5% shorter than those found in $\text{Ba}_2\text{SnS}_{1.2}\text{Te}_{2.8}$. The longer bond length of Sn-S in the latter structure is likely a result of Te presence in the tetrahedra.

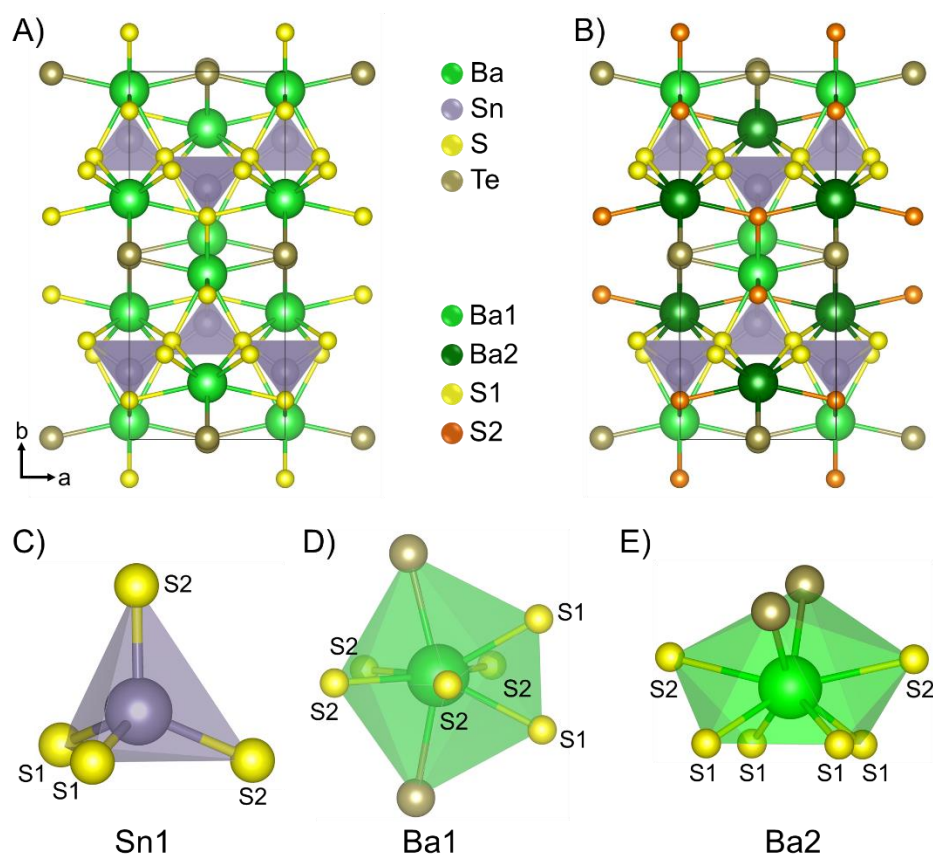


Figure 38: Crystal structure of $\text{Ba}_3\text{SnS}_4\text{Te}$. SnS_4 tetrahedra shown (A) without differentiating Ba and S sites and (B) with differentiating between Ba1 (light green), Ba2 (dark green), S1 (yellow) and S2 (orange) sites. The polyhedra of (C) SnS_4 , (D) BaS_6Te_2 for Ba1 and (E) BaS_6Te_2 for Ba2 are shown, with S1 and S2 sites labeled accordingly.

Ba-S polyhedra connect the SnQ_4 units into a three-dimensional framework, where the Ba1 coordination sphere connects via corner-sharing and the Ba2 sphere via edge-sharing, and the two Ba-S polyhedra connect via face-sharing. The Ba1 coordination sphere forms a distorted monocapped pentagonal bipyramid (Figure 38d) with Ba-S bond lengths of 3.0538(6) – 3.3683(6) Å and a Ba-Te bond length of 3.5562(1) Å. The highly distorted square antiprism of the Ba2 coordination sphere (Figure 38e) has Ba-S bond lengths of 3.4640(4) – 3.5749(2) Å and Ba-Te bond lengths of 3.4570(4) and 3.5756(4) Å. These bond lengths are in line with the Ba-S values in $\alpha\text{-Ba}_2\text{SnS}_4$ that range from 3.091(3) to 3.416(3) Å as well as the Ba-Te values in $\text{Ba}_2\text{GeSe}_2\text{Te}_2$ ranging 3.445(2) – 3.7606(6) Å.^{242, 246}

With the addition of a BaTe unit to the Ba_2SnS_4 composition, a BaTe rocksalt interlayer can be observed. As illustrated in Figure 39a, the structure shown in Figure 38a can be rendered to highlight the TeBa_6 distorted octahedra. When any bonds to sulfur are removed, as shown in

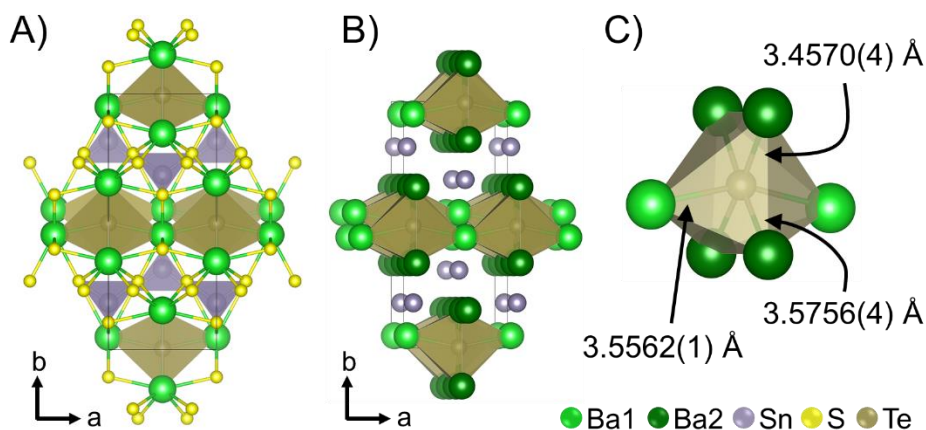


Figure 39b, the BaTe rocksalt interlayer becomes apparent. The Ba-Te bond lengths 3.4570(4), 3.5562(1), and 3.5756(4) Å are also in good agreement with the Ba-Te bond of 3.503(5)

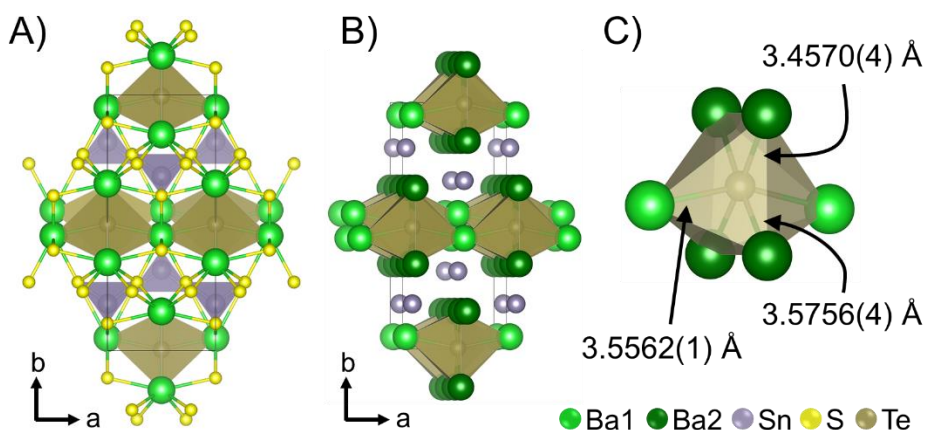
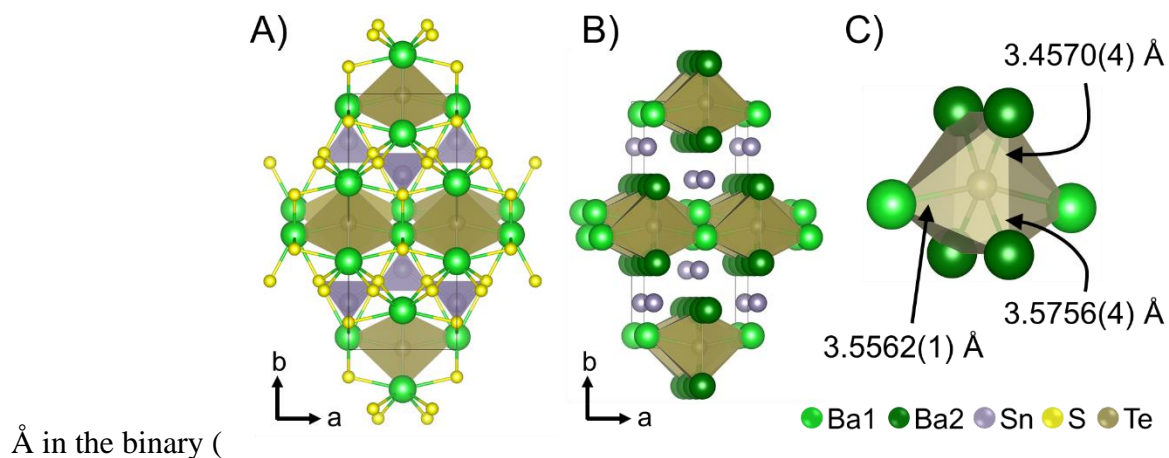


Figure 39: Structure of (A) $\text{Ba}_3\text{SnS}_4\text{Te}$ with the distorted TeBa_6 octahedra indicated, (B) $\text{Ba}_3\text{SnS}_4\text{Te}$ with the distorted TeBa_6 octahedra highlighted and all M-S bonds removed, and (C) the TeBa_6 distorted octahedra with bond lengths shown.

While $\text{Ba}_3\text{SnS}_4\text{Te}$ is nominally Ba_3MQ_5 , $\text{Ba}_3\text{SnS}_{5.62}\text{Te}_{0.13}$ is closer in structure to the only known 3-1-5 structure, Ba_3GeS_5 , and is, in fact isotopic to the structure (Figure 40a-b).²³³ Ba_3GeS_5 can be considered to have the formula $(\text{Ba}^{2+})_3(\text{GeS}_4^{4-})\text{S}^{2-}$, where the S^{2-} anions are isolated on the 4c Wyckoff site. This site is then replaced with a mixed occupancy S^{2-} and Te^{2-} (68% S1: 32% Te1). This mixed chalcogenide site is then one-fourth occupied, and the charge is counter balanced with the partial occupation of sulfides on neighboring 4c and 8d Wyckoff sites. The distance of these

sulfides are 2.222(5) and 2.249(6) Å, confirming these are disulfide bonds as they closely align with the disulfide bond length, 2.118(7) Å, in BaS₂.²⁴⁸ Each of these anions (mixed S²⁻/Te²⁻ and three S₂²⁻ units) is one-fourth occupied, such that the summed occupancy is shown of the left side of Figure 40c and the individual arrangements are shown on the right. One of the sulfurs on the 4c Wykoff site bonded to Sn also has mixed occupancy of Te that totals 5%. With the introduction of S₂²⁻ anions to the structure, the formula evolves from Ba₃SnS₅ to Ba₃SnS₄(³/₄ S₂ ¹/₄ S). The mixed occupancy of tellurium further changes the general formula to be Ba₃SnS₃(S_{1-x}Te_x)(³/₄S₂ ¹/₄[S_{1-y}Te_y]), where x = 0.05 and y = 0.32. When reduced, we arrive at the formula Ba₃SnS_{5.62}Te_{0.13}. Syntheses to form the full disulfide (Ba₃SnS₆) or without the telluride Ba₃SnS₄(³/₄ S₂ ¹/₄ S) using combinations of binaries and elemental precursors were attempted and ultimately unsuccessful. Perhaps an alternative synthesis approach may be fruitful as when Sr₂Sn and elemental S was used to make Sr₂SnS₄ when other synthetic attempts were unsuccessful.²⁴⁴

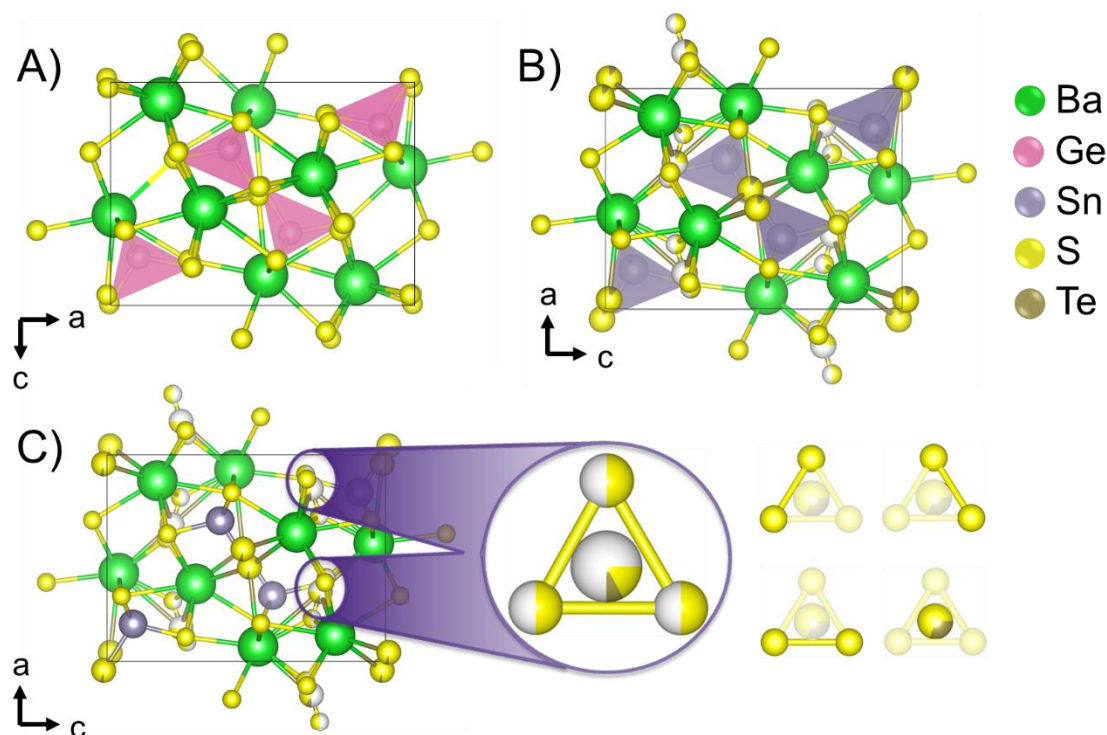


Figure 40: Crystal structure of (A) Ba_3GeS_5 with the GeS_4 tetrahedra shown in pink and of (B) $\text{Ba}_3\text{SnS}_{5.62}\text{Te}_{0.13}$ with the SnS_4 tetrahedra shown in purple. (C) The heteronanionic unit comprised of S^{2-} , Te^{2-} , and S_2^{2-} is highlighted (left) and the occupancy distribution (right) is shown.

During the phase exploration, solid solutions of $\text{Ba}_7\text{Sn}_5\text{Q}_{15}$ and $\text{Ba}_8\text{Sn}_4\text{Q}_{15}$ were also discovered. Both compounds are isostructural and show very little size deviation from their parent sulfide structures. When tellurium is introduced to these reactions, $\text{Ba}_7\text{Sn}_5\text{S}_{14.3}\text{Te}_{0.7}$ and $\text{Ba}_8\text{Sn}_4\text{S}_{14.24}\text{Te}_{0.76}$ form. $\text{Ba}_7\text{Sn}_5\text{S}_{14.3}\text{Te}_{0.7}$ (Figure 41a) crystallizes in a slightly larger $\text{P6}_3\text{cm}$ structure ($a = b = 25.3104(6)$ Å, $c = 8.5782(2)$ Å, $\alpha = \beta = 90^\circ$, $\gamma = 120^\circ$) than the full sulfide ($a = b = 25.1234(4)$ Å, $c = 8.4120(2)$ Å).²⁴⁹ Contrastingly, $\text{Ba}_8\text{Sn}_4\text{S}_{14.24}\text{Te}_{0.76}$ (Figure 41b) crystallizes in a slightly smaller $\text{Pca}2_1$ structure ($a = 28.730(5)$ Å, $b = 8.510(2)$ Å, $c = 25.256(5)$ Å, $\alpha = \beta = \gamma = 90^\circ$) compared to the full sulfide ($a = 28.727(5)$ Å, $b = 8.522(1)$ Å, $c = 25.438(4)$ Å).²⁵⁰ Notably, the tellurium is largely non-selective when incorporating into the structures. By virtue of their non-

centrosymmetry, potential anionic tunability, and favorable second harmonic generation (SHG) in their isostructural parent compounds, $\text{Ba}_7\text{Sn}_5\text{S}_{14.3}\text{Te}_{0.7}$ and $\text{Ba}_8\text{Sn}_4\text{S}_{14.24}\text{Te}_{0.76}$ show great promise as SHG materials.

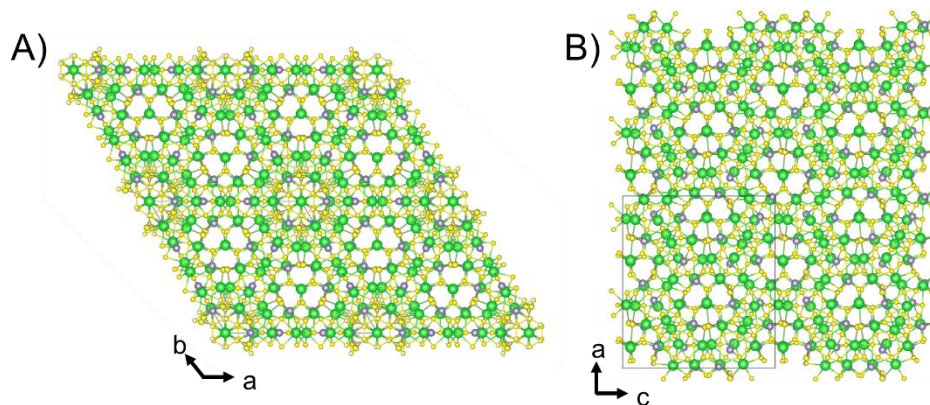


Figure 41: Crystal structure of (A) $\text{Ba}_7\text{Sn}_5\text{S}_{14.3}\text{Te}_{0.7}$ and (B) $\text{Ba}_8\text{Sn}_4\text{S}_{14.24}\text{Te}_{0.76}$ shown with $2 \times 2 \times 2$ unit cells.

6.5. Conclusion

With the harnessing of HSAB theory, five new quaternaries were discovered, where three are heteroanionic, $\text{Ba}_2\text{SnS}_{1.2}\text{Te}_{2.8}$, $\text{Ba}_3\text{SnS}_4\text{Te}$, and $\text{Ba}_3\text{SnS}_{5.62}\text{Te}_{0.13}$, and two are solid solutions, $\text{Ba}_7\text{Sn}_5\text{S}_{15-x}\text{Te}_x$ and $\text{Ba}_8\text{Sn}_4\text{S}_{15-y}\text{Te}_y$ ($x = 0.7$, $y = 0.76$). For each structure, the QM_2 motif that is prevalent in this structure type is conserved. Additionally, a new structure type is introduced with $\text{Ba}_3\text{SnS}_4\text{Te}$ that is otherwise not seen in the A_3MQ_5 ($\text{A} = \text{Sr}, \text{Ba}$; $\text{M} = \text{Ge}, \text{Sn}, \text{Pb}$; $\text{Q} = \text{S}, \text{Se}, \text{Te}$) compounds. With $\text{Ba}_2\text{SnS}_{1.2}\text{Te}_{2.8}$, $\text{Ba}_3\text{SnS}_4\text{Te}$, Te^{2-} anionic units are introduced into the material, while $\text{Ba}_3\text{SnS}_{5.62}\text{Te}_{0.13}$ structure introduces S_2^{2-} dumbbells.

Concluding Remarks and Outlook

Historically, *in situ* studies of materials synthesis had specialized use in crystallization rate observations. With the advent of more commercially available diffractometer setups, thereby no longer necessitating synchrotrons for certain systems, the synthesis science community will be able to access and use this powerful technique more routinely. As demonstrated in the studies discussed in this dissertation, panoramic synthesis has immense potential for materials discovery and unveiling the assembling principles for solid-state materials.

The investigation into the A-Pn-Q (A = alkali metal; Pn = Sb, Bi) compositional space encompassed three important features: (1) materials discovery in well-investigated systems, (2) investigations with different precursors, and (3) the discovery of a structural intermediate. Most importantly, a design principle was proposed that extends beyond the investigated system. The ability of KBiQ₂ to form both disordered and ordered phases, as discussed in Chapter 3, while NaBiQ₂ and RbBiQ₂ crystallize in the rocksalt and α -NaFeO₂ structure types, respectively, suggests that there is a site-sharing tolerance requirement for the six-coordinate cations: $\left(\frac{r^+}{r^{3+}}\right)$ should be 1.33 or less in order to form a cation-disordered rocksalt structure. Inspection of the antimony analogues, where NaSbS₂ crystallizes in both the rocksalt and KSbS₂ structure types, while KSbS₂ only forms a cation-ordered structure, yields a six-coordinate cation ratio $\left(\frac{Na^+}{Sb^{3+}}\right)$ of 1.3, corroborating that found for the bismuth ternaries. While this pioneering study proposes a new design principle for a chalcogenide system, the following chapter exploits the utility of *in situ* variable temperature PXRD to further our understanding of underexplored systems.

The potential insights provided by *in situ* variable temperature PXRD can be used to further

our understanding of burgeoning phase spaces, such as heteroanionic materials. Chapter 4 directs its focus to the heteroanionic BiOCuSe material. This study uncovers that the $\text{Bi}_2\text{O}_2\text{Se} + \text{Cu}_2\text{Se}$ reaction to form BiOCuSe proceeds without intermediates to direct product formation, while the $\text{Bi}_2\text{O}_3 + \text{Bi} + 3 \text{Cu} + 3 \text{Se}$ reaction forms many intermediates before the final product forms. These intermediates include CuSe, Cu_2Se , Bi_3Se_4 , and Bi_2Se_3 , where, surprisingly, “selenium-rich” CuSe and “selenium-poor” Bi_3Se_4 form first. It is determined that CuSe forms as a result of high stability and stoichiometric considerations and Bi_3Se_4 forms as competition for selenium with copper in accordance with HSAB theory. Chapter 6 links the selection of precursors to the reaction progression and establishes an understanding of the effects of the chosen precursors.

Chapter 7 and 8 harness HSAB theory to discover six new materials. First, a heteroanionic ternary, $\text{In}_8\text{S}_{3-x}\text{Te}_{6+x}(\text{Te}_2)_3$ ($x = 0.18$) is discussed. While the initial target was another composition, a novel structure comprising three heteroanions: S^{2-} , Te^{2-} , and Te_2^{2-} . Is uncovered during the investigative work. The 3D framework of $\text{In}_8\text{S}_{3-x}\text{Te}_{6+x}(\text{Te}_2)_3$ ($x = 0.18$) is complex and consists of corner-sharing InQ_4 tetrahedra with 3 Te_2^{2-} dumbbell dimers per formula unit. In the Ba-Sn-Q (Q = S, Se) phase space, five new quaternaries are discovered. $\text{Ba}_2\text{SnS}_{1.2}\text{Te}_{2.8}$, $\text{Ba}_3\text{SnS}_4\text{Te}$, and $\text{Ba}_3\text{SnS}_{5.62}\text{Te}_{0.13}$ are heteroanionic materials that introduce Te^{2-} anionic units into the material, while $\text{Ba}_3\text{SnS}_{5.62}\text{Te}_{0.13}$ structure introduces S_2^{2-} dumbbells, similar to the ditellurides in $\text{In}_8\text{S}_{2.82}\text{Te}_{6.18}(\text{Te}_2)_3$. The solid solutions $\text{Ba}_7\text{Sn}_5\text{S}_{15-x}\text{Te}_x$ and $\text{Ba}_8\text{Sn}_4\text{S}_{15-y}\text{Te}_y$ ($x = 0.7$, $y = 0.76$) were also discovered. Notably the SnM_4 motif that is prevalent in this phase space is conserved. The complicated structure of $\text{In}_8\text{S}_{2.82}\text{Te}_{6.18}(\text{Te}_2)_3$ in conjunction with its physical and electric properties of the material, that is its narrow band gap, heavy element constituents, and overlapping bands in the valence band maximum, indicate promise as a p-type thermoelectric material. Meanwhile the

non-centrosymmetric structures, $\text{Ba}_2\text{SnS}_{1.2}\text{Te}_{2.8}$, $\text{Ba}_7\text{Sn}_5\text{S}_{15-x}\text{Te}_x$ and $\text{Ba}_8\text{Sn}_4\text{S}_{15-y}\text{Te}_y$ show great promise as non-linear optical materials.

Given that this approach to materials discovery and reaction path identification is in its infancy, there is a lot of room for exploration. By more routinely pairing *in situ* panoramic materials syntheses with computational insight, to not only select productive phase spaces, but also rationalize the observed trends and progressions, work focusing on rational design may quickly advance.^{4, 35} At present, computational and text mining studies have already been used to investigate precursor choice on anthropogenic biases,⁷⁷ switchability,²⁵¹ and synthesis recipe.¹⁷⁸ Cataloging failed reactions is also of interest.⁷⁸ Rapid progress continues to be made in computationally-driven predictive syntheses of inorganic materials, but it too is in its infancy.²³ Other steps include extending parameters to other synthetic variables, such as pressure.²⁵²

Appendix A: Tips and Procedures for PXRD work at the Advanced Photon Source at Argonne National Laboratory

General APS Tips

- Plan out your heating profiles and order of samples beforehand. Have planned which reactions/samples you will drop, just in case. Also, have extra on hand just in case you have time or a previous reaction failed.
- Book the guesthouse right when you are allotted beamtime. It fills up quickly.
- It's cold inside – bring a jacket.
- Bring your own epoxy and/or clay if mounting or silica wool if at 17-BM and using furnace
- Have a plan for food, whether you: eat on-site at 401 Grill (check when they close), plan to drive and go out to eat, or bring your own food.

Tips for 17-BM-B

- If using the heat blower (goes up to max of 600-650°C)
 - Capillary should be 30-40 mm in length
 - Use epoxy when doing high temp – if you use clay, your sample may move as you rock or become soft (when heated) and therefore your sample will no longer be aligned
- If using resistive heater furnace (max of 1000°C)
 - Capillary should be 20-30 mm in length. Inner diameter of furnace is 0.9 mm.
 - If you are reaching a melt in your sample, you should raster since your material will diffuse out of the beam. However, **be careful**, rastering loosens the ceramics that the resistive heater is wrapped around. They may fall out and the coils may subsequently fail.
- Test your hard drive on the computer beforehand – I've had issues with the computer reading them. Also, FYI, the download of that data will take at least 30 minutes.

Tips for 11-BM-B

- When using the resistive heater, be careful you do not have a hook or wisp at the end of your capillary. As the capillary spins it will move the air by the thermocouple, making the

temperature reading more inaccurate. This will also prolong your run since the program measures the temperature every minute and, if that temperature reading is not within the given temperature window (due to fluctuations from the hook, for example), the program will keep the reaction at that target temperature until the temperature reads within that window.

- Widen the temperature window

Walk through guide to 17-BM-B

General need to know

- All motor movements are in mm.
- Ctrl + C is universal stop command in spec (the program they use to run commands)

Moving the detector

- To move absolute position of detector use “umv detz position” (e.g. position could = 700 → umv detz 700)
- To tweak the position of the motor, use “tw samh 2”
 - Will ask which way to go, hit enter to keep moving that direction in steps of 2 mm, switch +/- to change direction. To exit hit ctrl + c

Setting up the scan

1. Setting up sample using **resistive coil furnace**:
 - a. Align the center of rotation of the furnace using the goniometer head
 - i. Once it's done, it should be set for the rest of the experiment. If necessary, loosen screw beneath rocker and lift motor to turn goniometer and adjust goniometer as needed.
 - b. Set-up furnace
 - i. Slide your capillary into the 0.9 mm ID tubing and secure it using silica wool
 1. In order to fit a 0.5 or 0.7 mm capillary, you cannot have a hook or wisp where you sealed your capillary.
 - ii. Thread thermocouple through furnace then slide into tubing so it is along the side of your capillary.
 - iii. Attach resistive coils and assemble furnace.

1. Setting up sample using **heat blower**:

- a. Mount your sample. Move your sample horizontally as needed using “umvr samh distance” (This moves relative distance. If you put in “umvr samh -2” it will move 2 mm in the negative direction [e.g. to the right. Positive direction is to the left].)
 - i. Set samh 0 → sets x direction you have to be the zero point
 - b. Align your sample on goniometer.
 - i. Note: Camera underneath so adjust 90° from camera.
2. Align your sample (vertically) in the beam
 - a. Open the B-Station shutter, put the diode up, and open the experimental shutter.
 - b. Type in “lup samv -2 2 100 0.2” (Scans from 2 to -2 for a total of 4 mm in space in 100 steps with 0.2 sec exposure)
 - c. Right click in the middle of the transmission dip and hit “umv samv...” The motor will now move to this position.
 - d. Close experimental shutter and put the diode down.
 3. Optimize detector distance (on computer that shows the 2D diffraction patterns)
 - a. Can click “Live View” under Acquire tab to view at idle. You shouldn’t see anything – no remnants of rings. If so, make sure experimental shutter is closed then wait until the disappear.
 - b. Once dark, open experimental shutter and test detector distances using “umv detz ###”, then close experimental shutter.
 - i. 900 mm detector distance is good for resolution and Rietveld balance; 700 nm is good for Rietveld.
 4. Run test scan to see if you need to increase exposure and/or number of files to be summed.
 - a. **Rocking:** Use scanRPE(“filename”,1,10,1,20) – listed on document near computer. This will give 1 sec exposure, 10 summed frames, one total file, and 20° rocking angle. (If you don’t want rocking, use “scanPE” and drop the last number: scanPE(“filename”,1,10,1).)
 - b. **Rastering:** Use scanTHPE(“filename”,exposure,summed files,# images, range). The last number will be the range scanned; for example “8” would be +/-4 mm from the starting point. Be sure to take this into account when setting time interval!
 - i. Find thermocouple: “lup samh -8 8 200 0.2” ← using large range to find thermocouple
 - c. On computer with 2D pattern, change view by selecting “Display based on abs values” from dropdown menu.
 - d. Make sure you are not overexposing.
 - i. The maximum of each pixel is 50,000 counts. If you have ten files that will be summed with 1 second exposures, the maximum overall intensity

should be 600,000. (For 20 summed files, it would be 1,200,000 counts.) About half the intensity of maximum is fine as well.

- ii. On the window that shows the 2D diffraction plate, adjust the maximum according to the number of summed files you used. Zoom in on your brightest ring and see what the counts for that ring is. If it is less than half or $\frac{3}{4}$ to the maximum, adjust your exposure and/or number of summed scans accordingly.
 - iii. The last number in the first line is your counts.
 - iv. `p best exp ()` → negative number shows number pixels overexposed
5. Make your macro. You can modify previous macros.
- a. Transfer your exposure and summed files to the macro.
 - b. When indicating how many files, add a couple extra, so that you ensure you reach that temperature.
 - c. Note: if you need to adjust your heating profile during the reaction, you can do so. You will have to hit `ctrl+c` to stop all commands. Type or copy (by copying from the macro and hitting the scroll wheel when in the spec window) “`qdo your_macro_name.mac`” into spec (the command window) and hit enter. Next type in the name you used for your program (it was whatever comes after ‘`def`’ in your macro). Hit enter and it will restart!
 - i. You can also control the heating ramp manually using QPidCtrl Window.
6. Integrate your frames in GSAS
- a. Import image
 - i. Import > Image > from TIF image file
 - b. Load parameter file
 - i. Params > Load controls > Bkgnd&Calib > Select appropriate standard and detector distance
 - c. Integrate file
 - i. Integration > Integrate
 - ii. To auto integrate, go to Integration > Auto Integrate. This will open up a new window. Make a new folder to put the integrated files. Select the formats you want (e.g. `.csv`, `.fxye`, `.xye`) and check “Separate dir for each format.” This will make a new directory for each type of file. Then hit start. (To manipulate the graph in GSAS you’ll have to hit pause, otherwise it will continually upload files and return graph to default zoom settings. When you hit pause, also take a moment to save your GSAS file!)
7. Before you start:
- a. Resistive coil furnace controller should read -0.750 V

- b. Your main folder should be clean of images. (After experiment, transfer them to a new folder.)
- c. Check list:
 - i. Controller on
 - ii. B-station shutter (main shutter) open
 - iii. Ion counts > 2,500 counts
 - iv. Pin diode down
 - v. Experimental shutter closed
 - vi. Enter in “qdo ...”
 - vii. Enter in name of defined program

How to make the calibration file

1. Run standard then import image into GSAS
2. Show rings and determine the minimum d-spacing → mm calibration
 - a. Calibration > Calibration, then go to 1st ring (highest 2Theta) and put at least four spots spread around the ring.
 - b. Right click in the middle and then auto calibrates
3. Check “Penetration” then go to Calibration > Recalibration
 - a. Do this a few times until penetration number remains constant
4. Check “Show Int. Limits”
5. Find beam stop and hover over to find degrees. Then enter it into inner 2Theta. Do the same for the outer 2Theta
6. Make mask “5” to “-5”
7. Parm > Save controls
8. Integrate > Integrate

Types of scans

- ScanTRPE – sleeps for specific amount of time. The intervals in seconds. (If you want a scan every 60 seconds, the last number should be 60. FYI, dark image takes ca. 20 seconds and your exposure time * number of summed files is your image collection time.)
- ScanRPE – takes an immediate scan. Can you use if you want continuous collections
- ScanPE – takes an immediate scan as with RPE, but this one doesn’t have rocking.
- ScanTPE – similar to TRPE, but doesn’t have rocking.
- ScanTHPE – similar to TRPE, but rasters instead of rocks
 - Note with rastering – the temp won’t be in your metadata! You need to get the log file from the controller computer (e.g. the computer that has your macros)
- ScanHPE – similar to ScanPE, but rasters
 - scanHPE(“filename”,exposure,sum,# images,range)

- See comment above about rastering.

Note: Make sure the "s" in scanHPE, etc. is lower case!

A more direct way to move the detector and sample

- Sample and detector: use simple control
 - Careful, not relative movement, but absolute!
- Sample x
 - Move only 2-3 mm at a time
 - (+) moves to the left, (-) moves to the right

Appendix B: Supplementary Information for Chapter 3. Chapter 3.

Reprinted with permission from ‘Rebecca McClain, Christos D. Malliakas, Jiahong Shen, Jiangang He, Chris Wolverton, Gabriela B. González, and Mercouri G. ‘Mechanistic insight of KBiQ_2 (Q= S, Se) using panoramic synthesis towards synthesis-by-design.’ *Chemical Science*, 2021, 12, 4, 1378-1391.’

Copyright © 2021, The Royal Society of Chemistry

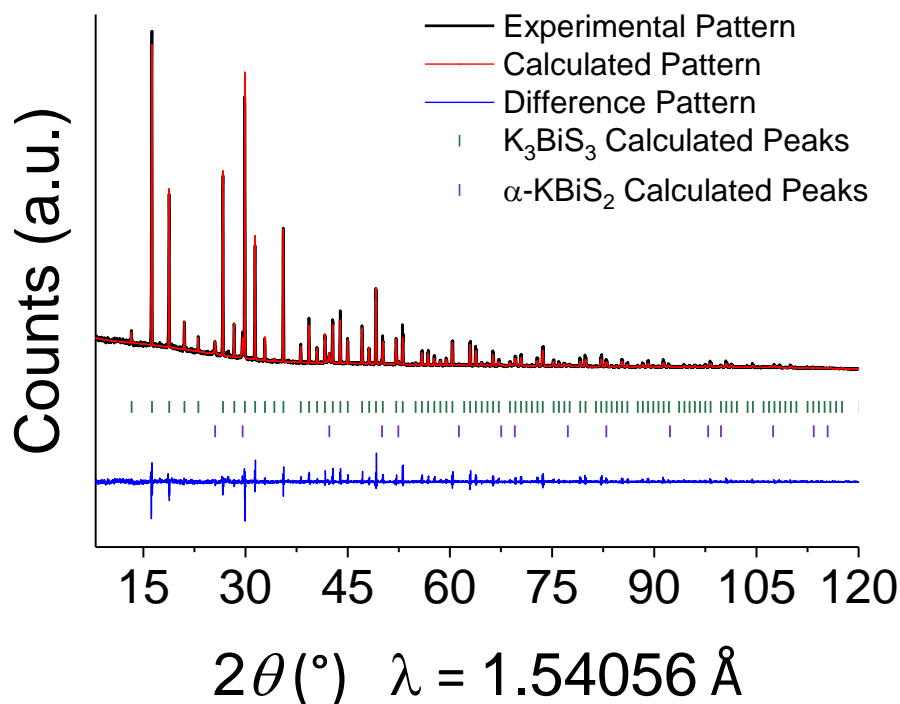


Figure S1: Structure solution for K_3BiS_3 from powder x-ray diffraction data.

Structure for K_3BiS_3 was solved from PXRD data collected on a STOE STADI P (Cu $\text{K}\alpha 1$ radiation) using Rietveld refinement. A 7.7(2) wt% impurity of $\alpha\text{-KBiS}_2$ was calculated in the sample.

Table S1. Crystal data and structure refinement for K_3BiS_3 at 298 K.

Empirical formula	$K_3 Bi_1 S_3$
Formula weight	422.5
Temperature	298 K
Wavelength	1.54056 Å
Crystal system	cubic
Space group	$P2_13$
Unit cell dimensions	$a = 9.44252(14)$ Å, $\alpha = 90^\circ$ $b = 9.44252(14)$ Å, $\beta = 90^\circ$ $c = 9.44252(14)$ Å, $\gamma = 90^\circ$
Volume	841.91(2) Å ³
Z	4
Density (calculated)	3.3329 g/cm ³
Absorption coefficient	60.678 mm ⁻¹
F(000)	64
2 θ range for data collection	3.000 to 124.680° [Step 0.015°]
Refinement method	Rietveld Refinement
Constraints / restraints / parameters	0 / 0 / 42
Goodness-of-fit	1.53
Profile R indices	$R_p = 0.0886$, $wR_p = 0.1362$
Final Bragg R indices [2σ]	$R_{Bragg} = 0.0586$, $wR_{Bragg} = 0.0631$
Bragg R indices [all data]	$R_{all} = 0.0663$, $wR_{all} = 0.0635$
Largest diff. peak and hole	0.72 and -1.83 e ⁻ Å ⁻³

$R = \frac{\sum ||F_o| - |F_c||}{\sum |F_o|}$, $wR = \left\{ \frac{\sum [w(|F_o|^2 - |F_c|^2)^2]}{\sum [w(|F_o|^4)]} \right\}^{1/2}$

Table S2: Atomic coordinates ($\times 10^4$) and equivalent isotropic displacement parameters (Å² $\times 10^3$) for K_3BiS_3 at 298 K with estimated standard deviations in parentheses.

Label	x	y	z	Occupancy	U_{eq}^*
K(1)	614(12)	614(12)	614(12)	1	88(3)
K(2)	5777(12)	5777(12)	5777(12)	1	146(6)
K(3)	8221(11)	8221(11)	8221(11)	1	159(5)
Bi(1)	2842(2)	2842(2)	2842(2)	1	108(1)
S(1)	412(11)	2612(11)	3524(9)	1	106(5)

* U_{eq} is defined as one third of the trace of the orthogonalized U_{ij} tensor.

Table S3: Selected bond lengths [\AA] for K_3BiS_3 at 298 K with estimated standard deviations in parentheses.

Label	Distances
K(1)-K(2)	3.655(16)
K(1)-K(3)	3.914(16)
K(1)-K(3)	4.515(15)
K(1)-Bi(1)	3.645(11)
K(1)-Bi(1)	4.430(11)
K(1)-S(1)	3.338(14)
K(1)-S(1)	3.105(15)
K(2)-K(3)	3.997(15)
K(2)-K(3)	4.580(15)
K(2)-Bi(1)	4.145(11)
K(2)-S(1)	3.210(14)
K(2)-S(1)	3.285(15)
K(3)-Bi(1)	3.867(10)
K(3)-S(1)	3.531 (14)
K(3)-S(1)	3.383(14)
Bi(1)-S(1)	2.393(10)

Symmetry transformations used to generate equivalent atoms:

(1) $-x+1/2, -y+1, z-1/2$ (2) $-x+1, y-1/2, -z+1/2$ (3) $x-1/2, -y+1/2, -z+1$ (4) $x-1, y-1, z-1$ (5) $-x+1/2, -y, z-1/2$ (6) $-x, y-1/2, -z+1/2$ (7) $x-1/2, -y+1/2, -z$ (8) z, x, y (9) $-z+1/2, -x, y-1/2$ (10) y, z, x (11) $y-1/2, -z+1/2, -x$ (12) $-x+3/2, -y+1, z-1/2$ (13) $-x+1, y-1/2, -z+3/2$ (14) $x-1/2, -y+3/2, -z+1$ (15) $-x+1/2, -y+1, z+1/2$ (16) $-x+1, y+1/2, -z+1/2$ (17) $x+1/2, -y+1/2, -z+1$ (18) $z+1/2, -x+1/2, -y+1$ (19) $-z+1, x+1/2, -y+1/2$ (20) $-y+1, z+1/2, -x+1/2$ (21) $-y+1/2, -z+1, x+1/2$ (22) $-x+3/2, -y+1, z+1/2$ (23) $-x+1, y+1/2, -z+3/2$ (24) $x+1/2, -y+3/2, -z+1$ (25) $-z+3/2, -x+1, y+1/2$ (26) $y+1/2, -z+3/2, -x+1$ (27) $x+1, y+1, z+1$ (28) $-x+1/2, -y, z+1/2$ (29) $-x, y+1/2, -z+1/2$ (30) $x+1/2, -y+1/2, -z$

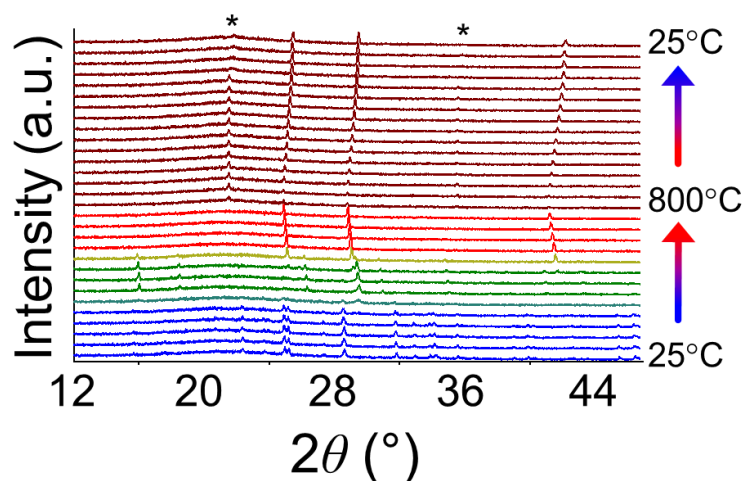


Figure S2: Overlaid diffraction patterns of 1.5 K₂S + 1 Bi₂S₃ panoramic synthesis.

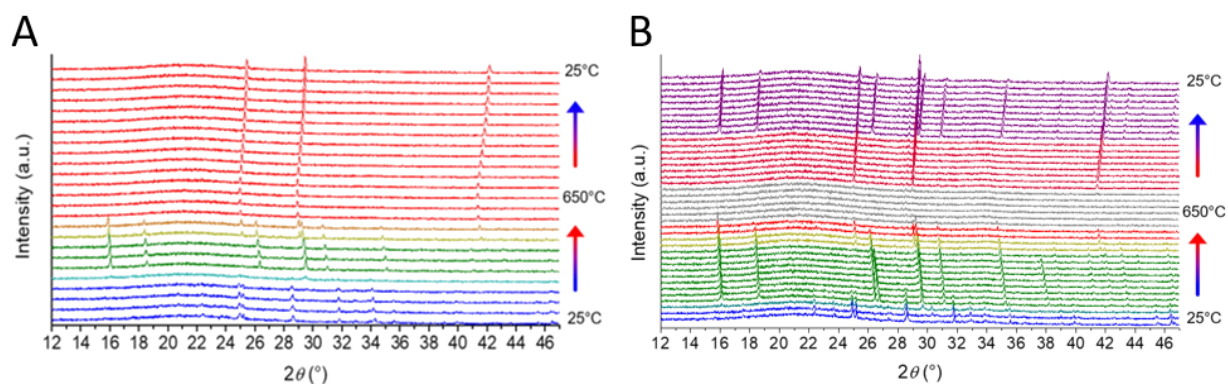


Figure S3: (a) Panoramic syntheses for 2 K₂S : 1 Bi₂S₃. (b) Panoramic synthesis for 5 K₂S : 1 Bi₂S₃. In this reaction, K₃BiS₃ appears earlier in the reaction (shown in green) and also as a final product with KBiS₂ (purple). The regime where materials are in a melt are shown in grey.

To study the influence of increased amounts of K₂S on the formation of KBiS₂ and investigate if additional potassium-rich phases exist, the amount of K₂S relative to Bi₂S₃ was increased. These reactions, and subsequent reactions, were conducted at a maximum temperature of 650°C to avoid the crystallization of the SiO₂ spacer to cristobalite. With an increase in the K₂S, the 2 K₂S : 1 Bi₂S₃ reaction features a pathway is similar to that of the 1.5:1 ratio, as shown in

Figure S3a. K_3BiS_3 forms at ca. 270°C and disappears at ca. 585°C , as indicated by the green patterns; KBiS_2 evolves at ca. 465°C , as denoted by the red patterns. However, when the amount of K_2S is further increased to a 5:1 ratio, the K_3BiS_3 appears at a lower temperature and as a final product.

The increased ratio of K_2S in the 5:1 ratio manifests in different behavior of the K-Bi-S system. The crystallization of the intermediate formed at a lower temperature, the intermediate appeared as a final product, and KBiS_2 melted at a temperature lower than 650°C . K_3BiS_3 crystallized at 180°C and KBiS_2 emerges at 420°C , as shown in green and red, respectively, in Figure S3b. In this ratio, K_3BiS_3 also appears as a final product after recrystallizing at 375°C upon cooling. The increased concentration of K_2S in this reaction appears to stabilize K_3BiS_3 at ambient temperature, as it is present as a final product in the 5:1 ratio. It is unclear if the concentration gradient drives the formation to a lower reaction temperature or if, for example, the excess of K_2S stabilizes the intermediate phase thereby enabling a lower reaction temperature. Additional characterization of the local structure, such as Pair Distribution Function, would elucidate if the earlier occurrence is a result of surface stabilizing effects. In this reaction, K_3BiS_3 and KBiS_2 persist until melting by 600°C ; this is the first instance of in this work that KBiS_2 melts below 750°C . Using in-situ techniques, we have discovered that the increased ratio of K_2S lowers the formation temperature for a key intermediate phase, promotes the melting of KBiS_2 , and manifests in the formation of the intermediate phase other not observed at ambient temperature.

Table S4: Crystal data and structure refinement for β -KBiS₂ at 293 K.

Empirical formula	K Bi S ₂
Formula weight	312.2
Temperature	293 K
Wavelength	0.45777 Å
Crystal system	trigonal
Space group	R-3m
Unit cell dimensions	a = 4.12983(3) Å, $\alpha = 90^\circ$ b = 4.12983(3) Å, $\beta = 90^\circ$ c = 22.09484(17) Å, $\gamma = 120^\circ$
Volume	326.351(4) Å ³
Z	3
Density (calculated)	4.7656 g/cm ³
Absorption coefficient	13.565 mm ⁻¹
F(000)	402
2 θ range for data collection	2.004 to 29.997° [Step 0.001°]
Refinement method	Rietveld
Constraints / restraints / parameters	0 / 0 / 25
Goodness-of-fit	1.21
Profile R indices	R _p = 0.1286, wR _p = 0.1662
Final Bragg R indices [2 σ]	R _{Bragg} = 0.0183, wR _{Bragg} = 0.0220
Bragg R indices [all data]	R _{all} = 0.0183, wR _{all} = 0.0220
Largest diff. peak and hole	0.63 and -0.68 e ⁻ Å ⁻³

$$R = \frac{\sum ||F_o| - |F_c||}{\sum |F_o|}, wR = \left\{ \frac{\sum [w(|F_o|^2 - |F_c|^2)^2]}{\sum [w(|F_o|^4)]} \right\}^{1/2}$$

Table S5: Atomic coordinates ($\times 10^4$) and equivalent isotropic displacement parameters ($\text{Å}^2 \times 10^3$) for β -KBiS₂ at 293 K with estimated standard deviations in parentheses.

Label	x	y	z	Occupancy	U _{eq} *
Bi(1)	0	0	0	1	39(1)
K(1)	3333.33	6666.67	1666.67	1	34(1)
S(1)	-3333.33	3333.33	710(1)	1	35(1)

*U_{eq} is defined as one third of the trace of the orthogonalized U_{ij} tensor.

Table S6: Anisotropic displacement parameters ($\text{\AA}^2 \times 10^3$) for $\beta\text{-KBiS}_2$ at 293 K with estimated standard deviations in parentheses.

Label	U_{11}	U_{22}	U_{33}	U_{12}	U_{13}	U_{23}
Bi(1)	38(1)	38(1)	41(1)	19(1)	0	0
K(1)	37(1)	37(1)	27(2)	19(1)	0	0
S(1)	37(1)	37(1)	31(2)	18(1)	0	0

The anisotropic displacement factor exponent takes the form: $-2\pi^2[h^2 a^{*2} U_{11} + \dots + 2hka^* b^* U_{12}]$.

Table S7: Selected bond lengths [\AA] for $\beta\text{-KBiS}_2$ at 293 K with estimated standard deviations in parentheses.

Label	Distances
Bi(1)-K(1)	4.38700(5)
Bi(1)-S(1)	2.8540(10)
K(1)-K(1)	4.12983(5)
K(1)-S(1)	3.1865(12)

Symmetry transformations used to generate equivalent atoms:

(1) $x-1, y-1, z$ (2) $x, y-1, z$ (3) $x+1/3, y+2/3, z+2/3$ (4) $x+1/3, y+2/3, z+2/3$ (5) $x+1/3, y+2/3, z+2/3$ (6) $x+1, y, z$ (7) $y-1, x, -z$ (8) $y, x, -z$ (9) $y, x+1, -z$ (10) $x-1, y, z$ (11) $x, y+1, z$ (12) $x+1, y+1, z$ (13) $y+2/3, x+1/3, -z+1/3$ (14) $y+2/3, x+1/3, -z+1/3$ (15) $y+2/3, x+1/3, -z+1/3$ (16) $x+2/3, y+1/3, z+1/3$ (17) $x+2/3, y+1/3, z+1/3$ (18) $x+2/3, y+1/3, z+1/3$

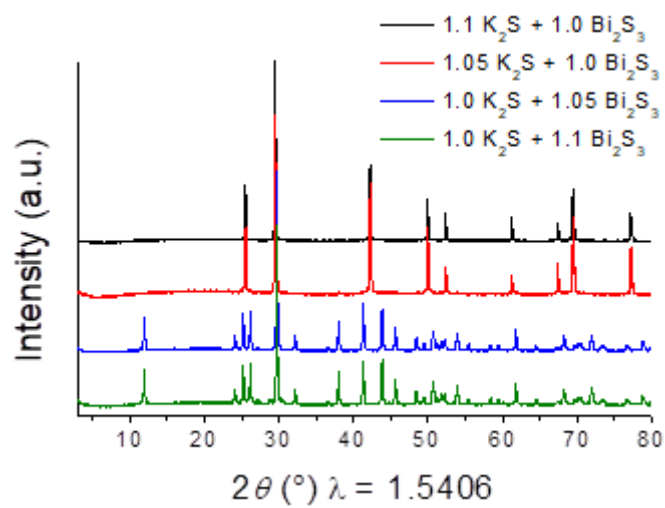


Figure S4: Reactions to test boundary of ordered vs disordered rocksalt formation for KBiS₂. Stoichiometric ratio yielded the ordered phase, while a 5% excess yielded disordered phase.

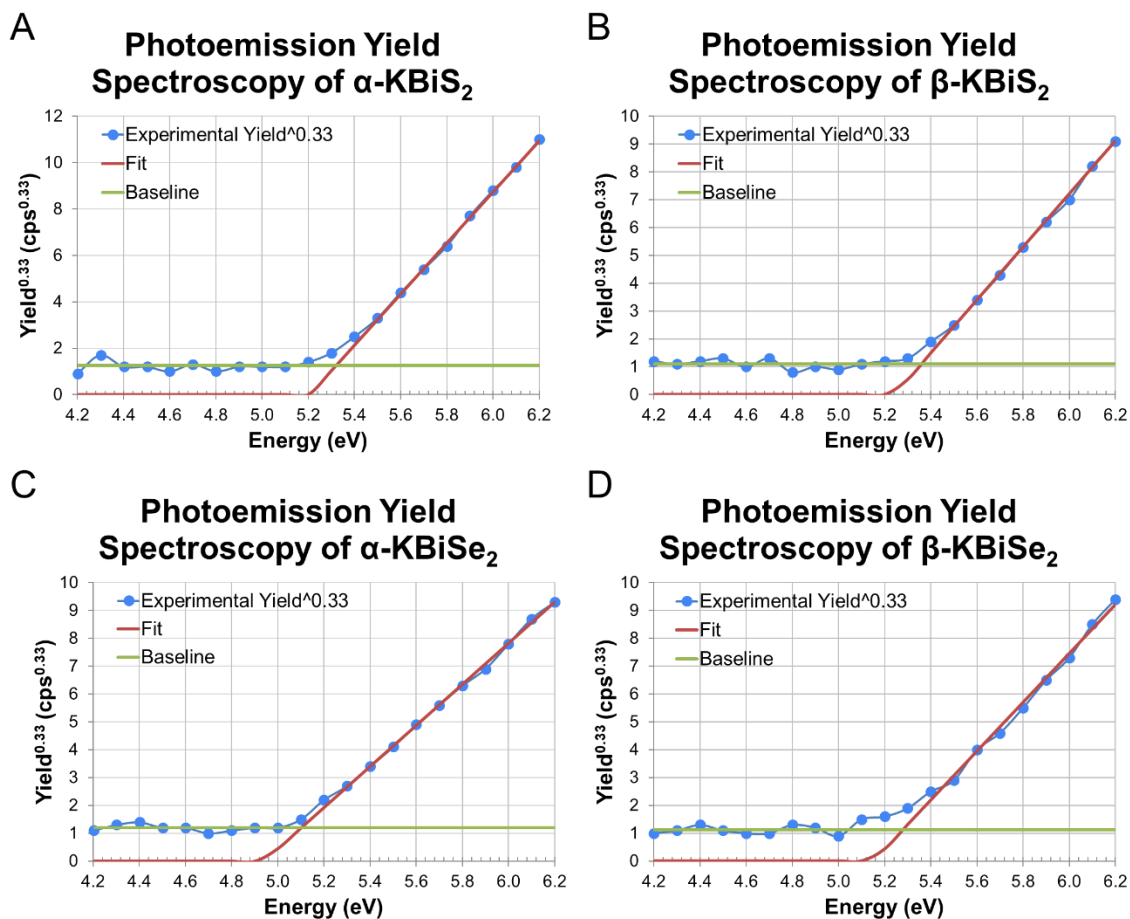
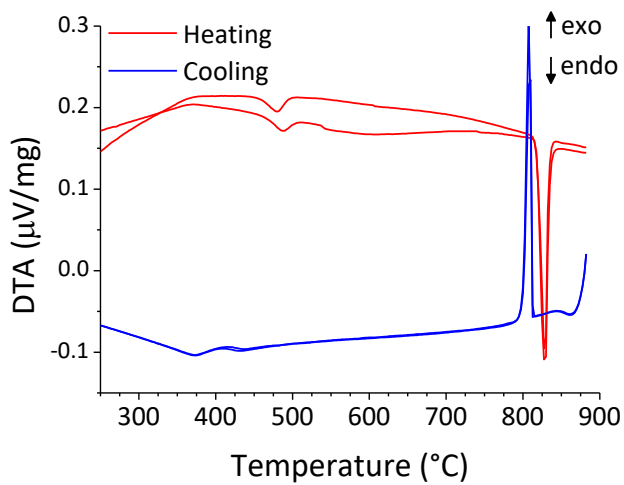


Figure S5: Photoemissions yield spectroscopy in air using a Kelvin Probe for (a) α -KBiS₂, (b) β -KBiS₂, (c) α -KBiSe₂ and (d) β -KBiSe₂.

Energy of valence band maxima is determined from the intersection of the baseline and fit line for the respective spectrum. Experimental energies of valence band maxima are shown in Table S11.

Table S8: Table of valence band maxima, conduction band minima, and band gap energies.

	Valence Band Maxima (eV)	Conduction Band Minima (eV)	Band Gap (eV)
α -KBiS ₂	5.32	4.09	1.23
β -KBiS ₂	5.36	3.81	1.55
α -KBiSe ₂	5.10	4.26	0.84
β -KBiSe ₂	5.28	4.19	1.09
Si	4.60	3.5	1.1
CdTe	4.95	3.5	1.5
a-TiO ₂	5.16	2.0	3.2
MAPbI ₃	5.44	3.92	1.52

Figure S6: β -KBiS₂ thermal analysis.

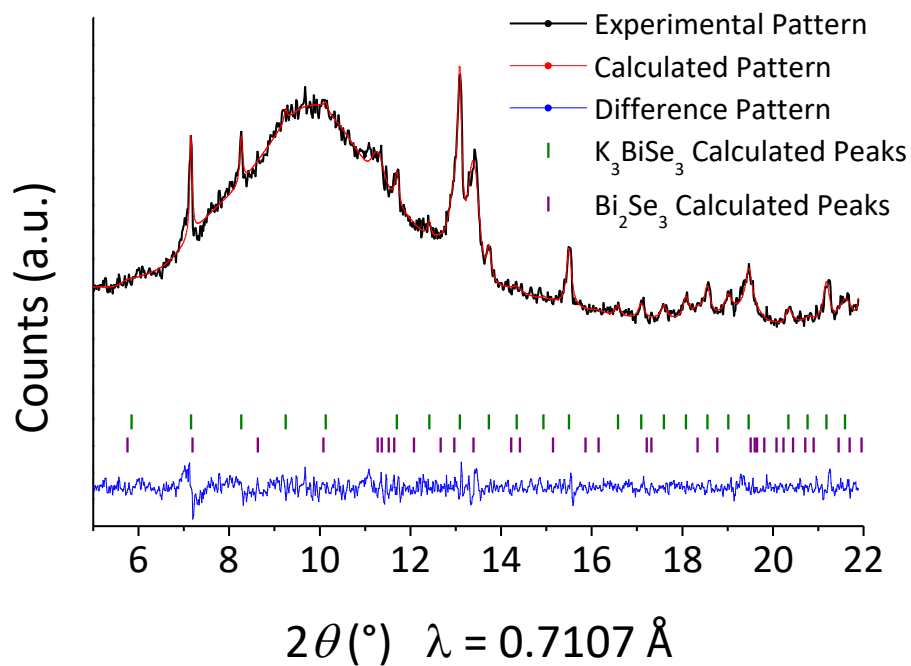


Figure S7: Le Bail refinement for PXRD collected at 195°C during $K_2Se + Bi_2Se_3$ panoramic synthesis. The lattice constant for K_3BiSe_3 expands to 9.8590(7) Å at 195°C. As shown by this refinement, Bi_2Se_3 persists at this temperature.

Table S9: Crystal data and structure refinement for β -KBiSe₂ at 298 K.

Empirical formula	K1 Bi1 Se2
Formula weight	406
Temperature	298 K
Wavelength	0.41283 Å
Crystal system	trigonal
Space group	R -3 m
Unit cell dimensions	a = 4.264423(14) Å, $\alpha = 90^\circ$ b = 4.264423(14) Å, $\beta = 90^\circ$ c = 23.02901(14) Å, $\gamma = 120^\circ$
Volume	362.682(3) Å ³
Z	3
Density (calculated)	5.5766 g/cm ³
Absorption coefficient	12.726 mm ⁻¹
F(000)	510
2 θ range for data collection	0.500 to 27.581° [Step 0.001°]
Refinement method	Rietveld Refinement
Constraints / restraints / parameters	0 / 0 / 26
Goodness-of-fit	1.10
Profile R indices	R _p = 0.1383, wR _p = 0.1762
Final Bragg R indices [3 σ]	R _{Bragg} = 0.0263, wR _{Bragg} = 0.0287
Bragg R indices [all data]	R _{all} = 0.0269, wR _{all} = N/A
Largest diff. peak and hole	1.04 and -3.45 e·Å ⁻³

$$R = \frac{\sum||F_o| - |F_c||}{\sum|F_o|}, wR = \left\{ \frac{\sum[w(|F_o|^2 - |F_c|^2)^2]}{\sum[w(|F_o|^4)]} \right\}^{1/2}$$

Table S10: Atomic coordinates ($\times 10^4$) and equivalent isotropic displacement parameters ($\text{Å}^2 \times 10^3$) for β -KBiSe₂ at 298 K with estimated standard deviations in parentheses.

Label	x	y	z	Occupancy	U _{eq} *
Bi(1)	3333.33	6666.67	1666.67	1	21(1)
K(1)	0	0	0	1	18(2)
Se(1)	0	0	2385(1)	1	16(1)

*U_{eq} is defined as one third of the trace of the orthogonalized U_{ij} tensor.

Table S11: Anisotropic displacement parameters ($\text{\AA}^2 \times 10^3$) for β -KBiSe₂ at 298 K with estimated standard deviations in parentheses.

Label	U ₁₁	U ₂₂	U ₃₃	U ₁₂	U ₁₃	U ₂₃
Bi(1)	19(1)	19(1)	25(1)	9(1)	0	0
K(1)	22(2)	22(2)	11(2)	11(1)	0	0
Se(1)	17(1)	17(1)	14(1)	9(1)	0	0

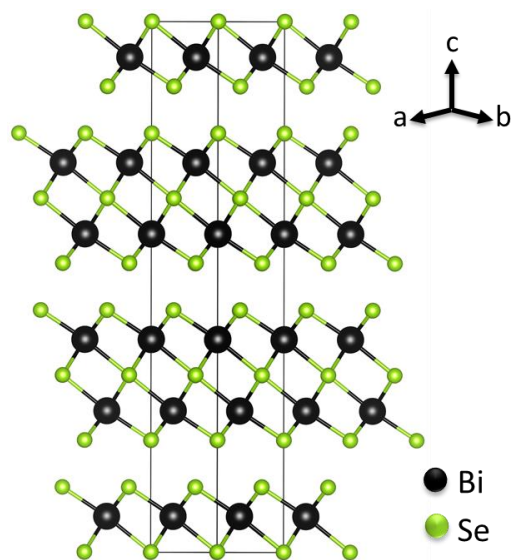
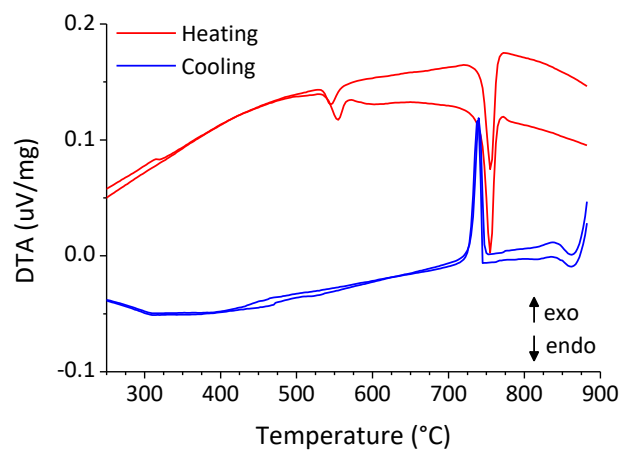
The anisotropic displacement factor exponent takes the form: $-2\pi^2[h^2a^{*2}U_{11} + \dots + 2hka^*b^*U_{12}]$.

Table S12: Bond lengths [\AA] for β -KBiSe₂ at 298 K with estimated standard deviations in parentheses.

Label	Distances
Bi(1)-K(1)	4.55997(4)
Bi(1)-Se(1)	2.9664 (6)
K(1)-K(1)	4.26442(4)
K(1)-Se(1)	3.2908(7)

Symmetry transformations used to generate equivalent atoms:

(1) $x, y+1, z$ (2) $x+1, y+1, z$ (3) $x+2/3, y+1/3, z+1/3$ (4) $x+2/3, y+1/3, z+1/3$ (5) $x+2/3, y+1/3, z+1/3$ (6) $y+2/3, x+1/3, -z+1/3$ (7) $y+2/3, x+1/3, -z+1/3$ (8) $y+2/3, x+1/3, -z+1/3$ (9) $x-1, y-1, z$ (10) $x-1, y, z$ (11) $x, y-1, z$ (12) $x+1, y, z$ (13) $x+1/3, y+2/3, z+2/3$ (14) $x+1/3, y+2/3, z+2/3$ (15) $x+1/3, y+2/3, z+2/3$ (16) $y+2/3, x+1/3, -z+1/3$ (17) $x+1/3, y+2/3, z+2/3$ (18) $x+2/3, y+1/3, z+1/3$

Figure S8: Extended structure of Bi_2Se_3 .Figure S9: $\beta\text{-KBiSe}_2$ thermal analysis.

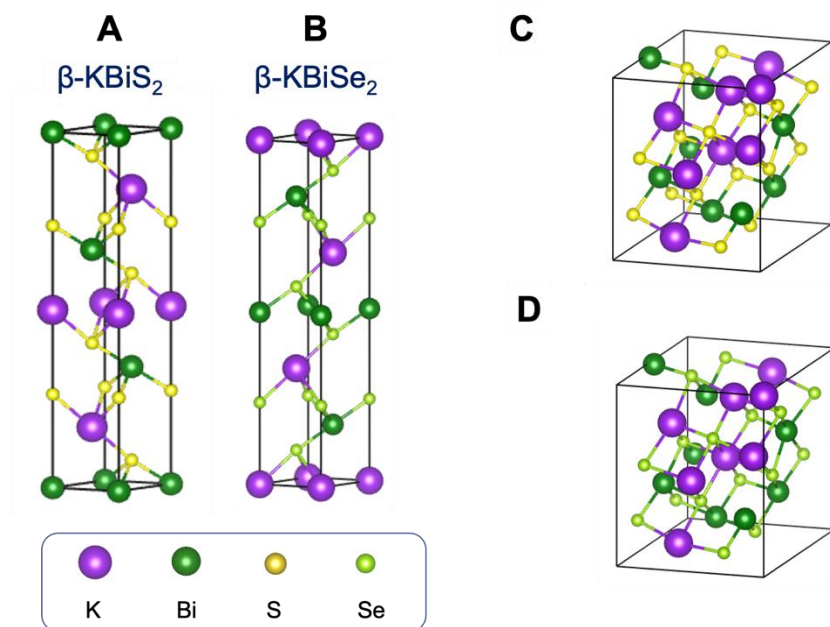


Figure S10: The crystal structures used in DFT calculations of (a) β - KBiS_2 , (b) β - KBiSe_2 , (c) α - KBiS_2 and (d) α - KBiSe_2 .

The β - KBiQ_2 has a $R\bar{3}m$ structure, which is an elongated rocksalt-structure in the $[111]$ direction. The α - KBiQ_2 ($Fm\bar{3}m$) is generated by both SQS (for formation energy calculations) and supercells (for band structure calculations).

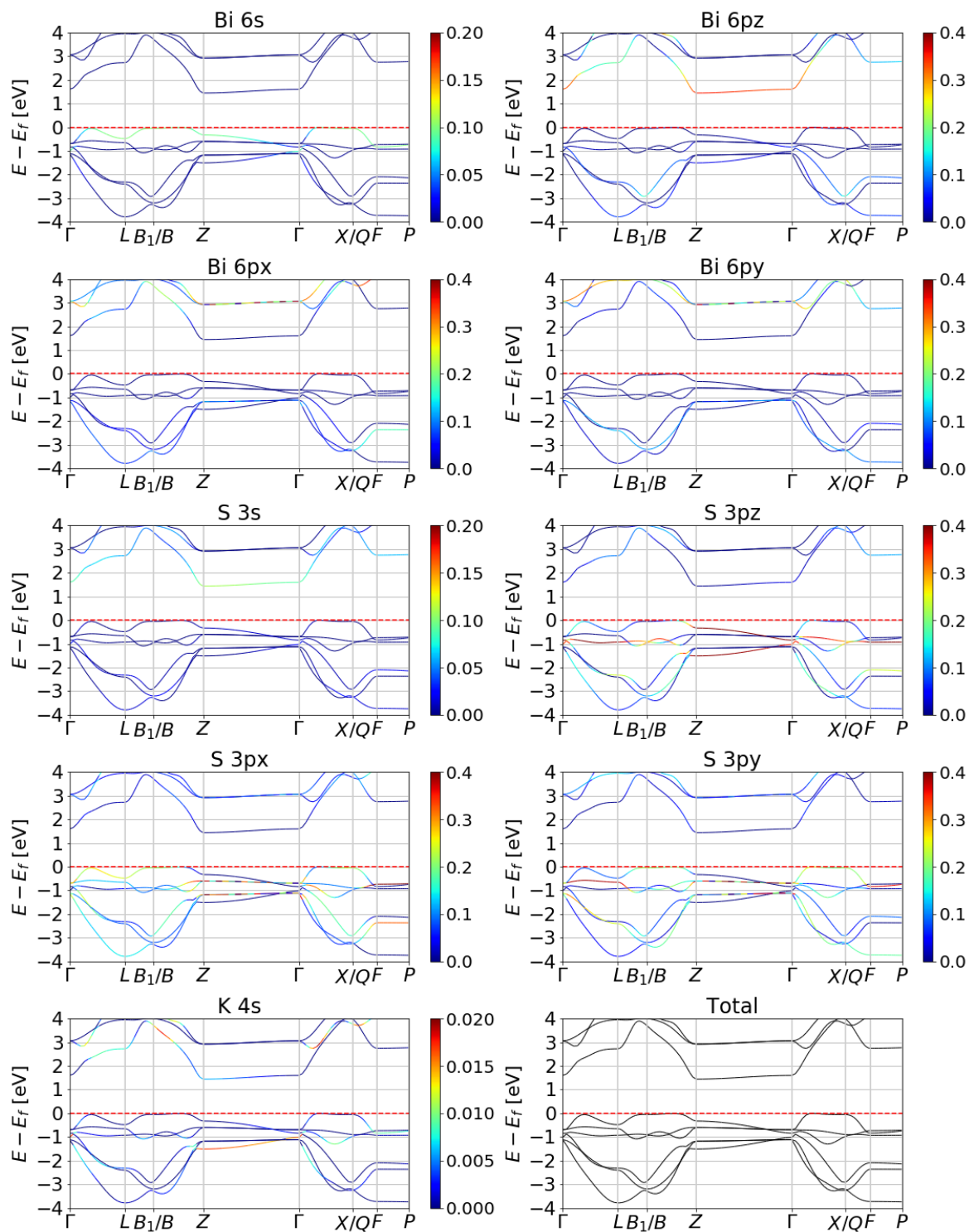


Figure S11: Orbital decomposed band structure, which shows the atomic orbital contribution to the β -KBiS₂ band structure.

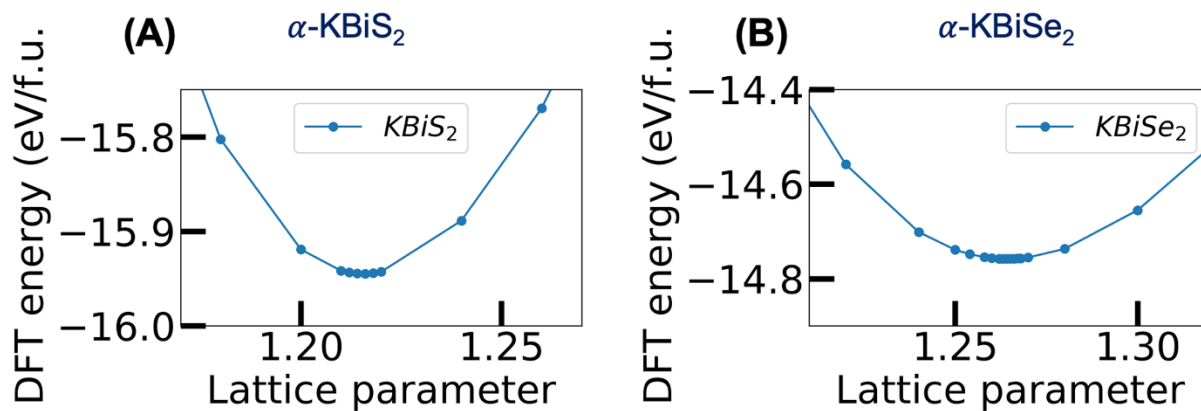


Figure S12: DFT total energies of (a) α - KBiS_2 and (b) α - KBiSe_2 as a function of lattice parameter scaled to the reference structure.

The lattice parameters of primitive rocksalt α - KBiQ_2 are determined by the lowest energy configurations as shown in Figure S12. The $2 \times 2 \times 2$ supercells are then generated using these lattice parameters and the lowest energy one is chosen from 10 randomly mixed cation-disordered supercells as the structures for α - KBiQ_2 .

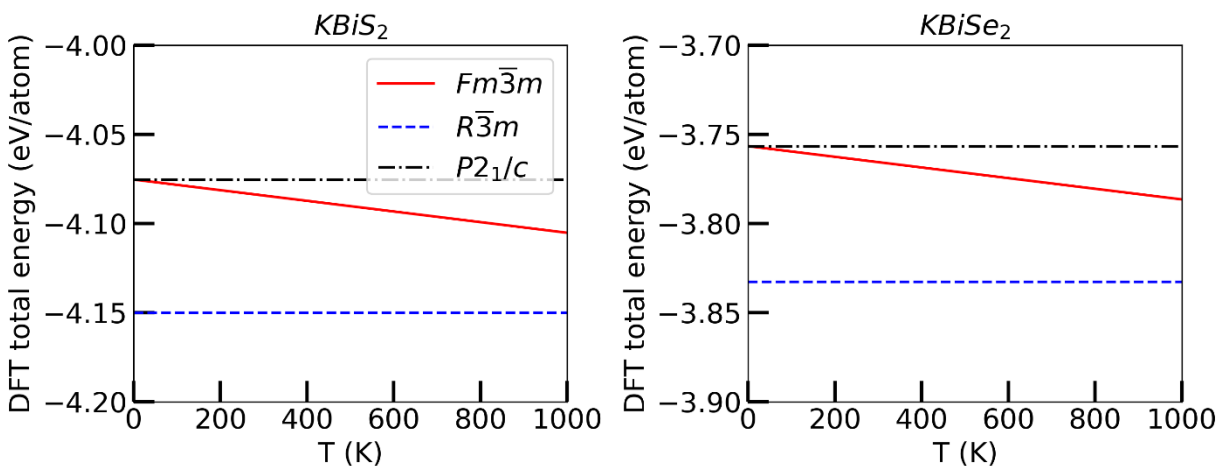


Figure S13: DFT mixing entropy calculations for the stability of KBiQ_2 ($Q = \text{S, Se}$) crystallized in the rocksalt ($Fm\bar{3}m$, red line), $\alpha\text{-NaFeO}_2$ ($R\bar{3}m$, blue line), and CsSbS_2 ($P2_1/c$, black line) structure types at finite temperatures.

DFT mixing entropy calculations confirm the energetic stability of KBiS_2 and KBiSe_2 crystallizing in the $\alpha\text{-NaFeO}_2$ ($R\bar{3}m$) structure type over the rocksalt and CsSbS_2 structure types. The calculations additionally highlight that the KBiQ_2 compositions are least stable in the monoclinic CsSbS_2 structure type compared to the $Fm\bar{3}m$ and $R\bar{3}m$ structures, thereby corroborating the experimental observation that KBiQ_2 does not crystallize in this monoclinic structure type.

Table S13: Energy differences (ΔE) in meV/atom between the CsSbS_2 ($P2_1/c$) and $\alpha\text{-NaFeO}_2$ ($R\bar{3}m$) structure types for reported ABiQ_2 ($A = \text{Li, Na, K, Rb, Cs}$; $Q = \text{S, Se, Te}$) compounds, where $\Delta E = E_{P2_1/c} - E_{R\bar{3}m}$.

	Li	Na	K	Rb	Cs
S	14	18	75	46	10
Se	–	23	76	–	–

Te	28	28	–	–	–
-----------	----	----	---	---	---

The structures of RbBiS_2 ($R\bar{3}m$) and CsBiS_2 ($P2_1/c$) are used as prototypes for the CsSbS_2 ($P2_1/c$) and $\alpha\text{-NaFeO}_2$ ($R\bar{3}m$) structure type while the SQS structure, as discussed in the main text, is used to simulate the disordered rocksalt structures.

Table S14: Fitted transition temperatures, in K, between the DFT-calculated ground state $\alpha\text{-NaFeO}_2$ and the rocksalt structure types for all ABiQ_2 ($A=\text{Li, Na, K, Rb, Cs}$; $Q=\text{S, Se, Te}$) compounds.

	Li	Na	K	Rb	Cs
S	260 K	440 K	730 K	1220 K	690 K
Se	–	430 K	750 K	–	–
Te	260 K	400 K	–	–	–

The transition temperature between the $\alpha\text{-NaFeO}_2$ and rocksalt structure types is proportional to the energy difference between the $T = 0$ K energy of the DFT-calculated ground state $\alpha\text{-NaFeO}_2$ structure type and the $T = 0$ K energy of the SQS¹¹⁷ rocksalt structures. By fitting the transition temperature of KBiS_2 (730K), we obtain the transition temperatures for all other compounds.

We note that the calculated transformation temperatures are fairly approximate, and should not be interpreted too quantitatively, but rather are only a guide of the order-disorder trends in these compounds. A more quantitative calculation of transformation temperature would involve determination of the configurational and vibrational entropy contributions, as shown by Hua *et al.*

Xia Hua, Shiqiang Hao, and Chris Wolverton, First-principles study of vibrational entropy effects on the PbTe-SrTe phase diagram, *Phys. Rev. Materials* 2, 095402.

Appendix C: Supplementary Information for Chapter 4.

Reprinted with permission from 'Rebecca McClain, Christos D. Malliakas, Jiahong Shen, Jiangang He, Christopher Wolverton, and Mercouri G. Kanatzidis. 'In Situ Mechanistic Studies of Two Divergent Synthesis Routes forming the Heteroanionic BiOCuSe.' *Journal of the American Chemical Society*, **2021**, 143, 31, 12090-12099.'

Copyright © 2021, American Chemical Society

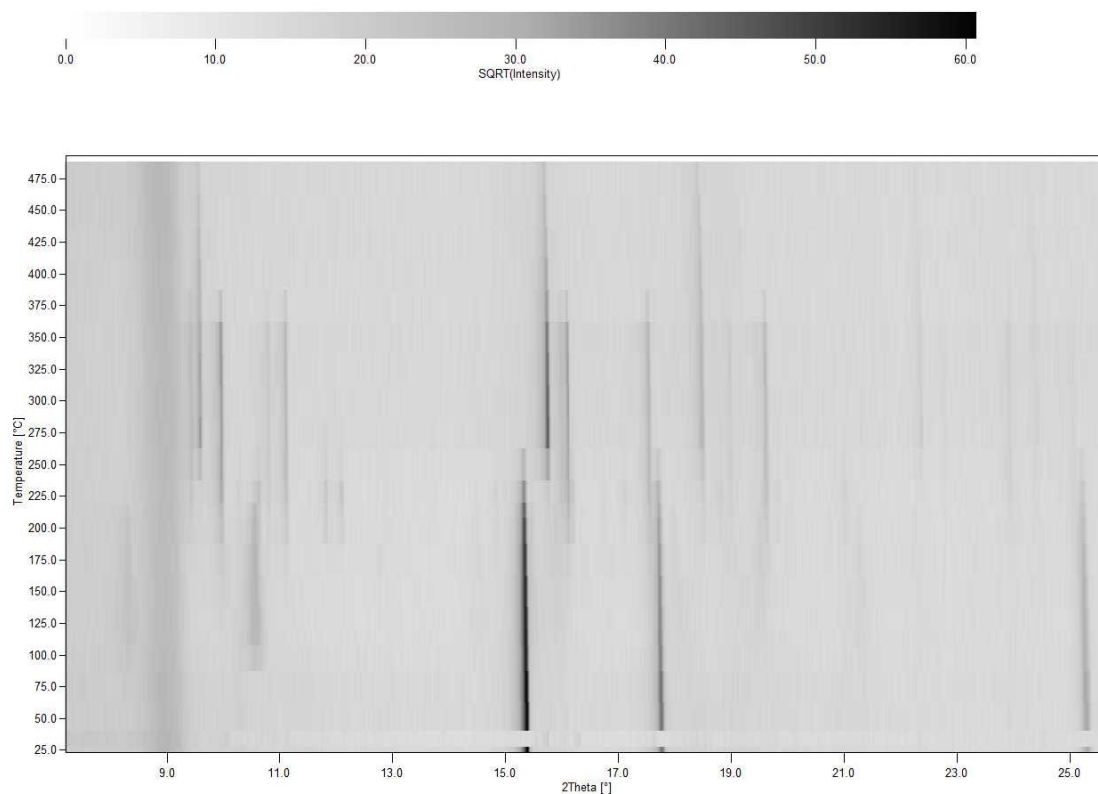


Figure S14: Heat map of 2Cu + Se reaction sieved <math><65\mu\text{m}</math> and heated at 4°C/min using Ag radiation. The persistent, diffuse peak at ca. 9°2θ is quartz from the quartz capillaries.

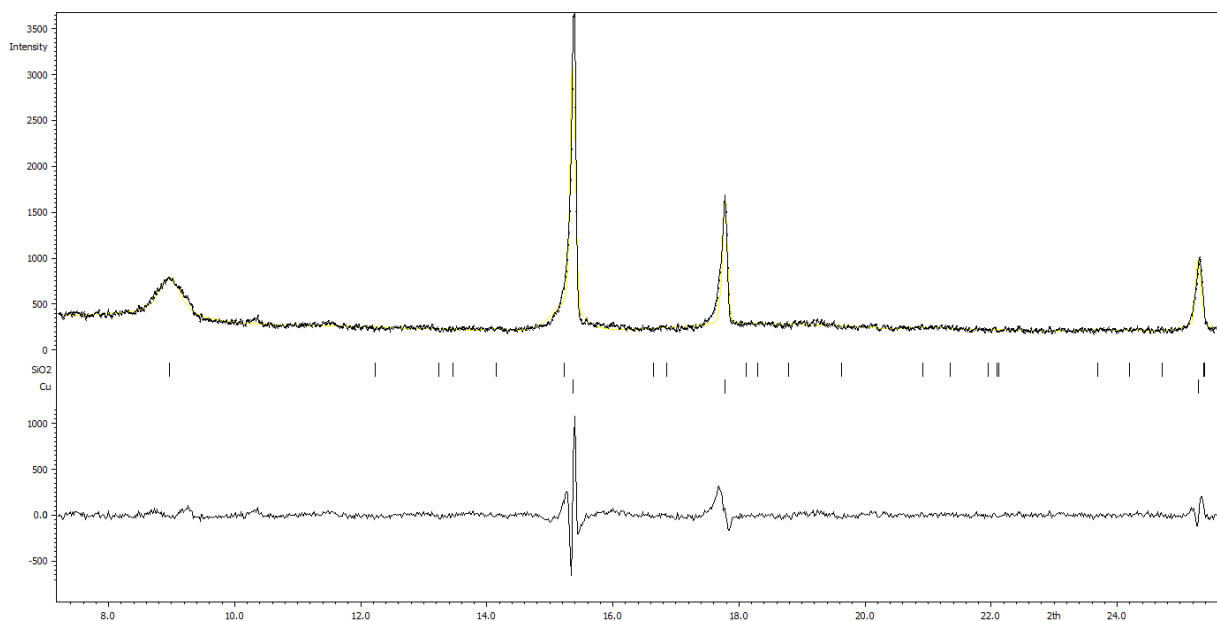


Figure S15: Rietveld refinement of the room temperature scan of 2Cu + Se in situ synthesis. As shown in the diffractogram, SiO₂ (as quartz) can be observed and is a result of the quartz capillaries used.

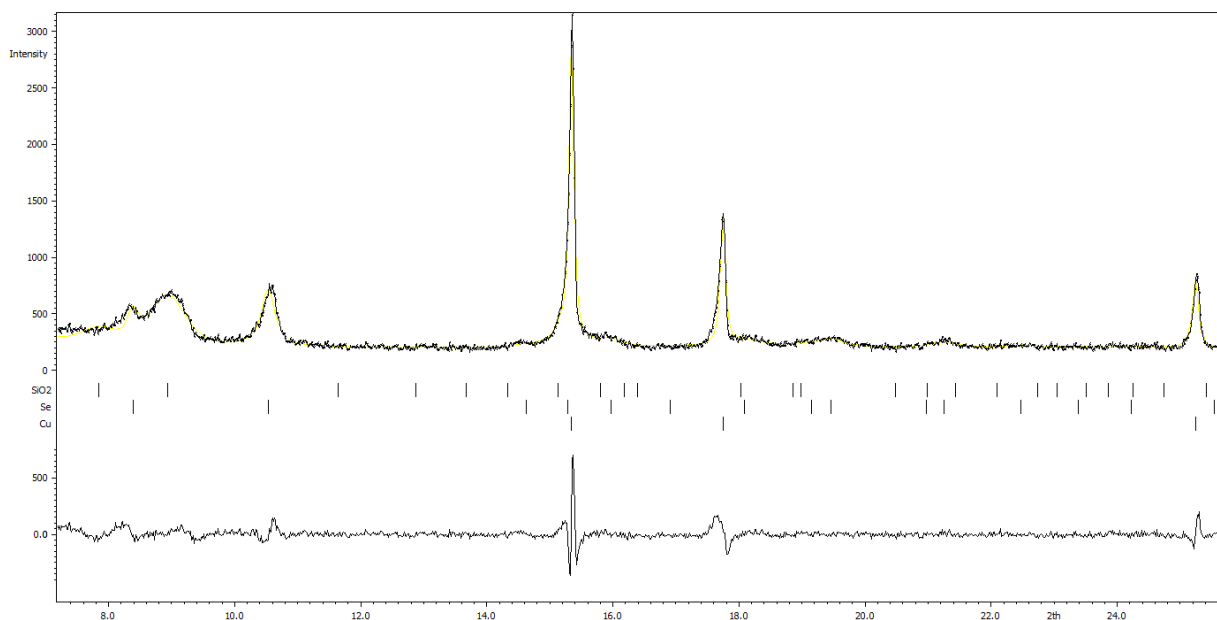


Figure S16: Rietveld refinement of the scan at 115°C showing the crystallization of Se in the 2Cu + Se in situ synthesis. This diffractogram is shown in place of the onset diffractogram, as peak is better observed as it intensifies. As before, SiO₂ (as quartz) is present as a result of the quartz capillaries used.

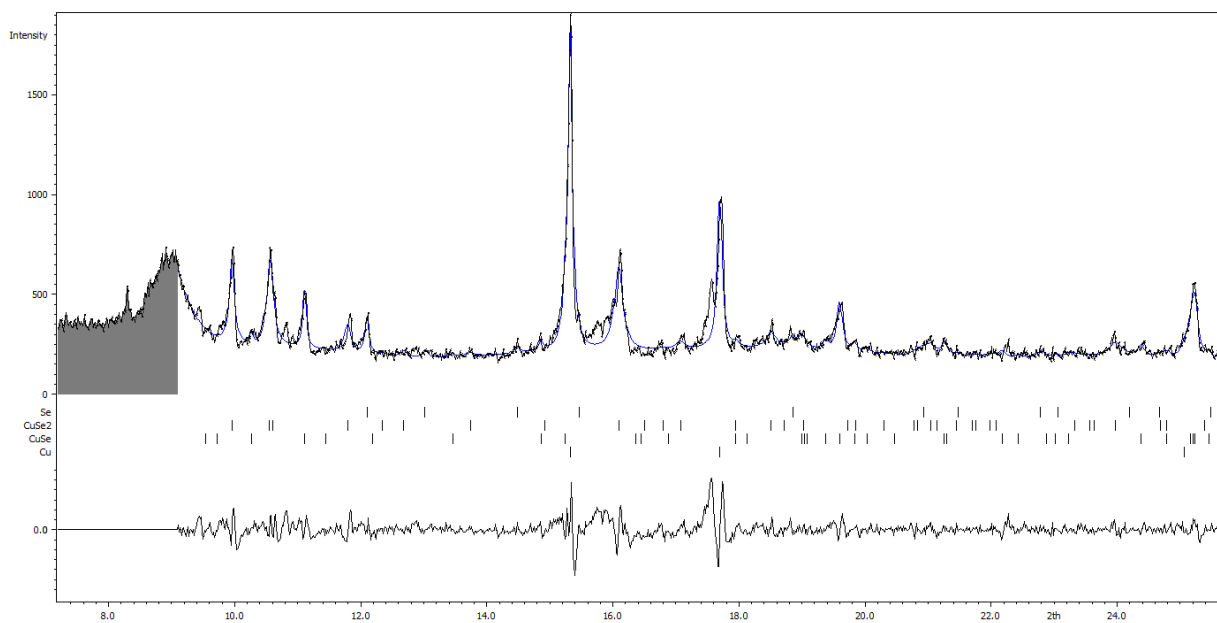


Figure S17: LeBail fitting of the 200°C scan indicating the presence of CuSe_2 and CuSe alongside Cu and Se . A portion of the SiO_2 broad peak is truncated in order to stabilize the fitting.

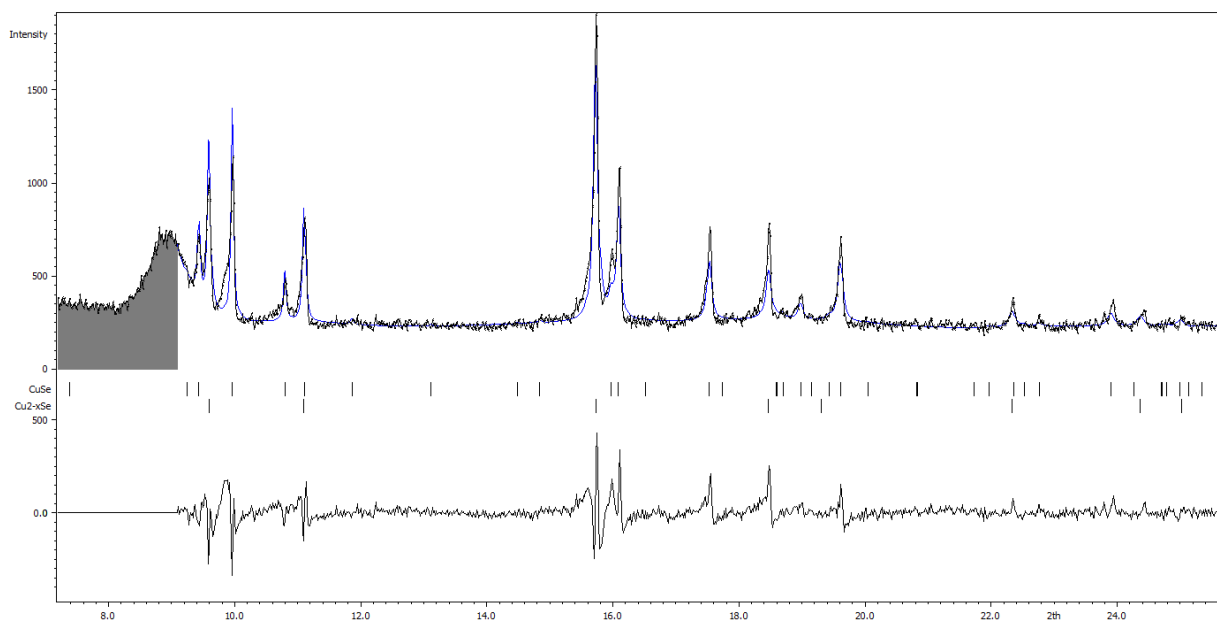


Figure S18: Rietveld refinement of the 300°C scan showing the presence of Cu_{2-x}Se , disappearance of CuSe_2 , and persistence of CuSe . Similar to the 200°C scan, a portion of the SiO_2 broad peak is truncated in order to stabilize the fitting.

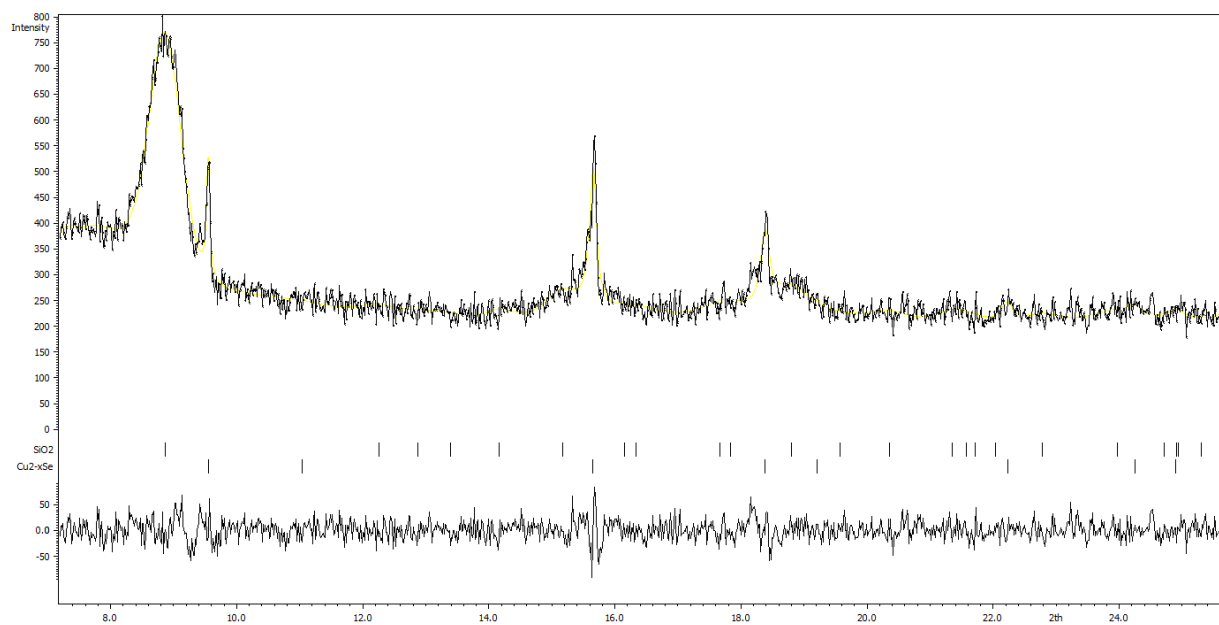


Figure S19: Rietveld refinement at 475°C showing the presence of only Cu_{2-x}Se and the quartz capillary signal.

Table S15. Lattice parameter changes for Bi₃Se₄ during Bi₂O₃ + Bi + 3Cu + 3Se reaction.

T1	T2	Avg. T	a-axis (Å)	Error in a (Å)	c-axis (Å)	Error in c (Å)	Volume (Å ³)	Error in Volume (Å ³)
203.8	203.7	203.8	4.248	0.001	40.36	0.02	630.9	0.3
221.7	225.1	223.4	4.2592	0.0006	40.27	0.01	632.7	0.2
246.2	243.2	244.7	4.2669	0.0006	40.20	0.01	633.8	0.2
275.9	269.9	272.9	4.2708	0.0002	40.29	0.01	636.41	0.07
328.1	325.9	327.0	4.2348	0.0006	40.375	0.004	627.1	0.2
378.2	375.4	376.8	4.2129	0.0006	40.44	0.01	621.6	0.2
427.5	428.1	427.8	4.2092	0.0007	40.47	0.02	620.9	0.3
476.7	478.0	477.4	4.227	0.001	40.10	0.02	620.5	0.4
502.1	502.5	502.3	4.202	0.002	40.38	0.04	617.4	0.8

Lattice parameters, volume, and associated errors are calculated from Rietveld refinements using Jana2006 software. T₁ and T₂ for each temperature point are the temperatures at the beginning and end of each measurement. The average temperatures are presented in Figure 6 of the manuscript.

The equation for negative thermal expansion is $\frac{l_{T_2} - l_{T_1}}{l_{T_2}(T_2 - T_1)}$, where l is the cell edge at T₁ or T₂. The a-axis is used in this calculation for the range 272.9°C (T₁) to 376.8°C (T₂). The equation becomes: $\frac{4.2129 \text{ \AA} - 4.2708 \text{ \AA}}{4.2708 \text{ \AA} ((376.8^\circ\text{C} - 272.9^\circ\text{C}) + 273.15)} = -3.59 \times 10^{-5} \text{ K}^{-1}$.

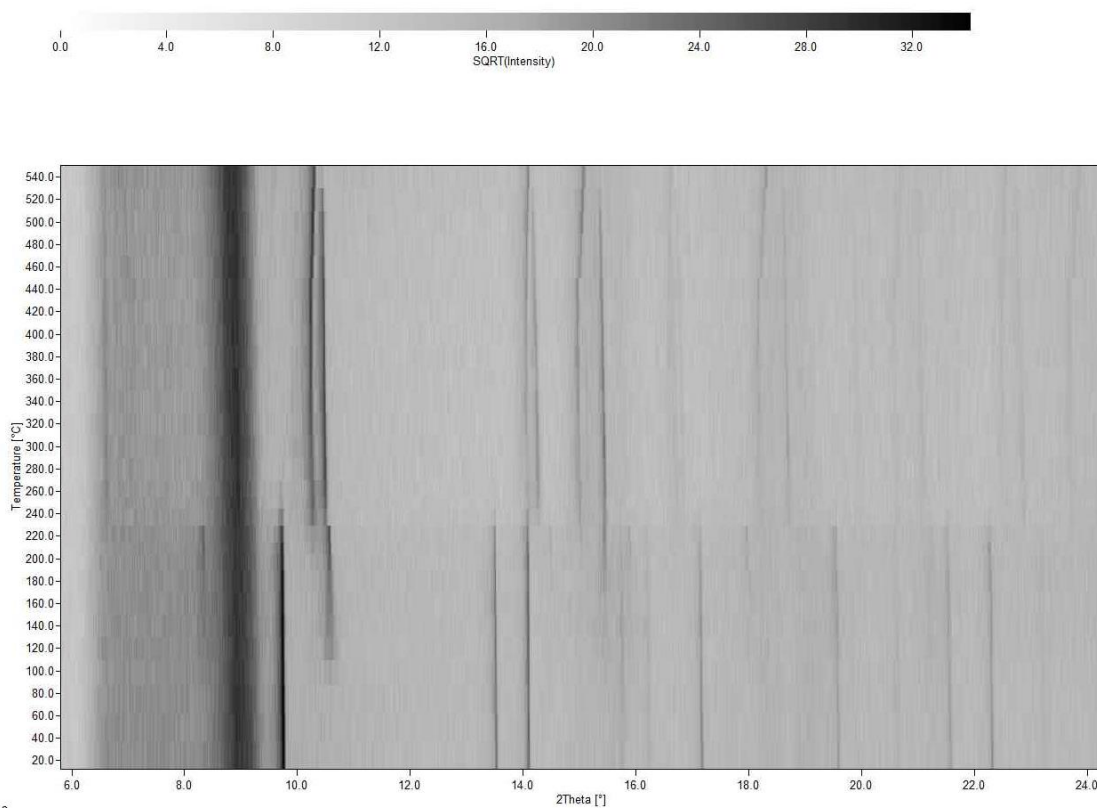


Figure S20: Heat map of the $2\text{Bi} + 3\text{Se}$ panoramic synthesis. Reactants were sieved $<65\mu\text{m}$ and heated at $4^\circ\text{C}/\text{min}$ using Ag radiation. The persistent, diffuse peak at ca. $9^\circ 2\theta$ is quartz from the quartz capillaries.

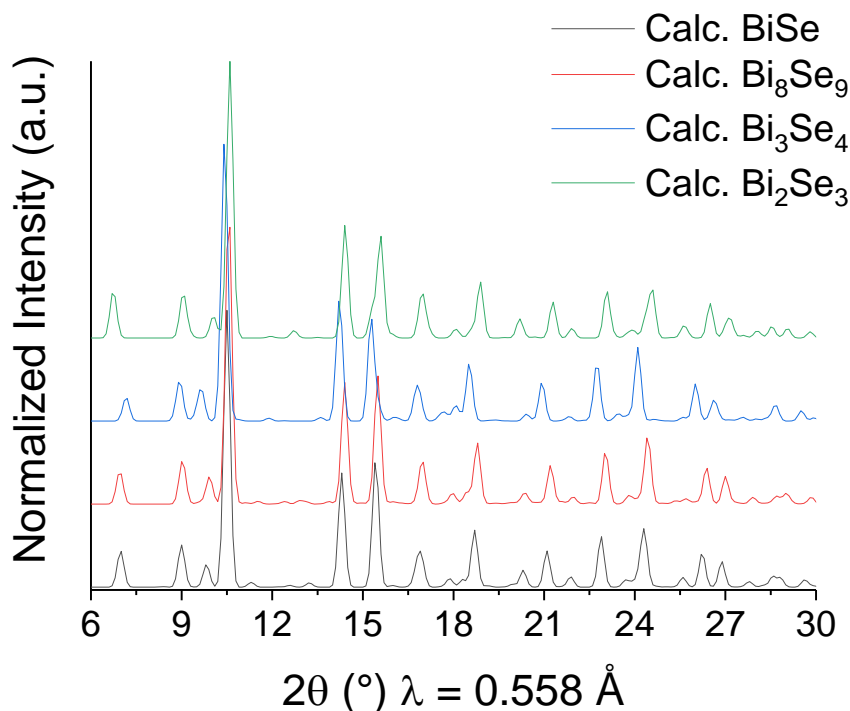


Figure S21: Bi_xSe_y comparison using Ag radiation. Notably, the 2θ that is able to be measured shows significant diffraction similarities between the compositions. In order to differentiate these materials, low angle data is needed, but is not possible with the current in-house set up.

Table S16. Calculations of reaction energies for both complex and elemental precursor pathways.

Complex Precursors:		
$\text{Bi}_2\text{O}_2\text{Se} + \text{Cu}_2\text{Se} \rightarrow 2 \text{BiOCuSe}$	-5.76	kJ/mol BiOCuSe
Elemental Precursors pathway:		
$\text{Se}_{(s)} \rightarrow \text{Se}_{(l)}$	-6.20	kJ/mol Se^{253}
$\text{Cu} + \text{Se} \rightarrow \text{CuSe}$	-26.80	kJ/mol CuSe
$\text{Bi} + 4 \text{Se} \rightarrow \text{Bi}_3\text{Se}_4$	-214.63	kJ/mol Bi_3Se_4
$2 \text{Bi}_3\text{Se}_4 + 2 \text{CuSe} \rightarrow 3 \text{Bi}_2\text{Se}_3 + \text{Cu}_2\text{Se}$	-32.11	kJ/mol Bi_2Se_3
$2 \text{Bi} + 3\text{Se} \rightarrow \text{Bi}_2\text{Se}_3$	-190.07	kJ/mol Bi_2Se_3
$2 \text{Cu} + \text{Se} \rightarrow \text{Cu}_2\text{Se}$	-28.21	kJ/mol Cu_2Se
$4 \text{Bi}_2\text{O}_3 + 6 \text{Cu}_2\text{Se} + 2 \text{Bi}_2\text{Se}_3 \rightarrow 12 \text{BiCuSeO}$	-12.75	kJ/mol BiOCuSe
In Total:		
$\text{Bi}_2\text{O}_3 + \text{Bi} + 3 \text{Cu} + 3 \text{Se} \rightarrow 3 \text{BiCuSeO}$	-58.53	kJ/mol BiOCuSe

DFT was used to confirm the hypothesis that the reactions are exothermic. When

considering the absence of peaks in the DTA data, one must consider first that DFT can only tell whether a reaction is exothermic or endothermic, but it is very hard to quantify the extent. For example, one can use the data in another database, such as Materials Project, to derive this property. The calculated reaction energy of $\text{Cu} + \text{Se} \rightarrow \text{CuSe}$ in Materials Project is -69 kJ/mol, while the reported experimental result in the database is -42 kJ/mol. Our calculations resulted in an enthalpy of is -27 kJ/mol. The discrepancies between the values are primarily a result of the different choice of pseudopotentials and the calculation approaches.

We hypothesize that the reactions are not observed in the DTA data as the release of energy is gradual, as was similarly seen for the NaFeS_2 intermediate observed in the $\text{Na}_2\text{S}_2 + \text{FeCl}_2$ reaction by Martinolich, *et al.*⁷⁹ As the formation of Bi_3Se_4 is reliant on the interfacial contact between Bi and Se to form, the reaction is diffusion limited. This limitation results in the reaction occurring over a period of time and therefore the energetic release is gradual as well. Selenium, on the other hand, can more expediently melt (i.e. over a shorter temperature range) as its melting is not dependent on other reactants in the mixture.

Appendix D: Supplementary Information for Chapter 4.

Table S17: Atomic coordinates (x104) and equivalent isotropic displacement parameters ($\text{\AA}^2 \times 10^3$) for In₈S_{2.82}Te_{12.18} at 293(2) K with estimated standard deviations in parentheses.

Label	x	y	z	Occupancy	U_{eq}^*
Te(07)	5006(1)	6006(1)	4872(1)	1	13(1)
Te(02)	7418(1)	2536(1)	6028(1)	1	14(1)
Te(03)	7246(1)	7488(1)	3481(1)	1	15(1)
Te(04)	8989(1)	5137(1)	7511(1)	1	16(1)
Te(05)	9950(1)	6558(1)	5268(1)	1	15(1)
Te(06)	6474(1)	4820(1)	7468(1)	1	18(1)
In(01)	8653(1)	4093(1)	5861(1)	1	14(1)
In(02)	6704(1)	5999(1)	5947(1)	1	15(1)
In(03)	8604(1)	6214(1)	3924(1)	1	17(1)
In(04)	6012(1)	6397(1)	8460(1)	1	17(1)
S(01)	5000	7518(1)	7500	0.817(5)	16(1)
Te(01)	5000	7518(1)	7500	0.183(5)	16(1)
S(02)	7585(1)	5007(1)	4808(1)	1	14(1)

* U_{eq} is defined as one third of the trace of the orthogonalized U_{ij} tensor.

Table S18: Anisotropic displacement parameters ($\text{\AA}^2 \times 10^3$) for In₈S_{2.82}Te_{12.18} at 293(2) K with estimated standard deviations in parentheses.

Label	U_{11}	U_{22}	U_{33}	U_{12}	U_{13}	U_{23}
Te(07)	12(1)	14(1)	14(1)	0(1)	0(1)	0(1)
Te(02)	13(1)	13(1)	16(1)	0(1)	0(1)	-1(1)
Te(03)	15(1)	14(1)	17(1)	0(1)	-1(1)	0(1)
Te(04)	24(1)	13(1)	13(1)	3(1)	0(1)	0(1)
Te(05)	14(1)	15(1)	15(1)	0(1)	1(1)	0(1)
Te(06)	24(1)	15(1)	15(1)	2(1)	-1(1)	0(1)
In(01)	13(1)	14(1)	15(1)	1(1)	0(1)	-1(1)
In(02)	14(1)	14(1)	16(1)	0(1)	-1(1)	-1(1)
In(03)	16(1)	18(1)	17(1)	2(1)	-2(1)	-1(1)
In(04)	18(1)	16(1)	18(1)	-3(1)	4(1)	-3(1)
S(01)	17(1)	14(1)	16(1)	0	-2(1)	0

Te(01)	17(1)	14(1)	16(1)	0	-2(1)	0
S(02)	14(1)	14(1)	15(1)	1(1)	0(1)	-1(1)

The anisotropic displacement factor exponent takes the form: $-2\pi^2[h^2a^{*2}U_{11} + \dots + 2hka^*b^*U_{12}]$.

Table S19: Bond lengths [\AA] for In₈S_{2.82}Te_{12.18} at 293(2) K with estimated standard deviations in parentheses.

Label	Distances
In(01)-S(02)	2.488(1)
In(01)-Te(02)	2.8554(5)
In(01)-Te(04)	2.8079(6)
In(01)-Te(05)	2.7387(5)
In(02)-S(02)	2.5013(14)
In(02)-Te(03)	2.7493(5)
In(02)-Te(06)	2.7588(6)
In(02)-Te(07)	2.8464(5)
In(03)-S(02)	2.592(1)
In(03)-Te(03)	2.7280(6)
In(03)-Te(04)	2.8403(6)
In(03)-Te(05)	2.7316(6)
In(04)-S(01)	2.5405(9)
In(04)-Te(02)	2.8570(6)
In(04)-Te(07)	2.8471(6)
In(04)-Te(07)	2.7435(6)
Te(02)-Te(02)	2.9246(8)
Te(04)-Te(04)	2.8916(8)
Te(07)-Te(07)	2.9029(7)

Symmetry transformations used to generate equivalent atoms:

(1) $-x+1, -y+1, -z+1$ (2) $-x+1, y, -z+3/2$ (3) $-x+3/2, -y+1/2, -z+1$ (4) $-x+3/2, y-1/2, -z+3/2$ (5) $-x+3/2, -y+3/2, -z+1$ (6) $-x+2, y, -z+3/2$ (7) $x, -y+1, z+1/2$ (8) $-x+2, -y+1, -z+1$ (9) $x, -y+1, z-1/2$ (10) $-x+3/2, y+1/2, -z+3/2$

Table S20: Bond angles [°] for In₈S_{2.82}Te_{12.18} at 293(2) K with estimated standard deviations in parentheses.

Label	Angles
In(02)-Te(07)-Te(07)#1	86.316(17)
In(02)-Te(07)-In(04)#2	89.998(17)
In(04)#2-Te(07)-Te(07)#1	95.019(18)
In(01)-Te(02)-Te(02)#3	83.451(17)
In(01)-Te(02)-In(04)#4	88.970(16)
In(04)#4-Te(02)-Te(02)#3	99.118(18)
In(03)-Te(03)-In(02)#5	94.339(17)
In(01)-Te(04)-Te(04)#6	98.599(18)
In(01)-Te(04)-In(03)#7	101.042(17)
In(03)#7-Te(04)-Te(04)#6	102.236(17)
In(03)-Te(05)-In(01)#8	92.554(17)
In(04)-Te(06)-In(02)	85.940(16)
Te(04)-In(01)-Te(02)	116.380(18)
Te(05)#8-In(01)-Te(02)	103.847(16)
Te(05)#8-In(01)-Te(04)	123.315(18)
S(02)-In(01)-Te(02)	94.90(3)
S(02)-In(01)-Te(04)	108.34(3)
S(02)-In(01)-Te(05)#8	106.00(4)
Te(03)#5-In(02)-Te(07)	127.731(18)
Te(03)#5-In(02)-Te(06)	108.800(19)
Te(06)-In(02)-Te(07)	107.983(18)
S(02)-In(02)-Te(07)	95.24(4)
S(02)-In(02)-Te(03)#5	111.05(4)
S(02)-In(02)-Te(06)	102.89(4)
Te(03)-In(03)-Te(04)#9	115.937(19)
Te(03)-In(03)-Te(05)	122.065(19)
Te(05)-In(03)-Te(04)#9	118.110(19)
S(02)-In(03)-Te(03)	98.84(3)
S(02)-In(03)-Te(04)#9	90.17(3)
S(02)-In(03)-Te(05)	100.30(4)
Te(07)#2-In(04)-Te(02)#10	108.101(18)

Te(06)-In(04)-Te(07)#2	113.120(18)
Te(06)-In(04)-Te(02)#10	113.885(19)
S(01)-In(04)-Te(07)#2	105.874(17)
S(01)-In(04)-Te(02)#10	102.41(3)
S(01)-In(04)-Te(06)	112.61(3)
In(04)#2-S(01)-In(04)	101.75(5)
In(01)-S(02)-In(02)	102.86(5)
In(01)-S(02)-In(03)	107.18(5)
In(02)-S(02)-In(03)	102.99(5)

Symmetry transformations used to generate equivalent atoms:

(1) $-x+1, -y+1, -z+1$ (2) $-x+1, y, -z+3/2$ (3) $-x+3/2, -y+1/2, -z+1$ (4) $-x+3/2, y-1/2, -z+3/2$ (5) $-x+3/2, -y+3/2, -z+1$ (6) $-x+2, y, -z+3/2$ (7) $x, -y+1, z+1/2$ (8) $-x+2, -y+1, -z+1$ (9) $x, -y+1, z-1/2$ (10) $-x+3/2, y+1/2, -z+3/2$

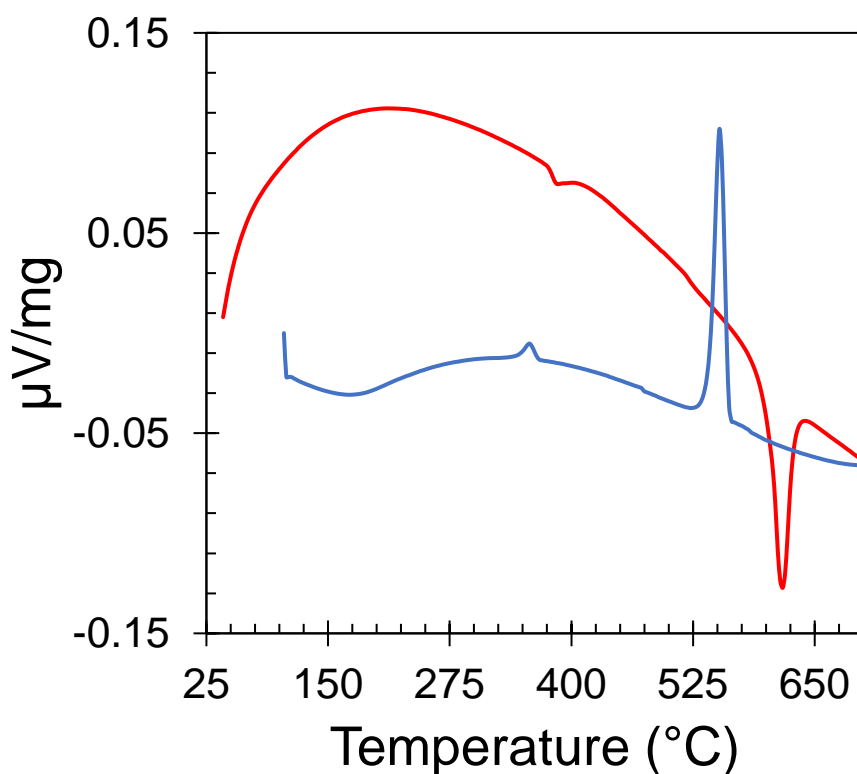


Figure S22: Differential thermal analysis of $\text{In}_8\text{S}_{2.82}\text{Te}_{12.18}$.

Using a rate of $10^\circ\text{C}/\text{min}$ to maximum temperature of 750°C , the melting point of this

material was determined to be 585°C. A small thermal peak was observed at 385°C and variable temperature PXRD was conducted to see if this thermal peak may be a phase transition (Figure S23).

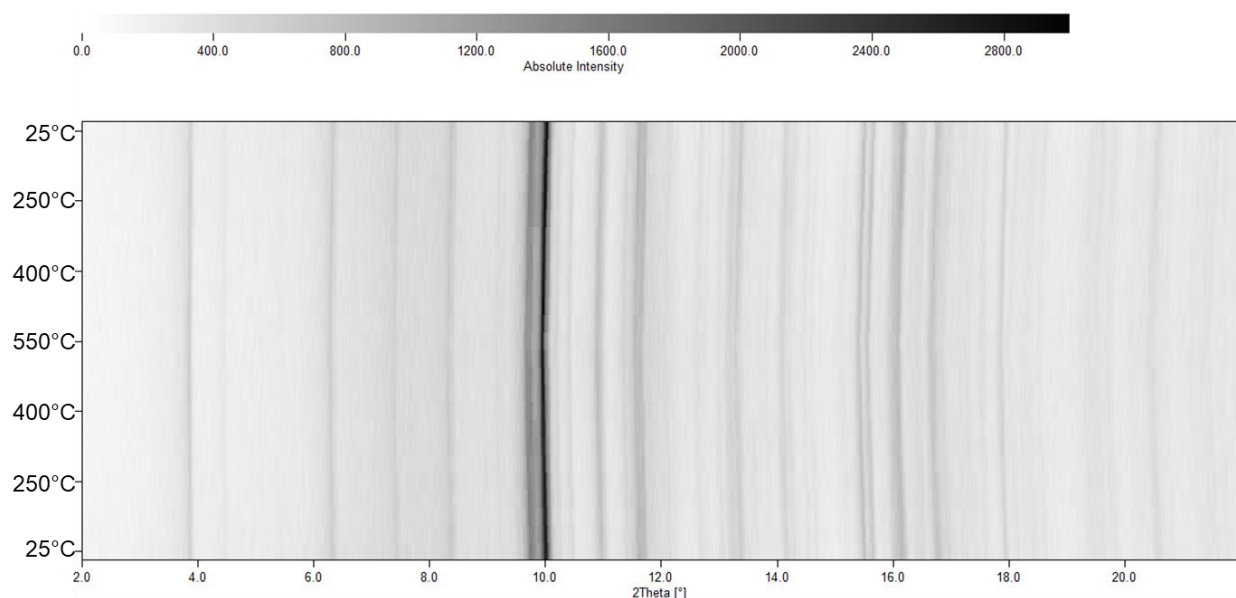


Figure S23: Variable temperature PXRD of $\text{In}_8\text{S}_{2.82}\text{Te}_{12.18}$, using Ag radiation.

VT-PXRD was conducted to determine if the small thermal peak at 385°C was a phase transition. As shown in Figure S23, the thermal peak cannot be attributed to a phase transition.

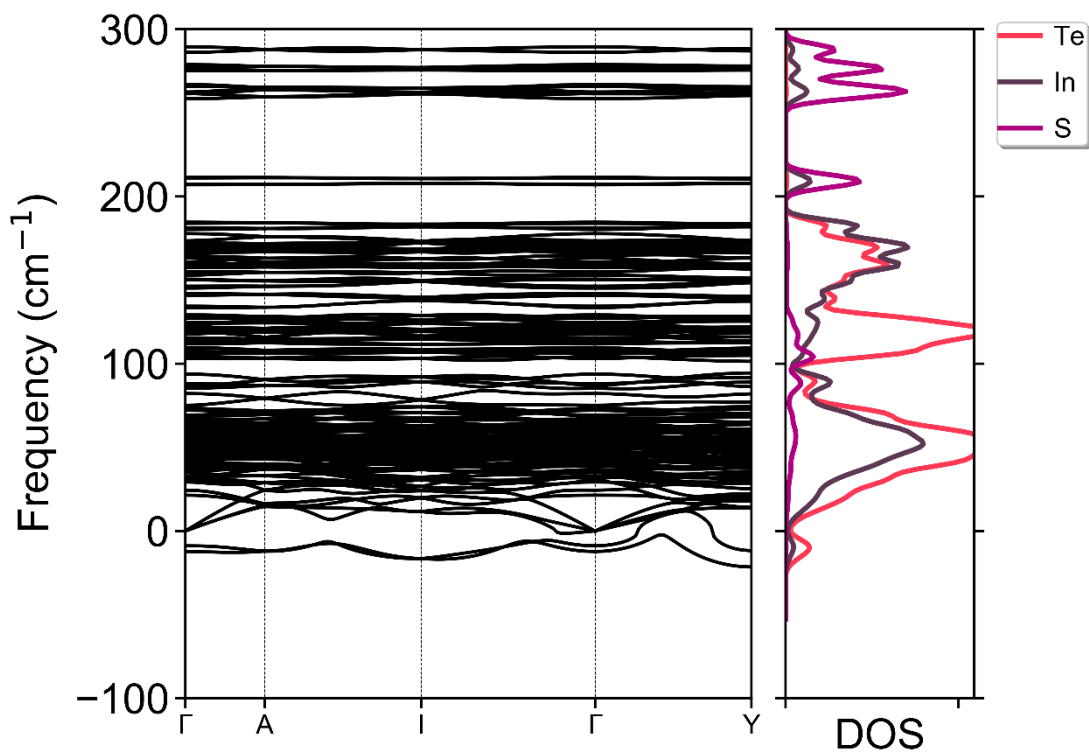


Figure S24: Calculation for thermal conductivity.

The thermal conductivity could not be calculated because the ordered structure used, $\text{In}_8\text{S}_3\text{Te}_{12}$, has imaginary phonon modes, shown in Figure S24. The negative frequency is relatively small, which means this structure would likely be stabilized by temperature. However, this restricts the calculation of this material's thermal conductivities.

Appendix E: Supplementary Information for Chapter 4.

Table S21: Atomic coordinates ($\times 10^4$) and equivalent isotropic displacement parameters ($\text{\AA}^2 \times 10^3$) for Ba₂S_{1.20}SnTe_{2.80} at 273.15 K with estimated standard deviations in parentheses.

Label	x	y	z	Occupancy	U_{eq}^*
Ba(1)	5000	5000	6600(1)	1	19(1)
Ba(2)	2500	6739(1)	1582(1)	1	27(1)
Te(1)	4488(1)	7831(1)	8448(1)	1	21(1)
Sn(1)	2500	7760(1)	6472(1)	1	16(1)
Te(2)	2500	9348(1)	4042(1)	0.8	17(1)
S(2)	2500	9348(1)	4042(1)	0.2	17(1)
S(1)	2500	5867(2)	5168(3)	1	16(1)

* U_{eq} is defined as one third of the trace of the orthogonalized U_{ij} tensor.

Table S22: Anisotropic displacement parameters ($\text{\AA}^2 \times 10^3$) for Ba₂S_{1.20}SnTe_{2.80} at 273.15 K with estimated standard deviations in parentheses.

Label	U_{11}	U_{22}	U_{33}	U_{12}	U_{13}	U_{23}
Ba(1)	16(1)	18(1)	24(1)	2(1)	0	0
Ba(2)	22(1)	44(1)	14(1)	0	0	1(1)
Te(1)	14(1)	30(1)	18(1)	-1(1)	-2(1)	-8(1)
Sn(1)	13(1)	18(1)	16(1)	0	0	-2(1)
Te(2)	17(1)	18(1)	17(1)	0	0	4(1)
S(2)	17(1)	18(1)	17(1)	0	0	4(1)
S(1)	14(2)	18(2)	15(2)	0	0	3(1)

The anisotropic displacement factor exponent takes the form: $-2\pi^2[h^2a^{*2}U_{11} + \dots + 2hka^*b^*U_{12}]$.

Table S23: Bond lengths [\AA] for Ba₂ S_{1.20} Sn Te_{2.80} at 273.15 K with estimated standard deviations in parentheses.

Label	Distances
Ba(1)-Ba(2)	4.6679(6)
Ba(1)-S(1)	3.1651(12)
Ba(1)-S(2)	3.4838(6)
Ba(1)-Te(1)	3.6301(6)
Ba(1)-Te(1)	3.6102(7)
Ba(1)-Te(2)	3.4838(6)
Ba(2)-Ba(1)	4.6678(6)
Ba(2)-S(1)	3.064(2)
Ba(2)-S(2)	3.4334(11)
Ba(2)-Te(1)	3.6975(6)
Ba(2)-Te(1)	3.5842(8)
Ba(2)-Te(2)	3.6009(11)
Ba(2)-Te(2)	3.4334(11)
Sn(1)-S(1)	2.421(3)
Sn(1)-Te(1)	2.7225(6)
Sn(1)-Te(2)	2.6816(10)

Symmetry transformations used to generate equivalent atoms:

(1) $x, y-1/2, z+1/2$ (2) $-x+1, -y+3/2, z+1/2$ (3) $x, y-1/2, z-1/2$ (4) $-x+1, -y+3/2, z-1/2$ (5) $-x+1, -y+1, z$ (6) $x-1/2, -y+3/2, z-1/2$ (7) $x, y+1/2, z-1/2$ (8) $-x+1/2, y, z-1$ (9) $x, y, z-1$ (10) $x, y+1/2, z+1/2$ (11) $x, y, z+1$ (12) $-x+1/2, y, z$ (13) $x-1/2, -y+1, z$

Table S24: Bond angles [°] for Ba₂ S_{1.20} Sn Te_{2.80} at 273.15 K with estimated standard deviations in parentheses.

Label	Angles
Ba(1)-Ba(2)-Ba(1)	72.880(11)
Ba(1)-S(1)-Ba(1)	122.33(7)
Ba(1)-Te(1)-Ba(1)	152.41(2)
Ba(1)-Te(1)-Ba(2)	79.134(15)
Ba(1)-Te(1)-Ba(2)	93.000(15)
Ba(1)-Te(2)-Ba(1)	105.47(3)
Ba(1)-Te(2)-Ba(2)	82.409(17)
Ba(2)-Te(1)-Ba(1)	80.904(18)
Ba(2)-Ba(1)-Ba(2)	179.66(2)
Ba(2)-S(1)-Ba(1)	116.63(4)
Ba(2)-Te(1)-Ba(1)	94.084(18)
Ba(2)-Te(1)-Ba(2)	152.90(2)
Ba(2)-Te(2)-Ba(1)	99.510(17)
Ba(2)-Te(2)-Ba(2)	176.77(3)
S(1)-Ba(1)-Ba(2)	105.40(4)
S(1)-Ba(1)-Ba(2)	74.47(4)
S(1)-Ba(1)-S(1)	137.18(8)
S(1)-Ba(1)-S(2)	146.70(5)
S(1)-Ba(1)-S(2)	65.00(4)
S(1)-Ba(1)-Te(1)	124.76(4)
S(1)-Ba(1)-Te(1)	70.27(4)
S(1)-Ba(1)-Te(1)	74.33(5)
S(1)-Ba(1)-Te(1)	79.80(5)
S(1)-Ba(1)-Te(2)	146.70(5)
S(1)-Ba(2)-Ba(1)	105.13(4)
S(1)-Ba(2)-S(2)	107.55(5)
S(1)-Ba(2)-Te(1)	141.450(14)
S(1)-Ba(2)-Te(1)	70.071(18)
S(1)-Ba(2)-Te(2)	107.55(5)
S(1)-Ba(2)-Te(2)	75.68(5)
S(1)-Sn(1)-Te(1)	106.36(4)

S(1)-Sn(1)-Te(2)	107.22(6)
S(2)-Ba(1)-Ba(2)	130.375(18)
S(2)-Ba(1)-Ba(2)	130.375(18)
S(2)-Ba(1)-Ba(2)	49.877(15)
S(2)-Ba(1)-S(2)	111.08(3)
S(2)-Ba(1)-Te(1)	132.305(13)
S(2)-Ba(1)-Te(1)	72.445(16)
S(2)-Ba(1)-Te(1)	80.590(17)
S(2)-Ba(1)-Te(1)	97.153(15)
S(2)-Ba(1)-Te(2)	0
S(2)-Ba(1)-Te(2)	111.1
S(2)-Ba(2)-Ba(1)	130.307(16)
S(2)-Ba(2)-Ba(1)	130.308(16)
S(2)-Ba(2)-Te(1)	110.527(14)
S(2)-Ba(2)-Te(1)	81.929(19)
S(2)-Ba(2)-Te(2)	0
S(2)-Ba(2)-Te(2)	176.8
Sn(1)-S(1)-Ba(1)	97.20(5)
Sn(1)-S(1)-Ba(2)	96.62(8)
Sn(1)-Te(1)-Ba(1)	124.13(2)
Sn(1)-Te(1)-Ba(1)	81.890(18)
Sn(1)-Te(1)-Ba(2)	119.80(2)
Sn(1)-Te(1)-Ba(2)	84.551(19)
Sn(1)-Te(2)-Ba(1)	124.118(14)
Sn(1)-Te(2)-Ba(2)	80.48(3)
Sn(1)-Te(2)-Ba(2)	96.29(3)
Te(1)-Ba(1)-Ba(2)	129.109(13)
Te(1)-Ba(1)-Ba(2)	130.378(18)
Te(1)-Ba(1)-Ba(2)	49.306(12)
Te(1)-Ba(1)-Ba(2)	51.071(10)
Te(1)-Ba(1)-Te(1)	131.47(3)
Te(1)-Ba(1)-Te(1)	152.42(2)
Te(1)-Ba(1)-Te(1)	72.122(5)

Te(1)-Ba(1)-Te(1)	90.37(2)
Te(1)-Ba(2)-Ba(1)	115.324(18)
Te(1)-Ba(2)-Ba(1)	49.791(13)
Te(1)-Ba(2)-Ba(1)	94.885(18)
Te(1)-Ba(2)-Te(1)	129.23(3)
Te(1)-Ba(2)-Te(1)	142.78(2)
Te(1)-Ba(2)-Te(1)	71.629(6)
Te(1)-Ba(2)-Te(1)	75.92(2)
Te(1)-Ba(2)-Te(2)	95.534(19)
Te(1)-Sn(1)-Te(1)	108.15(3)
Te(2)-Ba(1)-Ba(2)	130.375(18)
Te(2)-Ba(1)-Ba(2)	130.375(18)
Te(2)-Ba(1)-Ba(2)	49.877(15)
Te(2)-Ba(1)-S(2)	111.08(3)
Te(2)-Ba(1)-Te(1)	132.305(13)
Te(2)-Ba(1)-Te(1)	72.445(16)
Te(2)-Ba(1)-Te(1)	80.590(17)
Te(2)-Ba(1)-Te(1)	97.153(15)
Te(2)-Ba(1)-Te(2)	111.08(3)
Te(2)-Ba(2)-Ba(1)	130.307(16)
Te(2)-Ba(2)-Ba(1)	130.308(16)
Te(2)-Ba(2)-Ba(1)	47.714(12)
Te(2)-Ba(2)-Te(1)	70.355(14)
Te(2)-Ba(2)-Te(1)	81.929(19)
Te(2)-Ba(2)-Te(2)	176.77(3)
Te(2)-Sn(1)-Te(1)	114.09(2)

Symmetry transformations used to generate equivalent atoms:

(1) $x, y-1/2, z+1/2$ (2) $-x+1, -y+3/2, z+1/2$ (3) $x, y-1/2, z-1/2$ (4) $-x+1, -y+3/2, z-1/2$ (5) $-x+1, -y+1, z$ (6) $x-1/2, -y+3/2, z-1/2$ (7) $x, y+1/2, z-1/2$ (8) $-x+1/2, y, z-1$ (9) $x, y, z-1$ (10) $x, y+1/2, z+1/2$ (11) $x, y, z+1$ (12) $-x+1/2, y, z$ (13) $x-1/2, -y+1, z$

Table S25: Atomic coordinates (x104) and equivalent isotropic displacement parameters (Å²x103) for Ba₃ S₄ Sn Te at 100.01(10) K with estimated standard deviations in

parentheses.

Label	x	y	z	Occupancy	U_{eq}^*
Ba(1)	5000	4498(1)	7500	1	6(1)
Ba(2)	0	3462(1)	4834(1)	1	7(1)
Te(1)	0	5045(1)	2500	1	6(1)
Sn(1)	5000	3164(1)	2500	1	5(1)
S(1)	2270(1)	2314(1)	2500	1	9(1)
S(2)	5000	3934(1)	4519(1)	1	12(1)

* U_{eq} is defined as one third of the trace of the orthogonalized U_{ij} tensor.

Table S26: Anisotropic displacement parameters ($\text{\AA}^2 \times 10^3$) for Ba₃S₄SnTe at 100.01(10) K with estimated standard deviations in parentheses.

Label	U_{11}	U_{22}	U_{33}	U_{12}	U_{13}	U_{23}
Ba(1)	7(1)	6(1)	4(1)	0	0	0
Ba(2)	9(1)	7(1)	5(1)	0	0	0(1)
Te(1)	7(1)	5(1)	6(1)	0	0	0
Sn(1)	5(1)	4(1)	5(1)	0	0	0
S(1)	6(1)	7(1)	14(1)	-2(1)	0	0
S(2)	19(1)	11(1)	4(1)	0	0	-2(1)

The anisotropic displacement factor exponent takes the form: $-2\pi^2[h^2a^{*2}U_{11} + \dots + 2hka^*b^*U_{12}]$.

Table S27: Bond lengths [\AA] for Ba₃S₄SnTe at 100.01(10) K with estimated standard deviations in parentheses.

Label	Distances
Ba(1)-Ba(2)	4.66348(11)
Ba(1)-Ba(2)	4.66351(11)
Ba(1)-S(1)	3.3684(5)
Ba(1)-S(2)	3.0538(5)
Ba(1)-S(2)	3.2422(6)
Ba(1)-Sn(1)	3.8398(3)
Ba(1)-Te(1)	3.55617(7)
Ba(2)-Ba(2)	4.5576(3)
Ba(2)-S(1)	3.3515(4)
Ba(2)-S(1)	3.3516(4)

Ba(2)-S(1)	3.4640(4)
Ba(2)-S(2)	3.57484(14)
Ba(2)-Sn(1)	3.72815(19)
Ba(2)-Te(1)	3.45696(19)
Ba(2)-Te(1)	3.57565(18)
Sn(1)-S(1)	2.3553(5)
Sn(1)-S(2)	2.3421(6)

Symmetry transformations used to generate equivalent atoms:

(1) $x, y, -z+3/2$ (2) $x+1, y, -z+3/2$ (3) $-x+1, -y+1, -z+1$ (4) $-x, -y+1, -z+1$ (5) $x+1/2, -y+1/2, z+1/2$
(6) $-x+1/2, -y+1/2, -z+1$ (7) $-x+1, -y+1, z+1/2$ (8) $x-1, y, z$ (9) $x, y, -z+1/2$ (10) $x-1/2, -y+1/2, z+1/2$ (11)
 $-x, y, -z+1/2$ (12) $-x, -y+1, z-1/2$ (13) $-x+1/2, -y+1/2, z-1/2$ (14) $-x+1, y, -z+1/2$ (15) $x+1, y, z$

Table S28: Bond angles [°] for Ba₃ S₄ Sn Te at 100.01(10) K with estimated standard deviations in parentheses.

Label	Angles
Ba(1)-Ba(2)-Ba(1)	96.379(3)
Ba(1)-S(1)-Ba(2)	86.077(10)
Ba(1)-S(2)-Ba(1)	109.807(17)
Ba(1)-S(2)-Ba(2)	102.990(9)
Ba(1)-S(2)-Ba(2)	89.063(9)
Ba(1)-Te(1)-Ba(1)	155.614(8)
Ba(1)-Te(1)-Ba(2)	81.672(3)
Ba(2)3-Sn(1)-Ba(2)	88.541(6)
Ba(2)-Ba(1)-Ba(2)	137.215(5)
Ba(2)-Ba(1)-Ba(2)	67.840(3)
Ba(2)-Ba(1)-Ba(2)	96.378(3)
Ba(2)-Ba(2)-Ba(1)	123.920(2)
Ba(2)-S(1)-Ba(1)	106.022(12)
Ba(2)-S(1)-Ba(2)	167.328(16)
Ba(2)-S(1)-Ba(2)	85.676(13)
Ba(2)-S(1)-Ba(2)	87.365(3)
Ba(2)-S(1)-Ba(2)	97.401(13)
Ba(2)-S(2)-Ba(2)	152.982(18)
Ba(2)-Sn(1)-Ba(1)	135.730(3)
Ba(2)-Te(1)-Ba(1)	99.138(3)
Ba(2)-Te(1)-Ba(2)	174.535(5)
Ba(2)-Te(1)-Ba(2)	82.477(6)
Ba(2)-Te(1)-Ba(2)	92.058(3)
Ba(2)-Te(1)-Ba(2)	93.406(6)
S(1)-Ba(1)-Ba(2)	47.821(6)
S(1)-Ba(1)-Ba(2)	91.544(8)
S(1)-Ba(1)-S(1)	55.874(18)
S(1)-Ba(1)-Sn(1)	152.063(9)
S(1)-Ba(1)-Te(1)	130.130(10)
S(1)-Ba(1)-Te(1)	74.256(9)
S(1)-Ba(2)-Ba(1)	103.504(8)

S(1)-Ba(2)-Ba(1)	159.295(9)
S(1)-Ba(2)-Ba(1)	46.104(9)
S(1)-Ba(2)-Ba(1)	97.087(7)
S(1)-Ba(2)-Ba(2)	138.699(7)
S(1)-Ba(2)-Ba(2)	47.161(6)
S(1)-Ba(2)-S(1)	124.187(4)
S(1)-Ba(2)-S(1)	56.180(16)
S(1)-Ba(2)-S(1)	66.443(15)
S(1)-Ba(2)-S(1)	92.634(3)
S(1)-Ba(2)-S(2)	121.420(12)
S(1)-Ba(2)-S(2)	132.637(12)
S(1)-Ba(2)-S(2)	66.774(12)
S(1)-Ba(2)-S(2)	67.164(12)
S(1)-Ba(2)-Sn(1)	38.007(8)
S(1)-Ba(2)-Sn(1)	94.134(7)
S(1)-Ba(2)-Te(1)	151.685(8)
S(1)-Ba(2)-Te(1)	72.879(8)
S(1)-Ba(2)-Te(1)	88.538(8)
S(1)-Ba(2)-Te(1)	88.539(8)
S(1)-Sn(1)-Ba(1)	126.312(13)
S(1)-Sn(1)-Ba(2)3	64.909(9)
S(1)-Sn(1)-S(1)	107.37(3)
S(2)-Ba(1)-Ba(2)	114.920(7)
S(2)-Ba(1)-Ba(2)	114.920(7)
S(2)-Ba(1)-Ba(2)	128.965(4)
S(2)-Ba(1)-Ba(2)	50.037(3)
S(2)-Ba(1)-Ba(2)	87.158(7)
S(2)-Ba(1)-S(1)	134.547(9)
S(2)-Ba(1)-S(1)	74.481(10)
S(2)-Ba(1)-S(2)	144.74(2)
S(2)-Ba(1)-S(2)	145.065(13)
S(2)-Ba(1)-S(2)	70.193(17)
S(2)-Ba(1)-S(2)	74.872(19)

S(2)-Ba(1)-Sn(1)	107.629(11)
S(2)-Ba(1)-Sn(1)	37.436(10)
S(2)-Ba(1)-Te(1)	80.345(3)
S(2)-Ba(1)-Te(1)	93.667(2)
S(2)-Ba(2)-Ba(1)	133.917(9)
S(2)-Ba(2)-Ba(1)	40.900(9)
S(2)-Ba(2)-Ba(2)	85.058(9)
S(2)-Ba(2)-S(2)	152.983(18)
S(2)-Ba(2)-Sn(1)	102.451(9)
S(2)-Ba(2)-Te(1)	85.055(9)
S(2)-Sn(1)-Ba(1)	57.297(14)
S(2)-Sn(1)-Ba(2)	166.973(15)
S(2)-Sn(1)-Ba(2)3	78.432(14)
S(2)-Sn(1)-S(1)	108.660(9)
S(2)-Sn(1)-S(2)	114.59(3)
Sn(1)-Ba(1)-Ba(2)	111.392(3)
Sn(1)-Ba(2)-Ba(1)	82.626(3)
Sn(1)-Ba(2)-Ba(2)	134.269(3)
Sn(1)-S(1)-Ba(1)	154.25(2)
Sn(1)-S(1)-Ba(2)	92.666(13)
Sn(1)-S(1)-Ba(2)3	77.083(11)
Sn(1)-S(2)-Ba(1)	164.93(2)
Sn(1)-S(2)-Ba(1)	85.267(17)
Sn(1)-S(2)-Ba(2)	87.431(9)
Te(1)-Ba(1)-Ba(2)	143.666(2)
Te(1)-Ba(1)-Ba(2)	49.345(3)
Te(1)-Ba(1)-Sn(1)	77.807(4)
Te(1)-Ba(1)-Te(1)	155.613(8)
Te(1)-Ba(2)-Ba(1)	48.983(2)
Te(1)-Ba(2)-Ba(1)	95.369(3)
Te(1)-Ba(2)-Ba(2)	136.704(3)
Te(1)-Ba(2)-Ba(2)	48.762(3)
Te(1)-Ba(2)-S(1)	140.531(9)

Te(1)-Ba(2)-S(2)	77.287(9)
Te(1)-Ba(2)-Sn(1)	176.969(5)
Te(1)-Ba(2)-Sn(1)	89.028(4)
Te(1)-Ba(2)-Te(1)	87.942(3)

Symmetry transformations used to generate equivalent atoms:

(1) $x, y, -z+3/2$ (2) $x+1, y, -z+3/2$ (3) $-x+1, -y+1, -z+1$ (4) $-x, -y+1, -z+1$ (5) $x+1/2, -y+1/2, z+1/2$
 (6) $-x+1/2, -y+1/2, -z+1$ (7) $-x+1, -y+1, z+1/2$ (8) $x-1, y, z$ (9) $x, y, -z+1/2$ (10) $x-1/2, -y+1/2, z+1/2$ (11)
 $-x, y, -z+1/2$ (12) $-x, -y+1, z-1/2$ (13) $-x+1/2, -y+1/2, z-1/2$ (14) $-x+1, y, -z+1/2$ (15) $x+1, y, z$

Electron Image 3

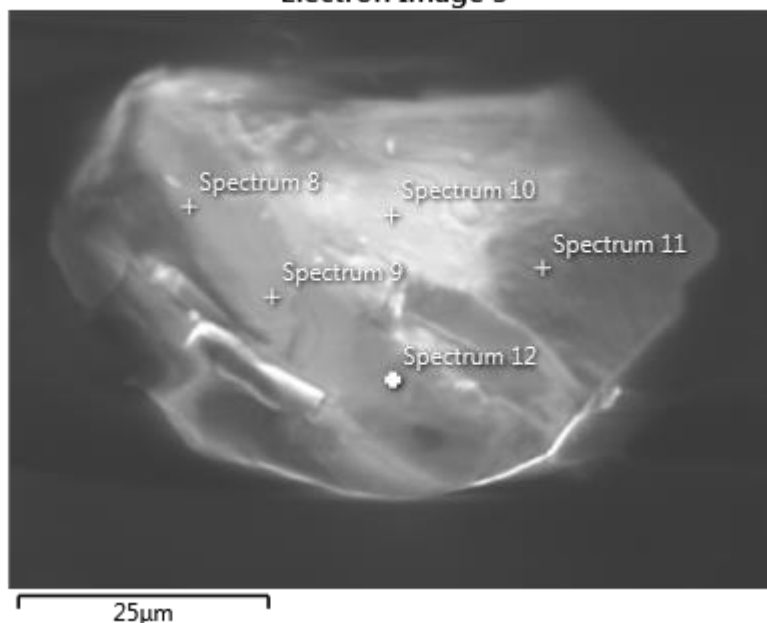


Figure S25: SEM image of $\text{Ba}_3\text{Sn}_4\text{Te}$. Orange crystal.

Table S29: Average EDS point values from $\text{Ba}_3\text{Sn}_4\text{Te}$ single crystal measured and shown in Figure S25.

Atomic % from Points

	Ba	Sn	S	Te
Average	33	11.4	45	10.3
STDEV	1	0.4	2	0.4
Sn-norm	2.93	1.00	3.92	0.90

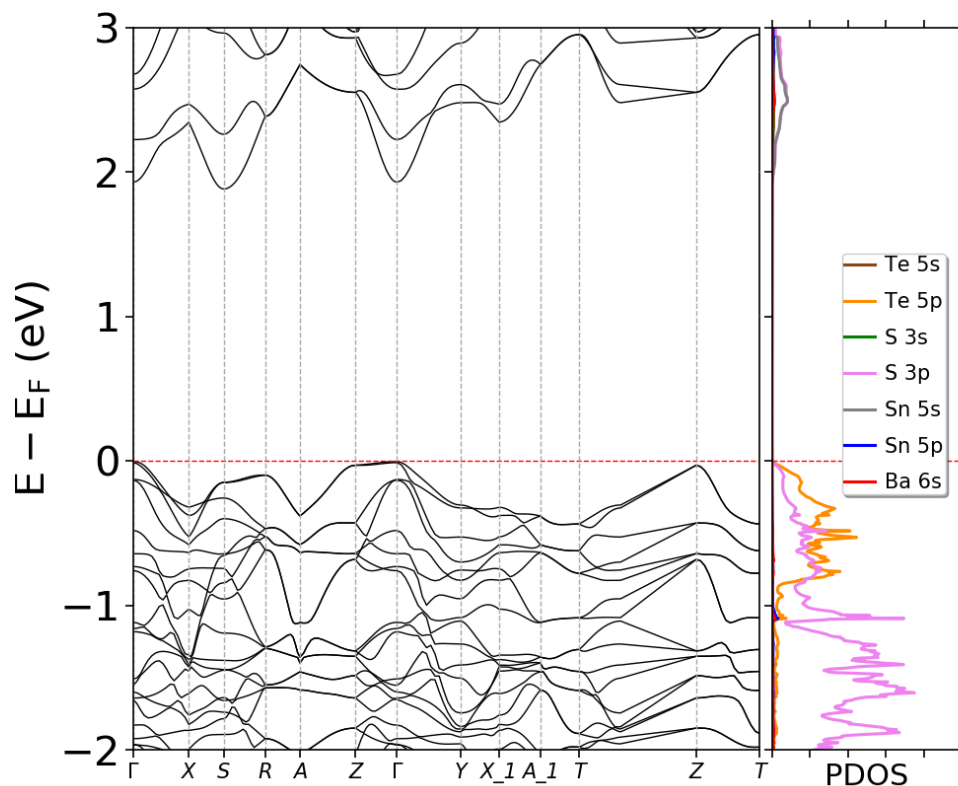


Figure S26: Band structure and partial density of states of $\text{Ba}_3\text{SnS}_4\text{Te}$.

Table S30: Atomic coordinates ($\times 10^4$) and equivalent isotropic displacement parameters ($\text{\AA}^2 \times 10^3$) for $\text{Ba}_3\text{S}_{5.62}\text{SnTe}_{0.13}$ at $100.01(10)$ K with estimated standard deviations in parentheses.

Label	x	y	z	Occupancy	U_{eq}^*
Ba(1)	9269(1)	7500	4580(1)	1	6(1)
Ba(2)	8748(1)	5019(1)	1812(1)	1	7(1)
Te(1)	11624(3)	7500	2662(2)	0.08	12(1)
Te(2)	4564(2)	2500	5118(1)	0.1	13(1)
Sn(1)	6809(1)	2500	4062(1)	1	5(1)
S(1)	11624(3)	7500	2662(2)	0.17	12(1)
S(2)	12941(4)	7500	2364(3)	0.5	28(1)
S(3)	10942(3)	8649(3)	2871(2)	0.5	30(1)
S(4)	8164(1)	4485(1)	4482(1)	1	8(1)
S(5)	6175(2)	2500	2175(1)	1	7(1)
S(6)	4564(2)	2500	5118(1)	0.9	13(1)

* U_{eq} is defined as one third of the trace of the orthogonalized U_{ij} tensor.

Table S31: Anisotropic displacement parameters ($\text{\AA}^2 \times 10^3$) for Ba₃S_{5.62}SnTe_{0.13} at 100.01(10) K with estimated standard deviations in parentheses.

Label	U_{11}	U_{22}	U_{33}	U_{12}	U_{13}	U_{23}
Ba(1)	8(1)	4(1)	6(1)	0	0(1)	0
Ba(2)	8(1)	5(1)	7(1)	0(1)	-2(1)	-1(1)
Te(1)	16(2)	12(2)	9(2)	0	-2(1)	0
Te(2)	11(1)	13(1)	15(1)	0	-1(1)	0
Sn(1)	6(1)	4(1)	6(1)	0	-1(1)	0
S(1)	16(2)	12(2)	9(2)	0	-2(1)	0
S(2)	26(2)	28(2)	28(2)	0	2(2)	0
S(3)	32(2)	28(2)	30(2)	1(1)	0(1)	0(1)
S(4)	11(1)	4(1)	8(1)	-2(1)	0(1)	0(1)
S(5)	10(1)	8(1)	4(1)	0	-3(1)	0
S(6)	11(1)	13(1)	15(1)	0	-1(1)	0

The anisotropic displacement factor exponent takes the form: $-2\pi^2[h^2a^{*2}U_{11} + \dots + 2hka^*b^*U_{12}]$.

Table S32: Bond lengths [\AA] for Ba₃S_{5.62}SnTe_{0.13} at 100.01(10) K with estimated standard deviations in parentheses.

Label	Distances
Ba(1)-S(2)	2.666(3)
Ba(1)-S(3)	2.818(2)
Ba(1)-S(4)	3.1187(8)
Ba(1)-S(4)	3.2429(9)
Ba(1)-S(5)	3.2013(11)
Ba(1)-S(6)	3.4959(10)
Ba(1)-Te(1)	3.173(3)
Ba(1)-Te(1)	3.644(3)
Ba(1)-Te(2)	3.4959(10)
Ba(2)-S(1)	3.1659(17)
Ba(2)-S(2)	2.7296(15)
Ba(2)-S(3)	2.709(2)
Ba(2)-S(3)	2.886(2)

Ba(2)-S(4)	3.3507(8)
Ba(2)-S(5)	3.4232(8)
Ba(2)-S(5)	3.5302(8)
Ba(2)-S(5)	3.5301(8)
Ba(2)-S(6)	3.4935(7)
Ba(2)-Te(1)	3.1659(17)
Ba(2)-Te(1)	3.713(2)
Ba(2)-Te(2)	3.4935(7)
Ba(2)-Te(2)	3.5407(7)
S(2)-S(3)	2.222(4)
S(3)-S(3)	2.250(5)
Sn(1)-S(4)	2.3551(8)
Sn(1)-S(5)	2.3803(11)
Sn(1)-Te(2)	2.4117(11)
Te(1)-S(2)	1.249(4)
Te(1)-S(3)	1.309(3)

Symmetry transformations used to generate equivalent atoms:

(1) $-x+1, -y+1, -z+1$ (2) $x-1/2, y, -z+1/2$ (3) $x, -y+3/2, z$ (4) $-x+2, -y+1, -z+1$ (5) $-x+2, y+1/2, -z+1$ (6) $-x+3/2, -y+1, z+1/2$ (7) $x+1/2, y, -z+1/2$ (8) $-x+3/2, -y+1, z-1/2$ (9) $x-1/2, -y+3/2, -z+1/2$ (10) $x+1/2, -y+3/2, -z+1/2$ (11) $-x+3/2, y-1/2, z+1/2$ (12) $x-1/2, -y+1/2, -z+1/2$ (13) $x, -y+1/2, z$

Table S33: Bond angles [°] for Ba₃S_{5.62}SnTe_{0.13} at 100.01(10) K with estimated standard deviations in parentheses.

Label	Angles
Te(1)-Ba(1)-Te(2)#1	138.37(5)
Te(1)-Ba(1)-S(4)#4	77.21(4)
Te(1)-Ba(1)-S(4)#5	77.21(4)
Te(1)-Ba(1)-S(5)#6	144.93(5)
Te(1)-Ba(1)-S(6)#1	138.37(5)
S(2)#2-Ba(1)-Te(1)	69.16(8)
S(2)#2-Ba(1)-Te(2)#1	69.21(7)
S(2)#2-Ba(1)-S(3)	65.24(8)
S(2)#2-Ba(1)-S(3)#3	65.23(8)
S(2)#2-Ba(1)-S(4)	79.66(2)

S(2)#2-Ba(1)-S(4)#3	79.66(2)
S(2)#2-Ba(1)-S(4)#4	129.82(5)
S(2)#2-Ba(1)-S(4)#5	129.82(5)
S(2)#2-Ba(1)-S(5)#6	145.91(7)
S(2)#2-Ba(1)-S(6)#1	69.21(7)
S(3)#3-Ba(1)-Te(1)	24.32(5)
S(3)-Ba(1)-Te(1)	24.32(5)
S(3)#3-Ba(1)-Te(2)#1	127.86(5)
S(3)-Ba(1)-Te(2)#1	127.86(5)
S(3)-Ba(1)-S(3)#3	47.05(10)
S(3)#3-Ba(1)-S(4)#3	121.47(5)
S(3)-Ba(1)-S(4)	121.47(5)
S(3)#3-Ba(1)-S(4)	76.51(5)
S(3)-Ba(1)-S(4)#5	68.73(5)
S(3)-Ba(1)-S(4)#3	76.51(5)
S(3)#3-Ba(1)-S(4)#5	96.63(5)
S(3)-Ba(1)-S(4)#4	96.63(5)
S(3)#3-Ba(1)-S(4)#4	68.73(5)
S(3)-Ba(1)-S(5)#6	143.52(5)
S(3)#3-Ba(1)-S(5)#6	143.52(5)
S(3)#3-Ba(1)-S(6)#1	127.86(5)
S(3)-Ba(1)-S(6)#1	127.86(5)
S(4)#3-Ba(1)-Te(1)	100.83(2)
S(4)-Ba(1)-Te(1)	100.826(19)
S(4)#3-Ba(1)-Te(2)#1	71.609(16)
S(4)#4-Ba(1)-Te(2)#1	132.578(18)
S(4)-Ba(1)-Te(2)#1	71.609(16)
S(4)#5-Ba(1)-Te(2)#1	132.578(18)
S(4)-Ba(1)-S(4)#3	142.23(3)
S(4)#3-Ba(1)-S(4)#5	71.19(2)
S(4)#3-Ba(1)-S(4)#4	144.219(18)
S(4)-Ba(1)-S(4)#5	144.219(18)
S(4)#5-Ba(1)-S(4)#4	73.61(3)

S(4)-Ba(1)-S(4)#4	71.19(2)
S(4)-Ba(1)-S(5)#6	89.872(16)
S(4)#3-Ba(1)-S(5)#6	89.872(16)
S(4)-Ba(1)-S(6)#1	71.609(16)
S(4)#3-Ba(1)-S(6)#1	71.609(16)
S(4)#5-Ba(1)-S(6)#1	132.578(18)
S(4)#4-Ba(1)-S(6)#1	132.578(18)
S(5)#6-Ba(1)-Te(2)#1	76.70(3)
S(5)#6-Ba(1)-S(4)#4	74.87(2)
S(5)#6-Ba(1)-S(4)#5	74.87(2)
S(5)#6-Ba(1)-S(6)#1	76.70(3)
S(6)#1-Ba(1)-Te(2)#1	0.0
Te(1)#2-Ba(2)-Te(2)#8	81.72(4)
Te(1)#2-Ba(2)-Te(2)#7	143.88(5)
Te(1)#2-Ba(2)-S(4)	79.93(4)
Te(1)#2-Ba(2)-S(4)#8	75.45(5)
Te(1)#2-Ba(2)-S(5)	96.39(4)
Te(1)#2-Ba(2)-S(5)#7	147.54(5)
Te(1)#2-Ba(2)-S(6)#7	143.88(5)
Te(2)#7-Ba(2)-Te(2)#8	89.806(6)
Te(2)#7-Ba(2)-S(5)#7	67.20(2)
S(1)#2-Ba(2)-Te(1)#2	0.0
S(1)#2-Ba(2)-Te(2)#8	81.72(4)
S(1)#2-Ba(2)-Te(2)#7	143.88(5)
S(1)#2-Ba(2)-S(4)#8	75.45(5)
S(1)#2-Ba(2)-S(4)	79.93(4)
S(1)#2-Ba(2)-S(5)#7	147.54(5)
S(1)#2-Ba(2)-S(5)	96.39(4)
S(1)#2-Ba(2)-S(6)#7	143.88(5)
S(2)#2-Ba(2)-Te(1)#2	22.96(8)
S(2)#2-Ba(2)-Te(2)#8	73.86(6)
S(2)#2-Ba(2)-Te(2)#7	159.15(6)
S(2)#2-Ba(2)-S(1)#2	22.96(8)

S(2)#2-Ba(2)-S(3)#9	46.52(8)
S(2)#2-Ba(2)-S(4)	74.69(6)
S(2)#2-Ba(2)-S(4)#8	92.67(7)
S(2)#2-Ba(2)-S(5)	114.20(6)
S(2)#2-Ba(2)-S(5)#7	131.20(7)
S(2)#2-Ba(2)-S(6)#7	159.15(6)
S(3)#9-Ba(2)-Te(1)#2	24.42(6)
S(3)#3-Ba(2)-Te(1)#2	88.89(7)
S(3)#3-Ba(2)-Te(2)#7	120.48(5)
S(3)#3-Ba(2)-Te(2)#8	68.42(5)
S(3)#9-Ba(2)-Te(2)#8	98.65(5)
S(3)#9-Ba(2)-Te(2)#7	126.64(5)
S(3)#3-Ba(2)-S(1)#2	88.89(7)
S(3)#9-Ba(2)-S(1)#2	24.42(6)
S(3)#3-Ba(2)-S(2)#2	65.92(8)
S(3)#3-Ba(2)-S(3)#9	111.47(7)
S(3)#3-Ba(2)-S(4)	74.03(5)
S(3)#9-Ba(2)-S(4)	78.44(5)
S(3)#9-Ba(2)-S(4)#8	66.14(5)
S(3)#3-Ba(2)-S(4)#8	135.46(5)
S(3)#9-Ba(2)-S(5)	72.95(5)
S(3)#3-Ba(2)-S(5)#7	73.14(5)
S(3)#9-Ba(2)-S(5)#7	144.90(5)
S(3)#3-Ba(2)-S(5)	141.73(5)
S(3)#9-Ba(2)-S(6)#7	126.64(5)
S(3)#3-Ba(2)-S(6)#7	120.48(5)
S(4)#8-Ba(2)-Te(2)#7	68.83(2)
S(4)-Ba(2)-Te(2)#7	125.641(19)
S(4)-Ba(2)-Te(2)#8	138.25(2)
S(4)#8-Ba(2)-Te(2)#8	68.20(2)
S(4)-Ba(2)-S(4)#8	139.966(8)
S(4)#8-Ba(2)-S(5)#7	135.90(2)
S(4)-Ba(2)-S(5)#7	69.35(2)

S(4)#8-Ba(2)-S(5)	82.13(2)
S(4)-Ba(2)-S(5)	69.72(2)
S(4)-Ba(2)-S(6)#7	125.641(19)
S(4)#8-Ba(2)-S(6)#7	68.83(2)
S(5)-Ba(2)-Te(2)#8	149.84(2)
S(5)-Ba(2)-Te(2)#7	73.98(2)
S(5)#7-Ba(2)-Te(2)#8	114.51(2)
S(5)-Ba(2)-S(5)#7	82.909(7)
S(5)-Ba(2)-S(6)#7	73.98(2)
S(6)#7-Ba(2)-Te(2)#8	89.8
S(6)#7-Ba(2)-Te(2)#7	0.0
S(6)#7-Ba(2)-S(5)#7	67.20(2)
Ba(1)-Te(1)-Ba(1)#7	178.86(9)
Ba(1)-Te(1)-Ba(2)	74.60(5)
Ba(1)#7-Te(1)-Ba(2)	104.57(5)
Ba(1)#7-Te(1)-Ba(2)#3	104.57(5)
Ba(1)-Te(1)-Ba(2)#3	74.59(5)
Ba(2)#7-Te(1)-Ba(1)#7	75.67(5)
Ba(2)#7-Te(1)-Ba(1)	105.02(6)
Ba(2)#10-Te(1)-Ba(1)	105.02(6)
Ba(2)#10-Te(1)-Ba(1)#7	75.67(5)
Ba(2)#7-Te(1)-Ba(2)	89.010(11)
Ba(2)#7-Te(1)-Ba(2)#3	170.48(6)
Ba(2)#10-Te(1)-Ba(2)	170.48(6)
Ba(2)#10-Te(1)-Ba(2)#3	89.010(11)
Ba(2)-Te(1)-Ba(2)#3	81.71(5)
Ba(2)#10-Te(1)-Ba(2)#7	100.18(7)
S(2)-Te(1)-Ba(1)	149.3(2)
S(2)-Te(1)-Ba(1)#7	31.85(17)
S(2)-Te(1)-Ba(2)#7	58.50(9)
S(2)-Te(1)-Ba(2)#10	58.50(9)
S(2)-Te(1)-Ba(2)	126.16(12)
S(2)-Te(1)-Ba(2)#3	126.16(12)

S(2)-Te(1)-S(3)	120.60(15)
S(2)-Te(1)-S(3)#3	120.60(15)
S(3)#3-Te(1)-Ba(1)#7	117.25(14)
S(3)-Te(1)-Ba(1)#7	117.25(14)
S(3)-Te(1)-Ba(1)	62.46(14)
S(3)#3-Te(1)-Ba(1)	62.46(14)
S(3)#3-Te(1)-Ba(2)	32.91(13)
S(3)#3-Te(1)-Ba(2)#7	65.71(13)
S(3)#3-Te(1)-Ba(2)#10	155.12(18)
S(3)#3-Te(1)-Ba(2)#3	106.54(17)
S(3)-Te(1)-Ba(2)#7	155.11(18)
S(3)-Te(1)-Ba(2)#3	32.91(13)
S(3)-Te(1)-Ba(2)	106.54(17)
S(3)-Te(1)-Ba(2)#10	65.71(13)
S(3)#3-Te(1)-S(3)	118.5(3)
Ba(1)#1-Te(2)-Ba(2)#6	111.60(2)
Ba(1)#1-Te(2)-Ba(2)#11	111.60(2)
Ba(2)#12-Te(2)-Ba(1)#1	81.993(19)
Ba(2)#2-Te(2)-Ba(1)#1	81.993(19)
Ba(2)#12-Te(2)-Ba(2)#11	90.195(6)
Ba(2)#6-Te(2)-Ba(2)#11	86.61(2)
Ba(2)#12-Te(2)-Ba(2)#6	166.26(3)
Ba(2)#2-Te(2)-Ba(2)#6	90.195(6)
Ba(2)#12-Te(2)-Ba(2)#2	89.76(2)
Ba(2)#2-Te(2)-Ba(2)#11	166.26(3)
Sn(1)-Te(2)-Ba(1)#1	153.67(4)
Sn(1)-Te(2)-Ba(2)#2	79.44(2)
Sn(1)-Te(2)-Ba(2)#11	87.05(2)
Sn(1)-Te(2)-Ba(2)#6	87.05(2)
Sn(1)-Te(2)-Ba(2)#12	79.44(2)
S(4)#13-Sn(1)-Te(2)	108.88(2)
S(4)-Sn(1)-Te(2)	108.88(2)
S(4)#13-Sn(1)-S(4)	111.17(4)

S(4)-Sn(1)-S(5)	109.72(2)
S(4)#13-Sn(1)-S(5)	109.72(2)
S(5)-Sn(1)-Te(2)	108.42(4)
Ba(1)#7-S(2)-Ba(2)#7	102.04(7)
Ba(1)#7-S(2)-Ba(2)#10	102.04(7)
Ba(2)#10-S(2)-Ba(2)#7	125.67(12)
Te(1)-S(2)-Ba(1)#7	133.8(2)
Te(1)-S(2)-Ba(2)#10	98.54(11)
Te(1)-S(2)-Ba(2)#7	98.54(11)
Te(1)-S(2)-S(3)	30.47(8)
Te(1)-S(2)-S(3)#3	30.47(8)
S(3)-S(2)-Ba(1)#7	128.14(13)
S(3)#3-S(2)-Ba(1)#7	128.14(13)
S(3)#3-S(2)-Ba(2)#7	70.44(7)
S(3)#3-S(2)-Ba(2)#10	124.48(13)
S(3)-S(2)-Ba(2)#7	124.48(13)
S(3)-S(2)-Ba(2)#10	70.44(8)
S(3)#3-S(2)-S(3)	60.83(15)
Ba(1)-S(3)-Ba(2)#10	123.72(8)
Ba(2)#3-S(3)-Ba(1)	98.72(7)
Ba(2)#3-S(3)-Ba(2)#10	119.66(9)
Te(1)-S(3)-Ba(1)	93.22(16)
Te(1)-S(3)-Ba(2)#3	131.87(18)
Te(1)-S(3)-Ba(2)#10	89.87(16)
Te(1)-S(3)-S(2)	28.94(12)
Te(1)-S(3)-S(3)#3	30.75(15)
S(2)-S(3)-Ba(1)	116.38(11)
S(2)-S(3)-Ba(2)#3	135.20(13)
S(2)-S(3)-Ba(2)#10	63.04(8)
S(2)-S(3)-S(3)#3	59.58(8)
S(3)#3-S(3)-Ba(1)	66.47(5)
S(3)#3-S(3)-Ba(2)#10	116.85(5)
S(3)#3-S(3)-Ba(2)#3	118.77(5)

Ba(1)-S(4)-Ba(1)#4	108.81(2)
Ba(1)#4-S(4)-Ba(2)#6	98.97(2)
Ba(1)#4-S(4)-Ba(2)	108.98(2)
Ba(1)-S(4)-Ba(2)	80.748(19)
Ba(1)-S(4)-Ba(2)#6	89.79(2)
Ba(2)-S(4)-Ba(2)#6	152.04(3)
Sn(1)-S(4)-Ba(1)	163.05(4)
Sn(1)-S(4)-Ba(1)#4	87.56(2)
Sn(1)-S(4)-Ba(2)	89.93(2)
Sn(1)-S(4)-Ba(2)#6	92.00(3)
Ba(1)#8-S(5)-Ba(2)#13	87.54(2)
Ba(1)#8-S(5)-Ba(2)#2	105.66(2)
Ba(1)#8-S(5)-Ba(2)	87.53(2)
Ba(1)#8-S(5)-Ba(2)#12	105.66(2)
Ba(2)#13-S(5)-Ba(2)	92.14(3)
Ba(2)-S(5)-Ba(2)#2	88.151(6)
Ba(2)#13-S(5)-Ba(2)#2	166.80(3)
Ba(2)#12-S(5)-Ba(2)#2	88.59(3)
Ba(2)#13-S(5)-Ba(2)#12	88.151(7)
Ba(2)-S(5)-Ba(2)#12	166.80(3)
Sn(1)-S(5)-Ba(1)#8	173.25(5)
Sn(1)-S(5)-Ba(2)#12	79.04(2)
Sn(1)-S(5)-Ba(2)#2	79.04(2)
Sn(1)-S(5)-Ba(2)	87.78(3)
Sn(1)-S(5)-Ba(2)#13	87.78(3)

Symmetry transformations used to generate equivalent atoms:

(1) $-x+1, -y+1, -z+1$ (2) $x-1/2, y, -z+1/2$ (3) $x, -y+3/2, z$ (4) $-x+2, -y+1, -z+1$ (5) $-x+2, y+1/2, -z+1$ (6) $-x+3/2, -y+1, z+1/2$ (7) $x+1/2, y, -z+1/2$ (8) $-x+3/2, -y+1, z-1/2$ (9) $x-1/2, -y+3/2, -z+1/2$ (10) $x+1/2, -y+3/2, -z+1/2$ (11) $-x+3/2, y-1/2, z+1/2$ (12) $x-1/2, -y+1/2, -z+1/2$ (13) $x, -y+1/2, z$

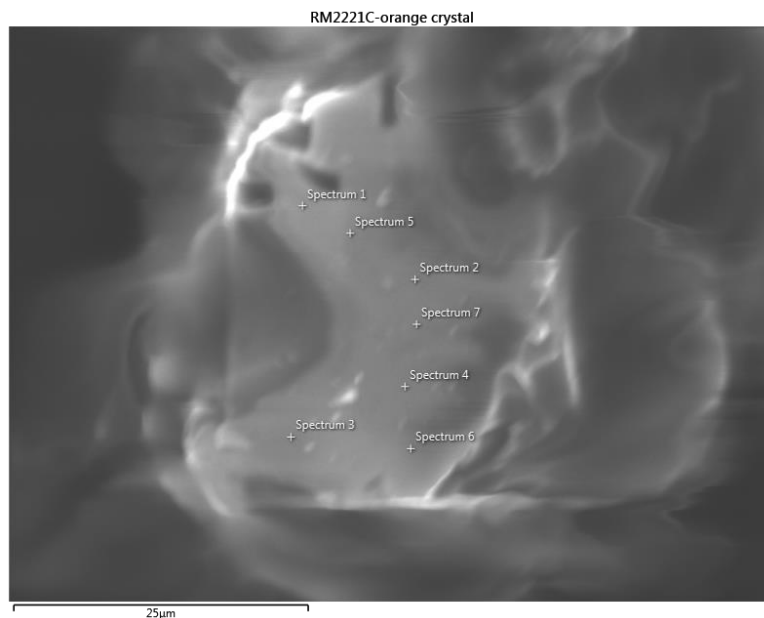


Figure S27: SEM image of $\text{Ba}_3\text{SnS}_{5.62}\text{Te}_{0.13}$. Orange crystal.

Table S34: Average EDS point values from $\text{Ba}_3\text{SnS}_{5.62}\text{Te}_{0.13}$ crystal measured and shown in Figure S27.

Atomic % from Points				
	Ba	Sn	S	Te
Average	34.6	12.3	51.7	1.4
STDEV	0.4	0.2	0.5	0.1
Sn-norm	2.81	1.00	4.18	0.11

Table S35: Average EDS map values from $\text{Ba}_3\text{SnS}_{5.62}\text{Te}_{0.13}$ crystal measured and shown in Figure S27.

Atomic % from Map				
	Ba	Sn	S	Te
Average	37.1	11.6	49.4	1.9
Sn-norm	3.2	1.00	4.26	0.16

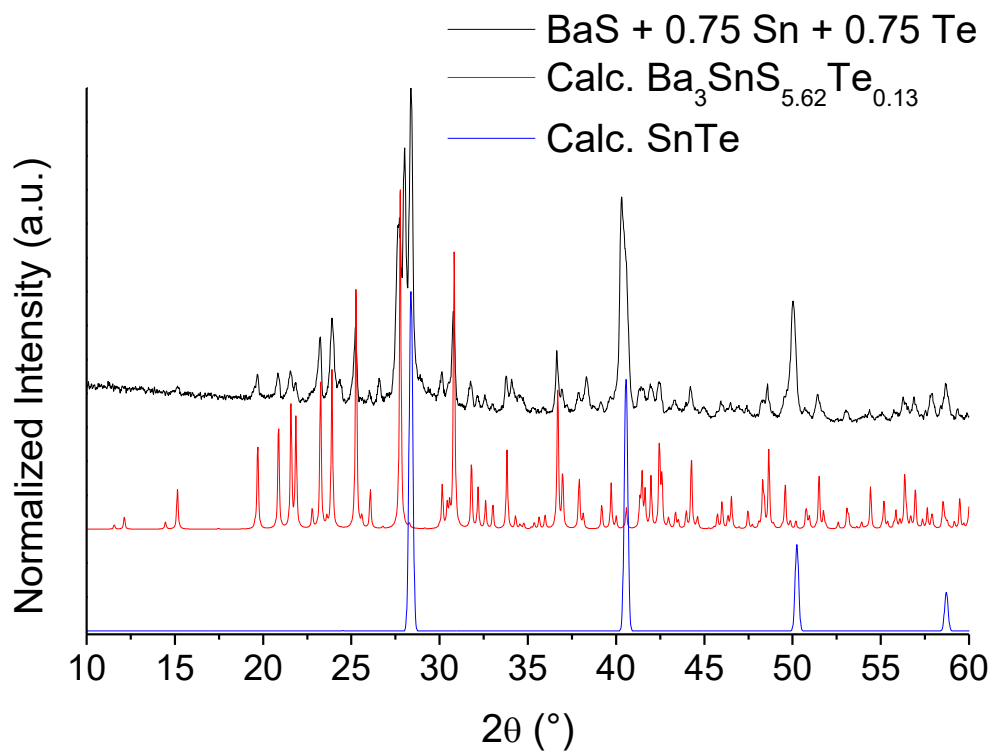


Figure S28: Synthesis of majority phase Ba₃SnS_{5.62}Te_{0.13}.

Table S36: Crystal data and structure refinement for Ba₇ S_{14.3} Sn₇ Te_{0.7} at 273.15 K.

Empirical formula	Ba ₇ S _{14.3} Sn ₇ Te _{0.7}
Formula weight	2142.50
Temperature	273.15 K
Wavelength	0.71073 Å
Crystal system	Hexagonal
Space group	P6 ₃ cm
Unit cell dimensions	a = 25.3104(6) Å, α = 90° b = 25.3104(6) Å, β = 90° c = 8.5782(2) Å, γ = 120°
Volume	4759.1(3) Å ³
Z	6
Density (calculated)	4.485 g/cm ³
Absorption coefficient	14.316 mm ⁻¹
F(000)	5558
Crystal size	0.09 x 0.04 x 0.03 mm ³
θ range for data collection	2.458 to 24.994°
Index ranges	-30 ≤ h ≤ 27, -30 ≤ k ≤ 26, -10 ≤ l ≤ 6
Reflections collected	27553
Independent reflections	2581 [R _{int} = 0.0553]
Completeness to θ = 24.994°	99.8%
Refinement method	Full-matrix least-squares on F ²
Data / restraints / parameters	2581 / 1 / 152
Goodness-of-fit	1.134
Final R indices [I > 2σ(I)]	R _{obs} = 0.0775, wR _{obs} = 0.1946
R indices [all data]	R _{all} = 0.0787, wR _{all} = 0.1954
Extinction coefficient	.
Largest diff. peak and hole	6.305 and -3.911 e·Å ⁻³

$$R = \frac{\sum ||F_o| - |F_c||}{\sum |F_o|}, \quad wR = \left\{ \frac{\sum [w(|F_o|^2 - |F_c|^2)^2]}{\sum [w(|F_o|^4)]} \right\}^{1/2} \quad \text{and} \\ w = 1 / [\sigma^2(F_o^2) + (0.0822P)^2 + 719.1233P] \quad \text{where } P = (F_o^2 + 2F_c^2) / 3$$

Table S37: Atomic coordinates ($\times 10^4$) and equivalent isotropic displacement parameters ($\text{\AA}^2 \times 10^3$) for Ba₇ S_{14.3} Sn₇ Te_{0.7} at 273.15 K with estimated standard deviations in parentheses.

Label	x	y	z	Occupancy	U_{eq}^*
Ba(0A)	0	0	3440(7)	1	23(2)
Ba(01)	0	5349(2)	2022(4)	1	14(1)
Ba(1A)	3333	6667	9225(6)	1	21(2)
Ba(02)	1456(2)	6565(2)	5762(4)	1	22(1)
Sn(03)	0	1664(2)	6981(7)	1	50(2)
Ba(2A)	1422(2)	3458(2)	5117(5)	1	38(1)
Te(01)	838(4)	1998(5)	8854(11)	0.14(2)	33(4)
Te(02)	2274(5)	4810(5)	3848(14)	0.11(2)	39(4)
Sn(01)	1678(2)	5093(2)	5570(4)	1	19(1)
Sn(02)	0	3558(2)	2985(6)	1	28(2)
Ba(04)	1890(2)	1890(2)	6999(7)	1	76(2)
Ba(05)	0	3084(2)	8790(6)	1	29(1)
S(01)	838(4)	1998(5)	8854(11)	0.86(2)	33(4)
S(02)	2274(5)	4810(5)	3848(14)	0.89(2)	39(4)
S(03)	0	4152(6)	605(19)	1	18(3)
S(04)	915(5)	5172(5)	4120(12)	1	19(2)
S(05)	2302(5)	6050(5)	6775(15)	1	24(2)
S(06)	869(5)	3399(6)	1710(14)	1	27(3)
S(07)	0	2429(6)	5334(18)	1	26(4)
S(08)	1064(5)	4245(6)	7299(14)	1	26(3)
S(09)	465(12)	1071(9)	5830(30)	0.57(5)	34(9)
S(10)	930(10)	2488(12)	8440(30)	0.55(6)	36(10)

* U_{eq} is defined as one third of the trace of the orthogonalized U_{ij} tensor.

Table S38: Anisotropic displacement parameters ($\text{\AA}^2 \times 10^3$) for Ba₇ S_{14.3} Sn₇ Te_{0.7} at 273.15 K with estimated standard deviations in parentheses.

Label	U_{11}	U_{22}	U_{33}	U_{12}	U_{13}	U_{23}
Ba(0A)	34(2)	34(2)	3(3)	17(1)	0	0
Ba(01)	17(2)	17(2)	7(2)	8(1)	0	-1(2)
Ba(1A)	22(2)	22(2)	20(3)	11(1)	0	0

Ba(02)	19(2)	20(2)	26(2)	8(1)	0(2)	-2(2)
Sn(03)	109(5)	47(2)	14(3)	54(3)	0	2(2)
Ba(2A)	27(2)	37(2)	56(2)	21(2)	-10(2)	-10(2)
Te(01)	15(4)	63(8)	11(5)	12(4)	-2(3)	-5(5)
Te(02)	43(7)	58(7)	32(7)	37(6)	-7(5)	6(5)
Sn(01)	15(2)	24(2)	17(2)	10(2)	-3(2)	3(2)
Sn(02)	28(2)	27(2)	29(3)	14(2)	0	3(2)
Ba(04)	67(2)	67(2)	19(3)	-24(3)	2(2)	2(2)
Ba(05)	37(2)	26(2)	28(2)	19(2)	0	4(2)
S(01)	15(4)	63(8)	11(5)	12(4)	-2(3)	-5(5)
S(02)	43(7)	58(7)	32(7)	37(6)	-7(5)	6(5)
S(03)	16(6)	27(5)	8(7)	8(3)	0	-7(6)
S(04)	27(5)	26(5)	7(5)	16(5)	-3(4)	3(4)
S(05)	18(5)	25(5)	21(7)	5(4)	-4(5)	2(5)
S(06)	18(5)	47(7)	23(7)	22(5)	3(5)	20(6)
S(07)	51(10)	31(6)	1(7)	25(5)	0	2(5)
S(08)	26(6)	28(6)	22(7)	12(5)	3(5)	3(5)
S(09)	64(16)	17(10)	24(15)	21(10)	-25(12)	-8(9)
S(10)	26(13)	41(17)	21(15)	2(10)	-8(10)	-1(11)

The anisotropic displacement factor exponent takes the form: $-2\pi^2[h^2a^{*2}U_{11} + \dots + 2hka^*b^*U_{12}]$.

Table S39: Bond lengths [\AA] for Ba₇ S_{14.3} Sn₇ Te_{0.7} at 273.15 K with estimated standard deviations in parentheses.

Label	Distances
Ba(0A)-S(09)#1	3.12(2)
Ba(0A)-S(09)#2	3.25(2)
Ba(0A)-S(09)#3	3.25(2)
Ba(0A)-S(09)#4	3.12(2)
Ba(0A)-S(09)#5	3.25(2)
Ba(0A)-S(09)#6	3.12(2)
Ba(0A)-S(09)#7	3.25(2)
Ba(0A)-S(09)	3.12(2)

Ba(0A)-S(09)#8	3.25(2)
Ba(0A)-S(09)#9	3.12(2)
Ba(0A)-S(09)#10	3.12(2)
Ba(0A)-S(09)#11	3.25(2)
Ba(01)-Ba(02)#12	4.512(3)
Ba(01)-Sn(01)#13	4.012(3)
Ba(01)-Sn(01)#12	4.012(3)
Ba(01)-Ba(05)#12	4.246(5)
Ba(01)-S(03)	3.263(15)
Ba(01)-S(03)#14	3.323(17)
Ba(01)-S(04)	3.137(11)
Ba(01)-S(04)#13	3.201(11)
Ba(01)-S(04)#12	3.201(11)
Ba(01)-S(04)#9	3.137(11)
Ba(01)-S(08)#12	3.336(12)
Ba(01)-S(08)#13	3.336(12)
Ba(1A)-Ba(1A)#15	4.28911(11)
Ba(1A)-Ba(1A)#16	4.28909(10)
Ba(1A)-Ba(02)#17	4.813(3)
Ba(1A)-Ba(02)#18	4.813(3)
Ba(1A)-Ba(02)#15	4.813(3)
Ba(1A)-S(05)#18	3.155(12)
Ba(1A)-S(05)#17	3.155(12)
Ba(1A)-S(05)#19	3.097(12)
Ba(1A)-S(05)#20	3.097(12)
Ba(1A)-S(05)	3.097(12)
Ba(1A)-S(05)#15	3.155(12)
Ba(02)-Te(02)#20	3.281(10)
Ba(02)-Te(02)#17	3.430(11)
Ba(02)-Sn(01)	4.039(4)
Ba(02)-Sn(02)#14	4.020(4)
Ba(02)-S(02)#17	3.430(11)
Ba(02)-S(02)#20	3.281(10)

Ba(02)-S(03)#14	3.194(3)
Ba(02)-S(04)#17	3.413(12)
Ba(02)-S(04)	3.386(11)
Ba(02)-S(05)	3.135(11)
Ba(02)-S(06)#17	3.393(12)
Ba(02)-S(08)#13	3.296(13)
Sn(03)-Te(01)#9	2.449(10)
Sn(03)-Te(01)	2.449(10)
Sn(03)-Ba(05)	3.917(7)
Sn(03)-S(01)#9	2.449(10)
Sn(03)-S(07)	2.398(16)
Sn(03)-S(09)	2.53(2)
Sn(03)-S(09)#9	2.53(2)
Sn(03)-S(10)	2.56(2)
Sn(03)-S(10)#9	2.56(2)
Ba(2A)-Te(01)#8	3.581(10)
Ba(2A)-Te(02)	3.188(12)
Ba(2A)-Sn(01)	3.875(4)
Ba(2A)-Ba(05)	4.515(5)
Ba(2A)-S(01)#8	3.581(10)
Ba(2A)-S(06)#18	3.190(11)
Ba(2A)-S(06)	3.212(12)
Ba(2A)-S(07)	3.226(5)
Ba(2A)-S(08)	3.178(13)
Ba(2A)-S(10)#8	3.01(2)
Ba(2A)-S(10)	3.56(3)
Te(01)-Ba(2A)#18	3.581(10)
Te(01)-Ba(04)#21	3.357(10)
Te(01)-Ba(04)	3.229(10)
Te(01)-S(09)#18	2.71(3)
Te(01)-S(10)	1.20(3)
Te(02)-Ba(02)#13	3.430(10)
Te(02)-Ba(02)#19	3.281(10)

Te(02)-Sn(01)	2.460(11)
Sn(01)-Ba(01)#14	4.012(3)
Sn(01)-S(04)	2.388(11)
Sn(01)-S(05)	2.367(12)
Sn(01)-S(08)	2.427(12)
Sn(02)-Ba(02)#12	4.020(4)
Sn(02)-Ba(02)#13	4.020(4)
Sn(02)-Ba(05)#22	3.793(7)
Sn(02)-S(03)	2.535(17)
Sn(02)-S(06)	2.660(11)
Sn(02)-S(06)#9	2.660(11)
Ba(04)-Te(01)#8	3.357(10)
Ba(04)-Te(01)#2	3.357(10)
Ba(04)-Te(01)#1	3.229(10)
Ba(04)-S(01)#2	3.357(10)
Ba(04)-S(01)#1	3.229(10)
Ba(04)-S(06)#18	3.330(13)
Ba(04)-S(06)#23	3.330(13)
Ba(04)-S(07)#23	3.170(17)
Ba(04)-S(09)#1	3.29(2)
Ba(04)-S(09)	3.29(2)
Ba(05)-Ba(01)#14	4.246(5)
Ba(05)-Sn(02)#24	3.793(7)
Ba(05)-Ba(04)#21	4.088(7)
Ba(05)-S(03)#24	3.119(15)
Ba(05)-S(06)#25	3.161(12)
Ba(05)-S(06)#24	3.161(12)
Ba(05)-S(07)	3.397(16)
Ba(05)-S(08)	3.099(12)
Ba(05)-S(08)#9	3.100(12)
Ba(05)-S(10)	3.39(3)
Ba(05)-S(10)#9	3.39(3)
S(03)-Ba(01)#12	3.323(17)

S(03)-Ba(02)#12	3.194(2)
S(03)-Ba(02)#13	3.194(2)
S(03)-Ba(05)#22	3.119(15)
S(04)-Ba(01)#14	3.201(11)
S(04)-Ba(02)#13	3.413(11)
S(05)-Ba(1A)#16	3.155(12)
S(06)-Ba(02)#13	3.393(12)
S(06)-Ba(2A)#8	3.190(11)
S(06)-Ba(04)#11	3.330(13)
S(06)-Ba(05)#22	3.161(12)
S(07)-Ba(2A)#9	3.226(5)
S(07)-Ba(04)#11	3.170(17)
S(08)-Ba(01)#14	3.337(12)
S(08)-Ba(02)#17	3.296(13)
S(09)-Ba(0A)#26	3.25(2)
S(09)-Te(01)#8	2.71(3)
S(09)-S(09)#9	2.04(5)
S(10)-Ba(2A)#18	3.01(2)
S(10)-Ba(04)#21	3.68(3)

Symmetry transformations used to generate equivalent atoms:

(1) y, x, z (2) $y, -x+y, z-1/2$ (3) $-x, -y, z-1/2$ (4) $x-y, -y, z$ (5) $x, x-y, z-1/2$ (6) $-y, x-y, z$ (7) $-y, -x, z-1/2$ (8) $-x+y, y, z-1/2$ (9) $-x, -x+y, z$ (10) $-x+y, -x, z$ (11) $x-y, x, z-1/2$ (12) $-x, -y+1, z-1/2$ (13) $x, x-y+1, z-1/2$ (14) $-x, -y+1, z+1/2$ (15) $-y+1, -x+1, z+1/2$ (16) $-y+1, -x+1, z-1/2$ (17) $x, x-y+1, z+1/2$ (18) $-x+y, y, z+1/2$ (19) $-y+1, x-y+1, z$ (20) $-x+y, -x+1, z$ (21) $x-y, x, z+1/2$ (22) $x, y, z-1$ (23) $y, -x+y, z+1/2$ (24) $x, y, z+1$ (25) $-x, -x+y, z+1$ (26) $-x, -y, z+1/2$

Table S40: Bond angles [$^{\circ}$] for Ba₇ S_{14.3} Sn₇ Te_{0.7} at 273.15 K with estimated standard deviations in parentheses.

Label	Angles
S(09)#1-Ba(0A)-S(09)#4	81.6(7)
S(09)#11-Ba(0A)-S(09)#5	92.5(8)
S(09)#9-Ba(0A)-S(09)#11	85.0(5)
S(09)#1-Ba(0A)-S(09)#6	97.6(9)
S(09)#9-Ba(0A)-S(09)#8	100.3(3)
S(09)#4-Ba(0A)-S(09)#6	38.1(10)

S(09)#6-Ba(0A)-S(09)#5	130.6(8)
S(09)#1-Ba(0A)-S(09)	50.4(8)
S(09)#1-Ba(0A)-S(09)#8	100.3(3)
S(09)#4-Ba(0A)-S(09)	97.6(9)
S(09)#1-Ba(0A)-S(09)#11	142.6(9)
S(09)#6-Ba(0A)-S(09)	81.6(7)
S(09)#2-Ba(0A)-S(09)#11	77.7(6)
S(09)#1-Ba(0A)-S(09)#9	81.6(7)
S(09)#3-Ba(0A)-S(09)#5	36.5(9)
S(09)#4-Ba(0A)-S(09)#9	81.6(7)
S(09)#3-Ba(0A)-S(09)#2	77.7(6)
S(09)#6-Ba(0A)-S(09)#9	50.4(8)
S(09)#6-Ba(0A)-S(09)#8	142.6(9)
S(09)-Ba(0A)-S(09)#9	38.1(10)
S(09)#7-Ba(0A)-S(09)#8	77.7(6)
S(09)#1-Ba(0A)-S(09)#10	38.1(10)
S(09)#6-Ba(0A)-S(09)#11	100.3(3)
S(09)#4-Ba(0A)-S(09)#10	50.4(8)
S(09)#3-Ba(0A)-S(09)#11	77.7(6)
S(09)#6-Ba(0A)-S(09)#10	81.6(6)
S(09)#1-Ba(0A)-S(09)#5	100.3(3)
S(09)-Ba(0A)-S(09)#10	81.6(6)
S(09)#9-Ba(0A)-S(09)#5	177.4(7)
S(09)#9-Ba(0A)-S(09)#10	97.6(9)
S(09)#2-Ba(0A)-S(09)#5	48.3(9)
S(09)#1-Ba(0A)-S(09)#3	130.6(8)
S(09)#10-Ba(0A)-S(09)#2	100.3(3)
S(09)#4-Ba(0A)-S(09)#3	85.0(5)
S(09)#7-Ba(0A)-S(09)#2	92.5(8)
S(09)#6-Ba(0A)-S(09)#3	100.3(3)
S(09)#4-Ba(0A)-S(09)#8	177.4(7)
S(09)-Ba(0A)-S(09)#3	177.4(7)
S(09)-Ba(0A)-S(09)#8	85.0(5)

S(09)#9-Ba(0A)-S(09)#3	142.6(9)
S(09)#3-Ba(0A)-S(09)#8	92.5(8)
S(09)#10-Ba(0A)-S(09)#3	100.3(3)
S(09)#2-Ba(0A)-S(09)#8	36.5(9)
S(09)#1-Ba(0A)-S(09)#7	177.4(7)
S(09)#4-Ba(0A)-S(09)#11	130.6(8)
S(09)#4-Ba(0A)-S(09)#7	100.3(3)
S(09)-Ba(0A)-S(09)#11	100.3(3)
S(09)#6-Ba(0A)-S(09)#7	85.0(5)
S(09)#10-Ba(0A)-S(09)#11	177.4(7)
S(09)-Ba(0A)-S(09)#7	130.6(8)
S(09)#7-Ba(0A)-S(09)#11	36.5(9)
S(09)#9-Ba(0A)-S(09)#7	100.3(3)
S(09)#8-Ba(0A)-S(09)#11	48.3(9)
S(09)#10-Ba(0A)-S(09)#7	142.6(9)
S(09)#4-Ba(0A)-S(09)#5	100.3(3)
S(09)#3-Ba(0A)-S(09)#7	48.2(9)
S(09)-Ba(0A)-S(09)#5	142.6(9)
S(09)#1-Ba(0A)-S(09)#2	85.0(5)
S(09)#10-Ba(0A)-S(09)#5	85.0(5)
S(09)#4-Ba(0A)-S(09)#2	142.6(9)
S(09)#7-Ba(0A)-S(09)#5	77.7(6)
S(09)#6-Ba(0A)-S(09)#2	177.4(7)
S(09)#8-Ba(0A)-S(09)#5	77.7(6)
S(09)-Ba(0A)-S(09)#2	100.3(3)
S(09)#9-Ba(0A)-S(09)#2	130.6(8)
S(09)#10-Ba(0A)-S(09)#8	130.6(8)
Sn(01)#12-Ba(01)-Ba(02)#12	56.21(5)
Sn(01)#13-Ba(01)-Ba(02)#12	137.80(10)
Sn(01)#12-Ba(01)-Sn(01)#13	132.96(13)
Sn(01)#12-Ba(01)-Ba(05)#12	82.93(7)
Sn(01)#13-Ba(01)-Ba(05)#12	82.93(7)
Ba(05)#12-Ba(01)-Ba(02)#12	134.97(4)

S(03)-Ba(01)-Ba(02)#12	45.05(4)
S(03)#14-Ba(01)-Ba(02)#12	118.32(17)
S(03)#14-Ba(01)-Sn(01)#13	101.06(11)
S(03)#14-Ba(01)-Sn(01)#12	101.06(11)
S(03)-Ba(01)-Sn(01)#13	96.71(13)
S(03)-Ba(01)-Sn(01)#12	96.71(13)
S(03)-Ba(01)-Ba(05)#12	179.0(3)
S(03)#14-Ba(01)-Ba(05)#12	46.7(3)
S(03)-Ba(01)-S(03)#14	134.2(4)
S(03)#14-Ba(01)-S(08)#12	70.3(3)
S(03)-Ba(01)-S(08)#12	133.4(2)
S(03)#14-Ba(01)-S(08)#13	70.3(3)
S(03)-Ba(01)-S(08)#13	133.4(2)
S(04)-Ba(01)-Ba(02)#12	104.4(2)
S(04)#12-Ba(01)-Ba(02)#12	48.5(2)
S(04)#13-Ba(01)-Ba(02)#12	102.9(2)
S(04)#9-Ba(01)-Ba(02)#12	49.1(2)
S(04)#9-Ba(01)-Sn(01)#12	73.7(2)
S(04)#12-Ba(01)-Sn(01)#13	110.2(2)
S(04)#13-Ba(01)-Sn(01)#12	110.2(2)
S(04)-Ba(01)-Sn(01)#12	153.2(2)
S(04)#12-Ba(01)-Sn(01)#12	36.52(19)
S(04)-Ba(01)-Sn(01)#13	73.7(2)
S(04)#9-Ba(01)-Sn(01)#13	153.2(2)
S(04)#13-Ba(01)-Sn(01)#13	36.52(19)
S(04)#12-Ba(01)-Ba(05)#12	108.9(2)
S(04)-Ba(01)-Ba(05)#12	105.9(2)
S(04)#13-Ba(01)-Ba(05)#12	108.9(2)
S(04)#9-Ba(01)-Ba(05)#12	105.9(2)
S(04)#9-Ba(01)-S(03)#14	70.4(3)
S(04)-Ba(01)-S(03)	74.9(3)
S(04)-Ba(01)-S(03)#14	70.4(3)
S(04)#12-Ba(01)-S(03)#14	137.6(2)

S(04)#13-Ba(01)-S(03)	70.4(3)
S(04)#13-Ba(01)-S(03)#14	137.6(2)
S(04)#9-Ba(01)-S(03)	74.9(3)
S(04)#12-Ba(01)-S(03)	70.4(3)
S(04)#9-Ba(01)-S(04)#12	91.1(3)
S(04)-Ba(01)-S(04)#9	79.5(4)
S(04)#12-Ba(01)-S(04)#13	77.6(4)
S(04)-Ba(01)-S(04)#13	91.1(3)
S(04)-Ba(01)-S(04)#12	145.22(18)
S(04)#9-Ba(01)-S(04)#13	145.22(18)
S(04)#12-Ba(01)-S(08)#12	69.7(3)
S(04)#12-Ba(01)-S(08)#13	121.9(3)
S(04)#9-Ba(01)-S(08)#13	140.4(3)
S(04)#13-Ba(01)-S(08)#12	121.9(3)
S(04)-Ba(01)-S(08)#13	82.9(3)
S(04)-Ba(01)-S(08)#12	140.4(3)
S(04)#9-Ba(01)-S(08)#12	82.9(3)
S(04)#13-Ba(01)-S(08)#13	69.7(3)
S(08)#12-Ba(01)-Ba(02)#12	89.8(2)
S(08)#13-Ba(01)-Ba(02)#12	170.0(2)
S(08)#12-Ba(01)-Sn(01)#13	119.0(2)
S(08)#13-Ba(01)-Sn(01)#13	37.1(2)
S(08)#13-Ba(01)-Sn(01)#12	119.0(2)
S(08)#12-Ba(01)-Sn(01)#12	37.1(2)
S(08)#13-Ba(01)-Ba(05)#12	46.4(2)
S(08)#12-Ba(01)-Ba(05)#12	46.4(2)
S(08)#13-Ba(01)-S(08)#12	88.7(4)
Ba(1A)#16-Ba(1A)-Ba(1A)#15	180.0
Ba(1A)#15-Ba(1A)-Ba(02)#17	74.10(7)
Ba(1A)#15-Ba(1A)-Ba(02)#15	74.10(7)
Ba(1A)#16-Ba(1A)-Ba(02)#17	105.90(7)
Ba(1A)#16-Ba(1A)-Ba(02)#15	105.90(7)
Ba(1A)#16-Ba(1A)-Ba(02)#18	105.90(7)

Ba(1A)#15-Ba(1A)-Ba(02)#18	74.10(7)
Ba(02)#15-Ba(1A)-Ba(02)#17	112.79(6)
Ba(02)#17-Ba(1A)-Ba(02)#18	112.79(6)
Ba(02)#15-Ba(1A)-Ba(02)#18	112.79(6)
S(05)#18-Ba(1A)-Ba(1A)#16	133.9(2)
S(05)#19-Ba(1A)-Ba(1A)#16	47.3(2)
S(05)#19-Ba(1A)-Ba(1A)#15	132.7(2)
S(05)#17-Ba(1A)-Ba(1A)#16	133.9(2)
S(05)#17-Ba(1A)-Ba(1A)#15	46.1(2)
S(05)-Ba(1A)-Ba(1A)#15	132.7(2)
S(05)#18-Ba(1A)-Ba(1A)#15	46.1(2)
S(05)#15-Ba(1A)-Ba(1A)#15	46.1(2)
S(05)#20-Ba(1A)-Ba(1A)#16	47.3(2)
S(05)-Ba(1A)-Ba(1A)#16	47.3(2)
S(05)#20-Ba(1A)-Ba(1A)#15	132.7(2)
S(05)#15-Ba(1A)-Ba(1A)#16	133.9(2)
S(05)#19-Ba(1A)-Ba(02)#17	107.4(2)
S(05)-Ba(1A)-Ba(02)#18	137.2(2)
S(05)#18-Ba(1A)-Ba(02)#18	39.9(2)
S(05)#17-Ba(1A)-Ba(02)#17	39.9(2)
S(05)#17-Ba(1A)-Ba(02)#18	115.6(2)
S(05)#15-Ba(1A)-Ba(02)#17	115.6(2)
S(05)#20-Ba(1A)-Ba(02)#17	137.2(2)
S(05)#18-Ba(1A)-Ba(02)#17	76.4(2)
S(05)#19-Ba(1A)-Ba(02)#18	61.7(2)
S(05)#15-Ba(1A)-Ba(02)#15	39.9(2)
S(05)#15-Ba(1A)-Ba(02)#18	76.4(2)
S(05)#18-Ba(1A)-Ba(02)#15	115.6(2)
S(05)#20-Ba(1A)-Ba(02)#15	61.7(2)
S(05)-Ba(1A)-Ba(02)#15	107.4(2)
S(05)-Ba(1A)-Ba(02)#17	61.7(2)
S(05)#20-Ba(1A)-Ba(02)#18	107.4(2)
S(05)#17-Ba(1A)-Ba(02)#15	76.4(2)

S(05)#19-Ba(1A)-Ba(02)#15	137.2(2)
S(05)#17-Ba(1A)-S(05)#15	77.3(3)
S(05)-Ba(1A)-S(05)#19	79.0(4)
S(05)-Ba(1A)-S(05)#15	146.2(4)
S(05)#20-Ba(1A)-S(05)#18	146.2(4)
S(05)-Ba(1A)-S(05)#17	87.4(3)
S(05)-Ba(1A)-S(05)#18	128.8(4)
S(05)#20-Ba(1A)-S(05)#19	79.0(4)
S(05)#19-Ba(1A)-S(05)#18	87.4(3)
S(05)#20-Ba(1A)-S(05)#17	128.8(4)
S(05)#17-Ba(1A)-S(05)#18	77.3(3)
S(05)#20-Ba(1A)-S(05)#15	87.4(3)
S(05)#15-Ba(1A)-S(05)#18	77.3(3)
S(05)#19-Ba(1A)-S(05)#15	128.8(4)
S(05)#20-Ba(1A)-S(05)	79.0(4)
S(05)#19-Ba(1A)-S(05)#17	146.2(4)
Te(02)#20-Ba(02)-Te(02)#17	80.55(8)
Te(02)#17-Ba(02)-Sn(01)	109.1(2)
Te(02)#20-Ba(02)-Sn(01)	111.6(2)
Te(02)#20-Ba(02)-Sn(02)#14	128.9(2)
Te(02)#17-Ba(02)-Sn(02)#14	84.9(2)
Te(02)#20-Ba(02)-S(02)#17	80.55(8)
Te(02)#20-Ba(02)-S(04)	116.5(3)
Te(02)#20-Ba(02)-S(04)#17	150.3(3)
Te(02)#20-Ba(02)-S(06)#17	88.0(3)
Te(02)#20-Ba(02)-S(08)#13	64.6(3)
Sn(02)#14-Ba(02)-Sn(01)	119.52(10)
S(02)#20-Ba(02)-Te(02)#20	0.0
S(02)#17-Ba(02)-Te(02)#17	0.0
S(02)#20-Ba(02)-Te(02)#17	80.5
S(02)#17-Ba(02)-Sn(01)	109.1(2)
S(02)#20-Ba(02)-Sn(01)	111.6(2)
S(02)#17-Ba(02)-Sn(02)#14	84.9(2)

S(02)#20-Ba(02)-Sn(02)#14	128.9(2)
S(02)#20-Ba(02)-S(02)#17	80.55(8)
S(02)#20-Ba(02)-S(04)	116.5(3)
S(02)#20-Ba(02)-S(04)#17	150.3(3)
S(02)#20-Ba(02)-S(06)#17	88.0(3)
S(02)#20-Ba(02)-S(08)#13	64.6(3)
S(03)#14-Ba(02)-Te(02)#17	123.5(4)
S(03)#14-Ba(02)-Te(02)#20	134.1(3)
S(03)#14-Ba(02)-Sn(01)	97.3(3)
S(03)#14-Ba(02)-Sn(02)#14	39.1(3)
S(03)#14-Ba(02)-S(02)#20	134.1(3)
S(03)#14-Ba(02)-S(02)#17	123.5(4)
S(03)#14-Ba(02)-S(04)	68.9(3)
S(03)#14-Ba(02)-S(04)#17	72.1(3)
S(03)#14-Ba(02)-S(06)#17	67.9(3)
S(03)#14-Ba(02)-S(08)#13	72.4(3)
S(04)#17-Ba(02)-Te(02)#17	71.2(3)
S(04)-Ba(02)-Te(02)#17	143.9(3)
S(04)#17-Ba(02)-Sn(01)	70.79(19)
S(04)-Ba(02)-Sn(01)	36.18(18)
S(04)-Ba(02)-Sn(02)#14	103.8(2)
S(04)#17-Ba(02)-Sn(02)#14	58.6(2)
S(04)-Ba(02)-S(02)#17	143.9(3)
S(04)#17-Ba(02)-S(02)#17	71.2(3)
S(04)-Ba(02)-S(04)#17	83.48(17)
S(04)-Ba(02)-S(06)#17	135.8(3)
S(05)-Ba(02)-Te(02)#20	94.3(3)
S(05)-Ba(02)-Te(02)#17	75.6(3)
S(05)-Ba(02)-Sn(01)	35.8(2)
S(05)-Ba(02)-Sn(02)#14	128.8(3)
S(05)-Ba(02)-S(02)#17	75.6(3)
S(05)-Ba(02)-S(02)#20	94.3(3)
S(05)-Ba(02)-S(03)#14	127.5(3)

S(05)-Ba(02)-S(04)#17	70.3(3)
S(05)-Ba(02)-S(04)	71.8(3)
S(05)-Ba(02)-S(06)#17	146.6(3)
S(05)-Ba(02)-S(08)#13	131.7(3)
S(06)#17-Ba(02)-Te(02)#17	72.0(3)
S(06)#17-Ba(02)-Sn(01)	160.4(2)
S(06)#17-Ba(02)-Sn(02)#14	41.0(2)
S(06)#17-Ba(02)-S(02)#17	72.0(3)
S(06)#17-Ba(02)-S(04)#17	91.8(3)
S(08)#13-Ba(02)-Te(02)#17	135.0(3)
S(08)#13-Ba(02)-Sn(01)	109.7(2)
S(08)#13-Ba(02)-Sn(02)#14	95.1(2)
S(08)#13-Ba(02)-S(02)#17	135.0(3)
S(08)#13-Ba(02)-S(04)	79.8(3)
S(08)#13-Ba(02)-S(04)#17	144.2(3)
S(08)#13-Ba(02)-S(06)#17	79.0(3)
Te(01)-Sn(03)-Te(01)#9	97.1(5)
Te(01)#9-Sn(03)-Ba(05)	79.7(3)
Te(01)-Sn(03)-Ba(05)	79.7(3)
Te(01)-Sn(03)-S(01)#9	97.1
Te(01)-Sn(03)-S(09)	83.2(5)
Te(01)-Sn(03)-S(09)#9	119.2(6)
Te(01)#9-Sn(03)-S(09)#9	83.2(6)
Te(01)#9-Sn(03)-S(09)	119.2(6)
Te(01)-Sn(03)-S(10)#9	107.9(6)
Te(01)#9-Sn(03)-S(10)	107.9(6)
Te(01)#9-Sn(03)-S(10)#9	27.5(7)
Te(01)-Sn(03)-S(10)	27.5(7)
S(01)#9-Sn(03)-Te(01)#9	0.0
S(01)#9-Sn(03)-Ba(05)	79.7(3)
S(01)#9-Sn(03)-S(09)	119.2(6)
S(01)#9-Sn(03)-S(09)#9	83.2(6)
S(01)#9-Sn(03)-S(10)	107.9(6)

S(01)#9-Sn(03)-S(10)#9	27.5(7)
S(07)-Sn(03)-Te(01)	117.2(4)
S(07)-Sn(03)-Te(01)#9	117.2(4)
S(07)-Sn(03)-Ba(05)	59.4(4)
S(07)-Sn(03)-S(01)#9	117.2(4)
S(07)-Sn(03)-S(09)	115.9(7)
S(07)-Sn(03)-S(09)#9	115.9(7)
S(07)-Sn(03)-S(10)	90.1(7)
S(07)-Sn(03)-S(10)#9	90.1(7)
S(09)#9-Sn(03)-Ba(05)	156.1(5)
S(09)-Sn(03)-Ba(05)	156.1(5)
S(09)#9-Sn(03)-S(09)	47.6(10)
S(09)#9-Sn(03)-S(10)#9	99.5(8)
S(09)-Sn(03)-S(10)	99.5(8)
S(09)-Sn(03)-S(10)#9	143.8(9)
S(09)#9-Sn(03)-S(10)	143.8(9)
S(10)#9-Sn(03)-Ba(05)	58.7(7)
S(10)-Sn(03)-Ba(05)	58.7(7)
S(10)-Sn(03)-S(10)#9	105.6(12)
Te(01)#8-Ba(2A)-Sn(01)	168.1(2)
Te(01)#8-Ba(2A)-Ba(05)	106.13(19)
Te(02)-Ba(2A)-Te(01)#8	133.0(3)
Te(02)-Ba(2A)-Sn(01)	39.3(2)
Te(02)-Ba(2A)-Ba(05)	120.2(2)
Te(02)-Ba(2A)-S(01)#8	133.0(3)
Te(02)-Ba(2A)-S(06)#18	93.3(3)
Te(02)-Ba(2A)-S(06)	77.6(3)
Te(02)-Ba(2A)-S(07)	140.3(3)
Te(02)-Ba(2A)-S(10)	146.1(5)
Sn(01)-Ba(2A)-Ba(05)	81.00(9)
S(01)#8-Ba(2A)-Te(01)#8	0.0
S(01)#8-Ba(2A)-Sn(01)	168.1(2)
S(01)#8-Ba(2A)-Ba(05)	106.13(19)

S(06)-Ba(2A)-Te(01)#8	80.0(3)
S(06)#18-Ba(2A)-Te(01)#8	78.2(3)
S(06)#18-Ba(2A)-Sn(01)	109.0(3)
S(06)-Ba(2A)-Sn(01)	88.7(2)
S(06)#18-Ba(2A)-Ba(05)	108.6(2)
S(06)-Ba(2A)-Ba(05)	110.0(2)
S(06)#18-Ba(2A)-S(01)#8	78.2(3)
S(06)-Ba(2A)-S(01)#8	80.0(3)
S(06)#18-Ba(2A)-S(06)	139.6(3)
S(06)#18-Ba(2A)-S(07)	126.2(4)
S(06)-Ba(2A)-S(07)	74.3(4)
S(06)#18-Ba(2A)-S(10)	68.7(4)
S(06)-Ba(2A)-S(10)	134.7(4)
S(07)-Ba(2A)-Te(01)#8	68.1(3)
S(07)-Ba(2A)-Sn(01)	112.3(3)
S(07)-Ba(2A)-Ba(05)	48.6(3)
S(07)-Ba(2A)-S(01)#8	68.1(3)
S(07)-Ba(2A)-S(10)	62.1(4)
S(08)-Ba(2A)-Te(01)#8	149.5(3)
S(08)-Ba(2A)-Te(02)	77.3(3)
S(08)-Ba(2A)-Sn(01)	38.7(2)
S(08)-Ba(2A)-Ba(05)	43.3(2)
S(08)-Ba(2A)-S(01)#8	149.5(3)
S(08)-Ba(2A)-S(06)	108.1(3)
S(08)-Ba(2A)-S(06)#18	108.1(3)
S(08)-Ba(2A)-S(07)	85.3(4)
S(08)-Ba(2A)-S(10)	81.3(5)
S(10)#8-Ba(2A)-Te(01)#8	18.4(6)
S(10)-Ba(2A)-Te(01)#8	73.1(5)
S(10)#8-Ba(2A)-Te(02)	114.9(6)
S(10)#8-Ba(2A)-Sn(01)	153.3(5)
S(10)-Ba(2A)-Sn(01)	118.1(5)
S(10)#8-Ba(2A)-Ba(05)	124.5(6)

S(10)-Ba(2A)-Ba(05)	47.8(5)
S(10)#8-Ba(2A)-S(01)#8	18.4(6)
S(10)-Ba(2A)-S(01)#8	73.1(5)
S(10)#8-Ba(2A)-S(06)	75.7(5)
S(10)#8-Ba(2A)-S(06)#18	72.8(6)
S(10)#8-Ba(2A)-S(07)	84.5(6)
S(10)#8-Ba(2A)-S(08)	167.8(6)
S(10)#8-Ba(2A)-S(10)	87.9(7)
Sn(03)-Te(01)-Ba(2A)#18	134.0(4)
Sn(03)-Te(01)-Ba(04)	104.8(3)
Sn(03)-Te(01)-Ba(04)#21	95.5(3)
Sn(03)-Te(01)-S(09)#18	109.6(6)
Ba(04)-Te(01)-Ba(2A)#18	85.9(2)
Ba(04)#21-Te(01)-Ba(2A)#18	90.9(2)
Ba(04)-Te(01)-Ba(04)#21	154.6(4)
S(09)#18-Te(01)-Ba(2A)#18	114.2(6)
S(09)#18-Te(01)-Ba(04)	93.7(6)
S(09)#18-Te(01)-Ba(04)#21	64.7(5)
S(10)-Te(01)-Sn(03)	81.4(12)
S(10)-Te(01)-Ba(2A)#18	52.6(11)
S(10)-Te(01)-Ba(04)#21	96.3(14)
S(10)-Te(01)-Ba(04)	101.6(14)
S(10)-Te(01)-S(09)#18	158.3(15)
Ba(02)#19-Te(02)-Ba(02)#13	158.6(4)
Ba(2A)-Te(02)-Ba(02)#13	102.9(3)
Ba(2A)-Te(02)-Ba(02)#19	90.0(3)
Sn(01)-Te(02)-Ba(02)#19	110.0(4)
Sn(01)-Te(02)-Ba(02)#13	88.2(3)
Sn(01)-Te(02)-Ba(2A)	85.6(3)
Ba(01)#14-Sn(01)-Ba(02)	68.16(7)
Ba(2A)-Sn(01)-Ba(01)#14	98.35(9)
Ba(2A)-Sn(01)-Ba(02)	164.37(9)
Te(02)-Sn(01)-Ba(01)#14	145.4(3)

Te(02)-Sn(01)-Ba(02)	133.0(3)
Te(02)-Sn(01)-Ba(2A)	55.1(3)
S(04)-Sn(01)-Ba(01)#14	52.9(3)
S(04)-Sn(01)-Ba(02)	56.8(3)
S(04)-Sn(01)-Ba(2A)	109.1(3)
S(04)-Sn(01)-Te(02)	110.5(4)
S(04)-Sn(01)-S(08)	101.8(4)
S(05)-Sn(01)-Ba(01)#14	102.8(3)
S(05)-Sn(01)-Ba(02)	50.8(3)
S(05)-Sn(01)-Ba(2A)	143.7(3)
S(05)-Sn(01)-Te(02)	111.6(4)
S(05)-Sn(01)-S(04)	107.2(4)
S(05)-Sn(01)-S(08)	116.3(4)
S(08)-Sn(01)-Ba(01)#14	56.1(3)
S(08)-Sn(01)-Ba(02)	117.9(3)
S(08)-Sn(01)-Ba(2A)	54.9(3)
S(08)-Sn(01)-Te(02)	108.9(4)
Ba(02)#12-Sn(02)-Ba(02)#13	105.10(13)
Ba(05)#22-Sn(02)-Ba(02)#12	70.77(9)
Ba(05)#22-Sn(02)-Ba(02)#13	70.77(9)
S(03)-Sn(02)-Ba(02)#13	52.59(7)
S(03)-Sn(02)-Ba(02)#12	52.59(7)
S(03)-Sn(02)-Ba(05)#22	54.8(4)
S(03)-Sn(02)-S(06)#9	90.2(4)
S(03)-Sn(02)-S(06)	90.2(4)
S(06)-Sn(02)-Ba(02)#13	56.8(3)
S(06)#9-Sn(02)-Ba(02)#13	126.0(3)
S(06)#9-Sn(02)-Ba(02)#12	56.8(3)
S(06)-Sn(02)-Ba(02)#12	126.0(3)
S(06)#9-Sn(02)-Ba(05)#22	55.4(3)
S(06)-Sn(02)-Ba(05)#22	55.4(3)
S(06)#9-Sn(02)-S(06)	91.4(6)
Te(01)-Ba(04)-Te(01)#2	137.7(4)

Te(01)#8-Ba(04)-Te(01)#2	66.3(3)
Te(01)#1-Ba(04)-Te(01)#2	83.02(9)
Te(01)#1-Ba(04)-Te(01)#8	137.7(4)
Te(01)-Ba(04)-Te(01)#8	83.02(9)
Te(01)#1-Ba(04)-Te(01)	103.9(4)
Te(01)#8-Ba(04)-S(01)#2	66.3(3)
Te(01)-Ba(04)-S(01)#2	137.7
Te(01)#1-Ba(04)-S(01)#2	83.02(9)
Te(01)#2-Ba(04)-S(01)#2	0.0(3)
Te(01)#1-Ba(04)-S(06)#18	142.1(3)
Te(01)#1-Ba(04)-S(06)#23	83.6(3)
Te(01)-Ba(04)-S(06)#18	83.6(3)
Te(01)-Ba(04)-S(06)#23	142.1(3)
Te(01)-Ba(04)-S(09)	60.9(5)
Te(01)#1-Ba(04)-S(09)	98.6(4)
Te(01)#1-Ba(04)-S(09)#1	60.9(5)
Te(01)-Ba(04)-S(09)#1	98.6(4)
S(01)#1-Ba(04)-Te(01)#8	137.7
S(01)#1-Ba(04)-Te(01)	103.9
S(01)#1-Ba(04)-Te(01)#1	0.0
S(01)#1-Ba(04)-Te(01)#2	83.0
S(01)#1-Ba(04)-S(01)#2	83.02(9)
S(01)#1-Ba(04)-S(06)#18	142.1(3)
S(01)#1-Ba(04)-S(06)#23	83.6(3)
S(01)#1-Ba(04)-S(09)	98.6(4)
S(01)#1-Ba(04)-S(09)#1	60.9(5)
S(06)#18-Ba(04)-Te(01)#2	116.4(3)
S(06)#18-Ba(04)-Te(01)#8	79.6(3)
S(06)#23-Ba(04)-Te(01)#2	79.6(3)
S(06)#23-Ba(04)-Te(01)#8	116.4(3)
S(06)#18-Ba(04)-S(01)#2	116.4(3)
S(06)#23-Ba(04)-S(01)#2	79.6(3)
S(06)#18-Ba(04)-S(06)#23	69.8(4)

S(07)#23-Ba(04)-Te(01)	73.4(3)
S(07)#23-Ba(04)-Te(01)#8	145.73(18)
S(07)#23-Ba(04)-Te(01)#2	145.73(18)
S(07)#23-Ba(04)-Te(01)#1	73.4(3)
S(07)#23-Ba(04)-S(01)#1	73.4(3)
S(07)#23-Ba(04)-S(01)#2	145.73(18)
S(07)#23-Ba(04)-S(06)#18	73.5(3)
S(07)#23-Ba(04)-S(06)#23	73.5(3)
S(07)#23-Ba(04)-S(09)	130.3(6)
S(07)#23-Ba(04)-S(09)#1	130.3(6)
S(09)#1-Ba(04)-Te(01)#2	48.0(5)
S(09)-Ba(04)-Te(01)#2	76.9(5)
S(09)#1-Ba(04)-Te(01)#8	76.9(5)
S(09)-Ba(04)-Te(01)#8	48.0(5)
S(09)#1-Ba(04)-S(01)#2	48.0(5)
S(09)-Ba(04)-S(01)#2	76.9(5)
S(09)-Ba(04)-S(06)#23	155.9(6)
S(09)-Ba(04)-S(06)#18	116.8(4)
S(09)#1-Ba(04)-S(06)#23	116.8(4)
S(09)#1-Ba(04)-S(06)#18	155.9(6)
S(09)#1-Ba(04)-S(09)	47.6(7)
Sn(03)-Ba(05)-Ba(01)#14	135.73(16)
Sn(03)-Ba(05)-Ba(04)#21	65.66(13)
Sn(02)#24-Ba(05)-Ba(01)#14	92.48(12)
Sn(02)#24-Ba(05)-Sn(03)	131.79(16)
Sn(02)#24-Ba(05)-Ba(04)#21	66.13(13)
Ba(04)#21-Ba(05)-Ba(01)#14	158.61(16)
S(03)#24-Ba(05)-Ba(01)#14	50.9(3)
S(03)#24-Ba(05)-Sn(03)	173.4(3)
S(03)#24-Ba(05)-Sn(02)#24	41.6(3)
S(03)#24-Ba(05)-Ba(04)#21	107.7(3)
S(03)#24-Ba(05)-S(06)#24	71.8(3)
S(03)#24-Ba(05)-S(06)#25	71.8(3)

S(03)#24-Ba(05)-S(07)	149.2(4)
S(03)#24-Ba(05)-S(10)	137.0(4)
S(03)#24-Ba(05)-S(10)#9	137.0(4)
S(06)#24-Ba(05)-Ba(01)#14	111.9(3)
S(06)#25-Ba(05)-Ba(01)#14	111.9(3)
S(06)#24-Ba(05)-Sn(03)	103.1(3)
S(06)#25-Ba(05)-Sn(03)	103.1(3)
S(06)#24-Ba(05)-Sn(02)#24	43.8(2)
S(06)#25-Ba(05)-Sn(02)#24	43.8(2)
S(06)#24-Ba(05)-Ba(04)#21	52.8(2)
S(06)#25-Ba(05)-Ba(04)#21	52.8(2)
S(06)#24-Ba(05)-S(06)#25	74.1(4)
S(06)#25-Ba(05)-S(07)	130.2(3)
S(06)#24-Ba(05)-S(07)	130.2(3)
S(06)#25-Ba(05)-S(10)	110.9(5)
S(06)#25-Ba(05)-S(10)#9	68.4(4)
S(06)#24-Ba(05)-S(10)#9	110.9(5)
S(06)#24-Ba(05)-S(10)	68.4(4)
S(07)-Ba(05)-Ba(01)#14	98.3(3)
S(07)-Ba(05)-Sn(03)	37.4(3)
S(07)-Ba(05)-Sn(02)#24	169.2(3)
S(07)-Ba(05)-Ba(04)#21	103.1(3)
S(08)-Ba(05)-Ba(01)#14	51.2(2)
S(08)#9-Ba(05)-Ba(01)#14	51.2(2)
S(08)#9-Ba(05)-Sn(03)	107.9(3)
S(08)-Ba(05)-Sn(03)	107.9(2)
S(08)#9-Ba(05)-Sn(02)#24	103.2(2)
S(08)-Ba(05)-Sn(02)#24	103.2(2)
S(08)-Ba(05)-Ba(04)#21	131.1(2)
S(08)#9-Ba(05)-Ba(04)#21	131.1(2)
S(08)#9-Ba(05)-S(03)#24	76.2(3)
S(08)-Ba(05)-S(03)#24	76.2(3)
S(08)#9-Ba(05)-S(06)#24	146.0(4)

S(08)-Ba(05)-S(06)#24	85.6(3)
S(08)#9-Ba(05)-S(06)#25	85.6(3)
S(08)-Ba(05)-S(06)#25	146.0(4)
S(08)#9-Ba(05)-S(07)	83.7(3)
S(08)-Ba(05)-S(07)	83.7(3)
S(08)-Ba(05)-S(08)#9	97.6(5)
S(08)#9-Ba(05)-S(10)#9	85.3(5)
S(08)-Ba(05)-S(10)#9	145.5(5)
S(08)#9-Ba(05)-S(10)	145.5(5)
S(08)-Ba(05)-S(10)	85.3(5)
S(10)-Ba(05)-Ba(01)#14	135.2(4)
S(10)#9-Ba(05)-Ba(01)#14	135.2(4)
S(10)#9-Ba(05)-Sn(03)	40.2(4)
S(10)-Ba(05)-Sn(03)	40.2(4)
S(10)#9-Ba(05)-Sn(02)#24	109.5(4)
S(10)-Ba(05)-Sn(02)#24	109.5(4)
S(10)-Ba(05)-Ba(04)#21	58.2(4)
S(10)#9-Ba(05)-Ba(04)#21	58.2(4)
S(10)-Ba(05)-S(07)	62.3(5)
S(10)#9-Ba(05)-S(07)	62.3(5)
S(10)#9-Ba(05)-S(10)	74.0(8)
Ba(01)-S(03)-Ba(01)#12	89.5(4)
Ba(02)#13-S(03)-Ba(01)	88.6(3)
Ba(02)#12-S(03)-Ba(01)#12	92.1(3)
Ba(02)#13-S(03)-Ba(01)#12	92.1(3)
Ba(02)#12-S(03)-Ba(01)	88.6(3)
Ba(02)#13-S(03)-Ba(02)#12	175.0(6)
Sn(02)-S(03)-Ba(01)	104.5(5)
Sn(02)-S(03)-Ba(01)#12	166.0(6)
Sn(02)-S(03)-Ba(02)#12	88.3(3)
Sn(02)-S(03)-Ba(02)#13	88.3(3)
Sn(02)-S(03)-Ba(05)#22	83.6(4)
Ba(05)#22-S(03)-Ba(01)#12	82.4(4)

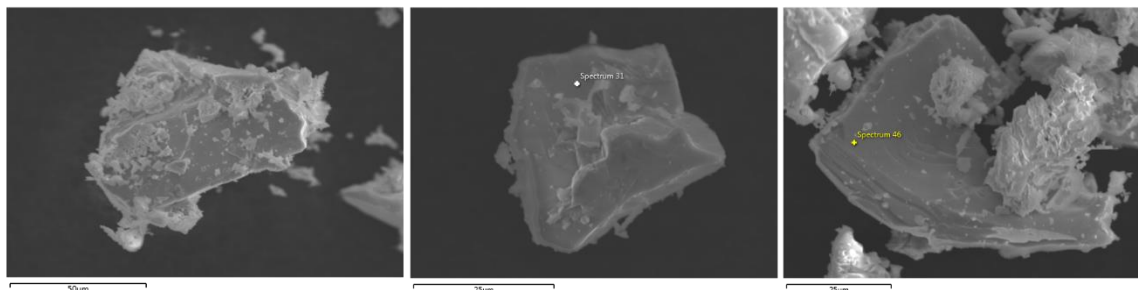
Ba(05)#22-S(03)-Ba(01)	171.9(6)
Ba(05)#22-S(03)-Ba(02)#13	91.6(3)
Ba(05)#22-S(03)-Ba(02)#12	91.6(3)
Ba(01)-S(04)-Ba(01)#14	94.1(3)
Ba(01)#14-S(04)-Ba(02)	86.4(3)
Ba(01)#14-S(04)-Ba(02)#13	148.6(4)
Ba(01)-S(04)-Ba(02)	91.9(3)
Ba(01)-S(04)-Ba(02)#13	87.0(3)
Ba(02)-S(04)-Ba(02)#13	124.9(3)
Sn(01)-S(04)-Ba(01)#14	90.6(3)
Sn(01)-S(04)-Ba(01)	175.2(5)
Sn(01)-S(04)-Ba(02)#13	89.8(3)
Sn(01)-S(04)-Ba(02)	87.0(3)
Ba(1A)-S(05)-Ba(1A)#16	86.6(3)
Ba(1A)-S(05)-Ba(02)	123.9(4)
Ba(02)-S(05)-Ba(1A)#16	99.8(3)
Sn(01)-S(05)-Ba(1A)	140.8(5)
Sn(01)-S(05)-Ba(1A)#16	99.6(4)
Sn(01)-S(05)-Ba(02)	93.4(3)
Ba(2A)#8-S(06)-Ba(02)#13	88.0(3)
Ba(2A)-S(06)-Ba(02)#13	103.2(4)
Ba(2A)#8-S(06)-Ba(2A)	90.9(3)
Ba(2A)-S(06)-Ba(04)#11	90.5(3)
Ba(2A)#8-S(06)-Ba(04)#11	98.6(3)
Sn(02)-S(06)-Ba(02)#13	82.3(3)
Sn(02)-S(06)-Ba(2A)	89.6(4)
Sn(02)-S(06)-Ba(2A)#8	170.1(5)
Sn(02)-S(06)-Ba(04)#11	91.2(3)
Sn(02)-S(06)-Ba(05)#22	80.8(3)
Ba(04)#11-S(06)-Ba(02)#13	164.8(4)
Ba(05)#22-S(06)-Ba(02)#13	87.3(3)
Ba(05)#22-S(06)-Ba(2A)	164.8(4)
Ba(05)#22-S(06)-Ba(2A)#8	100.6(4)

Ba(05)#22-S(06)-Ba(04)#11	78.0(3)
Sn(03)-S(07)-Ba(2A)	103.6(3)
Sn(03)-S(07)-Ba(2A)#9	103.6(3)
Sn(03)-S(07)-Ba(04)#11	100.6(5)
Sn(03)-S(07)-Ba(05)	83.1(4)
Ba(2A)#9-S(07)-Ba(2A)	150.3(5)
Ba(2A)#9-S(07)-Ba(05)	85.9(3)
Ba(2A)-S(07)-Ba(05)	85.9(3)
Ba(04)#11-S(07)-Ba(2A)#9	93.2(3)
Ba(04)#11-S(07)-Ba(2A)	93.2(3)
Ba(04)#11-S(07)-Ba(05)	176.3(6)
Ba(02)#17-S(08)-Ba(01)#14	90.0(3)
Ba(2A)-S(08)-Ba(01)#14	132.7(4)
Ba(2A)-S(08)-Ba(02)#17	137.1(4)
Sn(01)-S(08)-Ba(01)#14	86.7(3)
Sn(01)-S(08)-Ba(02)#17	102.2(4)
Sn(01)-S(08)-Ba(2A)	86.4(4)
Sn(01)-S(08)-Ba(05)	163.7(5)
Ba(05)-S(08)-Ba(01)#14	82.5(3)
Ba(05)-S(08)-Ba(02)#17	90.1(3)
Ba(05)-S(08)-Ba(2A)	92.0(3)
Ba(0A)-S(09)-Ba(0A)#26	84.6(5)
Ba(0A)#26-S(09)-Ba(04)	98.1(6)
Ba(0A)-S(09)-Ba(04)	124.5(9)
Sn(03)-S(09)-Ba(0A)#26	98.2(9)
Sn(03)-S(09)-Ba(0A)	133.5(9)
Sn(03)-S(09)-Te(01)#8	91.4(6)
Sn(03)-S(09)-Ba(04)	101.3(6)
Te(01)#8-S(09)-Ba(0A)	98.2(8)
Te(01)#8-S(09)-Ba(0A)#26	163.9(9)
Te(01)#8-S(09)-Ba(04)	67.2(6)
S(09)#9-S(09)-Ba(0A)#26	71.7(4)
S(09)#9-S(09)-Ba(0A)	70.9(5)

S(09)#9-S(09)-Sn(03)	66.2(5)
S(09)#9-S(09)-Te(01)#8	124.2(5)
S(09)#9-S(09)-Ba(04)	161.6(5)
Sn(03)-S(10)-Ba(2A)#18	179.1(11)
Sn(03)-S(10)-Ba(2A)	91.8(7)
Sn(03)-S(10)-Ba(04)#21	86.1(6)
Sn(03)-S(10)-Ba(04)	91.6(8)
Sn(03)-S(10)-Ba(05)	81.1(7)
Ba(2A)#18-S(10)-Ba(2A)	87.6(6)
Ba(2A)-S(10)-Ba(04)	86.5(6)
Ba(2A)#18-S(10)-Ba(04)#21	94.7(6)
Ba(2A)#18-S(10)-Ba(04)	87.7(6)
Ba(2A)-S(10)-Ba(04)#21	151.5(9)
Ba(2A)#18-S(10)-Ba(05)	99.4(8)
Te(01)-S(10)-Sn(03)	71.1(11)
Te(01)-S(10)-Ba(2A)#18	109.0(14)
Te(01)-S(10)-Ba(2A)	140.6(17)
Te(01)-S(10)-Ba(04)	59.8(13)
Te(01)-S(10)-Ba(04)#21	64.9(12)
Te(01)-S(10)-Ba(05)	128.2(15)
Ba(04)-S(10)-Ba(04)#21	122.0(8)
Ba(05)-S(10)-Ba(2A)	81.0(6)
Ba(05)-S(10)-Ba(04)	165.3(8)
Ba(05)-S(10)-Ba(04)#21	70.5(5)

Symmetry transformations used to generate equivalent atoms:

(1) y, x, z (2) $y, -x+y, z-1/2$ (3) $-x, -y, z-1/2$ (4) $x-y, -y, z$ (5) $x, x-y, z-1/2$ (6) $-y, x-y, z$ (7) $-y, -x, z-1/2$ (8) $-x+y, y, z-1/2$ (9) $-x, -x+y, z$ (10) $-x+y, -x, z$ (11) $x-y, x, z-1/2$ (12) $-x, -y+1, z-1/2$ (13) $x, x-y+1, z-1/2$ (14) $-x, -y+1, z+1/2$ (15) $-y+1, -x+1, z+1/2$ (16) $-y+1, -x+1, z-1/2$ (17) $x, x-y+1, z+1/2$ (18) $-x+y, y, z+1/2$ (19) $-y+1, x-y+1, z$ (20) $-x+y, -x+1, z$ (21) $x-y, x, z+1/2$ (22) $x, y, z-1$ (23) $y, -x+y, z+1/2$ (24) $x, y, z+1$ (25) $-x, -x+y, z+1$ (26) $-x, -y, z+1/2$

Figure S29: SEM images of "Ba₈Sn₄S₁₀S₆"

Crystals were retrieved from BaTe + $\frac{3}{4}$ Sn + $\frac{3}{4}$ S reaction. Yellow crystal.

Table S41: Crystal data and structure refinement for Ba₈ S_{14.24} Sn₄ Te_{0.76} at 100.03 K.

Empirical formula	Ba ₈ S _{14.24} Sn ₄ Te _{0.76}
Formula weight	2126.87
Temperature	100.03 K
Wavelength	0.71073 Å
Crystal system	Orthorhombic
Space group	Pca2 ₁
Unit cell dimensions	a = 28.730(5) Å, α = 90° b = 8.5099(15) Å, β = 90° c = 25.456(5) Å, γ = 90°
Volume	6223.8(19) Å ³
Z	8
Density (calculated)	4.540 g/cm ³
Absorption coefficient	14.737 mm ⁻¹
F(000)	7323
Crystal size	0.113 x 0.106 x 0.072 mm ³
θ range for data collection	1.418 to 27.228°
Index ranges	-36 ≤ h ≤ 36, -10 ≤ k ≤ 10, -32 ≤ l ≤ 32
Reflections collected	45334
Independent reflections	45334 [R _{int} = ?]
Completeness to θ = 25.242°	99.8%

Refinement method	Full-matrix least-squares on F^2
Data / restraints / parameters	45334 / 1 / 227
Goodness-of-fit	1.198
Final R indices [$I > 2\sigma(I)$]	$R_{\text{obs}} = 0.1402$, $wR_{\text{obs}} = 0.3446$
R indices [all data]	$R_{\text{all}} = 0.1428$, $wR_{\text{all}} = 0.3464$
Extinction coefficient	0.0041(3)
Largest diff. peak and hole	18.618 and $-6.348 \text{ e} \cdot \text{\AA}^{-3}$

$R = \sum ||F_o| - |F_c|| / \sum |F_o|$, $wR = \{ \sum [w(|F_o|^2 - |F_c|^2)^2] / \sum [w(|F_o|^4)] \}^{1/2}$ and $w = 1 / [\sigma^2(F_o^2) + (0.1387P)^2 + 2990.2307P]$ where $P = (F_o^2 + 2F_c^2) / 3$

Table S42: Atomic coordinates (x104) and equivalent isotropic displacement parameters ($\text{\AA}^2 \times 10^3$) for Ba₈ S_{14.24} Sn₄ Te_{0.76} at 100.03 K with estimated standard deviations in parentheses.

Label	x	y	z	Occupancy	U_{eq}^*
Ba(1)	-3585(2)	-1679(6)	-2681(2)	1	15(2)
Ba(2)	-4790(2)	-5520(6)	-5294(2)	1	12(1)
Ba(3)	-7562(2)	-5565(6)	-5474(2)	1	12(1)
Ba(4)	-4787(2)	-715(6)	-3603(2)	1	15(2)
Ba(5)	-6397(2)	-2451(6)	-1339(2)	1	11(1)
Ba(6)	-6285(2)	-5774(6)	-2614(2)	1	13(2)
Ba(7)	-7549(2)	-498(6)	-3465(2)	1	15(2)
Ba(8)	-6270(2)	-7099(5)	-4486(2)	1	6(1)
Ba(9)	-6299(2)	-525(5)	-6306(2)	1	8(1)
Ba(10)	-7728(2)	841(5)	-6804(2)	1	7(1)
Ba(11)	-7216(2)	-4334(5)	-7154(2)	1	9(1)
Ba(12)	-6197(2)	-2079(5)	-4486(2)	1	7(1)
Ba(13)	-3677(2)	-9148(6)	-4773(2)	1	11(1)
Ba(14)	-5233(2)	-6390(6)	-7089(2)	1	14(1)
Ba(15)	-4846(2)	-1459(6)	-6694(2)	1	16(2)
Ba(16)	-3626(2)	-3982(6)	-4167(2)	1	9(1)
Te(3)	-5588(5)	-2627(16)	-2940(6)	0.20(4)	12(5)
Te(4)	-2560(5)	-2529(17)	-4354(6)	0.19(4)	14(5)
Te(5)	-7615(4)	-2494(15)	-4578(5)	0.30(4)	18(4)
Sn(1)	-4934(2)	-5641(7)	-3689(2)	1	13(2)
Sn(2)	-6244(2)	-881(6)	-2807(2)	1	9(2)

Sn(3)	-2384(2)	-4313(6)	-3597(2)	1	8(2)
Sn(4)	-7416(2)	-788(6)	-5341(2)	1	10(2)
Sn(5)	-6261(2)	-5692(6)	-6085(2)	1	5(2)
Sn(6)	-4955(2)	-634(6)	-5176(2)	1	7(2)
Sn(7)	-3942(2)	2519(5)	-2953(2)	1	-1(1)
Sn(8)	-3800(2)	-3281(6)	-5985(2)	1	9(2)
S(1)	-6167(7)	820(20)	-2048(8)	1	6(3)
S(2)	-7416(7)	-2280(20)	-6153(8)	1	9(4)
S(3)	-5588(5)	-2627(16)	-2940(6)	0.80(4)	12(5)
S(4)	-2560(5)	-2529(17)	-4354(6)	0.81(4)	14(5)
S(5)	-7615(4)	-2494(15)	-4578(5)	0.70(4)	18(4)
S(6)	-6900(7)	-2300(20)	-2485(8)	1	7(4)
S(8)	-5416(7)	550(20)	-4519(9)	1	11(4)
S(9)	-6650(7)	-4540(20)	-3722(9)	1	10(4)
S(10)	-8125(7)	-720(20)	-2386(8)	1	5(4)
S(11)	-4390(7)	-4000(20)	-3238(8)	1	6(4)
S(12)	-3654(6)	-5510(20)	-5317(8)	0.94(4)	13(6)
Te(12)	-3654(6)	-5510(20)	-5317(8)	0.06(4)	13(6)
S(13)	-3629(7)	-470(20)	-3613(9)	1	11(4)
S(14)	-5441(6)	-2400(20)	-5708(8)	0.95(4)	13(7)
Te(14)	-5441(6)	-2400(20)	-5708(8)	0.05(4)	13(7)
S(15)	-5267(3)	2529(10)	-2982(4)	0.56(4)	10(3)
Te(15)	-5267(3)	2529(10)	-2982(4)	0.44(4)	10(3)
S(16)	-6911(7)	-7150(20)	-6417(8)	1	10(4)
S(17)	-6860(7)	-5740(20)	-1553(8)	1	8(4)
S(18)	-6061(6)	-3970(20)	-6809(7)	1	5(3)
S(19)	-6542(7)	-4540(20)	-5299(8)	1	6(4)
S(20)	-7350(7)	-7220(20)	-2814(8)	1	9(4)
S(21)	-8050(7)	890(20)	-5595(8)	1	10(4)
S(22)	-6690(8)	380(30)	-5229(9)	1	15(4)
S(23)	-5439(7)	-4650(20)	-4326(8)	1	12(4)
S(24)	-6464(7)	470(20)	-3591(8)	1	7(4)
S(25)	-4382(7)	-2140(20)	-4706(9)	1	12(4)

S(26)	-4348(7)	-7130(20)	-4151(8)	1	9(4)
S(27)	-4363(7)	-320(20)	-2338(7)	1	6(4)
S(28)	-4487(6)	1030(20)	-5736(7)	0.93(4)	11(6)
Te(28)	-4487(6)	1030(20)	-5736(7)	0.07(4)	11(6)
S(29)	-5603(7)	-5050(20)	-1534(8)	1	10(4)
S(30)	-3024(7)	-6040(20)	-3403(8)	1	10(4)
S(7)	-5607(5)	-7489(16)	-5907(6)	0.80(4)	16(5)
Te(7)	-5607(5)	-7489(16)	-5907(6)	0.20(4)	16(5)

* U_{eq} is defined as one third of the trace of the orthogonalized U_{ij} tensor.

Table S43: Anisotropic displacement parameters ($\text{\AA}^2 \times 10^3$) for Ba₈ S_{14.24} Sn₄ Te_{0.76} at 100.03 K with estimated standard deviations in parentheses.

--	--	--	--	--

The anisotropic displacement factor exponent takes the form: $-2\pi^2[h^2a^{*2}U_{11} + \dots + 2hka^*b^*U_{12}]$.

Table S44: Bond lengths [\AA] for Ba₈ S_{14.24} Sn₄ Te_{0.76} at 100.03 K with estimated standard deviations in parentheses.

Label	Distances
Ba(1)-Ba(7)#1	4.035(8)
Ba(1)-Ba(9)#2	3.985(7)
Ba(1)-Ba(10)#2	4.440(7)
Ba(1)-Ba(11)#3	4.313(7)
Ba(1)-Ba(14)#3	4.063(7)
Ba(1)-S(10)#1	2.543(19)
Ba(1)-S(11)	3.36(2)
Ba(1)-S(13)	2.59(2)
Ba(1)-S(16)#3	3.66(2)
Ba(1)-S(20)#4	3.69(2)
Ba(1)-S(27)	2.67(2)
Ba(2)-S(12)	3.263(19)

Ba(2)-S(14)	3.417(19)
Ba(2)-S(23)	3.18(2)
Ba(2)-S(25)	3.45(2)
Ba(2)-S(26)	3.46(2)
Ba(2)-S(28)#5	3.264(18)
Ba(2)-Te(28)#5	3.264(18)
Ba(2)-S(29)#6	3.39(2)
Ba(2)-S(7)	3.278(15)
Ba(3)-Te(4)#7	3.282(17)
Ba(3)-Te(5)	3.472(14)
Ba(3)-Sn(8)#7	3.910(8)
Ba(3)-S(2)	3.31(2)
Ba(3)-S(4)#7	3.282(17)
Ba(3)-S(12)#7	3.294(19)
Ba(3)-Te(12)#7	3.294(19)
Ba(3)-S(16)	3.33(2)
Ba(3)-S(17)#8	3.21(2)
Ba(3)-S(19)	3.09(2)
Ba(3)-S(21)#5	3.34(2)
Ba(4)-Ba(13)#9	4.563(7)
Ba(4)-Te(3)	3.284(15)
Ba(4)-Sn(7)	4.026(7)
Ba(4)-S(8)	3.14(2)
Ba(4)-S(11)	3.162(19)
Ba(4)-S(13)	3.33(2)
Ba(4)-S(15)	3.468(10)
Ba(4)-S(25)	3.27(2)
Ba(4)-S(26)#9	3.58(2)
Ba(4)-S(27)	3.46(2)
Ba(5)-Ba(10)#10	3.946(7)
Ba(5)-Ba(13)#3	4.218(7)
Ba(5)-Sn(8)#3	3.785(7)
Ba(5)-S(1)	3.383(19)

Ba(5)-S(2)#10	3.45(2)
Ba(5)-S(6)	3.26(2)
Ba(5)-S(12)#3	3.13(2)
Ba(5)-Te(12)#3	3.13(2)
Ba(5)-S(17)	3.14(2)
Ba(5)-S(28)#2	3.205(18)
Ba(5)-Te(28)#2	3.205(18)
Ba(5)-S(29)	3.21(2)
Ba(6)-Ba(10)#11	4.537(7)
Ba(6)-Te(3)	3.447(15)
Ba(6)-Sn(3)#7	4.029(8)
Ba(6)-S(1)#5	3.255(19)
Ba(6)-S(6)	3.462(19)
Ba(6)-S(9)	3.19(2)
Ba(6)-S(15)#5	3.394(10)
Ba(6)-Te(15)#5	3.394(10)
Ba(6)-S(17)	3.17(2)
Ba(6)-S(20)	3.34(2)
Ba(6)-S(29)	3.43(2)
Ba(7)-Ba(1)#12	4.035(8)
Ba(7)-Ba(10)#10	4.450(7)
Ba(7)-Te(4)#12	3.428(16)
Ba(7)-Te(5)	3.308(14)
Ba(7)-S(4)#12	3.428(16)
Ba(7)-S(6)	3.47(2)
Ba(7)-S(10)	3.21(2)
Ba(7)-S(13)#12	3.23(2)
Ba(7)-S(20)#9	3.30(2)
Ba(7)-S(24)	3.24(2)
Ba(7)-S(30)#7	3.25(2)
Ba(8)-Ba(12)#5	4.243(6)
Ba(8)-Te(4)#7	3.737(15)
Ba(8)-S(8)#5	3.17(2)

Ba(8)-S(9)	3.12(2)
Ba(8)-S(19)	3.103(19)
Ba(8)-S(22)#5	3.10(2)
Ba(8)-S(23)	3.20(2)
Ba(8)-S(24)#5	3.13(2)
Ba(9)-Ba(1)#13	3.985(7)
Ba(9)-Ba(12)	4.827(7)
Ba(9)-S(2)	3.56(2)
Ba(9)-S(10)#8	3.21(2)
Ba(9)-S(14)	3.306(19)
Ba(9)-S(16)#9	3.38(2)
Ba(9)-S(18)	3.273(19)
Ba(9)-S(22)	3.06(2)
Ba(9)-S(27)#13	3.323(19)
Ba(9)-S(7)#9	3.416(15)
Ba(9)-Te(7)#9	3.416(15)
Ba(10)-Ba(1)#13	4.440(7)
Ba(10)-Ba(5)#8	3.946(7)
Ba(10)-Ba(7)#8	4.450(7)
Ba(10)-Ba(11)#9	4.451(7)
Ba(10)-S(1)#8	3.236(19)
Ba(10)-S(2)	3.26(2)
Ba(10)-S(6)#8	3.36(2)
Ba(10)-S(10)#8	3.15(2)
Ba(10)-S(16)#9	3.07(2)
Ba(10)-S(17)#14	3.209(19)
Ba(10)-S(20)#14	3.07(2)
Ba(10)-S(21)	3.22(2)
Ba(11)-Ba(1)#6	4.313(7)
Ba(11)-Ba(10)#5	4.451(7)
Ba(11)-Sn(3)#6	4.018(8)
Ba(11)-S(2)	3.14(2)
Ba(11)-S(6)#8	3.19(2)

Ba(11)-S(10)#8	3.284(19)
Ba(11)-S(16)	3.17(2)
Ba(11)-S(17)#8	3.29(2)
Ba(11)-S(18)	3.445(19)
Ba(11)-S(20)#8	3.22(2)
Ba(11)-S(30)#6	3.27(2)
Ba(12)-Ba(8)#9	4.243(6)
Ba(12)-S(8)	3.17(2)
Ba(12)-S(9)	3.14(2)
Ba(12)-S(19)	3.11(2)
Ba(12)-S(22)	3.16(2)
Ba(12)-S(23)	3.11(2)
Ba(12)-S(24)	3.24(2)
Ba(13)-Te(5)#4	3.392(14)
Ba(13)-Sn(4)#4	3.900(8)
Ba(13)-Sn(6)#5	4.019(7)
Ba(13)-S(5)#4	3.392(14)
Ba(13)-S(12)	3.388(19)
Ba(13)-S(13)#5	3.16(2)
Ba(13)-S(21)#4	3.13(2)
Ba(13)-S(25)#5	3.26(2)
Ba(13)-S(26)	3.03(2)
Ba(13)-S(28)#5	3.384(18)
Ba(13)-Te(28)#5	3.384(18)
Ba(14)-Ba(1)#6	4.063(7)
Ba(14)-Ba(4)#6	4.574(8)
Ba(14)-Ba(15)#5	4.566(7)
Ba(14)-Te(3)#6	3.309(15)
Ba(14)-S(3)#6	3.309(15)
Ba(14)-S(11)#6	3.14(2)
Ba(14)-S(18)	3.226(19)
Ba(14)-S(27)#6	3.100(19)
Ba(14)-S(29)#6	3.04(2)

Ba(14)-S(7)	3.329(16)
Ba(15)-Ba(6)#6	4.646(7)
Ba(15)-Ba(14)#9	4.566(7)
Ba(15)-S(1)#13	3.09(2)
Ba(15)-S(14)	3.14(2)
Ba(15)-S(15)#13	3.417(11)
Ba(15)-Te(15)#13	3.417(11)
Ba(15)-S(27)#13	3.183(19)
Ba(15)-S(28)	3.390(18)
Ba(15)-S(29)#6	3.27(2)
Ba(16)-Ba(3)#4	4.533(7)
Ba(16)-Ba(13)#9	4.395(7)
Ba(16)-Te(4)	3.336(15)
Ba(16)-S(11)	3.23(2)
Ba(16)-S(12)	3.20(2)
Ba(16)-S(13)	3.31(2)
Ba(16)-S(25)	3.01(2)
Ba(16)-S(26)	3.39(2)
Ba(16)-S(30)	3.14(2)
Te(3)-Ba(14)#3	3.309(15)
Te(3)-Sn(2)	2.424(14)
Te(4)-Ba(3)#4	3.282(17)
Te(4)-Ba(7)#1	3.428(16)
Te(4)-Ba(8)#4	3.737(15)
Te(4)-Sn(3)	2.505(16)
Te(5)-Ba(13)#7	3.392(13)
Te(5)-Sn(4)	2.491(14)
Sn(1)-S(11)	2.39(2)
Sn(1)-S(15)#5	2.565(11)
Sn(1)-Te(15)#5	2.565(11)
Sn(1)-S(23)	2.33(2)
Sn(1)-S(26)	2.41(2)
Sn(2)-S(1)	2.42(2)

Sn(2)-S(6)	2.38(2)
Sn(2)-S(24)	2.39(2)
Sn(3)-Ba(6)#4	4.029(8)
Sn(3)-Ba(11)#3	4.018(8)
Sn(3)-S(9)#4	2.35(2)
Sn(3)-S(20)#4	2.38(2)
Sn(3)-S(30)	2.40(2)
Sn(4)-Ba(13)#7	3.900(8)
Sn(4)-S(2)	2.43(2)
Sn(4)-S(21)	2.40(2)
Sn(4)-S(22)	2.33(2)
Sn(5)-S(16)	2.40(2)
Sn(5)-S(18)	2.423(19)
Sn(5)-S(19)	2.37(2)
Sn(5)-S(7)	2.465(15)
Sn(6)-Ba(13)#9	4.018(7)
Sn(6)-S(8)	2.36(2)
Sn(6)-S(14)	2.46(2)
Sn(6)-S(25)	2.41(2)
Sn(6)-S(28)	2.418(18)
Sn(8)-Ba(3)#4	3.910(8)
Sn(8)-Ba(5)#6	3.785(7)
Sn(8)-S(12)	2.59(2)
Sn(8)-S(17)#6	2.53(2)
Sn(8)-S(29)#6	2.63(2)
S(1)-Ba(6)#9	3.255(19)
S(1)-Ba(10)#10	3.236(19)
S(1)-Ba(15)#2	3.093(19)
S(2)-Ba(5)#8	3.45(2)
S(6)-Ba(10)#10	3.36(2)
S(6)-Ba(11)#10	3.19(2)
S(8)-Ba(8)#9	3.17(2)
S(9)-Sn(3)#7	2.35(2)

S(10)-Ba(1)#12	2.543(19)
S(10)-Ba(9)#10	3.21(2)
S(10)-Ba(10)#10	3.15(2)
S(10)-Ba(11)#10	3.284(18)
S(11)-Ba(14)#3	3.14(2)
S(12)-Ba(3)#4	3.293(19)
S(12)-Ba(5)#6	3.13(2)
S(13)-Ba(7)#1	3.23(2)
S(13)-Ba(13)#9	3.16(2)
S(15)-Ba(6)#9	3.394(10)
S(15)-Ba(15)#2	3.417(11)
S(15)-Sn(1)#9	2.565(11)
S(16)-Ba(1)#6	3.66(2)
S(16)-Ba(9)#5	3.38(2)
S(16)-Ba(10)#5	3.07(2)
S(17)-Ba(3)#10	3.21(2)
S(17)-Ba(10)#11	3.209(19)
S(17)-Ba(11)#10	3.29(2)
S(17)-Sn(8)#3	2.53(2)
S(20)-Ba(1)#7	3.68(2)
S(20)-Ba(7)#5	3.30(2)
S(20)-Ba(10)#11	3.07(2)
S(20)-Ba(11)#10	3.22(2)
S(20)-Sn(3)#7	2.38(2)
S(21)-Ba(3)#9	3.34(2)
S(21)-Ba(13)#7	3.13(2)
S(22)-Ba(8)#9	3.10(2)
S(24)-Ba(8)#9	3.13(2)
S(25)-Ba(13)#9	3.26(2)
S(26)-Ba(4)#5	3.58(2)
S(27)-Ba(9)#2	3.322(19)
S(27)-Ba(14)#3	3.100(19)
S(27)-Ba(15)#2	3.183(19)

S(28)-Ba(2)#9	3.264(18)
S(28)-Ba(5)#13	3.205(18)
S(28)-Ba(13)#9	3.384(18)
S(29)-Ba(2)#3	3.39(2)
S(29)-Ba(14)#3	3.04(2)
S(29)-Ba(15)#3	3.27(2)
S(29)-Sn(8)#3	2.63(2)
S(30)-Ba(7)#4	3.25(2)
S(30)-Ba(11)#3	3.27(2)
S(7)-Ba(9)#5	3.416(15)

Symmetry transformations used to generate equivalent atoms:

(1) $x+1/2,-y,z$ (2) $-x-1,-y,z+1/2$ (3) $-x-1,-y-1,z+1/2$ (4) $x+1/2,-y-1,z$ (5) $x,y-1,z$ (6) $-x-1,-y-1,z-1/2$ (7) $x-1/2,-y-1,z$ (8) $-x-3/2,y,z-1/2$ (9) $x,y+1,z$ (10) $-x-3/2,y,z+1/2$ (11) $-x-3/2,y-1,z+1/2$ (12) $x-1/2,-y,z$ (13) $-x-1,-y,z-1/2$ (14) $-x-3/2,y+1,z-1/2$

Table S45: Bond angles [°] for Ba₈ S_{14.24} Sn₄ Te_{0.76} at 100.03 K with estimated standard deviations in parentheses.

Label	Angles
Ba(7)#1-Ba(1)-Ba(10)#2	63.14(12)
Ba(7)#1-Ba(1)-Ba(11)#3	96.99(15)
Ba(7)#1-Ba(1)-Ba(14)#3	170.39(18)
Ba(9)#2-Ba(1)-Ba(7)#1	106.27(16)
Ba(9)#2-Ba(1)-Ba(10)#2	63.52(12)
Ba(9)#2-Ba(1)-Ba(11)#3	98.14(15)
Ba(9)#2-Ba(1)-Ba(14)#3	78.16(14)
Ba(11)#3-Ba(1)-Ba(10)#2	61.12(11)
Ba(14)#3-Ba(1)-Ba(10)#2	126.08(16)
Ba(14)#3-Ba(1)-Ba(11)#3	90.71(14)
S(10)#1-Ba(1)-Ba(7)#1	52.7(5)
S(10)#1-Ba(1)-Ba(9)#2	53.6(5)
S(10)#1-Ba(1)-Ba(10)#2	44.0(4)
S(10)#1-Ba(1)-Ba(11)#3	105.1(5)
S(10)#1-Ba(1)-Ba(14)#3	130.5(5)
S(10)#1-Ba(1)-S(11)	162.8(6)

S(10)#1-Ba(1)-S(13)	88.7(7)
S(10)#1-Ba(1)-S(16)#3	75.9(6)
S(10)#1-Ba(1)-S(20)#4	74.4(5)
S(10)#1-Ba(1)-S(27)	89.5(6)
S(11)-Ba(1)-Ba(7)#1	124.7(4)
S(11)-Ba(1)-Ba(9)#2	126.2(4)
S(11)-Ba(1)-Ba(10)#2	153.1(4)
S(11)-Ba(1)-Ba(11)#3	92.0(3)
S(11)-Ba(1)-Ba(14)#3	48.9(3)
S(11)-Ba(1)-S(16)#3	118.6(5)
S(11)-Ba(1)-S(20)#4	118.2(5)
S(13)-Ba(1)-Ba(7)#1	53.1(5)
S(13)-Ba(1)-Ba(9)#2	127.8(5)
S(13)-Ba(1)-Ba(10)#2	115.9(5)
S(13)-Ba(1)-Ba(11)#3	128.6(5)
S(13)-Ba(1)-Ba(14)#3	117.4(5)
S(13)-Ba(1)-S(11)	79.3(6)
S(13)-Ba(1)-S(16)#3	159.0(6)
S(13)-Ba(1)-S(20)#4	93.7(6)
S(13)-Ba(1)-S(27)	94.9(6)
S(16)#3-Ba(1)-Ba(7)#1	105.9(4)
S(16)#3-Ba(1)-Ba(9)#2	52.3(3)
S(16)#3-Ba(1)-Ba(10)#2	43.2(3)
S(16)#3-Ba(1)-Ba(11)#3	45.9(3)
S(16)#3-Ba(1)-Ba(14)#3	83.6(3)
S(16)#3-Ba(1)-S(20)#4	68.7(5)
S(20)#4-Ba(1)-Ba(7)#1	50.3(3)
S(20)#4-Ba(1)-Ba(9)#2	106.4(4)
S(20)#4-Ba(1)-Ba(10)#2	43.1(3)
S(20)#4-Ba(1)-Ba(11)#3	46.7(3)
S(20)#4-Ba(1)-Ba(14)#3	137.4(3)
S(27)-Ba(1)-Ba(7)#1	125.5(4)
S(27)-Ba(1)-Ba(9)#2	55.8(4)

S(27)-Ba(1)-Ba(10)#2	118.6(4)
S(27)-Ba(1)-Ba(11)#3	133.5(4)
S(27)-Ba(1)-Ba(14)#3	49.7(4)
S(27)-Ba(1)-S(11)	79.5(5)
S(27)-Ba(1)-S(16)#3	99.1(5)
S(27)-Ba(1)-S(20)#4	161.6(5)
S(12)-Ba(2)-S(14)	122.7(5)
S(12)-Ba(2)-S(25)	70.5(5)
S(12)-Ba(2)-S(26)	69.4(5)
S(12)-Ba(2)-S(28)#5	74.2(5)
S(12)-Ba(2)-Te(28)#5	74.2(5)
S(12)-Ba(2)-S(29)#6	69.5(5)
S(12)-Ba(2)-S(7)	135.1(4)
S(14)-Ba(2)-S(25)	70.8(5)
S(14)-Ba(2)-S(26)	140.3(5)
S(23)-Ba(2)-S(12)	126.8(5)
S(23)-Ba(2)-S(14)	74.7(5)
S(23)-Ba(2)-S(25)	70.6(5)
S(23)-Ba(2)-S(26)	69.9(5)
S(23)-Ba(2)-S(28)#5	129.4(5)
S(23)-Ba(2)-Te(28)#5	129.4(5)
S(23)-Ba(2)-S(29)#6	152.3(5)
S(23)-Ba(2)-S(7)	94.0(5)
S(25)-Ba(2)-S(26)	80.8(5)
S(28)#5-Ba(2)-S(14)	137.7(5)
S(28)#5-Ba(2)-S(25)	144.0(5)
S(28)#5-Ba(2)-S(26)	80.5(5)
S(28)#5-Ba(2)-Te(28)#5	0.0(8)
S(28)#5-Ba(2)-S(29)#6	73.6(5)
S(28)#5-Ba(2)-S(7)	64.4(4)
Te(28)#5-Ba(2)-S(14)	137.7(5)
Te(28)#5-Ba(2)-S(25)	144.0(5)
Te(28)#5-Ba(2)-S(26)	80.5(5)

Te(28)#5-Ba(2)-S(29)#6	73.6(5)
Te(28)#5-Ba(2)-S(7)	64.4(4)
S(29)#6-Ba(2)-S(14)	77.6(5)
S(29)#6-Ba(2)-S(25)	99.9(5)
S(29)#6-Ba(2)-S(26)	135.9(5)
S(7)-Ba(2)-S(14)	81.9(4)
S(7)-Ba(2)-S(25)	151.2(5)
S(7)-Ba(2)-S(26)	117.4(4)
S(7)-Ba(2)-S(29)#6	82.4(5)
Te(4)#7-Ba(3)-Te(5)	78.5(4)
Te(4)#7-Ba(3)-Sn(8)#7	99.6(3)
Te(4)#7-Ba(3)-S(2)	150.5(5)
Te(4)#7-Ba(3)-S(12)#7	91.9(4)
Te(4)#7-Ba(3)-Te(12)#7	91.9(4)
Te(4)#7-Ba(3)-S(16)	115.2(5)
Te(4)#7-Ba(3)-S(21)#5	68.6(5)
Te(5)-Ba(3)-Sn(8)#7	111.6(3)
S(2)-Ba(3)-Te(5)	73.4(4)
S(2)-Ba(3)-Sn(8)#7	98.9(4)
S(2)-Ba(3)-S(16)	83.9(5)
S(2)-Ba(3)-S(21)#5	140.1(5)
S(4)#7-Ba(3)-Te(4)#7	0.0
S(4)#7-Ba(3)-Te(5)	78.5(4)
S(4)#7-Ba(3)-Sn(8)#7	99.6(3)
S(4)#7-Ba(3)-S(2)	150.5(5)
S(4)#7-Ba(3)-S(12)#7	91.9(4)
S(4)#7-Ba(3)-Te(12)#7	91.9(4)
S(4)#7-Ba(3)-S(16)	115.2(5)
S(4)#7-Ba(3)-S(21)#5	68.6(5)
S(12)#7-Ba(3)-Te(5)	70.7(4)
S(12)#7-Ba(3)-Sn(8)#7	41.0(3)
S(12)#7-Ba(3)-S(2)	87.1(5)
S(12)#7-Ba(3)-S(16)	137.4(5)

S(12)#7-Ba(3)-S(21)#5	82.2(5)
Te(12)#7-Ba(3)-Te(5)	70.7(4)
Te(12)#7-Ba(3)-Sn(8)#7	41.0(3)
Te(12)#7-Ba(3)-S(2)	87.1(5)
Te(12)#7-Ba(3)-S(12)#7	0.0
Te(12)#7-Ba(3)-S(16)	137.4(5)
Te(12)#7-Ba(3)-S(21)#5	82.2(5)
S(16)-Ba(3)-Te(5)	143.4(4)
S(16)-Ba(3)-Sn(8)#7	99.8(4)
S(16)-Ba(3)-S(21)#5	78.7(5)
S(17)#8-Ba(3)-Te(4)#7	136.2(5)
S(17)#8-Ba(3)-Te(5)	125.0(4)
S(17)#8-Ba(3)-Sn(8)#7	40.0(4)
S(17)#8-Ba(3)-S(2)	70.0(5)
S(17)#8-Ba(3)-S(4)#7	136.2(5)
S(17)#8-Ba(3)-S(12)#7	67.9(5)
S(17)#8-Ba(3)-Te(12)#7	67.9(5)
S(17)#8-Ba(3)-S(16)	69.9(5)
S(17)#8-Ba(3)-S(21)#5	70.3(5)
S(19)-Ba(3)-Te(4)#7	90.7(5)
S(19)-Ba(3)-Te(5)	74.6(4)
S(19)-Ba(3)-Sn(8)#7	168.8(4)
S(19)-Ba(3)-S(2)	73.6(5)
S(19)-Ba(3)-S(4)#7	90.7(5)
S(19)-Ba(3)-S(12)#7	143.9(5)
S(19)-Ba(3)-Te(12)#7	143.9(5)
S(19)-Ba(3)-S(16)	71.6(5)
S(19)-Ba(3)-S(17)#8	128.8(5)
S(19)-Ba(3)-S(21)#5	131.7(5)
S(21)#5-Ba(3)-Te(5)	136.2(4)
S(21)#5-Ba(3)-Sn(8)#7	50.3(4)
Te(3)-Ba(4)-Ba(13)#9	165.9(3)
Te(3)-Ba(4)-Sn(7)	123.4(3)

Te(3)-Ba(4)-S(13)	137.3(5)
Te(3)-Ba(4)-S(15)	83.2(3)
Te(3)-Ba(4)-S(26)#9	150.3(4)
Te(3)-Ba(4)-S(27)	79.5(4)
Sn(7)-Ba(4)-Ba(13)#9	69.35(12)
S(8)-Ba(4)-Ba(13)#9	79.5(4)
S(8)-Ba(4)-Te(3)	98.5(5)
S(8)-Ba(4)-Sn(7)	114.7(4)
S(8)-Ba(4)-S(11)	136.8(5)
S(8)-Ba(4)-S(13)	123.1(6)
S(8)-Ba(4)-S(15)	80.6(4)
S(8)-Ba(4)-S(25)	72.2(6)
S(8)-Ba(4)-S(26)#9	67.8(5)
S(8)-Ba(4)-S(27)	149.3(5)
S(11)-Ba(4)-Ba(13)#9	101.4(4)
S(11)-Ba(4)-Te(3)	70.3(4)
S(11)-Ba(4)-Sn(7)	105.5(4)
S(11)-Ba(4)-S(13)	72.4(5)
S(11)-Ba(4)-S(15)	135.6(4)
S(11)-Ba(4)-S(25)	78.2(5)
S(11)-Ba(4)-S(26)#9	137.8(5)
S(11)-Ba(4)-S(27)	71.7(5)
S(13)-Ba(4)-Ba(13)#9	43.9(4)
S(13)-Ba(4)-Sn(7)	50.1(4)
S(13)-Ba(4)-S(15)	110.5(4)
S(13)-Ba(4)-S(26)#9	65.9(5)
S(13)-Ba(4)-S(27)	69.5(5)
S(15)-Ba(4)-Ba(13)#9	110.1(2)
S(15)-Ba(4)-Sn(7)	60.54(18)
S(15)-Ba(4)-S(26)#9	68.9(4)
S(25)-Ba(4)-Ba(13)#9	45.5(4)
S(25)-Ba(4)-Te(3)	120.4(5)
S(25)-Ba(4)-Sn(7)	113.1(4)

S(25)-Ba(4)-S(13)	70.3(5)
S(25)-Ba(4)-S(15)	145.8(4)
S(25)-Ba(4)-S(26)#9	81.7(5)
S(25)-Ba(4)-S(27)	135.3(5)
S(26)#9-Ba(4)-Ba(13)#9	41.5(3)
S(26)#9-Ba(4)-Sn(7)	50.6(3)
S(27)-Ba(4)-Ba(13)#9	109.5(3)
S(27)-Ba(4)-Sn(7)	48.5(3)
S(27)-Ba(4)-S(15)	68.7(4)
S(27)-Ba(4)-S(26)#9	98.9(5)
Ba(10)#10-Ba(5)-Ba(13)#3	94.96(14)
Sn(8)#3-Ba(5)-Ba(10)#10	147.99(17)
Sn(8)#3-Ba(5)-Ba(13)#3	94.42(16)
S(1)-Ba(5)-Ba(10)#10	51.7(3)
S(1)-Ba(5)-Ba(13)#3	103.2(3)
S(1)-Ba(5)-Sn(8)#3	152.6(4)
S(1)-Ba(5)-S(2)#10	103.4(5)
S(2)#10-Ba(5)-Ba(10)#10	51.7(3)
S(2)#10-Ba(5)-Ba(13)#3	84.6(4)
S(2)#10-Ba(5)-Sn(8)#3	99.0(4)
S(6)-Ba(5)-Ba(10)#10	54.5(3)
S(6)-Ba(5)-Ba(13)#3	148.8(4)
S(6)-Ba(5)-Sn(8)#3	108.6(4)
S(6)-Ba(5)-S(1)	64.9(5)
S(6)-Ba(5)-S(2)#10	71.5(5)
S(12)#3-Ba(5)-Ba(10)#10	132.3(4)
S(12)#3-Ba(5)-Ba(13)#3	52.4(4)
S(12)#3-Ba(5)-Sn(8)#3	42.6(4)
S(12)#3-Ba(5)-S(1)	152.8(5)
S(12)#3-Ba(5)-S(2)#10	87.5(5)
S(12)#3-Ba(5)-S(6)	142.0(5)
S(12)#3-Ba(5)-S(17)	70.9(5)
S(12)#3-Ba(5)-S(28)#2	76.9(5)

S(12)#3-Ba(5)-Te(28)#2	76.9(5)
S(12)#3-Ba(5)-S(29)	73.4(5)
Te(12)#3-Ba(5)-Ba(10)#10	132.3(4)
Te(12)#3-Ba(5)-Ba(13)#3	52.4(4)
Te(12)#3-Ba(5)-Sn(8)#3	42.6(4)
Te(12)#3-Ba(5)-S(1)	152.8(5)
Te(12)#3-Ba(5)-S(2)#10	87.5(5)
Te(12)#3-Ba(5)-S(6)	142.0(5)
Te(12)#3-Ba(5)-S(12)#3	0.0
Te(12)#3-Ba(5)-S(17)	70.9(5)
Te(12)#3-Ba(5)-S(28)#2	76.9(5)
Te(12)#3-Ba(5)-Te(28)#2	76.9(5)
Te(12)#3-Ba(5)-S(29)	73.4(5)
S(17)-Ba(5)-Ba(10)#10	108.1(4)
S(17)-Ba(5)-Ba(13)#3	118.1(4)
S(17)-Ba(5)-Sn(8)#3	41.5(4)
S(17)-Ba(5)-S(1)	136.2(5)
S(17)-Ba(5)-S(2)#10	69.1(5)
S(17)-Ba(5)-S(6)	72.2(5)
S(17)-Ba(5)-S(28)#2	139.0(5)
S(17)-Ba(5)-Te(28)#2	139.0(5)
S(17)-Ba(5)-S(29)	70.3(5)
S(28)#2-Ba(5)-Ba(10)#10	112.3(3)
S(28)#2-Ba(5)-Ba(13)#3	52.1(3)
S(28)#2-Ba(5)-Sn(8)#3	97.5(3)
S(28)#2-Ba(5)-S(1)	77.9(5)
S(28)#2-Ba(5)-S(2)#10	134.6(5)
S(28)#2-Ba(5)-S(6)	139.9(5)
S(28)#2-Ba(5)-Te(28)#2	0.0(9)
S(28)#2-Ba(5)-S(29)	76.8(5)
Te(28)#2-Ba(5)-Ba(10)#10	112.3(3)
Te(28)#2-Ba(5)-Ba(13)#3	52.1(3)
Te(28)#2-Ba(5)-Sn(8)#3	97.5(3)

Te(28)#2-Ba(5)-S(1)	77.9(5)
Te(28)#2-Ba(5)-S(2)#10	134.6(5)
Te(28)#2-Ba(5)-S(6)	139.9(5)
Te(28)#2-Ba(5)-S(29)	76.8(5)
S(29)-Ba(5)-Ba(10)#10	153.3(4)
S(29)-Ba(5)-Ba(13)#3	109.4(4)
S(29)-Ba(5)-Sn(8)#3	43.2(4)
S(29)-Ba(5)-S(1)	110.1(5)
S(29)-Ba(5)-S(2)#10	138.9(5)
S(29)-Ba(5)-S(6)	101.8(5)
Te(3)-Ba(6)-Ba(10)#11	165.1(3)
Te(3)-Ba(6)-Sn(3)#7	107.0(3)
Te(3)-Ba(6)-S(6)	69.8(4)
Sn(3)#7-Ba(6)-Ba(10)#11	78.69(13)
S(1)#5-Ba(6)-Ba(10)#11	45.5(3)
S(1)#5-Ba(6)-Te(3)	137.6(4)
S(1)#5-Ba(6)-Sn(3)#7	111.9(4)
S(1)#5-Ba(6)-S(6)	140.6(5)
S(1)#5-Ba(6)-S(15)#5	69.7(4)
S(1)#5-Ba(6)-Te(15)#5	69.7(4)
S(1)#5-Ba(6)-S(20)	80.6(5)
S(1)#5-Ba(6)-S(29)	75.3(5)
S(6)-Ba(6)-Ba(10)#11	100.4(3)
S(6)-Ba(6)-Sn(3)#7	69.1(3)
S(9)-Ba(6)-Ba(10)#11	114.0(4)
S(9)-Ba(6)-Te(3)	73.8(5)
S(9)-Ba(6)-Sn(3)#7	35.6(4)
S(9)-Ba(6)-S(1)#5	136.0(5)
S(9)-Ba(6)-S(6)	68.5(5)
S(9)-Ba(6)-S(15)#5	100.4(4)
S(9)-Ba(6)-Te(15)#5	100.4(4)
S(9)-Ba(6)-S(20)	71.6(5)
S(9)-Ba(6)-S(29)	146.8(5)

S(15)#5-Ba(6)-Ba(10)#11	113.2(2)
S(15)#5-Ba(6)-Te(3)	76.3(3)
S(15)#5-Ba(6)-Sn(3)#7	120.8(2)
S(15)#5-Ba(6)-S(6)	146.1(4)
S(15)#5-Ba(6)-Te(15)#5	0.0(3)
S(15)#5-Ba(6)-S(29)	78.8(4)
Te(15)#5-Ba(6)-Ba(10)#11	113.2(2)
Te(15)#5-Ba(6)-Te(3)	76.3(3)
Te(15)#5-Ba(6)-Sn(3)#7	120.8(2)
Te(15)#5-Ba(6)-S(6)	146.1(4)
Te(15)#5-Ba(6)-S(29)	78.8(4)
S(17)-Ba(6)-Ba(10)#11	45.0(4)
S(17)-Ba(6)-Te(3)	120.1(4)
S(17)-Ba(6)-Sn(3)#7	96.9(4)
S(17)-Ba(6)-S(1)#5	71.7(5)
S(17)-Ba(6)-S(6)	69.2(5)
S(17)-Ba(6)-S(9)	125.4(5)
S(17)-Ba(6)-S(15)#5	133.6(4)
S(17)-Ba(6)-Te(15)#5	133.6(4)
S(17)-Ba(6)-S(20)	69.9(5)
S(17)-Ba(6)-S(29)	67.2(5)
S(20)-Ba(6)-Ba(10)#11	42.5(4)
S(20)-Ba(6)-Te(3)	141.5(4)
S(20)-Ba(6)-Sn(3)#7	36.2(4)
S(20)-Ba(6)-S(6)	82.0(5)
S(20)-Ba(6)-S(15)#5	126.3(4)
S(20)-Ba(6)-Te(15)#5	126.3(4)
S(20)-Ba(6)-S(29)	135.5(5)
S(29)-Ba(6)-Ba(10)#11	96.2(4)
S(29)-Ba(6)-Te(3)	73.8(4)
S(29)-Ba(6)-Sn(3)#7	160.3(4)
S(29)-Ba(6)-S(6)	93.5(5)
Ba(1)#12-Ba(7)-Ba(10)#10	62.87(12)

Te(4)#12-Ba(7)-Ba(1)#12	88.5(3)
Te(4)#12-Ba(7)-Ba(10)#10	115.9(3)
Te(4)#12-Ba(7)-S(6)	144.2(4)
Te(5)-Ba(7)-Ba(1)#12	128.1(3)
Te(5)-Ba(7)-Ba(10)#10	162.8(3)
Te(5)-Ba(7)-Te(4)#12	79.7(4)
Te(5)-Ba(7)-S(4)#12	79.7(4)
Te(5)-Ba(7)-S(6)	114.8(4)
S(4)#12-Ba(7)-Ba(1)#12	88.5(3)
S(4)#12-Ba(7)-Ba(10)#10	115.9(3)
S(4)#12-Ba(7)-Te(4)#12	0.0
S(4)#12-Ba(7)-S(6)	144.2(4)
S(6)-Ba(7)-Ba(1)#12	104.1(4)
S(6)-Ba(7)-Ba(10)#10	48.2(3)
S(10)-Ba(7)-Ba(1)#12	39.0(3)
S(10)-Ba(7)-Ba(10)#10	45.1(4)
S(10)-Ba(7)-Te(4)#12	127.1(4)
S(10)-Ba(7)-Te(5)	132.3(4)
S(10)-Ba(7)-S(4)#12	127.1(4)
S(10)-Ba(7)-S(6)	68.7(5)
S(10)-Ba(7)-S(13)#12	67.6(5)
S(10)-Ba(7)-S(20)#9	73.0(5)
S(10)-Ba(7)-S(24)	126.5(5)
S(10)-Ba(7)-S(30)#7	71.9(5)
S(13)#12-Ba(7)-Ba(1)#12	39.9(4)
S(13)#12-Ba(7)-Ba(10)#10	102.5(4)
S(13)#12-Ba(7)-Te(4)#12	73.9(5)
S(13)#12-Ba(7)-Te(5)	88.6(5)
S(13)#12-Ba(7)-S(4)#12	73.9(5)
S(13)#12-Ba(7)-S(6)	135.4(5)
S(13)#12-Ba(7)-S(20)#9	90.5(5)
S(13)#12-Ba(7)-S(24)	147.9(5)
S(13)#12-Ba(7)-S(30)#7	80.4(5)

S(20)#9-Ba(7)-Ba(1)#12	59.3(4)
S(20)#9-Ba(7)-Ba(10)#10	43.5(4)
S(20)#9-Ba(7)-Te(4)#12	72.3(4)
S(20)#9-Ba(7)-Te(5)	151.1(5)
S(20)#9-Ba(7)-S(4)#12	72.3(4)
S(20)#9-Ba(7)-S(6)	85.4(5)
S(24)-Ba(7)-Ba(1)#12	130.0(4)
S(24)-Ba(7)-Ba(10)#10	81.8(4)
S(24)-Ba(7)-Te(4)#12	75.7(4)
S(24)-Ba(7)-Te(5)	95.8(4)
S(24)-Ba(7)-S(4)#12	75.7(4)
S(24)-Ba(7)-S(6)	70.5(5)
S(24)-Ba(7)-S(20)#9	70.6(5)
S(24)-Ba(7)-S(30)#7	129.7(5)
S(30)#7-Ba(7)-Ba(1)#12	94.7(4)
S(30)#7-Ba(7)-Ba(10)#10	105.1(4)
S(30)#7-Ba(7)-Te(4)#12	135.2(5)
S(30)#7-Ba(7)-Te(5)	63.4(4)
S(30)#7-Ba(7)-S(4)#12	135.2(5)
S(30)#7-Ba(7)-S(6)	77.9(5)
S(30)#7-Ba(7)-S(20)#9	144.7(5)
Ba(12)#5-Ba(8)-Ba(3)	108.54(13)
Te(4)#7-Ba(8)-Ba(3)	44.2(3)
Te(4)#7-Ba(8)-Ba(12)#5	87.9(2)
S(8)#5-Ba(8)-Ba(3)	141.1(4)
S(8)#5-Ba(8)-Ba(12)#5	48.0(4)
S(8)#5-Ba(8)-Te(4)#7	135.9(5)
S(8)#5-Ba(8)-S(23)	80.6(5)
S(9)-Ba(8)-Ba(3)	82.0(4)
S(9)-Ba(8)-Ba(12)#5	135.7(4)
S(9)-Ba(8)-Te(4)#7	69.8(5)
S(9)-Ba(8)-S(8)#5	136.9(6)
S(9)-Ba(8)-S(23)	74.1(5)

S(9)-Ba(8)-S(24)#5	86.9(5)
S(19)-Ba(8)-Ba(3)	40.9(4)
S(19)-Ba(8)-Ba(12)#5	135.4(4)
S(19)-Ba(8)-Te(4)#7	82.5(4)
S(19)-Ba(8)-S(8)#5	128.3(5)
S(19)-Ba(8)-S(9)	80.6(5)
S(19)-Ba(8)-S(22)#5	88.8(6)
S(19)-Ba(8)-S(23)	79.4(5)
S(19)-Ba(8)-S(24)#5	154.7(5)
S(22)#5-Ba(8)-Ba(3)	63.6(4)
S(22)#5-Ba(8)-Ba(12)#5	47.9(4)
S(22)#5-Ba(8)-Te(4)#7	67.1(5)
S(22)#5-Ba(8)-S(8)#5	81.3(6)
S(22)#5-Ba(8)-S(9)	136.6(5)
S(22)#5-Ba(8)-S(23)	145.0(6)
S(22)#5-Ba(8)-S(24)#5	85.3(6)
S(23)-Ba(8)-Ba(3)	118.7(4)
S(23)-Ba(8)-Ba(12)#5	128.0(4)
S(23)-Ba(8)-Te(4)#7	141.7(5)
S(24)#5-Ba(8)-Ba(3)	115.8(4)
S(24)#5-Ba(8)-Ba(12)#5	49.3(4)
S(24)#5-Ba(8)-Te(4)#7	72.6(4)
S(24)#5-Ba(8)-S(8)#5	75.0(5)
S(24)#5-Ba(8)-S(23)	118.2(5)
Ba(1)#13-Ba(9)-Ba(12)	167.70(15)
S(2)-Ba(9)-Ba(1)#13	102.6(4)
S(2)-Ba(9)-Ba(12)	80.5(3)
S(10)#8-Ba(9)-Ba(1)#13	39.6(3)
S(10)#8-Ba(9)-Ba(12)	147.0(4)
S(10)#8-Ba(9)-S(2)	66.9(5)
S(10)#8-Ba(9)-S(14)	138.9(5)
S(10)#8-Ba(9)-S(16)#9	72.7(5)
S(10)#8-Ba(9)-S(18)	74.2(5)

S(10)#8-Ba(9)-S(27)#13	68.2(5)
S(10)#8-Ba(9)-S(7)#9	126.4(4)
S(10)#8-Ba(9)-Te(7)#9	126.4(4)
S(14)-Ba(9)-Ba(1)#13	133.9(4)
S(14)-Ba(9)-Ba(12)	51.7(3)
S(14)-Ba(9)-S(2)	114.8(5)
S(14)-Ba(9)-S(16)#9	146.7(5)
S(14)-Ba(9)-S(27)#13	92.3(5)
S(14)-Ba(9)-S(7)#9	78.1(4)
S(14)-Ba(9)-Te(7)#9	78.1(4)
S(16)#9-Ba(9)-Ba(1)#13	58.9(4)
S(16)#9-Ba(9)-Ba(12)	110.2(4)
S(16)#9-Ba(9)-S(2)	84.1(5)
S(16)#9-Ba(9)-S(7)#9	71.6(4)
S(16)#9-Ba(9)-Te(7)#9	71.6(4)
S(18)-Ba(9)-Ba(1)#13	95.5(4)
S(18)-Ba(9)-Ba(12)	96.8(3)
S(18)-Ba(9)-S(2)	81.7(5)
S(18)-Ba(9)-S(14)	66.0(5)
S(18)-Ba(9)-S(16)#9	146.9(5)
S(18)-Ba(9)-S(27)#13	76.3(5)
S(18)-Ba(9)-S(7)#9	132.3(4)
S(18)-Ba(9)-Te(7)#9	132.3(4)
S(22)-Ba(9)-Ba(1)#13	129.6(5)
S(22)-Ba(9)-Ba(12)	39.8(4)
S(22)-Ba(9)-S(2)	71.2(6)
S(22)-Ba(9)-S(10)#8	126.2(6)
S(22)-Ba(9)-S(14)	89.0(6)
S(22)-Ba(9)-S(16)#9	70.7(6)
S(22)-Ba(9)-S(18)	130.8(6)
S(22)-Ba(9)-S(27)#13	149.8(6)
S(22)-Ba(9)-S(7)#9	75.9(5)
S(22)-Ba(9)-Te(7)#9	75.9(5)

S(27)#13-Ba(9)-Ba(1)#13	41.6(3)
S(27)#13-Ba(9)-Ba(12)	141.6(4)
S(27)#13-Ba(9)-S(2)	133.9(5)
S(27)#13-Ba(9)-S(16)#9	92.8(5)
S(27)#13-Ba(9)-S(7)#9	74.8(4)
S(27)#13-Ba(9)-Te(7)#9	74.8(4)
S(7)#9-Ba(9)-Ba(1)#13	87.3(3)
S(7)#9-Ba(9)-Ba(12)	83.5(3)
S(7)#9-Ba(9)-S(2)	144.1(4)
Te(7)#9-Ba(9)-Ba(1)#13	87.3(3)
Te(7)#9-Ba(9)-Ba(12)	83.5(3)
Te(7)#9-Ba(9)-S(2)	144.1(4)
Te(7)#9-Ba(9)-S(7)#9	0.0
Ba(1)#13-Ba(10)-Ba(7)#8	53.99(11)
Ba(1)#13-Ba(10)-Ba(11)#9	58.04(10)
Ba(5)#8-Ba(10)-Ba(1)#13	143.71(15)
Ba(5)#8-Ba(10)-Ba(7)#8	102.54(14)
Ba(5)#8-Ba(10)-Ba(11)#9	157.74(15)
Ba(7)#8-Ba(10)-Ba(11)#9	89.28(12)
S(1)#8-Ba(10)-Ba(1)#13	137.6(4)
S(1)#8-Ba(10)-Ba(5)#8	55.1(3)
S(1)#8-Ba(10)-Ba(7)#8	89.5(4)
S(1)#8-Ba(10)-Ba(11)#9	106.9(3)
S(1)#8-Ba(10)-S(2)	111.3(5)
S(1)#8-Ba(10)-S(6)#8	65.4(5)
S(2)-Ba(10)-Ba(1)#13	98.8(4)
S(2)-Ba(10)-Ba(5)#8	56.2(4)
S(2)-Ba(10)-Ba(7)#8	103.0(4)
S(2)-Ba(10)-Ba(11)#9	139.7(4)
S(2)-Ba(10)-S(6)#8	72.7(5)
S(6)#8-Ba(10)-Ba(1)#13	98.0(4)
S(6)#8-Ba(10)-Ba(5)#8	52.2(3)
S(6)#8-Ba(10)-Ba(7)#8	50.4(3)

S(6)#8-Ba(10)-Ba(11)#9	137.4(4)
S(10)#8-Ba(10)-Ba(1)#13	34.1(3)
S(10)#8-Ba(10)-Ba(5)#8	109.7(4)
S(10)#8-Ba(10)-Ba(7)#8	46.2(4)
S(10)#8-Ba(10)-Ba(11)#9	92.1(4)
S(10)#8-Ba(10)-S(1)#8	132.1(5)
S(10)#8-Ba(10)-S(2)	71.5(5)
S(10)#8-Ba(10)-S(6)#8	70.8(5)
S(10)#8-Ba(10)-S(17)#14	139.6(5)
S(10)#8-Ba(10)-S(21)	132.7(5)
S(16)#9-Ba(10)-Ba(1)#13	54.7(4)
S(16)#9-Ba(10)-Ba(5)#8	141.9(4)
S(16)#9-Ba(10)-Ba(7)#8	108.1(4)
S(16)#9-Ba(10)-Ba(11)#9	45.3(4)
S(16)#9-Ba(10)-S(1)#8	144.7(5)
S(16)#9-Ba(10)-S(2)	94.6(5)
S(16)#9-Ba(10)-S(6)#8	148.5(6)
S(16)#9-Ba(10)-S(10)#8	77.9(5)
S(16)#9-Ba(10)-S(17)#14	73.3(5)
S(16)#9-Ba(10)-S(21)	84.6(5)
S(17)#14-Ba(10)-Ba(1)#13	105.5(4)
S(17)#14-Ba(10)-Ba(5)#8	110.5(4)
S(17)#14-Ba(10)-Ba(7)#8	119.2(4)
S(17)#14-Ba(10)-Ba(11)#9	47.5(4)
S(17)#14-Ba(10)-S(1)#8	71.4(5)
S(17)#14-Ba(10)-S(2)	137.8(5)
S(17)#14-Ba(10)-S(6)#8	135.0(5)
S(17)#14-Ba(10)-S(21)	72.0(5)
S(20)#14-Ba(10)-Ba(1)#13	55.2(4)
S(20)#14-Ba(10)-Ba(5)#8	133.0(4)
S(20)#14-Ba(10)-Ba(7)#8	47.8(4)
S(20)#14-Ba(10)-Ba(11)#9	46.4(4)
S(20)#14-Ba(10)-S(1)#8	85.1(5)

S(20)#14-Ba(10)-S(2)	147.9(6)
S(20)#14-Ba(10)-S(6)#8	91.1(5)
S(20)#14-Ba(10)-S(10)#8	77.1(5)
S(20)#14-Ba(10)-S(16)#9	85.0(6)
S(20)#14-Ba(10)-S(17)#14	72.8(5)
S(20)#14-Ba(10)-S(21)	144.8(5)
S(21)-Ba(10)-Ba(1)#13	136.4(4)
S(21)-Ba(10)-Ba(5)#8	62.5(4)
S(21)-Ba(10)-Ba(7)#8	164.7(4)
S(21)-Ba(10)-Ba(11)#9	105.9(4)
S(21)-Ba(10)-S(1)#8	84.3(5)
S(21)-Ba(10)-S(2)	66.6(5)
S(21)-Ba(10)-S(6)#8	114.4(5)
Ba(1)#6-Ba(11)-Ba(3)	103.30(13)
Ba(1)#6-Ba(11)-Ba(10)#5	60.85(11)
Ba(10)#5-Ba(11)-Ba(3)	61.57(10)
Sn(3)#6-Ba(11)-Ba(1)#6	69.06(13)
Sn(3)#6-Ba(11)-Ba(3)	137.44(15)
Sn(3)#6-Ba(11)-Ba(10)#5	79.85(12)
S(2)-Ba(11)-Ba(1)#6	142.0(4)
S(2)-Ba(11)-Ba(3)	47.2(4)
S(2)-Ba(11)-Ba(10)#5	106.9(4)
S(2)-Ba(11)-Sn(3)#6	148.0(4)
S(2)-Ba(11)-S(6)#8	76.5(5)
S(2)-Ba(11)-S(10)#8	71.2(5)
S(2)-Ba(11)-S(16)	89.5(5)
S(2)-Ba(11)-S(17)#8	71.2(5)
S(2)-Ba(11)-S(18)	85.4(5)
S(2)-Ba(11)-S(20)#8	140.8(6)
S(2)-Ba(11)-S(30)#6	140.6(5)
S(6)#8-Ba(11)-Ba(1)#6	140.4(4)
S(6)#8-Ba(11)-Ba(3)	101.6(4)
S(6)#8-Ba(11)-Ba(10)#5	106.9(4)

S(6)#8-Ba(11)-Sn(3)#6	71.7(4)
S(6)#8-Ba(11)-S(10)#8	71.3(5)
S(6)#8-Ba(11)-S(17)#8	71.1(5)
S(6)#8-Ba(11)-S(18)	141.8(5)
S(6)#8-Ba(11)-S(20)#8	88.1(5)
S(6)#8-Ba(11)-S(30)#6	81.8(5)
S(10)#8-Ba(11)-Ba(1)#6	121.5(4)
S(10)#8-Ba(11)-Ba(3)	117.0(4)
S(10)#8-Ba(11)-Ba(10)#5	177.6(4)
S(10)#8-Ba(11)-Sn(3)#6	100.9(4)
S(10)#8-Ba(11)-S(17)#8	131.6(5)
S(10)#8-Ba(11)-S(18)	71.0(5)
S(16)-Ba(11)-Ba(1)#6	56.0(4)
S(16)-Ba(11)-Ba(3)	47.5(4)
S(16)-Ba(11)-Ba(10)#5	43.5(4)
S(16)-Ba(11)-Sn(3)#6	113.8(4)
S(16)-Ba(11)-S(6)#8	142.1(6)
S(16)-Ba(11)-S(10)#8	137.2(5)
S(16)-Ba(11)-S(17)#8	71.0(5)
S(16)-Ba(11)-S(18)	69.6(5)
S(16)-Ba(11)-S(20)#8	80.8(5)
S(16)-Ba(11)-S(30)#6	126.2(5)
S(17)#8-Ba(11)-Ba(1)#6	106.9(4)
S(17)#8-Ba(11)-Ba(3)	45.3(4)
S(17)#8-Ba(11)-Ba(10)#5	46.0(3)
S(17)#8-Ba(11)-Sn(3)#6	95.2(4)
S(17)#8-Ba(11)-S(18)	133.8(5)
S(18)-Ba(11)-Ba(1)#6	68.7(3)
S(18)-Ba(11)-Ba(3)	89.6(3)
S(18)-Ba(11)-Ba(10)#5	110.5(3)
S(18)-Ba(11)-Sn(3)#6	122.2(3)
S(20)#8-Ba(11)-Ba(1)#6	56.3(4)
S(20)#8-Ba(11)-Ba(3)	103.4(4)

S(20)#8-Ba(11)-Ba(10)#5	43.5(4)
S(20)#8-Ba(11)-Sn(3)#6	36.3(4)
S(20)#8-Ba(11)-S(10)#8	137.2(5)
S(20)#8-Ba(11)-S(17)#8	69.8(5)
S(20)#8-Ba(11)-S(18)	125.0(5)
S(20)#8-Ba(11)-S(30)#6	69.4(5)
S(30)#6-Ba(11)-Ba(1)#6	70.2(4)
S(30)#6-Ba(11)-Ba(3)	172.1(4)
S(30)#6-Ba(11)-Ba(10)#5	110.7(4)
S(30)#6-Ba(11)-Sn(3)#6	36.7(4)
S(30)#6-Ba(11)-S(10)#8	70.8(5)
S(30)#6-Ba(11)-S(17)#8	131.1(5)
S(30)#6-Ba(11)-S(18)	92.1(5)
Ba(4)-Ba(12)-Ba(9)	115.88(12)
Ba(8)#9-Ba(12)-Ba(4)	78.40(11)
Ba(8)#9-Ba(12)-Ba(9)	73.95(10)
S(8)-Ba(12)-Ba(4)	40.6(4)
S(8)-Ba(12)-Ba(8)#9	47.9(4)
S(8)-Ba(12)-Ba(9)	79.9(4)
S(8)-Ba(12)-S(24)	73.4(5)
S(9)-Ba(12)-Ba(4)	102.8(4)
S(9)-Ba(12)-Ba(8)#9	130.2(4)
S(9)-Ba(12)-Ba(9)	138.8(4)
S(9)-Ba(12)-S(8)	141.3(6)
S(9)-Ba(12)-S(22)	128.9(5)
S(9)-Ba(12)-S(24)	85.0(5)
S(19)-Ba(12)-Ba(4)	138.4(4)
S(19)-Ba(12)-Ba(8)#9	131.2(4)
S(19)-Ba(12)-Ba(9)	61.7(4)
S(19)-Ba(12)-S(8)	133.1(5)
S(19)-Ba(12)-S(9)	80.3(5)
S(19)-Ba(12)-S(22)	84.6(6)
S(19)-Ba(12)-S(23)	80.6(5)

S(19)-Ba(12)-S(24)	147.7(5)
S(22)-Ba(12)-Ba(4)	120.1(4)
S(22)-Ba(12)-Ba(8)#9	46.8(4)
S(22)-Ba(12)-Ba(9)	38.4(4)
S(22)-Ba(12)-S(8)	80.4(6)
S(22)-Ba(12)-S(24)	82.6(6)
S(23)-Ba(12)-Ba(4)	61.0(4)
S(23)-Ba(12)-Ba(8)#9	137.3(4)
S(23)-Ba(12)-Ba(9)	111.1(4)
S(23)-Ba(12)-S(8)	90.2(5)
S(23)-Ba(12)-S(9)	75.0(6)
S(23)-Ba(12)-S(22)	149.1(6)
S(23)-Ba(12)-S(24)	123.0(6)
S(24)-Ba(12)-Ba(4)	73.0(4)
S(24)-Ba(12)-Ba(8)#9	47.1(4)
S(24)-Ba(12)-Ba(9)	118.5(4)
Te(5)#4-Ba(13)-Sn(4)#4	39.2(2)
Te(5)#4-Ba(13)-Sn(6)#5	171.6(3)
Sn(4)#4-Ba(13)-Sn(6)#5	138.60(18)
S(5)#4-Ba(13)-Te(5)#4	0.0
S(5)#4-Ba(13)-Sn(4)#4	39.2(2)
S(5)#4-Ba(13)-Sn(6)#5	171.6(3)
S(12)-Ba(13)-Te(5)#4	70.5(4)
S(12)-Ba(13)-Sn(4)#4	81.0(3)
S(12)-Ba(13)-Sn(6)#5	101.5(3)
S(12)-Ba(13)-S(5)#4	70.5(4)
S(13)#5-Ba(13)-Te(5)#4	88.3(5)
S(13)#5-Ba(13)-Sn(4)#4	107.5(4)
S(13)#5-Ba(13)-Sn(6)#5	99.6(4)
S(13)#5-Ba(13)-S(5)#4	88.3(5)
S(13)#5-Ba(13)-S(12)	134.8(5)
S(13)#5-Ba(13)-S(25)#5	72.6(6)
S(13)#5-Ba(13)-S(28)#5	136.3(5)

S(13)#5-Ba(13)-Te(28)#5	136.3(5)
S(21)#4-Ba(13)-Te(5)#4	77.1(4)
S(21)#4-Ba(13)-Sn(4)#4	38.0(4)
S(21)#4-Ba(13)-Sn(6)#5	101.9(4)
S(21)#4-Ba(13)-S(5)#4	77.1(4)
S(21)#4-Ba(13)-S(12)	98.5(5)
S(21)#4-Ba(13)-S(13)#5	115.5(6)
S(21)#4-Ba(13)-S(25)#5	91.3(5)
S(21)#4-Ba(13)-S(28)#5	86.1(5)
S(21)#4-Ba(13)-Te(28)#5	86.1(5)
S(25)#5-Ba(13)-Te(5)#4	150.9(5)
S(25)#5-Ba(13)-Sn(4)#4	125.9(4)
S(25)#5-Ba(13)-Sn(6)#5	36.8(4)
S(25)#5-Ba(13)-S(5)#4	150.9(5)
S(25)#5-Ba(13)-S(12)	138.3(5)
S(25)#5-Ba(13)-S(28)#5	69.2(5)
S(25)#5-Ba(13)-Te(28)#5	69.2(5)
S(26)-Ba(13)-Te(5)#4	105.2(5)
S(26)-Ba(13)-Sn(4)#4	142.5(4)
S(26)-Ba(13)-Sn(6)#5	74.3(4)
S(26)-Ba(13)-S(5)#4	105.2(5)
S(26)-Ba(13)-S(12)	73.1(5)
S(26)-Ba(13)-S(13)#5	74.9(6)
S(26)-Ba(13)-S(21)#4	169.5(6)
S(26)-Ba(13)-S(25)#5	91.1(6)
S(26)-Ba(13)-S(28)#5	85.2(5)
S(26)-Ba(13)-Te(28)#5	85.2(5)
S(28)#5-Ba(13)-Te(5)#4	134.9(4)
S(28)#5-Ba(13)-Sn(4)#4	111.8(3)
S(28)#5-Ba(13)-Sn(6)#5	36.9(3)
S(28)#5-Ba(13)-S(5)#4	134.9(4)
S(28)#5-Ba(13)-S(12)	71.1(4)
Te(28)#5-Ba(13)-Te(5)#4	134.9(4)

Te(28)#5-Ba(13)-Sn(4)#4	111.8(3)
Te(28)#5-Ba(13)-Sn(6)#5	36.9(3)
Te(28)#5-Ba(13)-S(5)#4	134.9(4)
Te(28)#5-Ba(13)-S(12)	71.1(4)
Te(28)#5-Ba(13)-S(28)#5	0.0
Ba(1)#6-Ba(14)-Ba(4)#6	58.67(12)
Ba(1)#6-Ba(14)-Ba(15)#5	84.45(13)
Ba(15)#5-Ba(14)-Ba(4)#6	70.96(12)
Te(3)#6-Ba(14)-Ba(1)#6	104.5(3)
Te(3)#6-Ba(14)-Ba(4)#6	45.9(3)
Te(3)#6-Ba(14)-Ba(15)#5	74.4(3)
Te(3)#6-Ba(14)-S(7)	138.6(4)
S(3)#6-Ba(14)-Ba(1)#6	104.5(3)
S(3)#6-Ba(14)-Ba(4)#6	45.9(3)
S(3)#6-Ba(14)-Ba(15)#5	74.4(3)
S(3)#6-Ba(14)-Te(3)#6	0.0
S(3)#6-Ba(14)-S(7)	138.6(4)
S(11)#6-Ba(14)-Ba(1)#6	53.7(4)
S(11)#6-Ba(14)-Ba(4)#6	43.7(3)
S(11)#6-Ba(14)-Ba(15)#5	113.0(4)
S(11)#6-Ba(14)-Te(3)#6	70.3(4)
S(11)#6-Ba(14)-S(3)#6	70.3(4)
S(11)#6-Ba(14)-S(18)	83.2(5)
S(11)#6-Ba(14)-S(7)	139.6(5)
S(18)-Ba(14)-Ba(1)#6	73.9(4)
S(18)-Ba(14)-Ba(4)#6	122.6(4)
S(18)-Ba(14)-Ba(15)#5	137.2(4)
S(18)-Ba(14)-Te(3)#6	146.2(4)
S(18)-Ba(14)-S(3)#6	146.2(4)
S(18)-Ba(14)-S(7)	75.0(4)
S(27)#6-Ba(14)-Ba(1)#6	41.0(4)
S(27)#6-Ba(14)-Ba(4)#6	49.1(4)
S(27)#6-Ba(14)-Ba(15)#5	44.1(4)

S(27)#6-Ba(14)-Te(3)#6	84.5(4)
S(27)#6-Ba(14)-S(3)#6	84.5(4)
S(27)#6-Ba(14)-S(11)#6	77.1(5)
S(27)#6-Ba(14)-S(18)	110.3(5)
S(27)#6-Ba(14)-S(7)	79.1(4)
S(29)#6-Ba(14)-Ba(1)#6	174.0(4)
S(29)#6-Ba(14)-Ba(4)#6	126.7(4)
S(29)#6-Ba(14)-Ba(15)#5	94.9(4)
S(29)#6-Ba(14)-Te(3)#6	81.0(5)
S(29)#6-Ba(14)-S(3)#6	81.0(5)
S(29)#6-Ba(14)-S(11)#6	131.5(5)
S(29)#6-Ba(14)-S(18)	102.9(5)
S(29)#6-Ba(14)-S(27)#6	138.9(6)
S(29)#6-Ba(14)-S(7)	87.0(5)
S(7)-Ba(14)-Ba(1)#6	87.2(3)
S(7)-Ba(14)-Ba(4)#6	127.9(3)
S(7)-Ba(14)-Ba(15)#5	67.3(3)
Ba(14)#9-Ba(15)-Ba(6)#6	122.57(15)
S(1)#13-Ba(15)-Ba(6)#6	44.3(3)
S(1)#13-Ba(15)-Ba(14)#9	89.9(4)
S(1)#13-Ba(15)-S(14)	142.2(5)
S(1)#13-Ba(15)-S(15)#13	71.2(4)
S(1)#13-Ba(15)-Te(15)#13	71.2(4)
S(1)#13-Ba(15)-S(27)#13	116.0(5)
S(1)#13-Ba(15)-S(28)	79.3(5)
S(1)#13-Ba(15)-S(29)#6	80.0(5)
S(14)-Ba(15)-Ba(6)#6	130.9(4)
S(14)-Ba(15)-Ba(14)#9	106.5(4)
S(14)-Ba(15)-S(15)#13	138.6(4)
S(14)-Ba(15)-Te(15)#13	138.6(4)
S(14)-Ba(15)-S(27)#13	98.2(5)
S(14)-Ba(15)-S(28)	75.5(5)
S(14)-Ba(15)-S(29)#6	83.3(5)

S(15)#13-Ba(15)-Ba(6)#6	46.79(17)
S(15)#13-Ba(15)-Ba(14)#9	93.7(2)
Te(15)#13-Ba(15)-Ba(6)#6	46.79(17)
Te(15)#13-Ba(15)-Ba(14)#9	93.7(2)
Te(15)#13-Ba(15)-S(15)#13	0.0
S(27)#13-Ba(15)-Ba(6)#6	118.7(4)
S(27)#13-Ba(15)-Ba(14)#9	42.7(3)
S(27)#13-Ba(15)-S(15)#13	72.5(4)
S(27)#13-Ba(15)-Te(15)#13	72.5(4)
S(27)#13-Ba(15)-S(28)	107.0(5)
S(27)#13-Ba(15)-S(29)#6	141.0(5)
S(28)-Ba(15)-Ba(6)#6	117.8(3)
S(28)-Ba(15)-Ba(14)#9	69.1(3)
S(28)-Ba(15)-S(15)#13	145.9(4)
S(28)-Ba(15)-Te(15)#13	145.9(4)
S(29)#6-Ba(15)-Ba(6)#6	47.6(4)
S(29)#6-Ba(15)-Ba(14)#9	169.6(4)
S(29)#6-Ba(15)-S(15)#13	80.8(4)
S(29)#6-Ba(15)-Te(15)#13	80.8(4)
S(29)#6-Ba(15)-S(28)	111.0(5)
Ba(3)#4-Ba(16)-Ba(4)	140.70(15)
Ba(13)#9-Ba(16)-Ba(3)#4	81.06(12)
Ba(13)#9-Ba(16)-Ba(4)	61.13(12)
Te(4)-Ba(16)-Ba(3)#4	46.3(3)
Te(4)-Ba(16)-Ba(4)	119.3(3)
Te(4)-Ba(16)-Ba(13)#9	68.5(3)
Te(4)-Ba(16)-S(26)	148.9(4)
S(11)-Ba(16)-Ba(3)#4	174.8(4)
S(11)-Ba(16)-Ba(4)	43.7(3)
S(11)-Ba(16)-Ba(13)#9	103.9(4)
S(11)-Ba(16)-Te(4)	136.9(5)
S(11)-Ba(16)-S(13)	72.0(5)
S(11)-Ba(16)-S(26)	64.5(5)

S(12)-Ba(16)-Ba(3)#4	46.6(3)
S(12)-Ba(16)-Ba(4)	121.1(4)
S(12)-Ba(16)-Ba(13)#9	93.4(3)
S(12)-Ba(16)-Te(4)	92.6(4)
S(12)-Ba(16)-S(11)	130.5(5)
S(12)-Ba(16)-S(13)	139.3(5)
S(12)-Ba(16)-S(26)	71.0(5)
S(13)-Ba(16)-Ba(3)#4	113.1(4)
S(13)-Ba(16)-Ba(4)	46.7(4)
S(13)-Ba(16)-Ba(13)#9	45.8(4)
S(13)-Ba(16)-Te(4)	74.2(5)
S(13)-Ba(16)-S(26)	135.1(5)
S(25)-Ba(16)-Ba(3)#4	101.3(4)
S(25)-Ba(16)-Ba(4)	45.6(4)
S(25)-Ba(16)-Ba(13)#9	47.8(4)
S(25)-Ba(16)-Te(4)	113.9(5)
S(25)-Ba(16)-S(11)	81.2(6)
S(25)-Ba(16)-S(12)	77.1(5)
S(25)-Ba(16)-S(13)	73.8(6)
S(25)-Ba(16)-S(26)	88.7(5)
S(25)-Ba(16)-S(30)	166.2(6)
S(26)-Ba(16)-Ba(3)#4	110.7(4)
S(26)-Ba(16)-Ba(4)	91.8(4)
S(26)-Ba(16)-Ba(13)#9	136.4(4)
S(30)-Ba(16)-Ba(3)#4	92.1(4)
S(30)-Ba(16)-Ba(4)	123.1(4)
S(30)-Ba(16)-Ba(13)#9	139.3(4)
S(30)-Ba(16)-Te(4)	77.8(5)
S(30)-Ba(16)-S(11)	85.2(5)
S(30)-Ba(16)-S(12)	110.7(5)
S(30)-Ba(16)-S(13)	103.9(5)
S(30)-Ba(16)-S(26)	83.6(5)
Ba(4)-Te(3)-Ba(6)	156.4(5)

Ba(4)-Te(3)-Ba(14)#3	87.8(3)
Ba(14)#3-Te(3)-Ba(6)	93.4(4)
Sn(2)-Te(3)-Ba(4)	108.3(5)
Sn(2)-Te(3)-Ba(6)	89.4(4)
Sn(2)-Te(3)-Ba(14)#3	128.1(6)
Ba(3)#4-Te(4)-Ba(7)#1	160.9(5)
Ba(3)#4-Te(4)-Ba(8)#4	83.2(3)
Ba(3)#4-Te(4)-Ba(16)	86.5(4)
Ba(7)#1-Te(4)-Ba(8)#4	96.5(4)
Ba(16)-Te(4)-Ba(7)#1	101.2(4)
Ba(16)-Te(4)-Ba(8)#4	153.2(5)
Sn(3)-Te(4)-Ba(3)#4	111.7(5)
Sn(3)-Te(4)-Ba(7)#1	86.9(5)
Sn(3)-Te(4)-Ba(8)#4	79.5(4)
Sn(3)-Te(4)-Ba(16)	81.4(4)
Ba(7)-Te(5)-Ba(3)	161.2(4)
Ba(7)-Te(5)-Ba(13)#7	88.0(3)
Ba(13)#7-Te(5)-Ba(3)	104.6(4)
Sn(4)-Te(5)-Ba(3)	85.2(4)
Sn(4)-Te(5)-Ba(7)	110.8(4)
Sn(4)-Te(5)-Ba(13)#7	81.5(4)
S(11)-Sn(1)-S(15)#5	105.1(6)
S(11)-Sn(1)-Te(15)#5	105.1(6)
S(11)-Sn(1)-S(26)	94.8(7)
Te(15)#5-Sn(1)-S(15)#5	0.0
S(23)-Sn(1)-S(11)	122.0(7)
S(23)-Sn(1)-S(15)#5	118.4(6)
S(23)-Sn(1)-Te(15)#5	118.4(6)
S(23)-Sn(1)-S(26)	106.6(7)
S(26)-Sn(1)-S(15)#5	106.4(6)
S(26)-Sn(1)-Te(15)#5	106.4(6)
S(1)-Sn(2)-Te(3)	114.0(6)
S(6)-Sn(2)-Te(3)	110.7(6)

S(6)-Sn(2)-S(1)	95.7(7)
S(6)-Sn(2)-S(24)	108.7(7)
S(24)-Sn(2)-Te(3)	112.6(6)
S(24)-Sn(2)-S(1)	113.8(7)
Ba(11)#3-Sn(3)-Ba(6)#4	70.23(14)
Te(4)-Sn(3)-Ba(6)#4	128.6(4)
Te(4)-Sn(3)-Ba(11)#3	145.0(4)
S(9)#4-Sn(3)-Ba(6)#4	52.2(5)
S(9)#4-Sn(3)-Ba(11)#3	105.2(6)
S(9)#4-Sn(3)-Te(4)	109.2(7)
S(9)#4-Sn(3)-S(20)#4	107.7(7)
S(9)#4-Sn(3)-S(30)	117.4(7)
S(20)#4-Sn(3)-Ba(6)#4	55.8(5)
S(20)#4-Sn(3)-Ba(11)#3	53.4(5)
S(20)#4-Sn(3)-Te(4)	108.7(6)
S(20)#4-Sn(3)-S(30)	101.1(7)
S(30)-Sn(3)-Ba(6)#4	118.9(5)
S(30)-Sn(3)-Ba(11)#3	54.5(5)
S(30)-Sn(3)-Te(4)	112.0(6)
Te(5)-Sn(4)-Ba(13)#7	59.3(3)
S(2)-Sn(4)-Ba(13)#7	108.0(5)
S(2)-Sn(4)-Te(5)	111.1(6)
S(21)-Sn(4)-Ba(13)#7	53.4(5)
S(21)-Sn(4)-Te(5)	112.5(6)
S(21)-Sn(4)-S(2)	94.6(7)
S(22)-Sn(4)-Ba(13)#7	142.4(6)
S(22)-Sn(4)-Te(5)	111.1(7)
S(22)-Sn(4)-S(2)	109.1(8)
S(22)-Sn(4)-S(21)	117.2(8)
S(16)-Sn(5)-S(18)	103.3(7)
S(16)-Sn(5)-S(7)	109.7(6)
S(18)-Sn(5)-S(7)	109.5(6)
S(19)-Sn(5)-S(16)	104.3(7)

S(19)-Sn(5)-S(18)	118.3(7)
S(19)-Sn(5)-S(7)	111.1(6)
S(8)-Sn(6)-Ba(13)#9	101.4(5)
S(8)-Sn(6)-S(14)	109.5(7)
S(8)-Sn(6)-S(25)	105.0(8)
S(8)-Sn(6)-S(28)	118.7(7)
S(14)-Sn(6)-Ba(13)#9	148.5(5)
S(25)-Sn(6)-Ba(13)#9	54.1(5)
S(25)-Sn(6)-S(14)	109.8(7)
S(25)-Sn(6)-S(28)	102.9(7)
S(28)-Sn(6)-Ba(13)#9	57.1(4)
S(28)-Sn(6)-S(14)	110.4(6)
Ba(5)#6-Sn(8)-Ba(3)#4	72.68(14)
S(12)-Sn(8)-Ba(3)#4	56.6(4)
S(12)-Sn(8)-Ba(5)#6	55.0(4)
S(12)-Sn(8)-S(29)#6	93.2(6)
S(17)#6-Sn(8)-Ba(3)#4	54.9(5)
S(17)#6-Sn(8)-Ba(5)#6	55.5(4)
S(17)#6-Sn(8)-S(12)	90.7(6)
S(17)#6-Sn(8)-S(29)#6	90.4(7)
S(29)#6-Sn(8)-Ba(3)#4	129.3(5)
S(29)#6-Sn(8)-Ba(5)#6	56.7(5)
Ba(6)#9-S(1)-Ba(5)	161.5(7)
Ba(10)#10-S(1)-Ba(5)	73.2(4)
Ba(10)#10-S(1)-Ba(6)#9	88.7(5)
Ba(15)#2-S(1)-Ba(5)	100.0(5)
Ba(15)#2-S(1)-Ba(6)#9	94.0(5)
Ba(15)#2-S(1)-Ba(10)#10	150.0(7)
Sn(2)-S(1)-Ba(5)	85.2(5)
Sn(2)-S(1)-Ba(6)#9	99.8(6)
Sn(2)-S(1)-Ba(10)#10	93.8(6)
Sn(2)-S(1)-Ba(15)#2	115.0(7)
Ba(3)-S(2)-Ba(5)#8	84.8(5)

Ba(3)-S(2)-Ba(9)	121.7(6)
Ba(5)#8-S(2)-Ba(9)	153.5(6)
Ba(10)-S(2)-Ba(3)	156.7(7)
Ba(10)-S(2)-Ba(5)#8	72.1(4)
Ba(10)-S(2)-Ba(9)	81.4(4)
Ba(11)-S(2)-Ba(3)	88.7(5)
Ba(11)-S(2)-Ba(5)#8	92.6(5)
Ba(11)-S(2)-Ba(9)	88.9(5)
Ba(11)-S(2)-Ba(10)	95.3(6)
Sn(4)-S(2)-Ba(3)	89.8(6)
Sn(4)-S(2)-Ba(5)#8	98.0(6)
Sn(4)-S(2)-Ba(9)	82.7(6)
Sn(4)-S(2)-Ba(10)	90.4(6)
Sn(4)-S(2)-Ba(11)	169.1(8)
Ba(5)-S(6)-Ba(6)	79.9(4)
Ba(5)-S(6)-Ba(7)	154.2(6)
Ba(5)-S(6)-Ba(10)#10	73.2(4)
Ba(6)-S(6)-Ba(7)	125.6(6)
Ba(10)#10-S(6)-Ba(6)	153.0(7)
Ba(10)#10-S(6)-Ba(7)	81.3(4)
Ba(11)#10-S(6)-Ba(5)	95.4(5)
Ba(11)#10-S(6)-Ba(6)	88.1(5)
Ba(11)#10-S(6)-Ba(7)	90.1(5)
Ba(11)#10-S(6)-Ba(10)#10	92.4(5)
Sn(2)-S(6)-Ba(5)	88.7(6)
Sn(2)-S(6)-Ba(6)	89.8(6)
Sn(2)-S(6)-Ba(7)	87.4(6)
Sn(2)-S(6)-Ba(10)#10	91.6(6)
Sn(2)-S(6)-Ba(11)#10	174.9(8)
Ba(4)-S(8)-Ba(8)#9	130.0(7)
Ba(4)-S(8)-Ba(12)	98.3(6)
Ba(8)#9-S(8)-Ba(12)	84.1(5)
Sn(6)-S(8)-Ba(4)	93.3(7)

Sn(6)-S(8)-Ba(8)#9	136.4(9)
Sn(6)-S(8)-Ba(12)	96.5(7)
Ba(8)-S(9)-Ba(6)	101.8(6)
Ba(8)-S(9)-Ba(12)	86.2(6)
Ba(12)-S(9)-Ba(6)	129.2(7)
Sn(3)#7-S(9)-Ba(6)	92.2(7)
Sn(3)#7-S(9)-Ba(8)	96.2(7)
Sn(3)#7-S(9)-Ba(12)	137.3(9)
Ba(1)#12-S(10)-Ba(7)	88.2(6)
Ba(1)#12-S(10)-Ba(9)#10	86.8(6)
Ba(1)#12-S(10)-Ba(10)#10	101.9(6)
Ba(1)#12-S(10)-Ba(11)#10	163.6(8)
Ba(7)-S(10)-Ba(11)#10	93.1(5)
Ba(9)#10-S(10)-Ba(7)	173.8(6)
Ba(9)#10-S(10)-Ba(11)#10	92.7(5)
Ba(10)#10-S(10)-Ba(7)	88.7(5)
Ba(10)#10-S(10)-Ba(9)#10	88.7(5)
Ba(10)#10-S(10)-Ba(11)#10	94.5(5)
Ba(4)-S(11)-Ba(1)	81.4(4)
Ba(4)-S(11)-Ba(16)	91.4(5)
Ba(14)#3-S(11)-Ba(1)	77.4(4)
Ba(14)#3-S(11)-Ba(4)	93.1(5)
Ba(14)#3-S(11)-Ba(16)	156.6(7)
Ba(16)-S(11)-Ba(1)	80.7(4)
Sn(1)-S(11)-Ba(1)	176.1(8)
Sn(1)-S(11)-Ba(4)	98.0(6)
Sn(1)-S(11)-Ba(14)#3	106.5(7)
Sn(1)-S(11)-Ba(16)	95.5(6)
Ba(2)-S(12)-Ba(3)#4	162.7(6)
Ba(2)-S(12)-Ba(13)	88.4(5)
Ba(3)#4-S(12)-Ba(13)	108.8(5)
Ba(5)#6-S(12)-Ba(2)	93.5(5)
Ba(5)#6-S(12)-Ba(3)#4	90.5(5)

Ba(5)#6-S(12)-Ba(13)	80.6(4)
Ba(5)#6-S(12)-Ba(16)	169.6(7)
Ba(16)-S(12)-Ba(2)	90.6(5)
Ba(16)-S(12)-Ba(3)#4	88.5(5)
Ba(16)-S(12)-Ba(13)	90.0(5)
Sn(8)-S(12)-Ba(2)	81.5(5)
Sn(8)-S(12)-Ba(3)#4	82.4(5)
Sn(8)-S(12)-Ba(5)#6	82.3(5)
Sn(8)-S(12)-Ba(13)	159.5(7)
Sn(8)-S(12)-Ba(16)	107.8(6)
Ba(1)-S(13)-Ba(4)	90.9(6)
Ba(1)-S(13)-Ba(7)#1	87.0(6)
Ba(1)-S(13)-Ba(13)#9	177.3(9)
Ba(1)-S(13)-Ba(16)	91.8(6)
Ba(7)#1-S(13)-Ba(4)	166.7(7)
Ba(7)#1-S(13)-Ba(16)	106.1(6)
Ba(13)#9-S(13)-Ba(4)	89.2(6)
Ba(13)#9-S(13)-Ba(7)#1	93.5(6)
Ba(13)#9-S(13)-Ba(16)	85.6(5)
Ba(16)-S(13)-Ba(4)	87.0(5)
Ba(9)-S(14)-Ba(2)	157.7(6)
Ba(15)-S(14)-Ba(2)	98.4(5)
Ba(15)-S(14)-Ba(9)	85.2(5)
Sn(6)-S(14)-Ba(2)	89.7(6)
Sn(6)-S(14)-Ba(9)	112.5(6)
Sn(6)-S(14)-Ba(15)	88.6(6)
Ba(6)#9-S(15)-Ba(4)	143.8(3)
Ba(6)#9-S(15)-Ba(15)#2	86.0(2)
Ba(15)#2-S(15)-Ba(4)	100.8(3)
Sn(1)#9-S(15)-Ba(4)	90.9(3)
Sn(1)#9-S(15)-Ba(6)#9	104.9(3)
Sn(1)#9-S(15)-Ba(15)#2	143.1(4)
Ba(3)-S(16)-Ba(1)#6	164.5(7)

Ba(3)-S(16)-Ba(9)#5	125.2(6)
Ba(9)#5-S(16)-Ba(1)#6	68.9(4)
Ba(10)#5-S(16)-Ba(1)#6	82.2(5)
Ba(10)#5-S(16)-Ba(3)	91.5(5)
Ba(10)#5-S(16)-Ba(9)#5	87.2(5)
Ba(10)#5-S(16)-Ba(11)	91.1(6)
Ba(11)-S(16)-Ba(1)#6	78.1(5)
Ba(11)-S(16)-Ba(3)	88.0(5)
Ba(11)-S(16)-Ba(9)#5	146.8(7)
Sn(5)-S(16)-Ba(1)#6	98.5(6)
Sn(5)-S(16)-Ba(3)	88.5(6)
Sn(5)-S(16)-Ba(9)#5	90.3(6)
Sn(5)-S(16)-Ba(10)#5	177.0(9)
Sn(5)-S(16)-Ba(11)	91.9(6)
Ba(3)#10-S(17)-Ba(11)#10	87.9(5)
Ba(5)-S(17)-Ba(3)#10	91.7(5)
Ba(5)-S(17)-Ba(6)	86.3(5)
Ba(5)-S(17)-Ba(10)#11	176.4(8)
Ba(5)-S(17)-Ba(11)#10	95.7(5)
Ba(6)-S(17)-Ba(3)#10	178.0(7)
Ba(6)-S(17)-Ba(10)#11	90.7(5)
Ba(6)-S(17)-Ba(11)#10	91.6(5)
Ba(10)#11-S(17)-Ba(3)#10	91.2(5)
Ba(10)#11-S(17)-Ba(11)#10	86.5(5)
Sn(8)#3-S(17)-Ba(3)#10	85.0(6)
Sn(8)#3-S(17)-Ba(5)	83.0(6)
Sn(8)#3-S(17)-Ba(6)	95.4(6)
Sn(8)#3-S(17)-Ba(10)#11	95.2(6)
Sn(8)#3-S(17)-Ba(11)#10	172.8(9)
Ba(9)-S(18)-Ba(11)	88.8(5)
Ba(14)-S(18)-Ba(9)	144.3(6)
Ba(14)-S(18)-Ba(11)	126.7(6)
Sn(5)-S(18)-Ba(9)	101.2(6)

Sn(5)-S(18)-Ba(11)	84.9(5)
Sn(5)-S(18)-Ba(14)	87.5(5)
Ba(3)-S(19)-Ba(8)	97.9(5)
Ba(3)-S(19)-Ba(12)	126.0(6)
Ba(8)-S(19)-Ba(12)	87.0(5)
Sn(5)-S(19)-Ba(3)	94.9(6)
Sn(5)-S(19)-Ba(8)	100.8(6)
Sn(5)-S(19)-Ba(12)	137.1(8)
Ba(6)-S(20)-Ba(1)#7	164.3(7)
Ba(7)#5-S(20)-Ba(1)#7	70.4(4)
Ba(7)#5-S(20)-Ba(6)	123.1(6)
Ba(10)#11-S(20)-Ba(1)#7	81.7(5)
Ba(10)#11-S(20)-Ba(6)	90.2(5)
Ba(10)#11-S(20)-Ba(7)#5	88.7(5)
Ba(10)#11-S(20)-Ba(11)#10	90.1(6)
Ba(11)#10-S(20)-Ba(1)#7	76.9(4)
Ba(11)#10-S(20)-Ba(6)	89.7(5)
Ba(11)#10-S(20)-Ba(7)#5	147.1(7)
Sn(3)#7-S(20)-Ba(1)#7	100.2(6)
Sn(3)#7-S(20)-Ba(6)	88.0(6)
Sn(3)#7-S(20)-Ba(7)#5	92.0(7)
Sn(3)#7-S(20)-Ba(10)#11	178.1(9)
Sn(3)#7-S(20)-Ba(11)#10	90.3(6)
Ba(10)-S(21)-Ba(3)#9	88.8(5)
Ba(13)#7-S(21)-Ba(3)#9	127.4(7)
Ba(13)#7-S(21)-Ba(10)	143.0(7)
Sn(4)-S(21)-Ba(3)#9	101.2(7)
Sn(4)-S(21)-Ba(10)	91.8(6)
Sn(4)-S(21)-Ba(13)#7	88.5(6)
Ba(8)#9-S(22)-Ba(12)	85.3(6)
Ba(9)-S(22)-Ba(8)#9	125.3(8)
Ba(9)-S(22)-Ba(12)	101.8(7)
Sn(4)-S(22)-Ba(8)#9	135.9(9)

Sn(4)-S(22)-Ba(9)	96.4(8)
Sn(4)-S(22)-Ba(12)	101.0(8)
Ba(2)-S(23)-Ba(8)	100.8(6)
Ba(12)-S(23)-Ba(2)	118.2(7)
Ba(12)-S(23)-Ba(8)	85.3(5)
Sn(1)-S(23)-Ba(2)	95.2(7)
Sn(1)-S(23)-Ba(8)	108.4(7)
Sn(1)-S(23)-Ba(12)	141.3(9)
Ba(8)#9-S(24)-Ba(7)	114.4(6)
Ba(8)#9-S(24)-Ba(12)	83.6(5)
Ba(12)-S(24)-Ba(7)	97.3(5)
Sn(2)-S(24)-Ba(7)	92.9(6)
Sn(2)-S(24)-Ba(8)#9	151.5(8)
Sn(2)-S(24)-Ba(12)	101.7(6)
Ba(4)-S(25)-Ba(2)	124.1(6)
Ba(13)#9-S(25)-Ba(2)	147.2(7)
Ba(13)#9-S(25)-Ba(4)	88.6(5)
Ba(16)-S(25)-Ba(2)	90.5(5)
Ba(16)-S(25)-Ba(4)	93.3(6)
Ba(16)-S(25)-Ba(13)#9	89.0(6)
Sn(6)-S(25)-Ba(2)	89.7(6)
Sn(6)-S(25)-Ba(4)	89.2(6)
Sn(6)-S(25)-Ba(13)#9	89.1(6)
Sn(6)-S(25)-Ba(16)	176.8(10)
Ba(2)-S(26)-Ba(4)#5	122.4(6)
Ba(13)-S(26)-Ba(2)	91.0(5)
Ba(13)-S(26)-Ba(4)#5	86.9(5)
Ba(13)-S(26)-Ba(16)	93.0(5)
Ba(16)-S(26)-Ba(2)	84.3(5)
Ba(16)-S(26)-Ba(4)#5	153.3(7)
Sn(1)-S(26)-Ba(2)	86.8(6)
Sn(1)-S(26)-Ba(4)#5	90.7(6)
Sn(1)-S(26)-Ba(13)	175.3(9)

Sn(1)-S(26)-Ba(16)	91.0(6)
Ba(1)-S(27)-Ba(4)	87.0(5)
Ba(1)-S(27)-Ba(9)#2	82.6(5)
Ba(1)-S(27)-Ba(14)#3	89.3(5)
Ba(1)-S(27)-Ba(15)#2	166.9(8)
Ba(9)#2-S(27)-Ba(4)	163.5(6)
Ba(14)#3-S(27)-Ba(4)	88.3(5)
Ba(14)#3-S(27)-Ba(9)#2	104.3(5)
Ba(14)#3-S(27)-Ba(15)#2	93.2(5)
Ba(15)#2-S(27)-Ba(4)	106.0(5)
Ba(15)#2-S(27)-Ba(9)#2	84.2(5)
Ba(2)#9-S(28)-Ba(13)#9	88.5(4)
Ba(2)#9-S(28)-Ba(15)	136.8(6)
Ba(5)#13-S(28)-Ba(2)#9	92.1(4)
Ba(5)#13-S(28)-Ba(13)#9	79.6(4)
Ba(5)#13-S(28)-Ba(15)	97.6(5)
Ba(13)#9-S(28)-Ba(15)	134.7(5)
Sn(6)-S(28)-Ba(2)#9	100.1(6)
Sn(6)-S(28)-Ba(5)#13	160.9(7)
Sn(6)-S(28)-Ba(13)#9	86.0(5)
Sn(6)-S(28)-Ba(15)	83.7(5)
Ba(2)#3-S(29)-Ba(6)	164.2(7)
Ba(5)-S(29)-Ba(2)#3	89.7(5)
Ba(5)-S(29)-Ba(6)	80.9(5)
Ba(5)-S(29)-Ba(15)#3	157.6(7)
Ba(14)#3-S(29)-Ba(2)#3	96.5(6)
Ba(14)#3-S(29)-Ba(5)	110.9(6)
Ba(14)#3-S(29)-Ba(6)	98.7(6)
Ba(14)#3-S(29)-Ba(15)#3	89.8(5)
Ba(15)#3-S(29)-Ba(2)#3	96.6(5)
Ba(15)#3-S(29)-Ba(6)	87.8(5)
Sn(8)#3-S(29)-Ba(2)#3	78.4(5)
Sn(8)#3-S(29)-Ba(5)	80.0(5)

Sn(8)#3-S(29)-Ba(6)	87.4(6)
Sn(8)#3-S(29)-Ba(14)#3	168.1(8)
Sn(8)#3-S(29)-Ba(15)#3	80.3(5)
Ba(7)#4-S(30)-Ba(11)#3	92.7(5)
Ba(16)-S(30)-Ba(7)#4	135.0(7)
Ba(16)-S(30)-Ba(11)#3	131.7(7)
Sn(3)-S(30)-Ba(7)#4	102.9(7)
Sn(3)-S(30)-Ba(11)#3	88.8(6)
Sn(3)-S(30)-Ba(16)	87.3(6)
Ba(2)-S(7)-Ba(9)#5	160.9(5)
Ba(2)-S(7)-Ba(14)	93.2(4)
Ba(14)-S(7)-Ba(9)#5	97.6(4)
Sn(5)-S(7)-Ba(2)	108.4(5)
Sn(5)-S(7)-Ba(9)#5	88.3(4)
Sn(5)-S(7)-Ba(14)	84.6(4)

Symmetry transformations used to generate equivalent atoms:

(1) $x+1/2, -y, z$ (2) $-x-1, -y, z+1/2$ (3) $-x-1, -y-1, z+1/2$ (4) $x+1/2, -y-1, z$ (5) $x, y-1, z$ (6) $-x-1, -y-1, z-1/2$
 (7) $x-1/2, -y-1, z$ (8) $-x-3/2, y, z-1/2$ (9) $x, y+1, z$ (10) $-x-3/2, y, z+1/2$ (11) $-x-3/2, y-1, z+1/2$ (12) $x-1/2, -y, z$
 (13) $-x-1, -y, z-1/2$ (14) $-x-3/2, y+1, z-1/2$

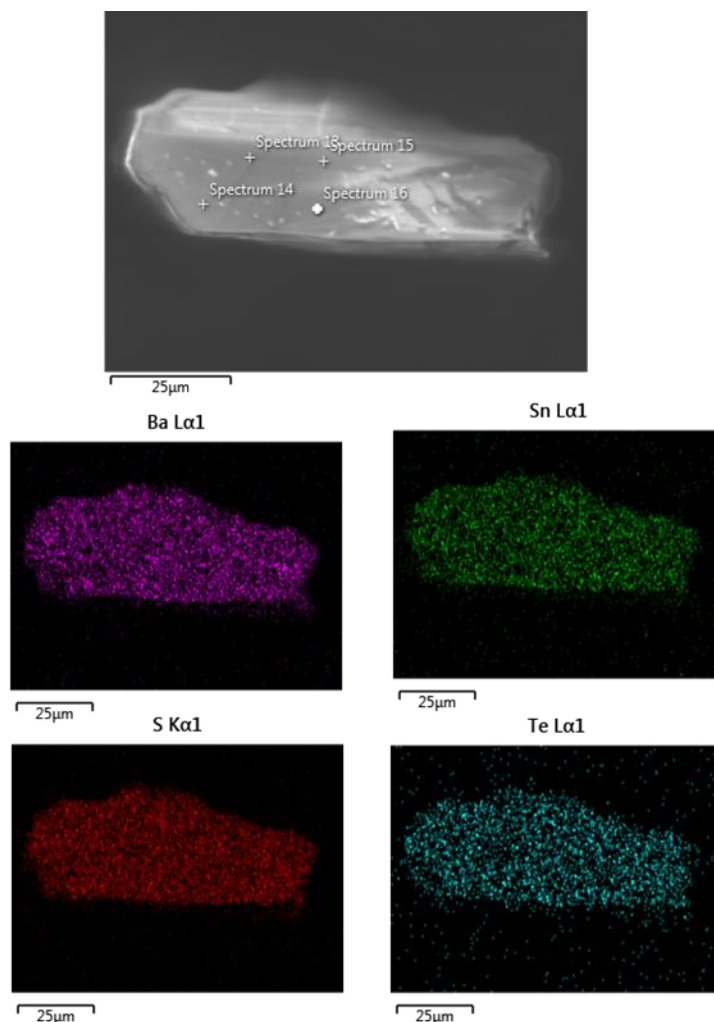


Figure S30: SEM image and EDS map of “Ba₈Sn₄S₁₄Te.” Yellow crystal.

Table S46: Average EDS point values from crystal shown in Figure S30.

Atomic % from Points				
	Ba	Sn	S	Te
Average	29.5	15.0	53	2.4
STDEV	0.3	0.2	1	0.1
Sn-norm	1.97	1.00	3.55	0.16

Table S47: Average EDS map values from crystal shown in Figure S30.

	Atomic % from Map			
	Ba	Sn	S	Te
Average	30.5	14.9	51.8	2.8
Sn-norm	2.05	1.00	3.48	0.19

References

References

1. Jain, A.; Ong, S. P.; Hautier, G.; Chen, W.; Richards, W. D.; Dacek, S.; Cholia, S.; Gunter, D.; Skinner, D.; Ceder, G.; Persson, K. A., Commentary: The Materials Project: A materials genome approach to accelerating materials innovation. *APL Materials* **2013**, *1* (1), 011002.
2. de Pablo, J. J.; Jackson, N. E.; Webb, M. A.; Chen, L.-Q.; Moore, J. E.; Morgan, D.; Jacobs, R.; Pollock, T.; Schlom, D. G.; Toberer, E. S., New frontiers for the materials genome initiative. *npj Computational Materials* **2019**, *5* (1), 41.
3. Oganov, A. R.; Pickard, C. J.; Zhu, Q.; Needs, R. J., Structure prediction drives materials discovery. *Nature Reviews Materials* **2019**, *4* (5), 331-348.
4. Butler, K. T.; Frost, J. M.; Skelton, J. M.; Svane, K. L.; Walsh, A., Computational materials design of crystalline solids. *Chem Soc Rev* **2016**, *45* (22), 6138-6146.
5. Butler, K. T.; Davies, D. W.; Cartwright, H.; Isayev, O.; Walsh, A., Machine learning for molecular and materials science. *Nature* **2018**, *559* (7715), 547-555.
6. Liu, Y.; Zhao, T.; Ju, W.; Shi, S., Materials discovery and design using machine learning. *Journal of Materiomics* **2017**, *3* (3), 159-177.
7. Gubernatis, J. E.; Lookman, T., Machine learning in materials design and discovery: Examples from the present and suggestions for the future. *Physical Review Materials* **2018**, *2* (12), 120301.
8. Pienack, N.; Bensch, W., In-situ monitoring of the formation of crystalline solids. *Angew Chem Int Ed Engl* **2011**, *50* (9), 2014-34.
9. Stock, N.; Biswas, S., Synthesis of Metal-Organic Frameworks (MOFs): Routes to Various MOF Topologies, Morphologies, and Composites. *Chemical Reviews* **2012**, *112* (2), 933-969.
10. Jensen, K. M.; Tyrsted, C.; Bremholm, M.; Iversen, B. B., In situ studies of solvothermal synthesis of energy materials. *ChemSusChem* **2014**, *7* (6), 1594-1611.
11. Hansen, T. C.; Kohlmann, H., Chemical Reactions followed by in situ Neutron Powder Diffraction. *Zeitschrift für anorganische und allgemeine Chemie* **2014**, *640* (15), 3044-3063.
12. Van Vleet, M. J.; Weng, T.; Li, X.; Schmidt, J. R., In Situ, Time-Resolved, and Mechanistic Studies of Metal–Organic Framework Nucleation and Growth. *Chemical Reviews* **2018**, *118* (7), 3681-3721.
13. Walton, R. I.; Smith, R. I.; O'Hare, D., Following the hydrothermal crystallisation of zeolites using time-resolved in situ powder neutron diffraction. *Microporous and mesoporous materials* **2001**, *48* (1-3), 79-88.
14. Gopalakrishnan, J., Chimie douce approaches to the synthesis of metastable oxide materials. *Chemistry of Materials* **1995**, *7* (7), 1265-1275.
15. Stein, A.; Keller, S. W.; Mallouk, T. E., Turning Down the Heat: Design and Mechanism in Solid-State Synthesis. *Science* **1993**, *259* (5101), 1558-1564.
16. Kanatzidis, M. G., New directions in synthetic solid state chemistry: chalcophosphate salt fluxes for discovery of new multinary solids. *Current Opinion in Solid State and Materials Science*

1997, 2 (2), 139-149.

17. Bugaris, D. E.; zur Loye, H.-C., Materials Discovery by Flux Crystal Growth: Quaternary and Higher Order Oxides. *Angewandte Chemie International Edition* **2012**, 51 (16), 3780-3811.
18. Kanatzidis, M. G., Discovery-Synthesis, Design, and Prediction of Chalcogenide Phases. *Inorganic Chemistry* **2017**, 56 (6), 3158-3173.
19. Boltersdorf, J.; King, N.; Maggard, P. A., Flux-mediated crystal growth of metal oxides: synthetic tunability of particle morphologies, sizes, and surface features for photocatalysis research. *CrystEngComm* **2015**, 17 (11), 2225-2241.
20. Kanatzidis, M. G.; Pöttgen, R.; Jeitschko, W., The metal flux: a preparative tool for the exploration of intermetallic compounds. *Angewandte Chemie International Edition* **2005**, 44 (43), 6996-7023.
21. Parkin, I., Solid state metathesis reaction for metal borides, silicides, pnictides and chalcogenides: ionic or elemental pathways. *Chemical Society Reviews* **1996**, 25 (3), 199-207.
22. Martinolich, A. J.; Neilson, J. R., Toward Reaction-by-Design: Achieving Kinetic Control of Solid State Chemistry with Metathesis. *Chemistry of Materials* **2017**, 29 (2), 479-489.
23. Alberi, K.; Nardelli, M. B.; Zakutayev, A.; Mitas, L.; Curtarolo, S.; Jain, A.; Fornari, M.; Marzari, N.; Takeuchi, I.; Green, M. L., The 2019 materials by design roadmap. *Journal of Physics D: Applied Physics* **2018**, 52 (1), 013001.
24. Cheetham, A. K.; Mellot, C. F., In Situ Studies of the Sol-Gel Synthesis of Materials. *Chemistry of Materials* **1997**, 9 (11), 2269-2279.
25. Francis, R. J.; O'Hare, D., The kinetics and mechanisms of the crystallisation of microporous materials. *Journal of the Chemical Society, Dalton Transactions* **1998**, (19), 3133-3148.
26. Munn, J.; Barnes, P.; Häusermann, D.; Axon, S. A.; Klinowski, J., In-situ studies of the hydrothermal synthesis of zeolites using synchrotron energy-dispersive X-ray diffraction. *Phase Transitions* **1992**, 39 (1-4), 129-134.
27. Polak, E.; Munn, J.; Barnes, P.; Tarling, S.; Ritter, C., Time-resolved neutron diffraction analyses of hydrothermal syntheses using a novel autoclave cell. *Journal of applied crystallography* **1990**, 23 (4), 258-262.
28. Walton, R. I.; Millange, F.; O'Hare, D.; Davies, A. T.; Sankar, G.; Catlow, C. R. A., An in Situ Energy-Dispersive X-ray Diffraction Study of the Hydrothermal Crystallization of Zeolite A. 1. Influence of Reaction Conditions and Transformation into Sodalite. *The Journal of Physical Chemistry B* **2001**, 105 (1), 83-90.
29. McClain, R.; Malliakas, C. D.; Shen, J.; He, J.; Wolverton, C.; González, G. B.; Kanatzidis, M. G., Mechanistic insight of KBiQ₂ (Q= S, Se) using panoramic synthesis towards synthesis-by-design. *Chemical Science* **2020**.
30. Jiang, Z.; Ramanathan, A.; Shoemaker, D. P., In situ identification of kinetic factors that expedite inorganic crystal formation and discovery. *Journal of Materials Chemistry C* **2017**, 5 (23), 5709-5717.
31. Geselbracht, M. J.; Noailles, L. D.; Ngo, L. T.; Pikul, J. H.; Walton, R. I.; Cowell, E. S.; Millange, F.; O'Hare, D., Probing Molten Salt Flux Reactions Using Time-Resolved in Situ High-Temperature Powder X-ray Diffraction: A New Synthesis Route to the Mixed-Valence NaTi₂O₄. *Chemistry of Materials* **2004**, 16 (6), 1153-1159.
32. Shoemaker, D. P.; Hu, Y. J.; Chung, D. Y.; Halder, G. J.; Chupas, P. J.; Soderholm, L.;

- Mitchell, J. F.; Kanatzidis, M. G., In situ studies of a platform for metastable inorganic crystal growth and materials discovery. *Proc Natl Acad Sci U S A* **2014**, *111* (30), 10922-7.
33. Haynes, A. S.; Stoumpos, C. C.; Chen, H.; Chica, D.; Kanatzidis, M. G., Panoramic synthesis as an effective materials discovery tool: the system Cs/Sn/P/Se as a test case. *Journal of the American Chemical Society* **2017**, *139* (31), 10814-10821.
34. Walton, R. I.; O'Hare, D., Watching solids crystallise using powder diffraction. *Chemical Communications* **2000**, (23), 2283-2291.
35. Bhutani, A.; Schiller, J. A.; Zuo, J. L.; Eckstein, J. N.; Greene, L. H.; Chaudhuri, S.; Shoemaker, D. P., Combined Computational and in Situ Experimental Search for Phases in an Open Ternary system, Ba–Ru–S. *Chemistry of Materials* **2017**, *29* (14), 5841-5849.
36. Jiang, Z.; Sharma, J.; Okasinski, J. S.; Chen, H.; Shoemaker, D. P., In situ energy-dispersive X-ray diffraction of local phase dynamics during solvothermal growth of Cu₄O₃. *Journal of Applied Crystallography* **2021**, *54* (1).
37. Evans, J. S. O.; Francis, R. J.; O'Hare, D.; Price, S. J.; Clark, S. M.; Flaherty, J.; Gordon, J.; Nield, A.; Tang, C. C., An apparatus for the study of the kinetics and mechanism of hydrothermal reactions by in situ energy dispersive x-ray diffraction. *Review of Scientific Instruments* **1995**, *66* (3), 2442-2445.
38. Westgren, A., Rontgen Spectrographic Investigation of Iron and Steel. *Iron and Steel Inst.(British)* **1921**, *103*, 303.
39. Delapalme, A.; Raison, P.; Lander, G. H.; Rebizant, J.; Schweiss, P.; Kanellakopoulos, B., Studies of U(C₅H₅)₃Cl: II-Temperature dependence of the molecular configurations. *Zeitschrift für Kristallographie - Crystalline Materials* **1994**, *209* (9), 727-732.
40. Jensen, K. M. Ø.; Tyrsted, C.; Bremholm, M.; Iversen, B. B., In Situ Studies of Solvothermal Synthesis of Energy Materials. *ChemSusChem* **2014**, *7* (6), 1594-1611.
41. Chupas, P. J.; Chapman, K. W.; Kurtz, C.; Hanson, J. C.; Lee, P. L.; Grey, C. P., A versatile sample-environment cell for non-ambient X-ray scattering experiments. *Journal of Applied Crystallography* **2008**, *41* (4), 822-824.
42. Riello, P.; Lausi, A.; Macleod, J.; Plaisier, J. R.; Zeraushek, G.; Fornasiero, P., In situ reaction furnace for real-time XRD studies. *Journal of Synchrotron Radiation* **2013**, *20* (1), 194-196.
43. Misture, S. T., Large-volume atmosphere-controlled high-temperature x-ray diffraction furnace. *Measurement Science and Technology* **2003**, *14* (7), 1091-1098.
44. Lundgren, R. J.; Cranswick, L. M.; Bieringer, M., In situ X-ray powder diffraction, synthesis, and magnetic properties of InVO₃. *Journal of Solid State Chemistry* **2006**, *179* (12), 3599-3606.
45. Shafi, S. P.; Lundgren, R. J.; Cranswick, L. M. D.; Bieringer, M., Formation, structure and magnetism of the metastable defect fluorite phases AVO_{3.5+x} (A=In, Sc). *Journal of Solid State Chemistry* **2007**, *180* (12), 3333-3340.
46. Shafi, S. P.; Kotyk, M. W.; Cranswick, L. M. D.; Michaelis, V. K.; Kroeker, S.; Bieringer, M., In Situ Powder X-ray Diffraction, Synthesis, and Magnetic Properties of the Defect Zircon Structure ScVO_{4-x}. *Inorganic Chemistry* **2009**, *48* (22), 10553-10559.
47. Lundgren, R. J.; Cranswick, L. M. D.; Bieringer, M., Phase Stability, Structural Evolution and Magnetic Properties of Sc(1-x)LuxVO₃ (0.0 ≤ x ≤ 1.0). *Chemistry of Materials* **2007**, *19* (16), 3945-3955.

48. Gauthier, V.; Bernard, F.; Gaffet, E.; Josse, C.; Larpin, J. P., In-situ time resolved X-ray diffraction study of the formation of the nanocrystalline NbAl₃ phase by mechanically activated self-propagating high-temperature synthesis reaction. *Materials Science and Engineering: A* **1999**, *272* (2), 334-341.
49. Moorhouse, S. J.; Vranješ, N.; Jupe, A.; Drakopoulos, M.; O'Hare, D., The Oxford-Diamond In Situ Cell for studying chemical reactions using time-resolved X-ray diffraction. *Review of Scientific Instruments* **2012**, *83* (8), 084101.
50. Xia, F.; Brugger, J.; Qian, G.; Ngothai, Y.; O'Neill, B.; Zhao, J.; Pullen, S.; Olsen, S.; Pring, A., Single-pass flow-through reaction cell for high-temperature and high-pressure in situ neutron diffraction studies of hydrothermal crystallization processes. *Journal of Applied Crystallography* **2012**, *45* (2), 166-173.
51. Ok, K. M.; O'Hare, D.; Smith, R. I.; Chowdhury, M.; Fikremariam, H., New large volume hydrothermal reaction cell for studying chemical processes under supercritical hydrothermal conditions using time-resolved in situ neutron diffraction. *Review of Scientific Instruments* **2010**, *81* (12), 125107.
52. Walton, R. I.; Millange, F.; Smith, R. I.; Hansen, T. C.; O'Hare, D., Real Time Observation of the Hydrothermal Crystallization of Barium Titanate Using in Situ Neutron Powder Diffraction. *Journal of the American Chemical Society* **2001**, *123* (50), 12547-12555.
53. Norby, P., Hydrothermal Conversion of Zeolites: An in Situ Synchrotron X-ray Powder Diffraction Study. *Journal of the American Chemical Society* **1997**, *119* (22), 5215-5221.
54. Becker, J.; Bremholm, M.; Tyrsted, C.; Pauw, B.; Jensen, K. M. O.; Eltzholt, J.; Christensen, M.; Iversen, B. B., Experimental setup for in situ X-ray SAXS/WAXS/PDF studies of the formation and growth of nanoparticles in near- and supercritical fluids. *Journal of Applied Crystallography* **2010**, *43* (4), 729-736.
55. Gvozdetzkyi, V.; Owens-Baird, B.; Hong, S.; Cox, T.; Bhaskar, G.; Harmer, C.; Sun, Y.; Zhang, F.; Wang, C.-Z.; Ho, K.-M.; Zaikina, J. V., From NaZn₄Sb₃ to HT-Na_{1-x}Zn_{4-y}Sb₃: Panoramic Hydride Synthesis, Structural Diversity, and Thermoelectric Properties. *Chemistry of Materials* **2019**, *31* (21), 8695-8707.
56. Abeysinghe, D.; Huq, A.; Yeon, J.; Smith, M. D.; zur Loye, H.-C., In Situ Neutron Diffraction Studies of the Flux Crystal Growth of the Reduced Molybdates La₄Mo₂O₁₁ and Ce₄Mo₂O₁₁: Revealing Unexpected Mixed-Valent Transient Intermediates and Determining the Sequence of Events during Crystal Growth. *Chemistry of Materials* **2018**, *30* (3), 1187-1197.
57. Moorhouse, S. J.; Wu, Y.; Buckley, H. C.; O'Hare, D., Time-resolved in situ powder X-ray diffraction reveals the mechanisms of molten salt synthesis. *Chemical Communications* **2016**, *52* (96), 13865-13868.
58. McClain, R.; Malliakas, C. D.; Shen, J.; He, J.; Wolverton, C.; González, G. B.; Kanatzidis, M. G., Mechanistic insight of KBiQ₂ (Q = S, Se) using panoramic synthesis towards synthesis-by-design. *Chemical Science* **2021**, *12* (4), 1378-1391.
59. Sagawa, M.; Fujimura, S.; Togawa, N.; Yamamoto, H.; Matsuura, Y., New material for permanent magnets on a base of Nd and Fe (invited). *Journal of Applied Physics* **1984**, *55* (6), 2083-2087.
60. Schlesinger, T. E.; Toney, J. E.; Yoon, H.; Lee, E. Y.; Brunett, B. A.; Franks, L.; James, R. B., Cadmium zinc telluride and its use as a nuclear radiation detector material. *Materials Science and Engineering: R: Reports* **2001**, *32* (4), 103-189.

61. Bierlein, J. D.; Vanherzeele, H., Potassium titanil phosphate: properties and new applications. *J. Opt. Soc. Am. B* **1989**, *6* (4), 622-633.
62. Maruska, H. P.; Tietjen, J. J., The preparation and properties of vapor-deposited single-crystal-line GaN. *Applied Physics Letters* **1969**, *15* (10), 327-329.
63. Chung, I.; Kanatzidis, M. G., Metal Chalcogenides: A Rich Source of Nonlinear Optical Materials. *Chemistry of Materials* **2014**, *26* (1), 849-869.
64. Tran, T. T.; Yu, H.; Rondinelli, J. M.; Poeppelmeier, K. R.; Halasyamani, P. S., Deep Ultraviolet Nonlinear Optical Materials. *Chemistry of Materials* **2016**, *28* (15), 5238-5258.
65. Wu, M. K.; Ashburn, J. R.; Torng, C. J.; Hor, P. H.; Meng, R. L.; Gao, L.; Huang, Z. J.; Wang, Y. Q.; Chu, C. W., Superconductivity at 93 K in a new mixed-phase Y-Ba-Cu-O compound system at ambient pressure. *Physical Review Letters* **1987**, *58* (9), 908-910.
66. Kamihara, Y.; Watanabe, T.; Hirano, M.; Hosono, H., Iron-Based Layered Superconductor La[O_{1-x}F_x]FeAs (x = 0.05–0.12) with T_c = 26 K. *Journal of the American Chemical Society* **2008**, *130* (11), 3296-3297.
67. Mizushima, K.; Jones, P. C.; Wiseman, P. J.; Goodenough, J. B., Li_xCoO₂ (0 < x < 1): A new cathode material for batteries of high energy density. *Materials Research Bulletin* **1980**, *15* (6), 783-789.
68. Padhi, A. K.; Nanjundaswamy, K. S.; Goodenough, J. B., Phospho-olivines as positive-electrode materials for rechargeable lithium batteries. *Journal of the electrochemical society* **1997**, *144* (4), 1188-1194.
69. Zhao, L.-D.; Lo, S.-H.; Zhang, Y.; Sun, H.; Tan, G.; Uher, C.; Wolverton, C.; Dravid, V. P.; Kanatzidis, M. G., Ultralow thermal conductivity and high thermoelectric figure of merit in SnSe crystals. *Nature* **2014**, *508*, 373.
70. Ovshinsky, S. R., Reversible Electrical Switching Phenomena in Disordered Structures. *Physical Review Letters* **1968**, *21* (20), 1450-1453.
71. Soderholm, L.; Mitchell, J. F., Perspective: Toward “synthesis by design”: Exploring atomic correlations during inorganic materials synthesis. *APL Materials* **2016**, *4* (5).
72. Chamorro, J. R.; McQueen, T. M., Progress toward Solid State Synthesis by Design. *Accounts of chemical research* **2018**, *51* (11), 2918-2925.
73. Kohlmann, H., Looking into the Black Box of Solid-State Synthesis. *European Journal of Inorganic Chemistry* **2019**, *2019* (39-40), 4174-4180.
74. Chung, D.-Y.; Choi, K.-S.; Iordanidis, L.; Schindler, J. L.; Brazis, P. W.; Kannewurf, C. R.; Chen, B.; Hu, S.; Uher, C.; Kanatzidis, M. G., High Thermopower and Low Thermal Conductivity in Semiconducting Ternary K–Bi–Se Compounds. Synthesis and Properties of β-K₂Bi₈Se₁₃ and K_{2.5}Bi_{8.5}Se₁₄ and Their Sb Analogues. *Chemistry of Materials* **1997**, *9* (12), 3060-3071.
75. Haynes, A. S.; Stoumpos, C. C.; Chen, H.; Chica, D.; Kanatzidis, M. G., Panoramic Synthesis as an Effective Materials Discovery Tool: The System Cs/Sn/P/Se as a Test Case. *J Am Chem Soc* **2017**, *139* (31), 10814-10821.
76. Martinolich, A. J.; Kurzman, J. A.; Neilson, J. R., Circumventing Diffusion in Kinetically Controlled Solid-State Metathesis Reactions. *J Am Chem Soc* **2016**, *138* (34), 11031-7.
77. Jia, X.; Lynch, A.; Huang, Y.; Danielson, M.; Lang’at, I.; Milder, A.; Ruby, A. E.; Wang, H.; Friedler, S. A.; Norquist, A. J.; Schrier, J., Anthropogenic biases in chemical reaction data hinder exploratory inorganic synthesis. *Nature* **2019**, *573* (7773), 251-255.

78. Raccuglia, P.; Elbert, K. C.; Adler, P. D. F.; Falk, C.; Wenny, M. B.; Mollo, A.; Zeller, M.; Friedler, S. A.; Schrier, J.; Norquist, A. J., Machine-learning-assisted materials discovery using failed experiments. *Nature* **2016**, *533* (7601), 73-76.
79. Martinolich, A. J.; Neilson, J. R., Pyrite formation via kinetic intermediates through low-temperature solid-state metathesis. *J Am Chem Soc* **2014**, *136* (44), 15654-9.
80. Terry, A. E.; Vaughan, G. B. M.; Kvik, Å.; Walton, R. I.; Norquist, A. J.; O'Hare, D., In-Situ time-resolved X-ray diffraction: The current state of the art. *Synchrotron Radiation News* **2002**, *15* (4), 4-13.
81. Bhella, S. S.; Shafi, S. P.; Trobec, F.; Bieringer, M.; Thangadurai, V., In-Situ Powder X-ray Diffraction Investigation of Reaction Pathways for the BaCO₃-CeO₂-In₂O₃ and CeO₂-In₂O₃ Systems. *Inorganic Chemistry* **2010**, *49* (4), 1699-1704.
82. Lundgren, R. J.; Cranswick, L. M. D.; Bieringer, M., In situ X-ray powder diffraction, synthesis, and magnetic properties of InVO₃. *Journal of Solid State Chemistry* **2006**, *179* (12), 3599-3606.
83. Wiley, J. B.; Kaner, R. B., Rapid Solid-State Precursor Synthesis of Materials. *Science* **1992**, *255* (5048), 1093-1097.
84. Haynes, A. S.; Saouma, F. O.; Otieno, C. O.; Clark, D. J.; Shoemaker, D. P.; Jang, J. I.; Kanatzidis, M. G., Phase-Change Behavior and Nonlinear Optical Second and Third Harmonic Generation of the One-Dimensional K_(1-x)Cs_xPSe₆ and Metastable β-CsPSe₆. *Chemistry of Materials* **2015**, *27* (5), 1837-1846.
85. Friedrich, D.; Schlosser, M.; Näther, C.; Pfitzner, A., In Situ X-ray Diffraction Study of the Thermal Decomposition of Selenogallates Cs₂[Ga₂(Se₂)_{2-x}Se_{2+x}] (x = 0, 1, 2). *Inorganic Chemistry* **2018**, Article ASAP.
86. Kanatzidis, M. G., Structural Evolution and Phase Homologies for "Design" and Prediction of Solid-State Compounds. *Accounts of Chemical Research* **2005**, *38* (4), 359-368.
87. Mrotzek, A.; Kanatzidis, M. G., "Design" in Solid-State Chemistry Based on Phase Homologies. The Concept of Structural Evolution and the New Megaseries Am[M₁+lSe₂+l]2m[M₂l+nSe₂+3l+n]. *Accounts of Chemical Research* **2003**, *36* (2), 111-119.
88. Kanatzidis, M. G.; McCarthy, T. J.; Tanzer, T. A.; Chen, L.-H.; Iordanidis, L.; Hogan, T.; Kannewurf, C. R.; Uher, C.; Chen, B., Synthesis and Thermoelectric Properties of the New Ternary Bismuth Sulfides KBi_{6.33}S₁₀ and K₂Bi₈S₁₃. *Chemistry of Materials* **1996**, *8* (7), 1465-1474.
89. Iordanidis, L.; Brazis, P. W.; Kannewurf, C. R.; Kanatzidis, M. G., Synthesis and Thermoelectric Properties of Cs₂Bi_{7.33}Se₁₂, A₂BiSe₁₃ (A= Rb, Cs), Ba_{4-x}Bi_{6+ 2/3x}Se₁₃, and Ba_{3+x}Pb_{3+x}Bi₆Se₁₅. *MRS Online Proceedings Library Archive* **1998**, 545.
90. Chung, D.-Y.; Hogan, T.; Brazis, P.; Rocci-Lane, M.; Kannewurf, C.; Bastea, M.; Uher, C.; Kanatzidis, M. G., CsBi₄Te₆: A high-performance thermoelectric material for low-temperature applications. *Science* **2000**, *287* (5455), 1024-1027.
91. Chung, D.-Y.; Hogan, T. P.; Rocci-Lane, M.; Brazis, P.; Ireland, J. R.; Kannewurf, C. R.; Bastea, M.; Uher, C.; Kanatzidis, M. G., A new thermoelectric material: CsBi₄Te₆. *Journal of the American Chemical Society* **2004**, *126* (20), 6414-6428.
92. Bazakutsa, V.; Gnidash, N.; Pod'Yachaya, E.; Voinova, L.; Kravtsova, N., Properties of incompletely bonded ternary chalcogenide semiconductors. *Soviet Physics Journal* **1991**, *34* (11), 992-996.
93. Slade, T. J.; Bailey, T. P.; Grovogui, J. A.; Hua, X.; Zhang, X.; Kuo, J. J.; Hadar, I.; Snyder,

- G. J.; Wolverton, C.; Dravid, V. P.; Uher, C.; Kanatzidis, M. G., High Thermoelectric Performance in PbSe–NaSbSe₂ Alloys from Valence Band Convergence and Low Thermal Conductivity. *Advanced Energy Materials* **2019**, *9* (30), 1901377.
94. Slade, T. J.; Grovogui, J. A.; Hao, S.; Bailey, T. P.; Ma, R.; Hua, X.; Guéguen, A.; Uher, C.; Wolverton, C.; Dravid, V. P.; Kanatzidis, M. G., Absence of Nanostructuring in NaPbmSbTem+2: Solid Solutions with High Thermoelectric Performance in the Intermediate Temperature Regime. *Journal of the American Chemical Society* **2018**, *140* (22), 7021-7031.
95. Bera, T. K.; Jang, J. I.; Song, J.-H.; Malliakas, C. D.; Freeman, A. J.; Ketterson, J. B.; Kanatzidis, M. G., Soluble Semiconductors AAsSe₂ (A = Li, Na) with a Direct-Band-Gap and Strong Second Harmonic Generation: A Combined Experimental and Theoretical Study. *Journal of the American Chemical Society* **2010**, *132* (10), 3484-3495.
96. McCarthy, T. J.; Ngeyi, S. P.; Liao, J. H.; DeGroot, D. C.; Hogan, T.; Kannewurf, C. R.; Kanatzidis, M. G., Molten salt synthesis and properties of three new solid-state ternary bismuth chalcogenides, beta-CsBiS₂, gamma-CsBiS₂, and K₂Bi₈Se₁₃. *Chemistry of Materials* **1993**, *5* (3), 331-340.
97. Boon, J. W., The crystal structure of NaBiS₂ and KBiS₂. *Recueil des Travaux Chimiques des Pays-Bas* **1944**, *63* (2), 32-34.
98. Gattow, G.; Zemann, J., Beitrag zur Kristallchemie komplexer Wismutchalkogenverbindungen. *Zeitschrift für anorganische und allgemeine Chemie* **1955**, *279* (5-6), 324-327.
99. Olivier-Fourcade, J.; Philippot, E.; Maurin, M., Structure des composés NaSbS_{2α} et NaSbS_{2β}. Etude de l'influence de la paire électronique E de l'antimoine III dans la transition NaSbS_{2α} → NaSbS_{2β}. *Zeitschrift für anorganische und allgemeine Chemie* **1978**, *446* (1), 159-168.
100. Saal, J. E.; Kirklín, S.; Aykol, M.; Meredig, B.; Wolverton, C., Materials design and discovery with high-throughput density functional theory: the open quantum materials database (OQMD). *Jom* **2013**, *65* (11), 1501-1509.
101. Peng, Y.; Sun, Q.; Chen, H.; Yin, W.-J., Disparity of the Nature of the Band Gap between Halide and Chalcogenide Single Perovskites for Solar Cell Absorbers. *The Journal of Physical Chemistry Letters* **2019**, *10* (16), 4566-4570.
102. Sun, J.-P.; McKeown Wessler, G. C.; Wang, T.; Zhu, T.; Blum, V.; Mitzi, D. B., Structural Tolerance Factor Approach to Defect-Resistant I2-II-IV-X4 Semiconductor Design. *Chemistry of Materials* **2020**, *32* (4), 1636-1649.
103. Fabry, J.; Havlak, L.; Dusek, M.; Vanek, P.; Drahokoupil, J.; Jurek, K., Structure determination of KLaS₂, KPrS₂, KEuS₂, KGdS₂, KLuS₂, KYS₂, RbYS₂, NaLaS₂ and crystal-chemical analysis of the group 1 and thallium(I) rare-earth sulfide series. *Acta Crystallographica Section B* **2014**, *70* (2), 360-371.
104. Momma, K.; Izumi, F., VESTA: a three-dimensional visualization system for electronic and structural analysis. *Journal of Applied Crystallography* **2008**, *41* (3), 653-658.
105. Toby, B. H.; Von Dreele, R. B., GSAS-II: the genesis of a modern open-source all purpose crystallography software package. *Journal of Applied Crystallography* **2013**, *46* (2), 544-549.
106. Juhas, P.; Davis, T.; Farrow, C. L.; Billinge, S. J. L., PDFgetX3: a rapid and highly automatable program for processing powder diffraction data into total scattering pair distribution functions. *Journal of Applied Crystallography* **2013**, *46* (2), 560-566.

107. Farrow, C. L.; Juhas, P.; Liu, J. W.; Bryndin, D.; Božin, E. S.; Bloch, J.; Proffen, T.; Billinge, S. J. L., PDFfit2 and PDFgui: computer programs for studying nanostructure in crystals. *Journal of Physics: Condensed Matter* **2007**, *19* (33), 335219.
108. Aroyo, M. I.; Perez-Mato, J. M.; Orobengoa, D.; Tasci, E.; de la Flor, G.; Kirov, A., Crystallography online: Bilbao Crystallographic Server. *Bulgarian Chemical Communications* **2011**, *43* (2), 183-197.
109. Aroyo, M. I.; Kirov, A.; Capillas, C.; Perez-Mato, J. M.; Wondratschek, H., Bilbao Crystallographic Server. II. Representations of crystallographic point groups and space groups. *Acta Crystallographica Section A* **2006**, *62* (2), 115-128.
110. Aroyo, M. I.; Perez-Mato, J. M.; Capillas, C.; Kroumova, E.; Ivantchev, S.; Madariaga, G.; Kirov, A.; Wondratschek, H., Bilbao Crystallographic Server: I. Databases and crystallographic computing programs. *Zeitschrift für Kristallographie - Crystalline Materials* **2006**, *221* (1), 15.
111. Blöchl, P. E., Projector augmented-wave method. *Physical review B* **1994**, *50* (24), 17953.
112. Kresse, G.; Joubert, D., From ultrasoft pseudopotentials to the projector augmented-wave method. *Physical Review B* **1999**, *59* (3), 1758.
113. Kresse, G.; Furthmüller, J., Efficient iterative schemes for ab initio total-energy calculations using a plane-wave basis set. *Physical review B* **1996**, *54* (16), 11169.
114. Kresse, G.; Furthmüller, J., Efficiency of ab-initio total energy calculations for metals and semiconductors using a plane-wave basis set. *Computational materials science* **1996**, *6* (1), 15-50.
115. Perdew, J. P.; Burke, K.; Ernzerhof, M., Generalized gradient approximation made simple. *Physical review letters* **1996**, *77* (18), 3865.
116. Kirklin, S.; Saal, J. E.; Meredig, B.; Thompson, A.; Doak, J. W.; Aykol, M.; Rühl, S.; Wolverton, C., The Open Quantum Materials Database (OQMD): assessing the accuracy of DFT formation energies. *npj Computational Materials* **2015**, *1*, 15010.
117. Zunger, A.; Wei, S. H.; Ferreira, L. G.; Bernard, J. E., Special quasirandom structures. *Physical Review Letters* **1990**, *65* (3), 353-356.
118. Van de Walle, A.; Tiwary, P.; De Jong, M.; Olmsted, D.; Asta, M.; Dick, A.; Shin, D.; Wang, Y.; Chen, L.-Q.; Liu, Z.-K., Efficient stochastic generation of special quasirandom structures. *Calphad* **2013**, *42*, 13-18.
119. van de Walle, A., Multicomponent multisublattice alloys, nonconfigurational entropy and other additions to the Alloy Theoretic Automated Toolkit. *Calphad* **2009**, *33* (2), 266-278.
120. Medeiros, P. V. C.; Stafström, S.; Björk, J., Effects of extrinsic and intrinsic perturbations on the electronic structure of graphene: Retaining an effective primitive cell band structure by band unfolding. *Physical Review B* **2014**, *89* (4), 041407.
121. Medeiros, P. V. C.; Tsirkin, S. S.; Stafström, S.; Björk, J., Unfolding spinor wave functions and expectation values of general operators: Introducing the unfolding-density operator. *Physical Review B* **2015**, *91* (4), 041116.
122. Glemser, O.; Filcek, M., Über Alkalithioarismutate(III). *Zeitschrift für anorganische und allgemeine Chemie* **1955**, *279* (5-6), 321-323.
123. Chen, B.; Uher, C.; Iordanidis, L.; Kanatzidis, M. G., Transport Properties of Bi₂S₃ and the Ternary Bismuth Sulfides KBi_{6.33}S₁₀ and K₂Bi₈S₁₃. *Chemistry of Materials* **1997**, *9* (7), 1655-1658.
124. Brandt, R. E.; Stevanović, V.; Ginley, D. S.; Buonassisi, T., Identifying defect-tolerant semiconductors with high minority-carrier lifetimes: beyond hybrid lead halide perovskites. *MRS Communications* **2015**, *5* (2), 265-275.

125. Pompe, C.; Pfitzner, A., Na₃SbS₃: Single Crystal X-ray Diffraction, Raman Spectroscopy, and Impedance Measurements. *Zeitschrift für anorganische und allgemeine Chemie* **2013**, *639* (2), 296-300.
126. West, C., The Crystal Structures of Some Alkali Hydrosulfides and Monosulfides. *Zeitschrift für Kristallographie-Crystalline Materials* **1934**, *88* (1-6), 97-115.
127. Gabrel'yan, B.; Lavrentiev, A.; Nikiforov, I. Y.; Sobolev, V., Electronic energy structure of MBiS₂ (M= Li, Na, K) calculated with allowance for the difference between the MS and Bi-S bond lengths. *Journal of Structural Chemistry* **2008**, *49* (5), 788-794.
128. VOROSHILOV, Y. V.; PERESH, E. Y.; GOLOVEI, M. I., Kristallstruktur Der Verbindungen RbBiS₂ und RbBiSe₂. *Chemischer Informationsdienst* **1972**, *3* (28).
129. Mather, G. C.; Dussarrat, C.; Etourneau, J.; West, A. R., A review of cation-ordered rock salt superstructure oxides. *Journal of Materials Chemistry* **2000**, *10* (10), 2219-2230.
130. Bianchini, M.; Wang, J.; Clément, R. J.; Ouyang, B.; Xiao, P.; Kitchaev, D.; Shi, T.; Zhang, Y.; Wang, Y.; Kim, H.; Zhang, M.; Bai, J.; Wang, F.; Sun, W.; Ceder, G., The interplay between thermodynamics and kinetics in the solid-state synthesis of layered oxides. *Nature Materials* **2020**.
131. West, A. R., *Solid State Chemistry and its Applications*. 2nd ed.; Wiley: 2014; p 401-403.
132. Rathore, E.; Juneja, R.; Culver, S. P.; Minafra, N.; Singh, A. K.; Zeier, W. G.; Biswas, K., Origin of Ultralow Thermal Conductivity in n-Type Cubic Bulk AgBiS₂: Soft Ag Vibrations and Local Structural Distortion Induced by the Bi 6s² Lone Pair. *Chemistry of Materials* **2019**, *31* (6), 2106-2113.
133. Fabini, D. H.; Laurita, G.; Bechtel, J. S.; Stoumpos, C. C.; Evans, H. A.; Kontos, A. G.; Raptis, Y. S.; Falaras, P.; Van der Ven, A.; Kanatzidis, M. G.; Seshadri, R., Dynamic Stereochemical Activity of the Sn²⁺ Lone Pair in Perovskite CsSnBr₃. *Journal of the American Chemical Society* **2016**, *138* (36), 11820-11832.
134. Laurita, G.; Fabini, D. H.; Stoumpos, C. C.; Kanatzidis, M. G.; Seshadri, R., Chemical tuning of dynamic cation off-centering in the cubic phases of hybrid tin and lead halide perovskites. *Chemical Science* **2017**, *8* (8), 5628-5635.
135. Božin, E. S.; Malliakas, C. D.; Souvatzis, P.; Proffen, T.; Spaldin, N. A.; Kanatzidis, M. G.; Billinge, S. J. L., Entropically Stabilized Local Dipole Formation in Lead Chalcogenides. *Science* **2010**, *330* (6011), 1660.
136. Knox, K. R.; Bozin, E. S.; Malliakas, C. D.; Kanatzidis, M. G.; Billinge, S. J. L., Local off-centering symmetry breaking in the high-temperature regime of SnTe. *Physical Review B* **2014**, *89* (1), 014102.
137. Walsh, A.; Payne, D. J.; Egdell, R. G.; Watson, G. W., Stereochemistry of post-transition metal oxides: revision of the classical lone pair model. *Chemical Society Reviews* **2011**, *40* (9), 4455-4463.
138. Androulakis, J.; Peter, S. C.; Li, H.; Malliakas, C. D.; Peters, J. A.; Liu, Z.; Wessels, B. W.; Song, J.-H.; Jin, H.; Freeman, A. J.; Kanatzidis, M. G., Dimensional Reduction: A Design Tool for New Radiation Detection Materials. *Advanced Materials* **2011**, *23* (36), 4163-4167.
139. Rumble, J. R., CRC Handbook of Chemistry and Physics. 99th ed.; CRC Press/Taylor & Francis: Boca Raton, FL, 2018; p Electron Work Function Of The Elements.
140. Bludau, W.; Onton, A.; Heinke, W., Temperature dependence of the band gap of silicon. *Journal of Applied Physics* **1974**, *45* (4), 1846-1848.
141. Fonthal, G.; Tirado-Mejía, L.; Marín-Hurtado, J. I.; Ariza-Calderón, H.; Mendoza-Alvarez,

- J. G., Temperature dependence of the band gap energy of crystalline CdTe. *Journal of Physics and Chemistry of Solids* **2000**, *61* (4), 579-583.
142. Spanopoulos, I.; Hadar, I.; Ke, W.; Tu, Q.; Chen, M.; Tsai, H.; He, Y.; Shekhawat, G.; Dravid, V. P.; Wasielewski, M. R.; Mohite, A. D.; Stoumpos, C. C.; Kanatzidis, M. G., Uniaxial Expansion of the 2D Ruddlesden–Popper Perovskite Family for Improved Environmental Stability. *Journal of the American Chemical Society* **2019**, *141* (13), 5518-5534.
143. Stevanović, V.; Lany, S.; Ginley, D. S.; Tumas, W.; Zunger, A., Assessing capability of semiconductors to split water using ionization potentials and electron affinities only. *Physical Chemistry Chemical Physics* **2014**, *16* (8), 3706-3714.
144. Tang, H.; Berger, H.; Schmid, P. E.; Lévy, F.; Burri, G., Photoluminescence in TiO₂ anatase single crystals. *Solid State Communications* **1993**, *87* (9), 847-850.
145. Kanatzidis, M. G., Counterion Size Versus Structure in Metal-Chalcogenide Salts. *Phosphorus, Sulfur, and Silicon and the Related Elements* **1994**, *93* (1-4), 159-172.
146. Kim, K.-W.; Kanatzidis, M. G., Counterion Effects in Pd Polyselenides: Evolution from Molecular to Three-Dimensional Framework Structures. *Journal of the American Chemical Society* **1998**, *120* (32), 8124-8135.
147. Lu, Y.-J.; Ibers, J. A., Alkali-Metal Substitution into Solid-State Chalcogenides: Effects on Dimensionality. *Comments on Inorganic Chemistry* **1993**, *14* (4), 229-243.
148. Tulsy, E. G.; Long, J. R., Dimensional Reduction: A Practical Formalism for Manipulating Solid Structures. *Chemistry of Materials* **2001**, *13* (4), 1149-1166.
149. Trippel, A. F.; Lazarev, V. B.; Berul, S. I., Synthesis and properties of some compounds ABiTe₂. *Zhurnal Neorganicheskoy Khimii* **1978**, *23* (3), 707-710.
150. Eisenmann, B.; Schäfer, H., Über Seleno- und Telluroarsenite, -antimonite und -bismutite. *Zeitschrift für anorganische und allgemeine Chemie* **1979**, *456* (1), 87-94.
151. Shannon, R. D., Revised effective ionic radii and systematic studies of interatomic distances in halides and chalcogenides. *Acta crystallographica section A: crystal physics, diffraction, theoretical and general crystallography* **1976**, *32* (5), 751-767.
152. Bugaris, D. E.; Wells, D. M.; Yao, J.; Skanthakumar, S.; Haire, R. G.; Soderholm, L.; Ibers, J. A., Dichalcogenide Bonding in Seven Alkali-Metal Actinide Chalcogenides of the KTh₂Se₆ Structure Type. *Inorganic chemistry* **2010**, *49* (18), 8381-8388.
153. Cenoz, K.; Gelato, L. M.; Penzo, M.; Parthe, E., Inorganic structure types with revised space groups. I. *Acta Crystallographica Section B* **1991**, *47* (4), 433-439.
154. Graf, H. A.; Schäfer, H., Darstellung und Kristallstruktur von KSbS₂. *Zeitschrift für anorganische und allgemeine Chemie* **1975**, *414* (3), 211-219.
155. Kageyama, H.; Hayashi, K.; Maeda, K.; Atfield, J. P.; Hiroi, Z.; Rondinelli, J. M.; Poeppelmeier, K. R., Expanding frontiers in materials chemistry and physics with multiple anions. *Nature Communications* **2018**, *9* (1), 772.
156. Kubo, A.; Giorgi, G.; Yamashita, K., Anion Ordering in CaTaO₂N: Structural Impact on the Photocatalytic Activity. Insights from First-Principles. *Chemistry of Materials* **2017**, *29* (2), 539-545.
157. Besara, T.; Ramirez, D.; Sun, J.; Whalen, J. B.; Tokumoto, T. D.; McGill, S. A.; Singh, D. J.; Siegrist, T., Ba₂TeO: A new layered oxytelluride. *Journal of Solid State Chemistry* **2015**, *222*, 60-65.
158. Kato, D.; Hongo, K.; Maezono, R.; Higashi, M.; Kunioku, H.; Yabuuchi, M.; Suzuki, H.;

- Okajima, H.; Zhong, C.; Nakano, K.; Abe, R.; Kageyama, H., Valence Band Engineering of Layered Bismuth Oxyhalides toward Stable Visible-Light Water Splitting: Madelung Site Potential Analysis. *Journal of the American Chemical Society* **2017**, *139* (51), 18725-18731.
159. Guittard, M.; Benazeth, S.; Dugue', J.; Jaulmes, S.; Palazzi, M.; Laruelle, P.; Flahaut, J., Oxysulfides and oxyselenides in sheets, formed by a rare earth element and a second metal. *Journal of Solid State Chemistry* **1984**, *51* (2), 227-238.
160. Clarke, S. J.; Adamson, P.; Herkelrath, S. J. C.; Rutt, O. J.; Parker, D. R.; Pitcher, M. J.; Smura, C. F., Structures, Physical Properties, and Chemistry of Layered Oxychalcogenides and Oxypnictides. *Inorganic Chemistry* **2008**, *47* (19), 8473-8486.
161. Harada, J. K.; Charles, N.; Poepelmeier, K. R.; Rondinelli, J. M., Heteroanionic Materials by Design: Progress Toward Targeted Properties. *Advanced Materials* **2019**, *31* (19), 1805295.
162. Poettgen, R.; Johrendt, D., Materials with ZrCuSiAs-type structure. *Zeitschrift für Naturforschung B* **2008**, *63* (10), 1135-1148.
163. Hiramatsu, H.; Kamioka, H.; Ueda, K.; Ohta, H.; Kamiya, T.; Hirano, M.; Hosono, H., Opto-electronic properties and light-emitting device application of widegap layered oxychalcogenides: LaCuOCh (Ch = chalcogen) and La₂CdO₂Se₂. *physica status solidi (a)* **2006**, *203* (11), 2800-2811.
164. Luu, S. D. N.; Vaqueiro, P., Layered oxychalcogenides: Structural chemistry and thermoelectric properties. *Journal of Materiomics* **2016**, *2* (2), 131-140.
165. Kusainova, A. M.; Berdonosov, P. S.; Akselrud, L. G.; Kholodkovskaya, L. N.; Dolgikh, V. A.; Popovkin, B. A., New Layered Compounds with the General Composition (MO) (CuSe), Where M = Bi, Nd, Gd, Dy, and BiOCuS: Syntheses and Crystal Structure. *Journal of Solid State Chemistry* **1994**, *112* (1), 189-191.
166. Berdonosov, P. S.; Kusainova, A. M.; Kholodkovskaya, L. N.; Dolgikh, V. A.; Akselrud, L. G.; Popovkin, B. A., Powder X-Ray and IR Studies of the New Oxyselenides MOCuSe (M = Bi, Gd, Dy). *Journal of Solid State Chemistry* **1995**, *118* (1), 74-77.
167. Hiramatsu, H.; Yanagi, H.; Kamiya, T.; Ueda, K.; Hirano, M.; Hosono, H., Crystal Structures, Optoelectronic Properties, and Electronic Structures of Layered Oxychalcogenides MCuOCh (M = Bi, La; Ch = S, Se, Te): Effects of Electronic Configurations of M³⁺ Ions. *Chemistry of Materials* **2008**, *20* (1), 326-334.
168. Zhao, L. D.; Berardan, D.; Pei, Y. L.; Byl, C.; Pinsard-Gaudart, L.; Dragoe, N., Bi_{1-x}Sr_xCuSeO oxyselenides as promising thermoelectric materials. *Applied Physics Letters* **2010**, *97* (9), 092118.
169. Zhao, L.-D.; He, J.; Berardan, D.; Lin, Y.; Li, J.-F.; Nan, C.-W.; Dragoe, N., BiCuSeO oxyselenides: new promising thermoelectric materials. *Energy & Environmental Science* **2014**, *7* (9), 2900-2924.
170. Zhou, Y.; Zhao, L.-D., Promising Thermoelectric Bulk Materials with 2D Structures. *Advanced Materials* **2017**, *29* (45), 1702676.
171. Zhang, X.; Chang, C.; Zhou, Y.; Zhao, L.-D., BiCuSeO Thermoelectrics: An Update on Recent Progress and Perspective. *Materials* **2017**, *10* (2), 198.
172. Stampler, E. S.; Sheets, W. C.; Bertoni, M. I.; Prellier, W.; Mason, T. O.; Poepelmeier, K. R., Temperature Driven Reactant Solubilization Synthesis of BiCuOSe. *Inorganic Chemistry* **2008**, *47* (21), 10009-10016.
173. Chen, H.; McClain, R.; He, J.; Zhang, C.; Olding, J. N.; dos Reis, R.; Bao, J.-K.; Hadar, I.;

- Spanopoulos, I.; Malliakas, C. D.; He, Y.; Chung, D. Y.; Kwok, W.-K.; Weiss, E. A.; Dravid, V. P.; Wolverton, C.; Kanatzidis, M. G., Antiferromagnetic Semiconductor BaFMn_{0.5}Te with Unique Mn Ordering and Red Photoluminescence. *Journal of the American Chemical Society* **2019**, *141* (43), 17421-17430.
174. Charles, N.; Saballos, R. J.; Rondinelli, J. M., Structural Diversity from Anion Order in Heteroanionic Materials. *Chemistry of Materials* **2018**, *30* (10), 3528-3537.
175. Attfield, J. P., Principles and Applications of Anion Order in Solid Oxynitrides. *Crystal Growth & Design* **2013**, *13* (10), 4623-4629.
176. Bianchini, M.; Wang, J.; Clément, R. J.; Ouyang, B.; Xiao, P.; Kitchaev, D.; Shi, T.; Zhang, Y.; Wang, Y.; Kim, H.; Zhang, M.; Bai, J.; Wang, F.; Sun, W.; Ceder, G., The interplay between thermodynamics and kinetics in the solid-state synthesis of layered oxides. *Nature Materials* **2020**, *19* (10), 1088-1095.
177. He, T.; Sun, W.; Huo, H.; Kononova, O.; Rong, Z.; Tshitoyan, V.; Botari, T.; Ceder, G., Similarity of precursors in solid-state synthesis as text-mined from scientific literature. *Chemistry of Materials* **2020**, *32* (18), 7861-7873.
178. Kononova, O.; Huo, H.; He, T.; Rong, Z.; Botari, T.; Sun, W.; Tshitoyan, V.; Ceder, G., Text-mined dataset of inorganic materials synthesis recipes. *Scientific Data* **2019**, *6* (1), 203.
179. Barber, C. B.; Dobkin, D. P.; Huhdanpaa, H., The quickhull algorithm for convex hulls. *ACM Transactions on Mathematical Software (TOMS)* **1996**, *22* (4), 469-483.
180. R. Akbarzadeh, A.; Ozoliņš, V.; Wolverton, C., First-principles determination of multicomponent hydride phase diagrams: application to the Li-Mg-N-H system. *Advanced Materials* **2007**, *19* (20), 3233-3239.
181. Togo, A.; Tanaka, I., First principles phonon calculations in materials science. *Scripta Materialia* **2015**, *108*, 1-5.
182. Li, Z.; Xiao, C.; Fan, S.; Deng, Y.; Zhang, W.; Ye, B.; Xie, Y., Dual Vacancies: An Effective Strategy Realizing Synergistic Optimization of Thermoelectric Property in BiCuSeO. *Journal of the American Chemical Society* **2015**, *137* (20), 6587-6593.
183. Liu, Y.; Zhao, L.-D.; Zhu, Y.; Liu, Y.; Li, F.; Yu, M.; Liu, D.-B.; Xu, W.; Lin, Y.-H.; Nan, C.-W., Synergistically Optimizing Electrical and Thermal Transport Properties of BiCuSeO via a Dual-Doping Approach. *Advanced Energy Materials* **2016**, *6* (9), 1502423.
184. Yang, D.; Su, X.; Yan, Y.; Hu, T.; Xie, H.; He, J.; Uher, C.; Kanatzidis, M. G.; Tang, X., Manipulating the Combustion Wave during Self-Propagating Synthesis for High Thermoelectric Performance of Layered Oxychalcogenide Bi_{1-x}Pb_xCuSeO. *Chemistry of Materials* **2016**, *28* (13), 4628-4640.
185. Ren, G.-K.; Wang, S.; Zhou, Z.; Li, X.; Yang, J.; Zhang, W.; Lin, Y.-H.; Yang, J.; Nan, C.-W., Complex electronic structure and compositing effect in high performance thermoelectric BiCuSeO. *Nature Communications* **2019**, *10* (1), 2814.
186. Richard, A. P.; Russell, J. A.; Zakutayev, A.; Zakharov, L. N.; Keszler, D. A.; Tate, J., Synthesis, structure, and optical properties of BiCuOCh (Ch=S, Se, and Te). *Journal of Solid State Chemistry* **2012**, *187*, 15-19.
187. Gulay, L.; Daszkiewicz, M.; Strok, O.; Pietraszko, A., Crystal structure of Cu₂Se. *Chemistry of metals and alloys* **2011**, (4, № 3-4), 200-205.
188. Oliveria, M.; McMullan, R. K.; Wuensch, B. J., Single crystal neutron diffraction analysis of the cation distribution in the high-temperature phases α -Cu_{2-x}S, α -Cu_{2-x}Se, and α -Ag₂Se.

Solid State Ionics **1988**, 28-30, 1332-1337.

189. Brown, D. R.; Day, T.; Borup, K. A.; Christensen, S.; Iversen, B. B.; Snyder, G. J., Phase transition enhanced thermoelectric figure-of-merit in copper chalcogenides. *APL Materials* **2013**, 1 (5), 052107.
190. Berry, L., The crystal structure of covellite, cuse and klockmannite, cuse. *American Mineralogist: Journal of Earth and Planetary Materials* **1954**, 39 (5-6), 504-509.
191. Azuma, M.; Chen, W.-t.; Seki, H.; Czapski, M.; Olga, S.; Oka, K.; Mizumaki, M.; Watanuki, T.; Ishimatsu, N.; Kawamura, N.; Ishiwata, S.; Tucker, M. G.; Shimakawa, Y.; Atfield, J. P., Colossal negative thermal expansion in BiNiO₃ induced by intermetallic charge transfer. *Nature Communications* **2011**, 2 (1), 347.
192. Mary, T.; Evans, J.; Vogt, T.; Sleight, A., Negative thermal expansion from 0.3 to 1050 Kelvin in ZrW₂O₈. *Science* **1996**, 272 (5258), 90-92.
193. Lightfoot, P.; Woodcock, D. A.; Maple, M. J.; Villaescusa, L. A.; Wright, P. A., The widespread occurrence of negative thermal expansion in zeolites. *Journal of Materials Chemistry* **2001**, 11 (1), 212-216.
194. P. Atfield, M., Strong negative thermal expansion in siliceous faujasite. *Chemical Communications* **1998**, (5), 601-602.
195. Takenaka, K.; Takagi, H., Giant negative thermal expansion in Ge-doped anti-perovskite manganese nitrides. *Applied Physics Letters* **2005**, 87 (26), 261902.
196. Ablitt, C.; Mostofi, A. A.; Bristowe, N. C.; Senn, M. S., Control of Uniaxial Negative Thermal Expansion in Layered Perovskites by Tuning Layer Thickness. *Frontiers in Chemistry* **2018**, 6 (455).
197. Ge, X.-J.; Yao, K.-L.; Lü, J.-T., Comparative study of phonon spectrum and thermal expansion of graphene, silicene, germanene, and blue phosphorene. *Physical Review B* **2016**, 94 (16), 165433.
198. Huang, L.-F.; Gong, P.-L.; Zeng, Z., Phonon properties, thermal expansion, and thermomechanics of silicene and germanene. *Physical Review B* **2015**, 91 (20), 205433.
199. Hemberger, J.; von Nidda, H. A. K.; Tsurkan, V.; Loidl, A., Large Magnetostriction and Negative Thermal Expansion in the Frustrated Antiferromagnet ZnCr_2Se_4 . *Physical Review Letters* **2007**, 98 (14), 147203.
200. Tsurkan, V.; Ehlers, D.; Felea, V.; Krug von Nidda, H. A.; Loidl, A., Critical magnetic behavior of ferromagnetic CdCr_2S_4 . *Physical Review B* **2013**, 88 (14), 144417.
201. Chen, J.; Hu, L.; Deng, J.; Xing, X., Negative thermal expansion in functional materials: controllable thermal expansion by chemical modifications. *Chemical Society Reviews* **2015**, 44 (11), 3522-3567.
202. Sillén, L. G., Die Kristallstruktur des monoklinen α -Bi₂O₃. *Naturwissenschaften* **1940**, 28 (13), 206-207.
203. Todd, P. K.; Wustrow, A.; McAuliffe, R. D.; McDermott, M. J.; Tran, G. T.; McBride, B. C.; Boeding, E. D.; O'Nolan, D.; Liu, C.-H.; Dwaraknath, S. S.; Chapman, K. W.; Billinge, S. J. L.; Persson, K. A.; Huq, A.; Veith, G. M.; Neilson, J. R., Defect-Accommodating Intermediates Yield Selective Low-Temperature Synthesis of YMnO₃ Polymorphs. *Inorganic Chemistry* **2020**, 59 (18), 13639-13650.
204. Li, Y.-Y.; Wang, W.-J.; Wang, H.; Lin, H.; Wu, L.-M., Mixed-Anion Inorganic Compounds: A Favorable Candidate for Infrared Nonlinear Optical Materials. *Crystal Growth &*

Design **2019**, *19* (7), 4172-4192.

205. Valldor, M., Anion Ordering in Bichalcogenides. *Inorganics* **2016**, *4* (3), 23.
206. Kanatzidis, M. G., Molten alkali-metal polychalcogenides as reagents and solvents for the synthesis of new chalcogenide materials. *Chemistry of Materials* **1990**, *2* (4), 353-363.
207. Kanatzidis, M. G.; Huang, S.-P., Coordination chemistry of heavy polychalcogenide ligands. *Coordination Chemistry Reviews* **1994**, *130* (1), 509-621.
208. Smith, D. M.; Ibers, J. A., Syntheses and solid-state structural chemistry of polytelluride anions. *Coordination Chemistry Reviews* **2000**, *200-202*, 187-205.
209. Sheldrick, W. S., Polychalcogenide Anions: Structural Diversity and Ligand Versatility. *Zeitschrift für anorganische und allgemeine Chemie* **2012**, *638* (15), 2401-2424.
210. Furuseth, S.; Brattas, L.; Kjekshus, A., Crystal Structure of HfTe₅. *Acta Chemica Scandinavica* **1973**, *27* (7), 2367-2374.
211. Lowhorn, N. D.; Tritt, T. M.; Abbott, E. E.; Kolis, J. W., Enhancement of the power factor of the transition metal pentatelluride HfTe₅ by rare-earth doping. *Applied Physics Letters* **2006**, *88* (2), 022101.
212. Miller, S. A.; Witting, I.; Aydemir, U.; Peng, L.; Rettie, A. J. E.; Gorai, P.; Chung, D. Y.; Kanatzidis, M. G.; Grayson, M.; Stevanović, V.; Toberer, E. S.; Snyder, G. J., Polycrystalline ZrTe₅ Parametrized as a Narrow-Band-Gap Semiconductor for Thermoelectric Performance. *Physical Review Applied* **2018**, *9* (1), 014025.
213. Chen, X.; Huang, X.; Li, J., Rb₄Hg₅(Te₂)₂(Te₃)₂Te₃, [Zn(en)₃]₄In₁₆(Te₂)₄(Te₃)Te₂₂, and K₂Cu₂(Te₂)(Te₃): Novel Metal Polytellurides with Unusual Metal–Tellurium Coordination. *Inorganic Chemistry* **2001**, *40* (6), 1341-1346.
214. Böttcher, P., Tellurium-Rich Tellurides. *Angewandte Chemie International Edition in English* **1988**, *27* (6), 759-772.
215. Canadell, E.; Jovic, S.; Brec, R.; Rouxel, J., Electronic structure and properties of anionic mixed valence and layered CrTe₃: The question of extended tellurium bonding in transition metal tellurides. *Journal of Solid State Chemistry* **1992**, *98* (1), 59-70.
216. Mar, A.; Ibers, J. A., The layered ternary germanium tellurides ZrGeTe₄, HfGeTe₄, and TiGeTe₆: structure, bonding, and physical properties. *Journal of the American Chemical Society* **1993**, *115* (8), 3227-3238.
217. Fenske, D.; Baum, G.; Wolkers, H.; Schreiner, B.; Weller, F.; Dehnicke, K., Die Kristallstrukturen der Polytelluride [Ca(DMF)₆]₂Te₄, [Sr(15-Krone-5)₂]₂Te₄ · H₂O, {[BaCl(18-Krone-6)(DMF)₂]₂[BaCl(18-Krone-6)(DMF)(H₂O)]₂(Te₄)₂} und [Ph₃PNPPh₃]₂Te₅ · 2 DMF. *Zeitschrift für anorganische und allgemeine Chemie* **1993**, *619* (3), 489-499.
218. Huang, F. Q.; Ibers, J. A., Syntheses, Structures, and Theoretical Study of LaCuSTe and SmCuSTe. *Inorganic Chemistry* **1999**, *38* (26), 5978-5983.
219. Maier, S.; Ohno, S.; Yu, G.; Kang, S. D.; Chasapis, T. C.; Ha, V. A.; Miller, S. A.; Berthebaud, D.; Kanatzidis, M. G.; Rignanese, G. M.; Hautier, G.; Snyder, G. J.; Gascoin, F., Resonant Bonding, Multiband Thermoelectric Transport, and Native Defects in n-Type BaBiTe_{3-x}Sex (x = 0, 0.05, and 0.1). *Chemistry of Materials* **2018**, *30* (1), 174-184.
220. Chung, D.-Y.; Jovic, S.; Hogan, T.; Kannewurf, C. R.; Brec, R.; Rouxel, J.; Kanatzidis, M. G., Oligomerization Versus Polymerization of Tex_n- in the Polytelluride Compound BaBiTe₃. Structural Characterization, Electronic Structure, and Thermoelectric Properties. *Journal of the American Chemical Society* **1997**, *119* (10), 2505-2515.

221. Zhang, Q.; Malliakas, C. D.; Kanatzidis, M. G., {[Ga(en)₃]₂(Ge₂Te₁₅)_n}: A Polymeric Semiconducting Polytelluride with Boat-Shaped Te₈₄⁻ Rings and Cross-Shaped Te₅₆⁻ Units. *Inorganic Chemistry* **2009**, *48* (23), 10910-10912.
222. Patschke, R.; Kanatzidis, M. G., Polytelluride compounds containing distorted nets of tellurium. *Physical Chemistry Chemical Physics* **2002**, *4* (14), 3266-3281.
223. Zhang, X.; Li, J.; Foran, B.; Lee, S.; Guo, H.-Y.; Hogan, T.; Kannewurf, C. R.; Kanatzidis, M. G., Distorted Square Nets of Tellurium in the Novel Quaternary Polytelluride K_{0.33}Ba_{0.67}AgTe₂. *Journal of the American Chemical Society* **1995**, *117* (42), 10513-10520.
224. Mayasree, O.; Sankar, C. R.; Assoud, A.; Kleinke, H., New Barium Copper Chalcogenides Synthesized Using Two Different Chalcogen Atoms: Ba₂Cu_{6-x}S_{Te₄} and Ba₂Cu_{6-x}Se_yTe_{5-y}. *Inorganic Chemistry* **2011**, *50* (10), 4580-4585.
225. Zhang, X.; Kanatzidis, M. G., AMTeS₃ (A = K, Rb, Cs; M = Cu, Ag): A New Class of Compounds Based on a New Polychalcogenide Anion, TeS₃₂. *Journal of the American Chemical Society* **1994**, *116* (5), 1890-1898.
226. Schleid, T.; Klein, E. K., Nd₂S₂Te: Neodymium(III) Sulfide Telluride with Ce₂O₂S-Type Crystal Structure. *Zeitschrift für anorganische und allgemeine Chemie* **2001**, *627* (5), 807-808.
227. Hume-Rothery, W.; Powell, H. M., On the Theory of Super-Lattice Structures in Alloys. *Zeitschrift für Kristallographie - Crystalline Materials* **1935**, *91* (1-6), 23-47.
228. Troć, R.; Kaczorowski, D.; Shlyk, L.; Potel, M.; Noël, H., Crystal structure, magnetic and electrical transport studies of single crystals of the uranium mixed chalcogenides: US₂Se, U₂Te and USeTe. *Journal of Physics and Chemistry of Solids* **1994**, *55* (9), 815-823.
229. Luo, Z.-Z.; Lin, C.-S.; Cheng, W.-D.; Yang, Y.; Li, Y.-B.; Zhang, H.; Zhang, W.-L.; He, Z.-Z., Syntheses, crystal and electronic structures, and characterizations of the mixed anions compounds Ba₄In₂Te₂Q₅ (Q = S, Se). *CrystEngComm* **2013**, *15* (23), 4773-4778.
230. Hodges, J. M.; Xia, Y.; Malliakas, C. D.; Alexander, G. C. B.; Chan, M. K. Y.; Kanatzidis, M. G., Two-Dimensional CsAg₅Te_{3-x}S_x Semiconductors: Multi-anion Chalcogenides with Dynamic Disorder and Ultralow Thermal Conductivity. *Chemistry of Materials* **2018**, *30* (20), 7245-7254.
231. Madsen, G. K.; Singh, D. J., BoltzTraP. A code for calculating band-structure dependent quantities. *Computer Physics Communications* **2006**, *175* (1), 67-71.
232. Hong, M.; Chen, Z.-G.; Zou, J., Fundamental and progress of Bi₂Te₃-based thermoelectric materials. *Chinese Physics B* **2018**, *27* (4), 048403.
233. Pan, M.-Y.; Xia, S.-Q.; Liu, X.-C.; Tao, X.-T., Ba₃GeS₅ and Ba₃InS₄Cl: Interesting size effects originated from the tetrahedral anions. *Journal of Solid State Chemistry* **2014**, *219*, 74-79.
234. Assoud, A.; Soheilnia, N.; Kleinke, H., The new semiconducting polychalcogenide Ba₂SnSe₅ exhibiting Se₃₂⁻ units and distorted SnSe₆ octahedra. *Journal of Solid State Chemistry* **2005**, *178* (4), 1087-1093.
235. Zelinska, M.; Assoud, A.; Graf, C.; Kleinke, H., Reversible Reconstructive Phase Transition of Ba₂SnSe₅: A New High Temperature Modification with Completely Different Structural Motifs. *Inorganic Chemistry* **2010**, *49* (3), 1090-1093.
236. Graf, C.; Assoud, A.; Zelinska, M.; Kleinke, H., The metastable m-Ba₂SnSe₅ – Synthesis, Phase Transition, Crystal Structure, Structural Relations and Electronic Structure *Zeitschrift für anorganische und allgemeine Chemie* **2010**, *636* (9-10), 1821-1826.
237. Li, J.; Liszewski, Y. Y.; MacAdams, L. A.; Chen, F.; Mulley, S.; Proserpio, D. M.,

Synthesis and Characterization of Ba₂SnTe₅: A New Zintl Phase Containing Unique One-Dimensional Chains of (SnTe₃)₂- and Dimeric Units of (Te₂)₂. *Chemistry of Materials* **1996**, *8* (3), 598-600.

238. Duan, R.-H.; Liu, P.-F.; Lin, H.; Huangfu, S.-X.; Wu, L.-M., Syntheses and characterization of three new sulfides with large band gaps: acentric Ba₄Ga₄SnS₁₂, centric Ba₁₂Sn₄S₂₃ and Ba₇Sn₃S₁₃. *Dalton Transactions* **2017**, *46* (43), 14771-14778.

239. Pocha, R.; Johrendt, D., Crystal Structures of Sr₄Sn₂Se₉ and Sr₄Sn₂Se₁₀ and the Oxidation State of Tin in an Unusual Geometry. *Inorganic Chemistry* **2004**, *43* (21), 6830-6837.

240. Kugimiya, K.; Steinfink, H., Influence of crystal radii and electronegativities on the crystallization of AB₂X₄ stoichiometries. *Inorganic Chemistry* **1968**, *7* (9), 1762-1770.

241. Susa, K.; Steinfink, H., Ternary sulfide compounds AB₂S₄: The crystal structures of GePb₂S₄ and SnBa₂S₄. *Journal of Solid State Chemistry* **1971**, *3* (1), 75-82.

242. Jumas, J.-C.; Philippot, E.; Vermot-Gaud-Daniel, F.; Ribes, M.; Maurin, M., Etude de la tétracoordination de l'étain dans deux orthothiostannates: Na₄SnS₄ et Ba₂SnS₄ (α). *Journal of Solid State Chemistry* **1975**, *14* (4), 319-327.

243. Wu, K.; Su, X.; Yang, Z.; Pan, S., An investigation of new infrared nonlinear optical material: BaCdSnSe₄, and three new related centrosymmetric compounds: Ba₂SnSe₄, Mg₂GeSe₄, and Ba₂Ge₂S₆. *Dalton Transactions* **2015**, *44* (46), 19856-19864.

244. Pocha, R.; Tampier, M.; Hoffmann, R.-D.; Mosel, B. D.; Pöttgen, R.; Johrendt, D., Crystal Structures and Properties of the Thiostannates Eu₂SnS₄ and Sr₂SnS₄ and the Selenogermanate γ-Sr₂GeSe₄. *Zeitschrift für anorganische und allgemeine Chemie* **2003**, *629* (7-8), 1379-1384.

245. Li, J.; Guo, H.-Y.; Proserpio, D. M.; Sironi, A., Exploring Tellurides: Synthesis and Characterization of New Binary, Ternary, and Quaternary Compounds. *Journal of Solid State Chemistry* **1995**, *117* (2), 247-255.

246. Assoud, A.; Soheilnia, N.; Kleinke, H., From yellow to black: new semiconducting Ba chalcogeno-germanates. *Zeitschrift für Naturforschung B* **2004**, *59* (9), 975-979.

247. Grzybowski, T., High-Pressure X-Ray and Optical Studies of BaSe and BaTe. *High Pressure in Science and Technology. III.--General Topics* **1983**, 43-47.

248. Kawada, I.; Kato, K.; Yamaoka, S., Barium disulphide. *Acta Crystallographica Section B* **1975**, *31* (12), 2905-2906.

249. Luo, Z.-Z.; Lin, C.-S.; Cheng, W.-D.; Zhang, H.; Zhang, W.-L.; He, Z.-Z., Syntheses, Characterization, and Optical Properties of Ternary Ba–Sn–S System Compounds: Acentric Ba₇Sn₅S₁₅, Centric BaSn₂S₅, and Centric Ba₆Sn₇S₂₀. *Inorganic Chemistry* **2013**, *52* (1), 273-279.

250. Luo, Z.-Z.; Lin, C.-S.; Zhang, W.-L.; Zhang, H.; He, Z.-Z.; Cheng, W.-D., Ba₈Sn₄S₁₅: A Strong Second Harmonic Generation Sulfide with Zero-Dimensional Crystal Structure. *Chemistry of Materials* **2014**, *26* (2), 1093-1099.

251. He, T.; Sun, W.; Huo, H.; Kononova, O.; Rong, Z.; Tshitoyan, V.; Botari, T.; Ceder, G., Similarity of Precursors in Solid-State Synthesis as Text-Mined from Scientific Literature. *Chemistry of Materials* **2020**.

252. Phelan, W. A.; Zahn, J.; Kennedy, Z.; McQueen, T. M., Pushing boundaries: High pressure, supercritical optical floating zone materials discovery. *Journal of Solid State Chemistry* **2019**, *270*, 705-709.

253. Wunderlich, B.; Shu, H.-C., The crystallization and melting of selenium. *Journal of Crystal*

Growth **1980**, 48 (2), 227-239.

Curriculum Vitae

Rebecca D. McClain

2145 Sheridan Rd. | Evanston, IL 60208
rmcclain@u.northwestern.edu | (214)755-2416

Education

- Northwestern University**, Evanston IL 2016 – Present (Expected in 2021)
Chemistry PhD Candidate
Advisor: Professor Mercuri Kanatzidis
Research Project: “Panoramic Synthesis of Multinary Semiconductor Chalcogenides”
- Wellesley College**, Wellesley, MA May 2013
B.A. Chemistry (Honors), *Magna Cum Laude*

Research and Work Experience

Graduate Research Assistant, Northwestern University | Evanston, IL Sept. 2016 – Present
Mercuri Kanatzidis, Department of Chemistry

- Study new and known multinary chalcogenides using in-situ powder X-ray diffraction to understand the progression of solid-state reactions and how the reaction pathway influences product identity and formation.
- Elucidate design factors for formation of multinary chalcogenides for potential use in optical or thermoelectric applications.
- Conduct exploratory solid-state synthesis and discovered six new chalcogenide materials, which were subsequently characterized using X-ray diffraction (powder and single crystal), scanning electron microscopy, energy dispersive spectroscopy, thermal gravimetric analysis, and diffuse reflectance spectroscopy.
- Discovered four intermediate phases and developed novel synthetic routes to isolate observed phases.
- Wrote several successful national lab proposals and conducted six variable temperature synchrotron powder X-ray diffraction experiments at the Advanced Photon Source at Argonne National Laboratory.

R&D Chemist, ZS Pharma, Inc. | Coppell, TX Oct. 2014 – July 2016
Research & Development Department

- Conducted exploratory syntheses of microporous materials through hydrothermal methods.
- Assessed potential of company-patented compounds for potential ion-exchange applications.
- Developed characterization methods for materials based on the proprietary selective ion-trap technology.
- Trained in cGxP experimental planning and documentation for research work in a pharmaceutical environment.

Fulbright Fellow, Technische Universität Braunschweig | Braunschweig, Germany Oct. 2013 – July 2014

Georg Garnweitner, Institute for Particle Technology

- Established the influence of non-aqueous synthesis on the catalytic activity of perovskite nanomaterials in metal-air battery systems.
- Developed solvothermal syntheses for perovskite nanomaterials and characterized them via X-ray diffraction.
- Devised protocol for electrochemical measurements using a rotating disk electrode set-up.

Undergraduate Research Assistant, Wellesley College | Wellesley, MA Feb. 2012 – May 2013

Nolan Flynn, Department of Chemistry

- Developed new synthetic protocol for iron oxide core-gold shell nanoparticles to be used in therapeutic platform for targeted cancer therapy.

Distinctions and Fellowships

2019	Margaret C. Etter – Student Lecturer Award (for oral presentation at ACA Conference)
2017 – 2018	Hierarchical Materials Cluster Program Fellowship
2013 – 2014	Fulbright Fellowship – U.S. Student Program
2013	Dudley Folk Templeton Senior Prize (Awarded for accomplished writing on Religion)
2012 – 2013	Jerome A. Schiff Fellowship (\$2000 merit award for outstanding senior honors thesis)
2011	Organic Chemistry Award (for high achievement in organic chemistry)
2010	First Year Chemistry Award (for high achievement in general chemistry)

Manuscripts and Presentations

McClain, R., Shen, J., Malliakas, C. D., Wolverton, C., Kanatzidis, M. G. Mechanistic studies of two divergent synthesis routes forming the heteroanionic BiOCuSe. *Journal of the American Chemical Society*. 2021, *31*, 12090-12099.

Zhang, C., He, J., **McClain, R.**, Xie, H., Cai, S., Walters, L., Shen, J., Rondinelli, J., Kanatzidis, M. G. Wolverton, C., Dravid, V. Y., Poeppelmeier, K. R. Hydrothermal Synthesis of BiOAgSe and its Origin of Ultralow Thermal Conductivity. *In preparation*.

McClain, R., Malliakas, C. D., Shen, J., He, J., Wolverton, C., Gonzalez, G. B., Kanatzidis, M. G. Mechanistic Insight of KBiQ₂ (Q= S, Se) using Panoramic Synthesis towards Synthesis-by-Design. *Chemical Science*. 2021, *12*, 1378-1391.

Hoffman, J. M., Malliakas, C. D., Sidhik, S., Hadar, I., **McClain, R.**, Mohite, A. D., Kanatzidis, M. G. Long periodic ripple in a 2D hybrid halide perovskite structure using branched organic spacers. *Chemical Science*. 2020, *11*, 12139-12148.

Chen, H.; **McClain, R.**, He, J., Zhang, C., Olding, J. N., dos Reis, R., Bao, J.-K., Hadar, I., Spanopoulos, I., Malliakas, C. D., He, Y., Chung, D. Y., Kwok, W.-K., Weiss, E. A., Dravid, V. P., Wolverton, C., Kanatzidis, M. G. Antiferromagnetic Semiconductor BaFMn_{0.5}Te with Unique

Mn Ordering and Red Photoluminescence. *Journal of the American Chemical Society*. 2019, *141*, 17421–17430.

McClain, R., Kanatzidis, M. G. Mechanistic Insight of KBiQ_2 (Q= S, Se) using Panoramic Synthesis towards Synthesis-by-Design. *Oral Presentation* at American Crystallography Association, Covington, KY, July 2019.

McClain, R., Kanatzidis, M. G. Mechanistic Insight of KBiQ_2 (Q= S, Se) using Panoramic Synthesis towards Synthesis-by-Design. *Poster Presentation* at North American Solid-State Chemistry Conference, Golden, CO, July 2019.

Pedagogical Training

Teaching Certificate Program, Northwestern University Sept. 2020 – 2021

- Design a course in discipline of materials chemistry, including developing a course outline, sample lesson plan, sample assessment, grading scheme, evaluation plan, and interpretation of teaching effectiveness.
- Participate in 12+ seminars and workshops on learning- and teaching-related topics.

Evidenced-Based Undergraduate STEM Teaching (MOOC), CIRTL Fall 2019

- Learned fundamental elements of course design, including development of learning objectives and assessments aligned with those learning objectives.
- Created a lesson plan for an advanced class on x-ray diffraction, incorporating high-impact, evidence-based effective instructional practices.

Mentored Discussions of Teaching, Northwestern University Fall 2017

- Observed Northwestern chemistry faculty teaching undergraduate, post-baccalaureate course.
- Discussed pedagogical approaches to engaging and teaching post-baccalaureate students.

Teaching Experience

Course Facilitator, Northwestern University | Evanston, IL Winter 2021

Northwestern Prison Education Program – CHEM 242: Thermodynamics

- Coordinated and prepared weekly homework packets and worksheets for teaching via correspondence at Stateville Correctional Center in Crest Hill, IL.
- Oversaw tutors of incarcerated students enrolled in the course and addressed individual student concerns or questions that arose in their weekly letters to their tutors.

Teaching Assistant, Northwestern University | Evanston, IL Summers 2017 – 2020

Bridge Program

- Organized and led extended problem-solving sessions for 15-20 incoming first-generation and/or low-income students in general chemistry for a two-week intensive pre-orientation program.
- Graded assigned problems and provided detailed feedback to students on where their problem solving may have gone array, which was repeatedly commended in end-of-program student feedback.

“Super” Teaching Assistant, Northwestern University | Evanston, IL Fall 2016; Fall 2017
CHEM 110

- Contributed significantly to developing a new general chemistry course (CHEM 110) focusing on quantitative reasoning for general chemistry, including mini-projects introducing excel soft skills as well as graph interpretation and formulation.
- Wrote assessments (weekly quizzes, midterms, and final exam) and weekly homework assignments. The homework assignment included a “warm-up” section with single-concept problems to assist in student-learning of the concept at all stages.
- Led and managed 10+ teaching assistants, review sessions, and grading sessions.

CHEM 101

- Wrote assessments (weekly quizzes, midterms, and final exam) for 450+ student general chemistry course.
- Prepared and held multiple review sessions in preparation for exams and weekly office hours.
- Led and managed 15+ teaching assistants (TAs) as well as provided additional practice problems for TAs to review during their recitation.

Teaching Assistant (Recitation, Lab), Northwestern University | Evanston, IL Winter 2017;
Winter 2019

- Prepared and delivered content for review in recitation or laboratory lectures to reinforce course content.
- Oversaw quizzes administered in recitation and student laboratory work during laboratory assignments.

Leadership in Outreach

Board Member, Graduate Liaison Committee, Northwestern University 2017 – 2021

- Identify and execute projects and events as a committee to facilitate faculty-student interaction, promote department community, and enhance graduate student experience. Write and analyze surveys to determine opportunities for improvement within the department.
- Personally devised and implemented annual First-Year Check-Ins and quarterly ChemConnect event to build community within a cohort as well as the Chemistry Department with 300+ graduate students and post-doctoral fellows.

Service Chair, Phi Lambda Upsilon, Northwestern University 2018 – 2019

- Coordinated and oversaw outreach and service events, including an outreach program of 20+ volunteers that holds six yearly science lessons for 130 third grade students.
- Redesigned and streamlined in-class worksheets to emphasize key concepts and vocabulary according evidenced-based teaching methods.
- Recruited STEM graduate students outside the Chemistry Department as volunteers for the first time for yearlong outreach program for 3rd and 4th grades at local Chicago elementary school.